# JSR A

## JOURNAL OF
# SCIENTIFIC REPORTS A

JOURNAL OF SCIENTIFIC REPORTS A · DECEMBER 2021 · NUMBER 47

gate of
science

Journal of Scientific Reports-A started its publication life in 2000 as name of Journal of Science and Technology of Dumlupınar University and is a national peer-reviewed journal published regularly twice a year in June and December. The language of the journal is English. Articles submitted to the journal are evaluated by at least two referees who are experts in the subject and selected by the editorial board. All articles submitted to the journal are evaluated by the double-blind method. Articles submitted to our journal for review should not be previously published, accepted for publication and in the process of being evaluated for publication in another journal. All responsibility for the articles published in the journal belongs to the author(s).

The journal aims to share scientific studies carried out in the fields of science and engineering at national and international level with scientists and the public. Original research articles, review articles and short notes in science and engineering disciplines are accepted for the journal. Original research articles are expected to contain theoretical and experimental results and should not be published in other journals. In the review articles, it is expected that scientific, technological and current developments on a specific subject are reflected by using an extensive bibliography and made a satisfying evaluation of these. Short notes should be brief writings prepared to announce the first findings of an original study.

**Editorial Policy**
The journal is open access and the article evaluation period is between 2-3 months.

**Advisory Board**

# JOURNAL OF SCIENTIFIC REPORTS-A
## E-ISSN: 2687-6167

## CONTENTS

**RESEARCH ARTICLES**

## RESEARCH ARTICLES

**RESEARCH ARTICLES**

*RESEARCH ARTICLE*

# RESERVOIR-TARGETED OIL and GAS EXPLORATION in METAMORPHIC and MAGMATIC ROCKS of the NİĞDE MASSIF (CENTRAL ANATOLIA, TURKEY)

Adil OZDEMIR[1,*], Alperen ŞAHİNOĞLU[2], Yildiray PALABIYIK[3], Atilla KARATAŞ[4]

[1] Ataturk University, Division of Geological Engineering, Erzurum, adilozdemir2000@yahoo.com,
ORCID: 0000-0002-3975-2846
[2] Istanbul Esenyurt University, Institute of Science and Technology, İstanbul, alperensahinoglu@esenyurt.edu.tr,
ORCID: 0000-0002-1930-6574
[3] Istanbul Technical University, Department of Petroleum and Natural Gas Engineering, İstanbul, palabiyiky@itu.edu.tr,
ORCID: 0000-0002-6452-2858
[4] Marmara University, Department of Geography, İstanbul, atilla.karatas@marmara.edu.tr,
ORCID: 0000-0001-9159-6804

## ABSTRACT

Basement rock reservoirs are a special type of oil and/or gas reservoir, which has been usually neglected until recently as a target for exploration. In this study, it is aimed to investigate the hydrocarbon potential of Niğde Massif. The n-alkane hydrocarbons found in the water samples collected are the mature petroleum hydrocarbons, which are the geochemical evidence for a working petroleum system in the study area. The dom structures in which they are suitable to be entrapped and protected for hydrocarbons in a predominantly SW-NE orientation, where metamorphic rocks in which granite has been located in its center have formed, is the possible hydrocarbon reservoir in the study area. The geochemical exploration methodology used in this study may be a new method that can eliminate the discovery of hydrocarbons in the metamorphic massif and granitic rocks by chance.

**Keywords:** *Basement rock, Metamorphic rock, Granite, Reservoir-targeted oil and gas exploration, Hydrocarbon-rich water*

## 1. INTRODUCTION

There are many metamorphic and granitic oil and gas production fields in the world including giant reservoirs [1-9]. Nelson [5] presented a list of 370 fields where substantial amounts of hydrocarbons are produced from basement rocks. It is estimated that only BP Amoco has produced 21 billion barrels of oil to date. Moreover, oil discoveries have been performed in fractured granitic and metamorphic rocks in the Masila basin (Yemen) [10]. So far, 100 million barrels of oil have been produced from basement rocks in Venezuela, California (USA), Kansas (USA), and Morocco. Initial productions are as high as 17,000 barrels per day and most of the reservoirs are fractured metamorphic and magmatic rocks. The trapping mechanism has been caused by an anticline or a formation structure with heterogeneous permeability. All the known base rock hydrocarbon accumulations are located at higher elevations than those of the sediments around the basement rock. The sedimentary cover on the basement rock may or may not contain petroleum reservoirs. Oil and gas reservoirs in most basement

rocks were found by chance [2,3]. Parnell [11] examined granitic plutons containing biogenic hydrocarbons in the onshore UK and the migration of those hydrocarbons to these plutons while McNaughton [1], P'an [3], and Harrelson [4] investigated the migration and accumulation conditions of hydrocarbons in magmatic and metamorphic rocks in terms of geological perspective. In Mesozoic-Cenozoic rift basins in Eastern China [12-14], Southeast Asia [15-18], and North-South America [6,19,20], the fractured basement reservoirs were discovered. Hydrocarbons are produced from fractured Precambrian crystalline basement rocks in North Africa, in the Sirte basin of Libya [21,22], and in the Suez Gulf [23,24]. Most of these reservoirs were discovered by chance because the basement rocks are not primary targets in petroleum exploration. Historically, hydrocarbon accumulations in the basement rocks were generally discovered 10 to 30 years later after a certain amount of petroleum had been produced from the sedimentary rocks overlying them. For instance, the La Paz-Mara field in the Maracaibo basin in Venezuela [19] can be given as a good example for such a discovery. However, the Lancaster, 205 West in West of Shetland [25,26], and the Jinzhou 25-1S site in the Bohai basin [14,27] are some basement rock reservoirs that were discovered by a consequence of consciously basement-targeted explorations. To sum up, it has been revealed that the only way to discover oil and gas reservoirs in basement rocks does not have to be a coincidence.

The standard definition of crystalline basement rock was made by petroleum geologists as any metamorphic or magmatic rock having unconformity with a sedimentary sequence. However, it is not necessary that crystalline rocks were not subject to significant metamorphism or older ones than sedimentary covers [28]. A more suitable definition for the crystalline basement was performed by Landes et al. [2]. According to this definition, oil-generating formation (source rock) is not located below the basement rock reservoir. In basement rock reservoirs, the generally accepted theory for oil migration is "upward orientation" [1]. The examples of hydrocarbons that form a basement rock reservoir by migrating to older porous metamorphic or magmatic rocks are the Japanese volcanic reservoirs, oilfields of the Mexico and the Maracaibo basin in Venezuela [29]. Excessively and long-term regional erosion of basement uplifted and the presence of younger sediments that serve as a source of hydrocarbons on faulted limbs fallen down or directly situated on the fractured basement and provide an opportunity for trapping of petroleum in the basement rock are suitable conditions for exploration of basement rock reservoirs [4,10]. Basement rock reservoirs are a special type of oil and/or gas reservoir, which have been usually neglected until recently as a target for exploration. Most of the basement rock reservoirs are formed either in platforms or in intermontane basins whereas they are rare in foredeep basins. They always occur at high elevations within a basin or subsequent uplifts and are exposed as a consequence of long-time erosion and weathering phenomena. Petroleum can accumulate in sandstones and carbonate rocks containing secondary cracks, caves, or primary porosity, or in any magmatic, metamorphic, or sedimentary rock. Carbonates are the best basement rock reservoirs among the formations mentioned above because they are hard and brittle and do not only tend to develop secondary cracks, but also easily dissolve in groundwater. Thus, primary pores can expand and new porosity can be formed. Basement reservoirs are characterized by thick formations and porosity and permeability of the rock exhibit heterogeneous distributions. Production obtained from those types of reservoirs is generally high and the reserves are large [2,3,28]. Fractured basement reservoirs in areas near the active faults have a high potential of hydrocarbon production [30].

Ozdemir and Palabiyik [31-34] stated that accumulations, which are capable of occurring operable-size metallic ore deposits, have a shallow and reliable indicator for hydrocarbon deposits. There are Gümüşler mercury deposit in the Niğde Massif that were operated in the past [35]. All major mercury

deposits in Turkey are epithermal and was occurred in the depth varying from 1 to 600 m by the upwelling of hot fluids (50°C to 200°C). The ore is located in veins or disseminated in sandstones and schists [35,36]. Oil or bitumen was found in the mercury deposits [37-40]. Bailey [41] and Shabo et al. [42] suggested that cinnabar (HgS) and bitumen precipitated by a common fluid. The presence of bitumens with mercury ores together has led to the assumption that mercury is precipitated by organic matter. However, in many cases, mercury appears along with oil rather than solid bitumen [43]. Chakhmakchev et al. [44] reported that mercury is enriched in light oil while many other metals are in heavy oil. Mueller [37] suggested that near-surface and low-pressure conditions prevalent during mercury mineralization are appropriate for the accumulation of a series of organic deposits specific to this mineralization. The maximum concentrations of bitumen in organic matter have been determined to be associated with the highest mercury content mineralization. Mercury is abundant in oil and gas fields and an important data used for hydrocarbon exploration [43,45,46]. In particular, formation waters of gasfields contain high amounts of mercury [45].

Until now, no research hasn't been conducted on the oil and gas potential of massifs and granitic plutons in different ages which cover expansive areas in Turkey. It was reported by Erentöz and Ternek [47] that there was an oil seep in the southeast of the Niğde Massif. Therefore, in this study, it is aimed to investigate the oil and gas potential of Niğde Massif by conducting TPH (total petroleum hydrocarbon) analyses on the samples taken from massif and the natural cold-water resources surrounding it (Fig. 1). As a result of analyses, mature petroleum hydrocarbons, which are evidence for the working petroleum system in the study area.

## 2. GEOLOGICAL SETTING

The Anatolian region is a part of the Alpine-Himalayan orogenic belt and today the outcropping rocks in regions contain the geological records of the closure history of the Neotethys ocean as a result of the convergence of the African-Eurasian continents during the Late Mesozoic-Cenozoic period. The location of the ophiolite mélange which outcrops along the Izmir-Ankara-Erzincan Suture Zone (IAESZ) indicates the location of the northern branch of the Neotethys. The Central Anatolian Crystalline Complex (CACC) consisting of metamorphic rocks, magmatic intrusions, and ophiolites located in the south of the IAESZ are the largest metamorphic complex which outcropped in Turkey. This crystalline complex has been subjected to complex tectonic events such as the local Barrovian metamorphism and magmatic intrusion, in which the ophiolite nappes has settled on Paleozoic-Mesozoic sedimentary units in the Late Cretaceous. However, in the previous metamorphic, magmatic and structural studies in the Central Anatolia Region, no consensus has been reached on the geodynamic evolution of the CACC in the Cretaceous [48].

The Niğde Massif, which is the study area, forms the southern end of the CACC under the influences of the Tuz Gölü Fault (TGF) Zone, the Ecemiş Fault Zone (CAFZ), and the Niğde Fault Zone (Fig. 1). The Niğde Massif is located on the southern boundary between the Anatolides and the Taurides in terms of its geotectonic position. It is the common opinion of all the geologists who studied in the massif that the Alpine orogenesis completed its development during the Laramian phase. During granite intrusion into the massif, dome structures and important fracture systems developed [49]. The Niğde Fault is an NW-SE trending fault zone consisting of at least three possible segments parallel to each other. The northwestern margin of the Niğde Massif is the fault escarpmentness that regressed in the SE direction during the Middle Miocene - Lower Pliocene [50]. Tuz Gölü and Ecemiş Faults are strike-slip and Niğde Fault is dip-slip. The presence of thick slope debris on the northwest of the

massif supports this opinion. The massive limited by the Ecemiş Fault (CAFZ) from the east and the Tuz Gölü Fault (TGF) from the west have been subjected to large tectonic effects. The Ulukışla Sedimentary Basin is located in the south of the massif (Fig. 1).
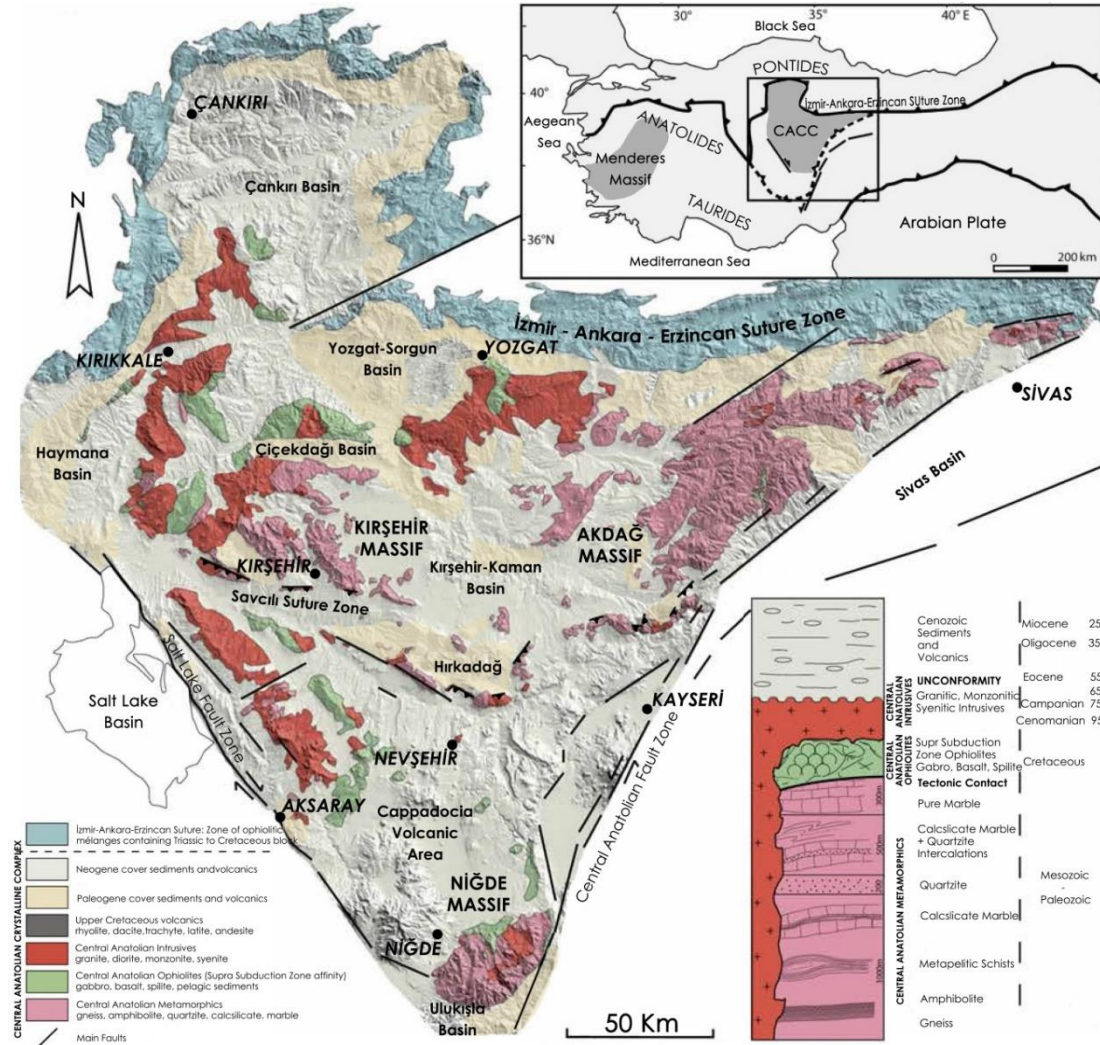


**Figure 1.** Geological map of the study area and its surroundings (modified from [48]).

The metamorphic rocks constituting the Niğde Massif have formed a largely irregular dome defined by slightly inclined foliation surfaces. The dom center is in the northwestern part of the region. The lower part of the metamorphic series consists mostly of paragneisses and mica schists subjected to partial melting in varying degrees. In the higher parts of the series, recrystallized quartzites and marbles are commonly dominant. In the massif, granitoids are abundant and show various degrees of deformation. The main intrusion is represented by Üçkapılı Granite and its associated dyke flock. In addition to these units, there are ophiolitic rocks. The ophiolites in the southern part of the massif are

located as thin slices at higher levels of the high-grade metamorphic unit [51]. Low-grade metamorphic rocks form the autochthonous cover of the massif. These units are tectonically covered by flyschoid sediments and island arc rocks. The youngest units of the region are continental and volcanic rocks. The Niğde Massif metamorphics have undergone ductile deformation and folding at least in four stages. In the first stage, the rocks of the massif were folded as flat-isoclinal and foliated structure parallel to the axis planes. Due to the isoclinal and severe folding of the layer planes of the rocks, layer transposition developed and plain folding structures were formed. In the second stage, NE-SW oriented and both northeast and southwest dipped folds were developed by deformation. As a result of the interference of the folds, mushroom-like folds were formed in the region. The mesoscopic folds in the second stage are congested-isoclinal geometry and offer asymmetric and curved folds. As a consequence of the folding in the 3rd stage, a large dom structure has been developed in the region. The folds in the 4th stage have formed sinform and antiform structures, which are approximately perpendicular to the 2nd stage, and NW-SE trending and dipping to the southeast. The deformation has occurred in the 4th stage and the basement and cover rocks have been jointly deformed. Microscopic analysis shows that the Cretaceous-Eocene rocks were metamorphosed at low-grade greenschist facies by deformation at this stage. The geometry of the end-stage folds reflects the folding pattern specific to the regions where the basement and cover rocks are deformed together [52].

## 3. HYDROCARBON SHOWS IN THE REGION

In the adjacent basins of the study area, Ulukışla and Tuz Lake Basins (Fig. 1), there have been studies for petroleum geology purposes, and many hydrocarbon shows are available (Fig. 2). The units of the Ulukışla Basin are continuous from Upper Cretaceous to Miocene, although they exhibit local unconformities. In these sequences, the units with the characteristics of petroleum source rock, reservoir rock, and cover rock exist [53-55]. The data obtained from the wells drilled in the Ereğli-Bor Basin [56], which is a sub-basin of the Tuz Gölü Basin, are the most important signs of the oil generation in the region. As a result of the surveys initiated by MTA in 2006, 15 wells were drilled totally in the region. In 10 wells, petroleum shows were encountered and thick oil shale levels were drilled. Within the scope of the project, in 2007, a deep exploration well (NBK-07/02) of 1168.4 meters in depth, which was drilled to the north of Badak Village (Bor province), liquid crude oil was found between 1035.0 and 1168.4 meters (Fig. 2). The crude oil was occasionally observed in the drilling mud as well. In addition, in 2008, liquid crude oil and oil shale were observed in 8 wells drilled around Yeniköy and Acıkuyu Villages (Ereğli). In KEY-08/02 core drilling in Yeniköy Village (from 437.8 meters) and in KEY-08/04 core drilling in Acikuyu Village (from 350 meters), oil shale levels and liquid crude oil shows emerged (Fig. 2). Crude oil is in the liquid form and dense, and is located in the cracks and pores between the foliations of dolomites, siltstones, and oil shales in Upper Miocene lacustrine deposits in the basin (Fig. 3). Crude oil and oil shales are in a 171-meter zone between 437.8-608.7 meters. While the oil shales reach a total thickness of 85 meters in the Yeniköy well, it has 55 meters thick in the Acıkuyu Village well. In the other drillings in the basin, the average oil shale levels of 40 meters thick have been met. The fact that oil shales were drilled in all the wells in the basin and that the oil shales are observed at an average thickness of 40 meters indicate that this basin has significant oil shale reserve. The potential reserve is reported as 8 billion tons [57]. Oil shales in the basin spread over a large area of approximately 100 km$^2$ [58]. The effect of increasing temperature and pressure with the burial of oil shales which is suitable for oil generation depending on the types of kerogen, and the circulation of hydrothermal solutions caused by young volcanic activities in the basin have caused significant oil generation and primary migration [59].

**Figure 2.** The hydrocarbon shows in the study area and its surroundings. Red polygon: Niğde Massif, yellow circles: the water samples, turquoise triangle: hydrocarbon show indicated by Erentöz and Ternek [47], black squares: shallow and deep wells also indicating hydrocarbon shows in the region, Hg: formerly operated Gümüşler mercury mine.



**Figure 3.** Views of oil shales and crude oil encountered in mineral exploration drilling in Ereğli-Bor Basin [59].

Sağlam [58] expressed that according to the average TOC amount of 4.72% and oil potential values obtained from the analysis results of 5 oil shale core samples taken during the drilling studies performed in the Ulukışla Basin, those formations have excellent hydrocarbon source rock potential. Besides, as the burial depth and TOC amount of oil shales in Acıkuyu (Ereğli) Village increase, oil and gas yield increase, the gas yield is higher than oil yield, and this result is thought to be caused by the kerogen types (Type II-III) (Fig. 2). Another finding of the same study indicates that oil and gas loss may be up to 0.5% if oil shale samples are kept in the open air for more than one week, and in some cases, this loss may be even greater. It has also considered that the samples had been waiting for 3 months in the open air before the experiment and the results obtained from the analyses might have been adversely affected under these conditions. In this case, it has been stated that the analysis results (oil and gas yield) obtained from the original samples taken from the subsurface should be higher than the determined values. Pusat [55], Sonel and Sarı [54], and Sonel et al. [53] expressed that various

units in Ulukışla Basin have hydrocarbon source rock and reservoir rock potential. Besides, the map of gas outflow locations given by Sağlam [58] contains important data for the presence of a petroleum system in the region. TG-9 well having the depth of 1770 m drilled in 1979 and TG-10 well having the depth of 2075 m drilled in 1979 and 1980 for stratigraphic purposes in Eregli-Bor Basin by Turkey Petroleum Corporation (TPAO) were completed as dry wells [60]. Seismic, gravity, and magnetic studies were carried out by TPAO in the basin after the determination of significant petroliferous levels in core drillings in Badak (Bor), Yeniköy, and Acıkuyu (Ereğli) villages. In 2008, exploration well (Bor-1) was drilled at a depth of 2500 meters (Fig. 2); however, no economic oil was discovered [57]. In Bor-1 well, Paleocene-Lower Eocene sandstone, shale, sandstone, and limestone units were passed through from the depths of 1750 m to 2500 m. These units are overlain by 250 m thick lithological units characterized by Oligocene sandstone, shale, and evaporite. At the top of them, Middle-Upper Miocene, Pliocene oil shale, dolomite, siltstone, sandstone, mudstone, anhydrite, salt, and shale units with a thickness of 1500 m are located [58,61].

Oil shales observed in the Ulukışla Formation were deposited in a shallow lake environment towards the Altay Village (Ulukışla) in the south of the basin. In the vicinity of the Altay Village, rather than oil shale, the transition to limestones containing dense crude oil-smelling freshwater fossils is observed. Therefore, the depth of the lake environment that deposited lacustrine Paleocene-Eocene units in the Bor-Ulukışla Basin increase from south to north and west to east. The levels containing crude oil which was encountered in the drilled wells firstly observed in Badak village (Bor) by MTA and then TPAO exist in oil shales (Fig. 2). Hence, the source rock in which the crude oil has been formed in the region is Miocene oil shale levels [58]. Sonel and Sarı [54] claimed that the rock samples taken from the Çiftehan (Upper Cretaceous), Halkapınar (Lower Paleocene-Lower Eocene), and Hasangazi (Middle-Upper Eocene) Formations have generated inconsiderable amount of gas and moderate amount of oil along with gas content at medium level and certain amount of oil and oil/gas and that the suitable conditions are available for hydrocarbon occurrence in Ereğli-Ulukışla Basin. The most important indicator for hydrocarbons in the Ulukışla Basin is the gas outflow in the water well in the Alpağut region (Ulukışla) (Figs. 2 and 4). Turkish Petroleum (TPAO) conducted TPH (Total Petroleum Hydrocarbons) analyses on the water samples taken from the water well containing a high amount of flammable gas in the depth of 130 m in Alpağut region and another water well which is located about 300 meters away from this well without gas outflow. According to the results of the analyses, the presence of n-alkane hydrocarbons in the C13-C40 carbon range has been detected in both water samples. The TPH values (4.50 and 7.49) of the water samples in the Ulukışla Basin are considerably higher than the recommended limit values for groundwaters. The water samples on which TPH analysis are conducted and gas sample taken from the same water well in Ulukışla have been compared with gas sample taken from Bor-1 well and correlations have been developed depending on those comparisons. According to bulk components and isotope analysis results, the sample taken from Ulukışla gas outflow and the gas sample taken from the Bor-1 oil well are located into the same area, which indicates that both samples are the products of a working petroleum system and have been featured by the thermogenic origin (Fig. 5). Besides, it was determined that the sample from Ulukışla gas seep was generated from the source rock containing highly mature Type-II kerogen, which shows that it is highly oil-prone. It has been evaluated that the Ulukışla gas sample could be generated from a source rock of about 1.50% V Ro maturity. This situation is supported by the fact that the Ulukışla gas sample was generated from Type-II kerogen characterized by the high-maturation level. In addition, it was observed that Ulukışla gas sample had a 5% biogenic gas mixture and this has been considered as a possible contribution for such a gas sample taken at a shallow depth of 130 m. The results of TPH analysis in regions as well as those of the organic geochemical analysis

of the gas samples in the region from where the water samples have been taken are compatible with each other [62].



**Figure 4.** The image of gas outflow in the water well in the Alpağut region (Ulukışla) and the locations of the wells from where the gas and water samples taken.
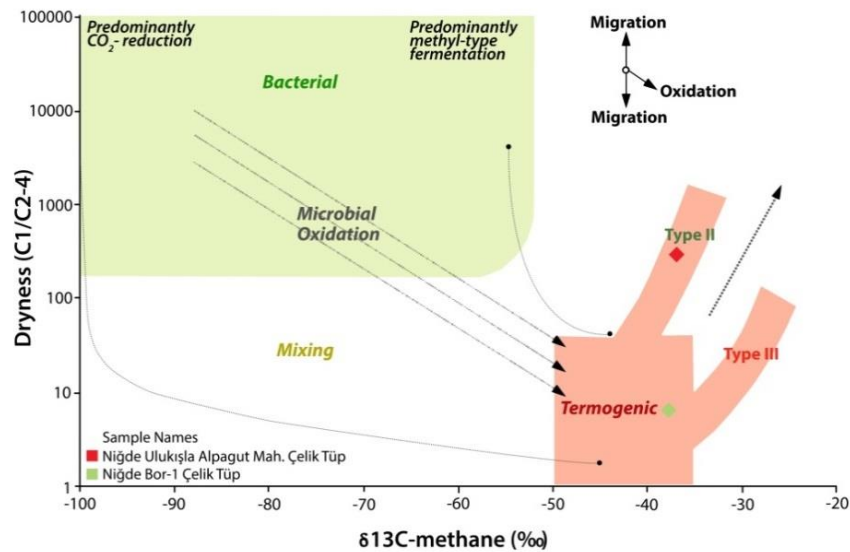


**Figure 5.** The origin of the gas samples taken from Ulukışla (Niğde) waterwell and Bor-1 (Niğde) oilwell [62].

## 4. FINDINGS AND DISCUSSION

### 4.1. Geochemical Findings

The study was based on the methods used and applied in the previous studies [63-66] as the material and the applied method. These studies contain detailed information. Hydrocarbon contents (Total Petroleum Hydrocarbons/TPH value) of water samples are extremely higher than the limit values that

should be found in surface and groundwater (Table 1) [63-66]. According to Carbon Preference Index (CPI), hydrocarbons sign the high-mature organic matter derived from terrestrial plants (Fig. 6). According to the NAR (Natural n-alkane Ratio) parameter (Table 1), the n-alkanes show natural petroleum hydrocarbons. Ph/n-C18 values of all the water samples are less than 1 and therefore, the hydrocarbons are non-biodegraded.

**Table 2.** Analysis results.

| Sample No | Water Resources | Coordinates X | Coordinates Y | TPH (mg/L) | CPI | NAR | TAR | n-C17/n-C31 | Waxiness İndex | Pr/Ph | Pr/n-C17 | Ph/n-C18 | n-alkane maximum |
|---|---|---|---|---|---|---|---|---|---|---|---|---|---|
| 1 | Natural flowing water | 4208407 | 662593 | 0.73 | 1.67 | 0.19 | - | 0.12 | - | 3.23 | 0.26 | 0.16 | C29 |
| 2 | Natural flowing water | 4204364 | 663056 | 0.49 | 1.64 | 0.06 | - | 0.11 | - | 13.30 | 0.32 | 0.06 | C29 |
| 3 | Natural flowing water | 4202047 | 663171 | 0.43 | 1.61 | 0.04 | - | 0.11 | - | 24.50 | 0.35 | 0.03 | C29 |
| 4 | Natural flowing water | 4203024 | 663201 | 0.68 | 1.63 | 0.04 | 6.42 | 0.32 | 4.32 | 9.18 | 0.19 | 0.07 | C29 |
| 5 | Natural flowing water | 4199235 | 666321 | 0.60 | 1.58 | 0.02 | 6.64 | 0.33 | 5.14 | 13.84 | 0.26 | 0.06 | C28 |
| 6 | Natural flowing water | 4198613 | 666693 | 0.47 | 1.62 | 0.03 | - | 0.12 | - | 9.04 | 0.29 | 0.06 | C29 |
| 7 | Natural flowing water | 4198190 | 666984 | 0.48 | 1.62 | 0.01 | 10.10 | 0.15 | 3.87 | 10.64 | 0.28 | 0.05 | C29 |
| 8 | Natural flowing water | 4196513 | 668288 | 0.75 | 1.62 | 0.05 | 10.10 | 0.19 | 3.94 | 7.83 | 0.23 | 0.08 | C29 |
| 9 | Natural flowing water | 4192745 | 671044 | 0.53 | 1.63 | 0.08 | - | 0.13 | - | 8.23 | 0.31 | 0.08 | C29 |
| 10 | Natural flowing water | 4187250 | 671945 | 0.54 | 1.62 | 0.08 | 10.61 | 0.15 | 3.04 | 10.55 | 0.38 | 0.07 | C29 |
| 11 | Natural flowing water | 4183998 | 667497 | 0.42 | 1.63 | 0.03 | - | 0.10 | - | 8.30 | 1.00 | 0.09 | C31 |
| 12 | Natural flowing water | 4183058 | 668410 | < 0.40 | 1.59 | 0.01 | - | 0.11 | - | - | 0.41 | - | C31 |
| 13 | Natural flowing water | 4184657 | 664998 | 0.60 | 1.68 | 0.01 | 11.47 | 0.14 | 3.88 | 10.94 | 0.29 | 0.06 | C31 |
| 14 | Natural flowing water | 4182373 | 664010 | 0.41 | 1.65 | 0.09 | - | 0.13 | - | 10.70 | 0.38 | 0.09 | C31 |
| 15 | Natural flowing water | 4177442 | 654394 | 0.41 | 1.57 | 0.07 | 10.22 | 0.16 | 4.54 | 7.86 | 0.37 | 0.12 | C31 |

CPI = {[(C23+C25+C27) + (C25+C27+C29)] / [2 *(C24+C26+C28)]} [67,68], TAR = (C27+C29+C31)/(C15+C17+C19) [69], NAR = [Σn-alk (C$_{19-32}$) - 2Σ even n-alk (C$_{20-32}$)] / Σ n-alk (C$_{19-32}$) [70], Waxiness Index = ∑ (n-C21-n-C31)/∑ (n-C15-n-C20) [71], - : Could not be calculated.

The parameter TAR (Terrestrial/aquatic hydrocarbon ratio) reflects the ratio of the n-alkanes derived from terrestrial organic matter to the n-alkanes derived from aquatic algae [69,72-74]. High TAR values (> 1) sign terrestrial plant source whereas its low values (< 1) refer to marine algae source [75]. They have been calculated as very high for the tested water samples (> 1) (Table 1) indicating that the n-alkanes with high carbon numbers representing terrestrial organic matter are dominant in the water samples in the study area.

Waxiness index can be used to determine the amount of terrestrial organic matter based on the assumption that regional terrestrial organic matter contributes to extracts with high molecular weight n-alkane components [71]. It is seen that the water samples in the investigation area show high Waxiness values reflecting high amounts of biomarkers derived from terrestrial plant (Table 1). This finding is also supported by the fact that the analyzed water samples exhibit high TAR values.

The n-C17/n-C31 ratio indicates the source of the organic matter-derived hydrocarbons in the environment. Its high values (> 2) show marine algae while its low values (< 2) indicate land plant sources [76]. The ratio of n-C17/n-C31 of the water samples ranged from 0.10 to 0.33, indicating the terrestrial organic matter. This result is also consistent with TAR and Waxiness values.

The source rocks which derived the hydrocarbons are deposited in the oxic terrestrial environment (Type-III kerogen) and are high mature level (Figs. 7-10). Sonel et al. [77] determined that the kerogen types of Halkapınar and Hasangazi formations containing turbiditic sequences of Ulukışla basin are predominantly Type-III (gas-prone). The results of this study are compatible with the results of the Sonel et al. [77] study, and hydrocarbons should be derived from highly mature parts of those formations mentioned above (Fig. 7).
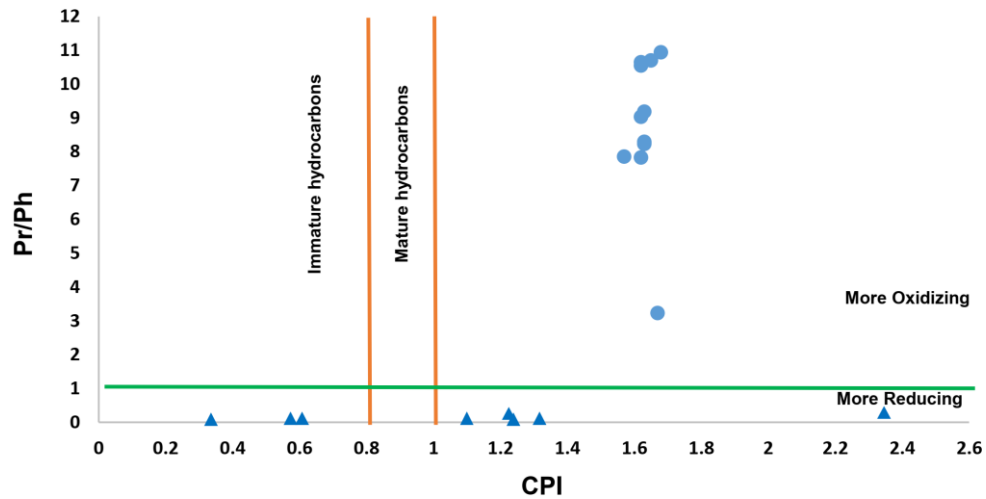
**Figure 6.** Pr/Ph vs CPI plot (the plot: from [78]). Blue circles: the water samples (this study), blue triangles: oil shales and crude oil samples obtained from Yeşilköy drillings [79].
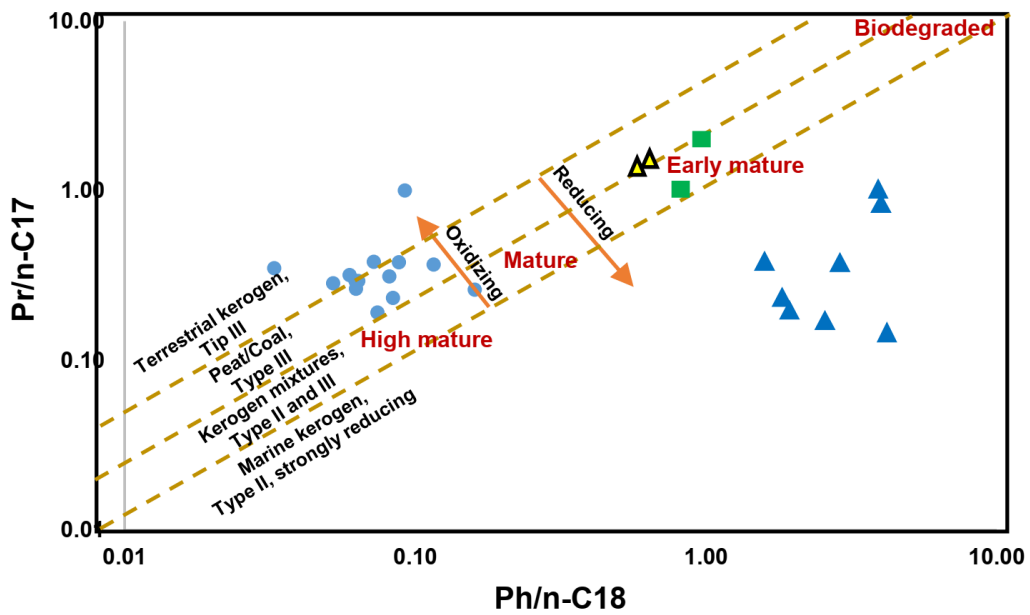


**Figure 7.** Pr/n-C17 vs Ph/n-C18 plot (the plot: from [80]). Blue circles: the water samples (this study), yellow triangles: source rock samples of Hasangazi formation [81], green rectangles: source rock samples of Halkapınar formation [81], blue triangles: oil shales and crude oil samples obtained from Yeşilköy drillings [79].
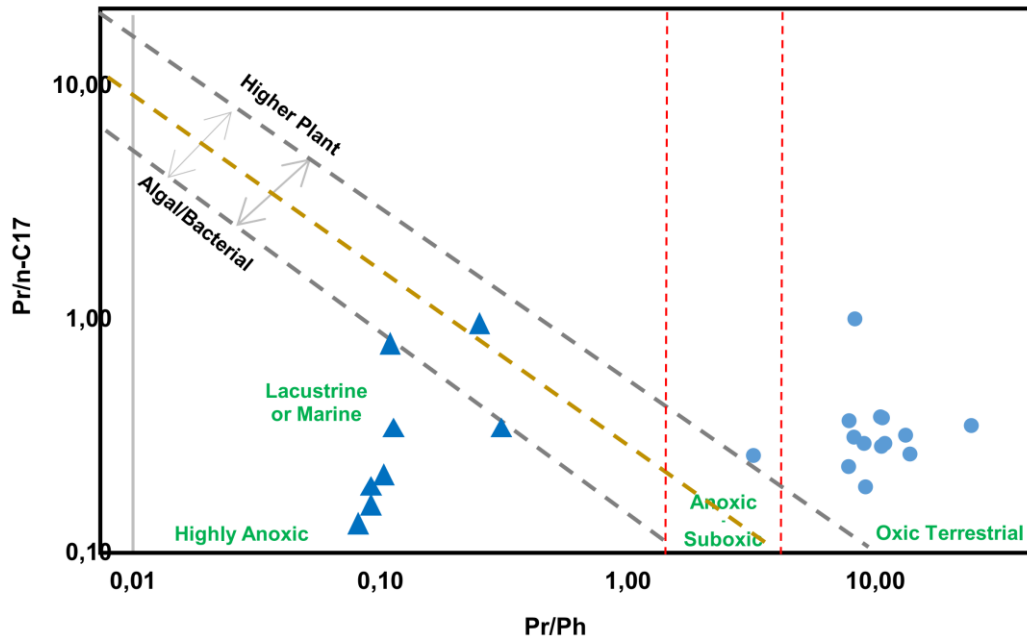
**Figure 8.** Pr/n-C17 vs Pr/Ph plot (the plot: from [82-84]). Blue circles: the water samples (this study), blue triangles: oil shales and crude oil samples obtained from Yeşilköy drillings [79].
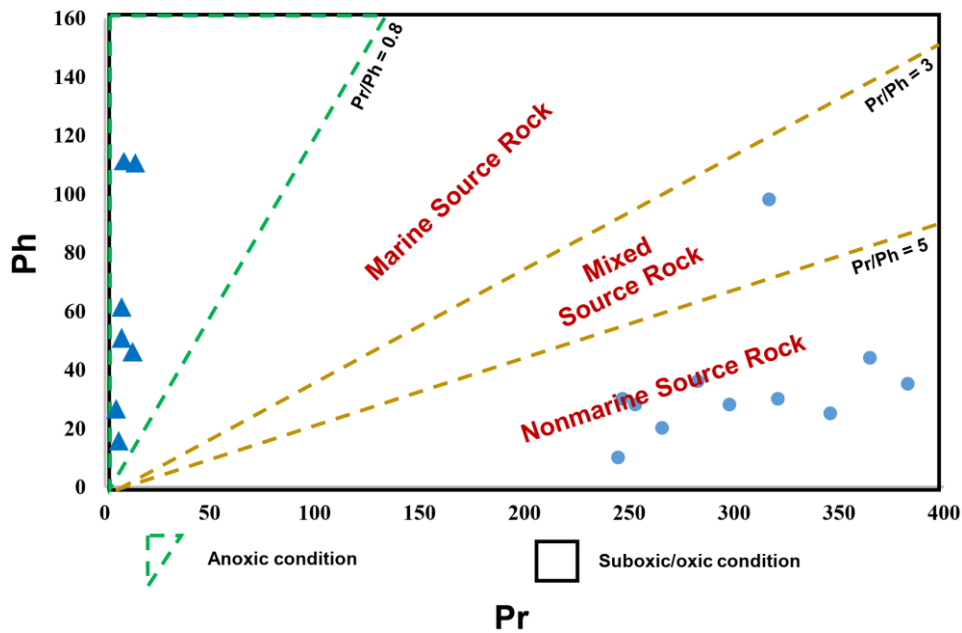


**Figure 9.** Ph vs Pr plot (the plot: from [85]). Blue circles: the water samples (this study), blue triangles: oil shales and crude oil samples of Yeşilköy drillings [79].
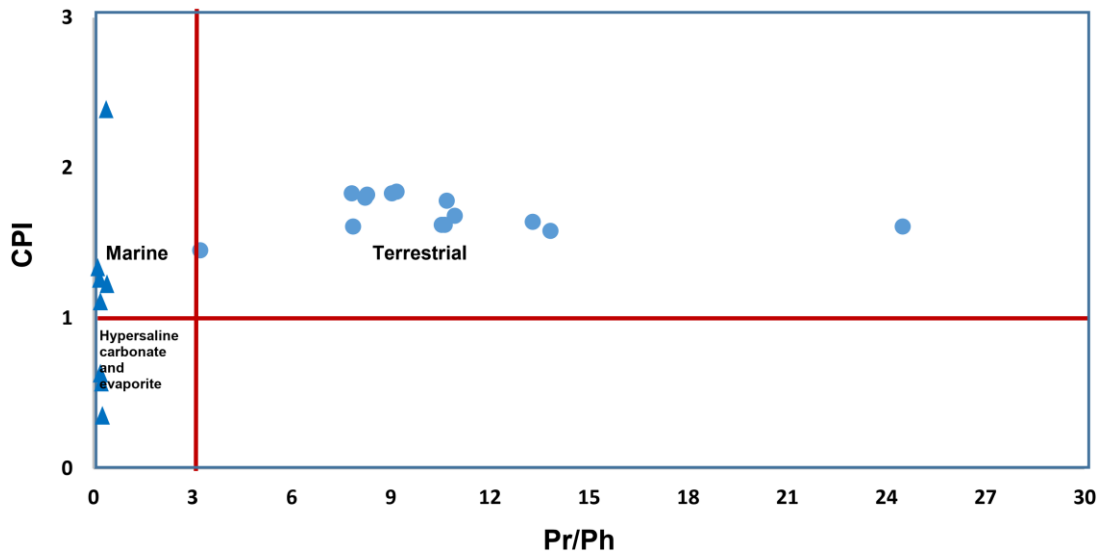
**Figure 10.** CPI vs Pr/Ph plot (the plot: from [86]). Blue circles: the water samples (this study), blue triangles: oil shales and crude oil samples obtained from Yeşilköy drillings [79].

### 4.2. Geophysical Findings

The Niğde Massif has a large dome structure (Fig. 11). Within this main structure, there are two distinct and small domes, one in the northwest and another one in the southeast. These structures are clearly seen in the images taken by utilizing the Landsat satellite (Fig. 12) [49]. These domes constitute the most important structures of the massif both geologically and economically. It is also possible that other dom structures else may exist in the massif. The settlement process of granite intrusion was effective in the formation of domes. The Gümüşler Dome, located in the northwest of the massif, is situated in the southeast of Gümüşler village [87]. An anticline extending in the NE-SW direction and dipping its axis to the southwest has formed the main structure of this dome. The granite intrusion, which causes the formation of the dome, cuts all the units and outcrops in the southern part of the dome [88]. The deformation phases during the tectonic development of the massif were explained in detail by Kleyn [89]. In the first stage, sedimentary units were metamorphosed and folded. Towards the end of this period, block faults occurred. The second stage took place when the rocks were no longer plastic. At the beginning of this stage, granite intrusion was settled into metamorphic rocks. The third stage was in conformity with the main phases of the occurrence of the Taurus mountains and the massif was significantly influenced by this mountain occurrence. These impacts are also observed in Tertiary units and the massive has gained the dome structure at this stage [89]. The Ören Dome is located in the southeast of the massif and in the north of Ören village. In the center of the dome, Üçkapılı granite exposes. The anticline, which forms the main structure of Ören Domu, extends in NW-SE direction and its axis is dipped to the southeast [87]. The Niğde Massif is bounded by the Ecemiş Fault (CAFZ) in the NNE-SSW orientation from the east (Figs 1 and 11). The Tuz Gölü Fault (TGF) in the west extends to the massif. The Niğde Massif is compressed by these two active fault systems (Fig 1).

In the literature, there are many studies using gravity and magnetic methods for petroleum exploration [63-66,90-100]. In this study, gravity and magnetic data and maps were used to determine the areas where possible oil and/or gas traps are located (Figs, 13 and 14).
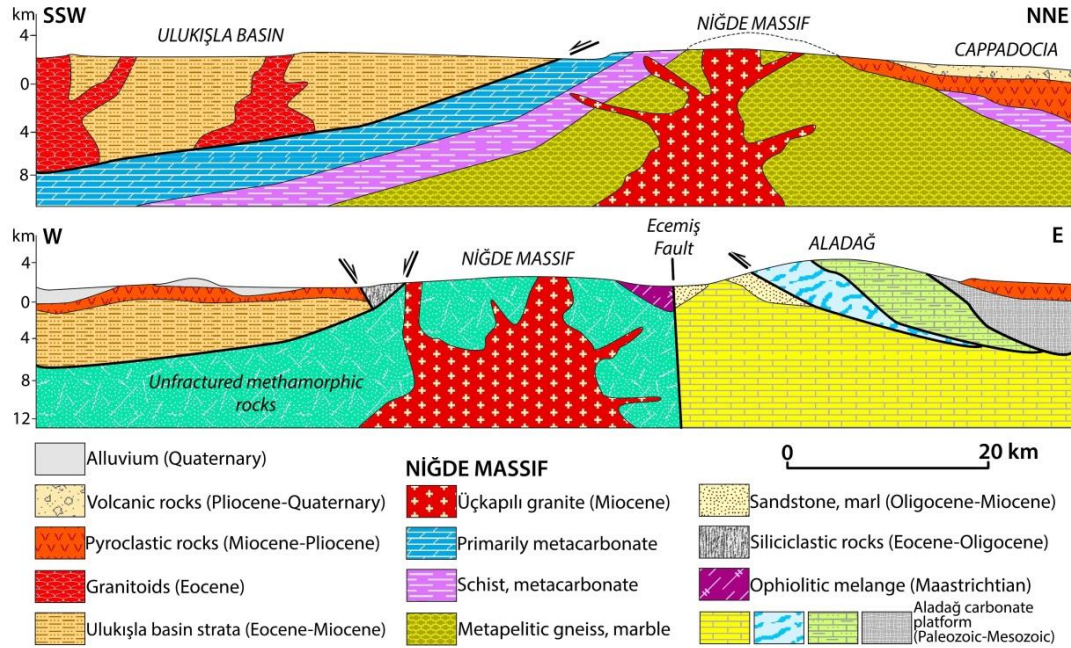


**Figure 11.** Geological cross-section of the study area (modified from [101]) (also see Figure 1).

As stated by Henden [49], Viljoen and Ileri [87], and Dennis [88], the dome structures (Fig. 12) extending in NE-SW orientation have been determined in the gravity map prepared for the study area (Fig. 13). Oil and gas accumulations in West Siberia have been observed in the areas where gravity and magnetic values caused by decrease in density and magnetism of the basement rocks are both low. It is also widely met that the gravity and magnetic values of the basement rocks exposed to the secondary alteration effects are less than their average values. The oil and gas fields above basement rocks with low magnetic and gravity are primarily located in the negative gravity and magnetic anomaly contours, i,e, in low gravity and magnetism areas. The revealed negative anomalies are in good agreement with the theory that epigenetic processes play an important role in the generation of hydrocarbon accumulations [102]. In the investigation area, both gravity and magnetism values of granites and metamorphic rocks, which are expected to be normally high gravity and magnetism, are very low (Figs. 13 and 14).
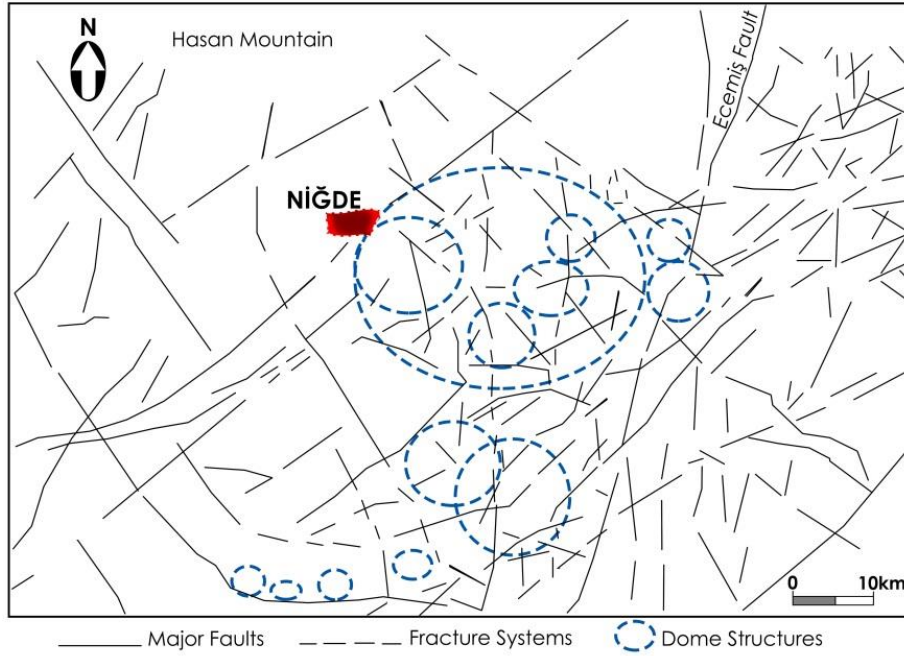
**Figure 12.** The fracture and fault systems in the Niğde Region obtained from Landsat satellite image (modified from [49]).
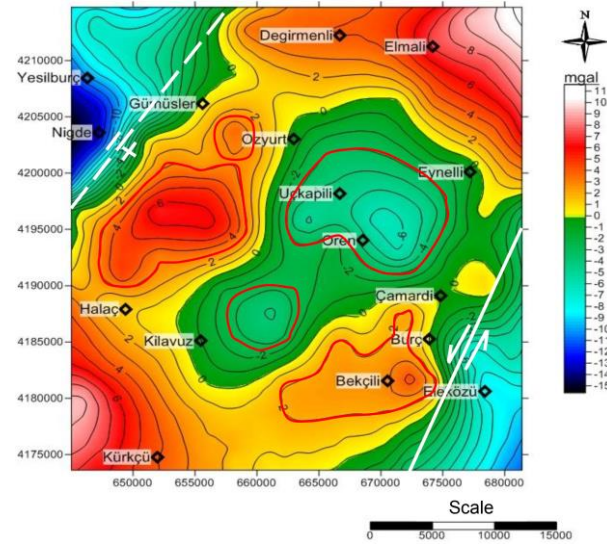


**Figure 13.** Colored contour map of gravity anomalies of the study area. Red polygons: Dom structures, white solid line: Ecemiş Fault, white dashed line: Niğde Fault.
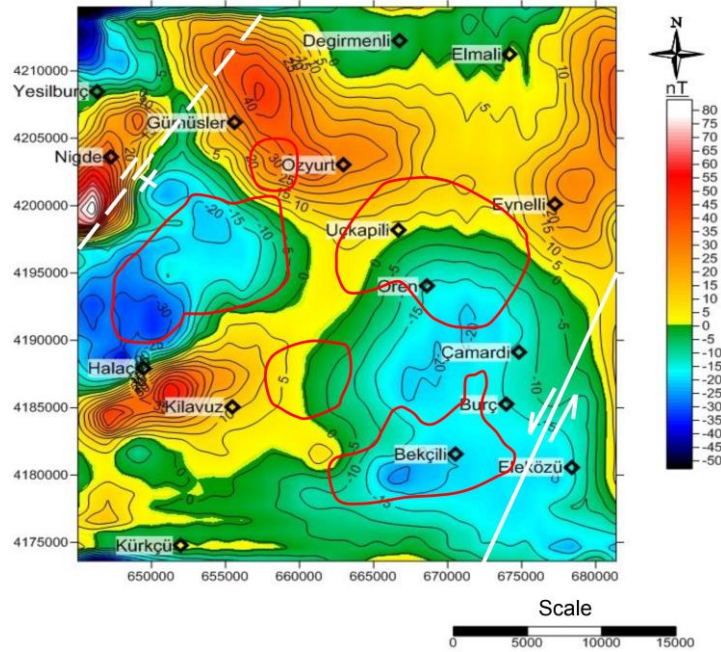
**Figure 14.** Colored contour map of aeromagnetic anomalies of the study area. Red polygons: Dom structures, white solid line: Ecemiş Fault, white dashed line: Niğde Fault.

### 4.3. Conceptual Model of Occurrence, Migration and Accumulation of Hydrocarbons

The understanding of the occurrence of petroleum source rocks is critical in oil and gas exploration. The factors controlling the occurrence and accumulation of the petroleum source rocks are related to the events and changes such as dynamics, chemistry, biology, etc. of an ocean system that take place through geological time. On the sedimentation in the Tethys Region, there is a great control of the paleogeographic location and the tectonic past, which have led to the formation, migration, and trapping of hydrocarbons in the region. Ozdemir and Palabiyik [103,104] have expressed that source rocks were formed in the mid-ocean ridges and in the continental rifts (spreading centers). Therefore, the source rocks which generated the hydrocarbons in the study area should have formed in the geological periods that involved the rifting process.

The water samples containing the mature hydrocarbons are evidence for a working petroleum system in the study area. Thus, high contents of mature hydrocarbons according to geochemical analysis results, and gravity and magnetic data indicate the presence of an oil and/or gas reservoir in the study area. The predominantly SW-NE orientation dome structures that can be trapped and protected of the hydrocarbons, formed by metamorphic rocks with granite in the center, are possible gas reservoir(s) in the study area. The fact that the structures are located between two fault zones and contain intense fracture zones increases the possibility of being accumulated in these dome structures of the hydrocarbons. In the formations, highly developed secondary permeability and porosity is expected thanks to the fractures and cracks caused by tectonic impacts (Figs, 14-16).

Parnell [11] examined the granitic plutons containing biogenic petroleum hydrocarbons in the onshore UK and the migration of hydrocarbons to these plutons and proposed the mechanisms for interrelations of granitic plutons with biogenic hydrocarbons (Fig. 15). It is also stated that the presence of hydrocarbons in granitic plutons and other basic rocks is not evidence that these hydrocarbons are of abiogenic origin and that they host for the fluids migrating from peripheral environments to plutons, owing to being intensely fractured and heat center of plutons, including waters and biogenic hydrocarbons. Thus, it is suggested that hydrocarbons in plutons and other basement rocks are related to biogenic sedimentary source rocks in all conditions. The generated hydrocarbons maturing from the source rocks in the adjacent basin (Ulukışla basin) of the study area (Figs. 1 and 11) should have migrated to Niğde Massif units which uplifted during the settlement of Üçkapılı granite and accumulated in cracked and fractured zones and dome structures of the massif (Fig. 15). A and D mechanisms (Fig. 15) proposed by Parnell [11] are consistent with the geological units and their histories in and around the investigation area. According to the mechanism A, the intrusion of a pluton into an organic-rich sedimentary source rock causes a thermal change in organic matter in the source rock. A kilometer-scale pluton will have a extensively peripheral zone where the thermal maturation will occur (Fig. 15). The maturation of the organic matter in the source rock close to the hot intrusion causes the formation of liquid hydrocarbons and source rock generates a large number of hydrocarbons. According to the mechanism D, the granites around and in sedimentary basins help basin boundaries form. The reason for that higher topographic position of granites is generally caused by erosion and sediment accumulation. The boundary between granite and basin may be an unconformity and/or a fault. The upwelling migration of hydrocarbons from source rocks within a basin bounded by a granite can be realized through the fractures and cracks in granite and surrounding rocks. This process reveals the existence of biogenic petroleum hydrocarbons in the fractured granitic and other basement rocks. The hydrocarbons in the water samples should have migrated from the possible metamorphic-granitic reservoirs and mixed with shallow groundwaters (Fig. 16).
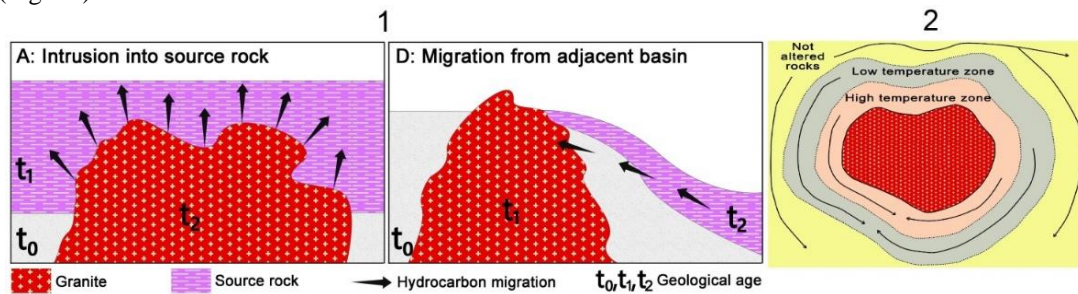


**Figure 15.** 1). The mechanisms which biogenic hydrocarbons are associated with granitic plutons (modified from Parnell [11]). 2) The metamorphic belt around the Üçkapılı granite.
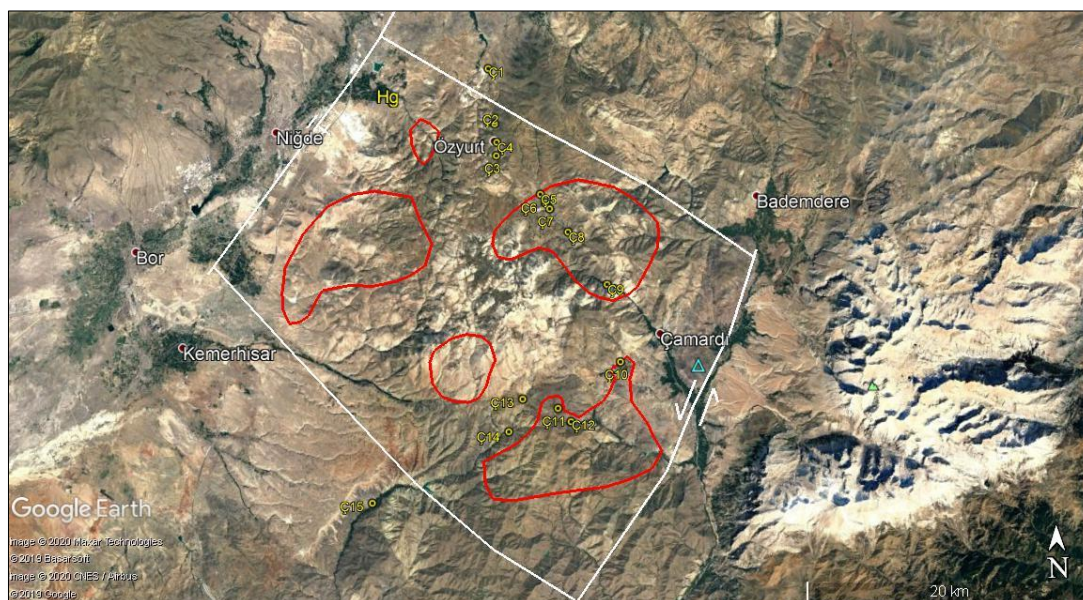
**Figure 16.** The possible hydrocarbon traps in the study area (red polygons). Yellow circles: the water samples containing mature petroleum hydrocarbons, turquoise triangle: hydrocarbon show indicated by Erentöz and Ternek [47], Hg: formerly operated Gümüşler mercury mine.

## 5. CONCLUSIONS

In the samples, the n-alkane hydrocarbons with high carbon number representing terrestrial organic matter seem to be dominant. The hydrocarbons are non-biodegraded. The source rocks generated the hydrocarbons are deposited in suboxic-oxic terrestrial environment (Type-III kerogen) and have a high level of maturity.

The mature hydrocarbon-rich waters are geochemical evidence for a working petroleum systems in the area where both gravity and magnetism values of granites and metamorphic rocks, which are expected to be normally high gravity and magnetism, are significantly low. It is also frequently encountered that the gravity and magnetic values of the basement rocks exposed to the secondary alteration effect are lower than their average values. The oil and gas fields above the basement rocks with low magnetic and gravity are primarily situated in the negative gravity and magnetic anomaly contours, i.e, in low gravity and magnetism areas. Hence, geochemical analysis results sign the presence of gas reservoir(s) in the area. The dome structures that can be trapped and protected of the hydrocarbons, formed by metamorphic rocks with granite in the center where predominantly SW-NE orientation, determined by gravity and magnetic maps, are the possible gas reservoirs in the study area.

The fact that the structure is located between two fault zones and contains intense fracture zones increase the possibility of hydrocarbons being accumulated in those structures because the locations of hydrocarbon-containing water samples are near and above these dome structures. In the units, it is expected that high degrees of secondary permeability and porosity due to the fractures and cracks

caused by tectonic effects. The generated hydrocarbons maturing from the source rocks in the adjacent basin (Ulukışla basin) of the study area should have migrated to Niğde Massif units which uplifted during the settlement of Üçkapılı granite and accumulated in cracked-fractured zones and dome structures of the massif. The hydrocarbons in the study area should have migrated from the possible metamorphic-granitic reservoirs and mixed with shallow groundwaters.

Isotope analyzes (oxygen, Re-Os, etc.) should be performed to investigate the deep hydrocarbon system sources of the hydrocarbons in the water samples in the study area and to determine their geological ages. It is also important to determine the permeability and porosity of the crystalline rocks (metamorphic and granitic) in the study area.

Determining the hydrocarbon potential of the metamorphic massifs and granitic plutons is often impossible or long-term and very expensive by classic exploration methods. The method used in this study is thought that can be to change the framework of oil and gas exploration in the metamorphic massif and granitic rocks.

## ACKNOWLEDGEMENT

## REFERENCES

[1]   McNaughton, D.A., (1953), Dilatancy in migration and accumulation of oil in metamorphic rocks. AAPG Bulletin, 37(2), 217-231

[2]   Landes, K.K., Amoruso, J.J., Charlesworth, L.J., Heany, F., and Lesperance, P.J., (1960), Petroleum resources in basement rocks. American Association of Petroleum Geologists Bulletin, 44, 1682-1691

[3]   P'an, C-H., (1982), Petroleum in basement rocks. AAPG Bulletin, 66(10), 1597-1643

[4]   Harrelson, D.W., (1989), Hydrocarbon occurrences in igneous and metamorphic rocks: The plays of the 1990's. Transactions of the Gulf Coast Association of Geological Societies, XXXIX, 85-95

[5]   Nelson, R.A., (2001), Geologic Analysis of Naturally Fractured Reservoirs, 2nd Edition: Gulf Publishing Company Book Division, 332 p

[6]   Koning, T., (2003), Oil and gas production from basement reservoirs: examples from Indonesia, USA and Vietnam, *in* Petford, N., and McCaffrey, K.J.W., eds., Hydrocarbons in Crystalline Rocks, Geological Society, London, Special Publications, 214, 83-92

[7]   Zou, C., (2013), Unconventional Petroleum Geology. Elsevier, 384 p.

[8]     Dou, L., Wang, J., Wang, R., Wei, X., and Shrivastava, C., (2018), Precambrian basement reservoirs: Case study from the northern Bongor Basin, the Republic of Chad. AAPG Bulletin, 102 (9), 1803-1824

[9]     Koning, T., (2019), Exploring in Asia, Africa and the Americas for oil & gas in naturally fractured basement reservoirs: best practices & lessons learned. Georesources, 21(4), 10-18. doi. org/10.18599/grs.2019.4.10-18

[10]    Nani, A.S., and Albanna, K., (2008), Hydrocarbon discoveries in the fractured granitic and metamorphic basement rocks in Yemen and worldwide. International Geological Congress, Abstracts, v. 33, 1202819

[11]    Parnell, J., (1988), Migration of biogenic hydrocarbons into granites: A review of hydrocarbons in British plutons. Marine and Petroleum Geology, 5, 385-396

[12]    Tong, X.G., and Huang, Z., (1991), Buried-hill discoveries of the Damintun Depression in north China. AAPG Bulletin, 75(4), 780-794

[13]    Gao, X.L., (2012), Precambrian base structure and reservoir characteristics of Chengdao oilfield in Bohai Bay Basin. Journal of Oil and Gas Technology, 34(1), 45-49

[14]    Deng, Y.H., (2015), Formation mechanism and exploration practice of large-medium buried hill oil fields in Bohai Sea (in Chinese with English abstract). Acta Petrolei Sinica, 31(3), 253-261

[15]    Ginfder, D., and Fielding, K., (2005), The petroleum system and future potential of the South Sumatra Basin: IPA05-G039: Proceedings, Indonesian Petroleum Association, 30th Annual Convention & Exhibition, Jakarta, Indonesia, August 30–September 1, 2005, 67-90

[16]    Achiat, R., Guttormsen, J., and Waworuntu, R., (2009), Complex geomodeling: Dayung Field, a fractured pre-Tertiary reservoir in the Southern Sumatra basin, Indonesia: Proceedings, Indonesian Petroleum Association, 33rd Annual Convention & Exhibition, Jakarta, Indonesia, May 5-9, 2009, IPA09-G-148, 18

[17]    Cuong, T.X., and Warren, J.K., (2009), Bach Ho field, a fractured granitic basement reservoir, Cuu Dank Long Basin, offshore SE Vietnam: A "buried-hill" play. Journal of Petroleum Geology, 32 (2), 129-156

[18]    Satyanaryana, P., Sinha, P.K. Gupta, D.K., Sathe, A.V., and Katuyar, G.C., (2010), Hydrocarbon prospectivity of the basement of Mumbai High Field. 8th Biennial International Conference & Exposition on Petroleum Geophysics, SPG 2010, Heyderabad

[19]    Nelson, R.A., Bueno, E., Moldovanyi, E.P., Matcek, C.C., and Azqiritxaga, I., (2000), Production characteristics of the fractured reservoirs of the La Paz field, Maracaibo basin, Venezuela. AAPG Bulletin, 84 (11), 1791-1809

[20]    Sorenson, R.P., (2005), A dynamic model for the Permian Panhandle and Hugoton fields, western Anadarko basin. AAPG Bulletin, 89(7), 921-938

[21] Williams, J.J., (1972), Augila field, Libya, depositional environment and diagenesis of sediment reservoir and description of igneous reservoir. in R.E. King, (ed.), Stratigraphic Oil and Gas Field, AAPG Memoir. 16, 623-632

[22] Belgasem, B.A., (1991), An evaluation of an oil-bearing granite reservoir from well-logs. Transactions Canadian Well Logging Society 13th Formation Evaluation Symposium, Calgary, Alberta, Canada, September 11-13, 1991, v. 1, p. K1-K16

[23] Salah, M.G., and Alsharhan, A.S., (1998), The Precambrian basement, a major reservoir in the rifted basin, Gulf of Suez. Journal of Petroleum Science and Engineering, 19(3-4), 201-222

[24] Younes, A.I., Engelder, T., and Bosworth, W., (1998), Fracture distribution in faulted basement block, Gulf of Suez, Egypt, in M. P. Coward, T. S. Daltaban, and H. Johnson, eds., Structural geology in reservoir characterization: Geological Society, London, Special Publications, 127, 167-190

[25] Trice, R., (2014), Basement exploration, West of Shetlands. Progress in opening a new play on the UKCS, in S. J. C. Cannon and D. Ellis, eds., Hydrocarbon exploration to exploitation west of Shetlands, Geological Society, London, Special Publications, 397, 81-105

[26] Belaidi, A., Bonter, D.A., Slightam, C., and Trice, R.C., (2016), The Lancaster Field: Progress in opening the UK's fractured basement play, in, M. Bowman and B. Levell, eds., Petroleum Geology of NW Europe: 50 years of learning-Proceedings of the 8th Petroleum Geology Conference, London, September 26, 2016, 385-398

[27] Deng, Y.H., and Peng, W.X., (2009), Discovering large buried-hill oil and gas fields of migmatitic granite on Jinzhou 25-1S in Bohai Sea (in Chinese with English abstract). China Offshore Oil and Gas, 21 (3), 145-150

[28] Petford, N., and McCaffrey, K.J.W., (2003), Hydrocarbons in Crystalline Rocks. Geological Society Special Publication 214, 242 p.

[29] Schutter, S.R., (2003), Hydrocarbon occurrence and exploration in and around igneous rocks. in Petford, N., and McCaffrey, K.J.W., eds., Hydrocarbons in Crystalline Rocks, Geological Society Special Publications, 214, 7-33

[30] Tamagawa, T., and Pollard, D.D., (2008), Fracture permeability created by perturbed stress fields around active faults in a fractured basement reservoir. AAPG Bulletin, 92(6), 743-764

[31] Ozdemir, A., and Palabiyik, Y., (2019), A shallow and reliable indicator for deep oil and gas accumulations in the subsurface: Metallic ore deposits. IV. International Congress of Scientific and Professional Studies - Engineering Sciences (BILMES EN), November 07 - 10, Ankara, Turkey, 40-57

[32] Ozdemir, A. and Palabiyik, Y., (2019), Significance of relationships between hydrocarbons and metallic ore deposits in oil and gas exploration: Part III. Lead and zinc deposits. BİLTEK

International Symposium on Recent Developments in Science, Technology and Social Studies, December 21-22, Ankara, Turkey, 240-250

[33] Ozdemir, A. and Palabiyik, Y., (2019), Significance of relationships between hydrocarbons and metallic ore deposits in oil and gas exploration: Part II. Copper deposits. BİLTEK International Symposium on Recent Developments in Science, Technology and Social Studies, December 21-22, Ankara, Turkey, 230-239

[34] Ozdemir, A. and Palabiyik, Y., (2019), Significance of relationships between hydrocarbons and metallic ore deposits in oil and gas exploration: Part I. Gold deposits. BİLTEK International Symposium on Recent Developments in Science, Technology and Social Studies, December 21-22, Ankara, Turkey, 219-229

[35] Yıldız, M., and Bailey, E.H., (1978), Mercury Deposits in Turkey: Mineralogy, geologic setting, size-grade of mercury ore bodies; brief history of productive mines. U.S. Geological Survey Report, 80 p.

[36] Gemici, Ü., (2008), Evaluation of former mercury deposits in Western Anatolia in terms of environmental geology. International Symposium on Medical Geology, 133-145 (in Turkish)

[37] Mueller, G., (1951), A genetical and geochemical survey of Derbyshire mineral deposits. PhD. Thesis, London University

[38] Geissman, T.A., Sun, K.Y., and Murdoch, J., (1967), Organic minerals. Picene and chrysene as constituents of the mineral curtisite. Experientia, 23, 793-794

[39] Peabody, C.E., (1993), The association of cinnabar and bitumen in mercury deposits of the California Coast Ranges. In: Parnell J, Kucha H, Landais P (eds) Bitumen in Ore Deposits. Springer, 178-209

[40] Peabody, C.E., and Einaudi, M.T., (1992), Origin of petroleum and mercury in the Culver-Baer cinnabar deposit, Mayacmas district, California. Economic Geology, 87, 1078-1103

[41] Bailey, E.H., (1959), Froth veins formed by immiscible hydrothermal fluids in mercury deposits. California. Bull. Geol. Soc. America, 70, 661-664

[42] Shabo, Z.V., Alekseyeva, N.I., Mamchur, G.P., and Manzhas, N.I., (1983), Organic compounds of the Slavyansk ore shows and their association with endogenic mineral formation. International Geology Review, 25, 299-308

[43] Parnell, J., (1988), Metal enrichments in solid bitumens. Miner Deposita, 23, 191-199

[44] Chakhmakchev, V.A., Kurganskaya, E.V., and Punanova, S.A., (1981), Distribution of trace elements in petroleum fractions. Geochemical International, 18, 177-181

[45] Chilingar, G.V., Buryakovsky, L.A., Eremenko, N.A., and Gorfunkel, M.V., (2005), Geology and Geochemistry of Oil and Gas (Developments in Petroleum Science, Volume 52), Elsevier B.V., 390 p.

[46] Yan, Q., Han, Z., and Wang, S., (2017), Geochemical characteristics of mercury in oil and gas. International Conference on Environmental and Energy Engineering (IC3E 2017), IOP Conf. Ser.: Earth Environ. Sci. 63 012024, doi :10.1088/1755-1315/63/1/012024

[47] Erentöz, C., and Ternek, Z., (1959), Oil possibilities in the sedimentary basins of Turkey. MTA Bulletin, 53, 21-36

[48] Lefebvre, C., (2011), The tectonics of the Central Anatolian Crystalline Complex: a structural, metamorphic and paleomagnetic study. Utrecht University, Thesis, 139 p.

[49] Henden, I., (1981), Lineaments map of Turkey from Landsat imagery and selecting target areas for mineral exploration, relationship of regional lineaments to earthquake epicenters, mineral waters and hot springs. MTA Bulletin, 95/96, 68-76

[50] Ballı, F., Sönmez, M., and Lermi, A., (2018), Geology of SE part of Nigde and new findings on Nigde Fault. Omer Halisdemir University Journal of Engineering Sciences, 7(3), 1180-1185 (in Turkish with English abstract)

[51] Gautier, P., Bozkurt, E., Hallot, E., and Dirik, K., (2002), Dating the exhumation of a metamorphic dome: geological evidence for pre-Eocene unroofing of the Niğde Massif (central Anatolia, Turkey). Geological Magazine 139, 559-576

[52] Demircioğlu, R., and Eren, Y., (2017), Structural features of the Niğde Massif in the Çamardı (Niğde) district, MTA Bulletin, 154, 15-26

[53] Sonel, N., Sarı, A., Toprak, Ö., and Şengüler, İ., (1999), Geochemical investigation of bituminous shales in Ulukışla (Niğde). Selçuk Univ. Eng. Arch. Fac. J., 4(2), 77-88 (in Turkish with English abstract)

[54] Sonel, N., and Sarı, A., (2004), Investigation of hydrocarbon potential of Ereğli-Ulukışla (Konya-Niğde) basin. Eng. Arch. Fac. J., 19(4), 393-403 (in Turkish with English abstract)

[55] Pusat, M., (2005), Geochemistry and geology of bituminous shales of Ulukışla (Niğde). Niğde University, Graduate School of Natural and Applied Sciences, MSc. Thesis, 43 p. (in Turkish)

*[56]* İztan, Y.H., Yılmaz, E., Sancay, R.H., Türesin, F.M., and Tekin, T., (2007), Geochemical Evaluation of Niğde Region and Studies in NBK-2007/2 Well. Turkish Petroleum Corporation (TPAO) Report No. 3255 (in Turkish)

[57] Murat, A., (2010), Investigation of newly determined oil shale potential reserves and shale oil production in Turkey. MTA Natural Resources and Economy Bulletin, 9, 1-7 (in Turkish)

[58] Sağlam, Ç., (2011), The Relationship Between Bituminous Shale and Oil in Bor-Ulukışla (Niğde) Neogene. Niğde University, Graduate School of Natural and Applied Sciences, MSc. Thesis, 41 p. (in Turkish)

[59] Kadınkız, G., Pekgöz, M., Karakaş, M., and Murat, A., (2017), Sodium sulfate (Glauberite-Bloedite) - halite association in the Tertiary (Upper Miosene-Pliocene) Katrandedetepe Formation, Ereğli-Bor Basin, Turkey. MTA Bulletin, 154, 137-158

[60] Durgut, E., (2011), Sedimentology and geochemical characterization of sequences containing petroleum in geothermal fields, Ankara University, Institute of Science and Technology, MSc Thesis, 55 p. (in Turkish with English abstract)

[61] Sancay, R.H., Türesin, F.M., İzatan, Y.H., Işık, U., and Akça, N., (2010), Lithostratigraphic, biostratigraphic and geochemical report of Bor-1 oilwell. Turkish Petroleum Corporation (TPAO), Research Center Report No. 3505 (in Turkish) (Unpublished)

[62] Akar, Ç., Yılmazer, P., Tokoğlu, E.E., Aracı, B., Günaydın, S., and Çetin, S., (2018), Geochemical Assessment Report of Niğde-Ulukışla Gas and Water Samples. Turkish Petroleum Company, Report No. 4310 (in Turkish) (Unpublished)

[63] Ozdemir, A., Karataş, A., Palabiyik, Y., Yaşar, E., and Sahinoglu, A., (2020), Oil and gas exploration in Seferihisar Uplift (Western Turkey) containing an operable-size gold deposit: Geochemical evidence for the presence of a working petroleum system. Geomechanics and Geophysics for Geo-Energy and Geo-Resources, 6(1), Doi: 10.1007/s40948-020-00152-2

[64] Ozdemir, A., Palabiyik, Y., Karataş, A., and Sahinoglu, A., (2020), Organic geochemical evidence of the working petroleum system in Beypazarı Neogene Basin and potential traps (Northwest Central Anatolia, Turkey). Turkish Journal of Geosciences, 1(2), 35-52

[65] Ozdemir, A., Palabiyik, Y., Karataş, A., and Sahinoglu, A., (2020), Mature petroleum hydrocarbons contamination in surface and subsurface waters of Kızılırmak Graben (Central Anatolia, Turkey): Geochemical evidence for a working petroleum system associated with a possible salt diapir. Turkish Journal of Engineering, 6(1), 1-15

[66] Ozdemir, A., Karataş, A., Palabiyik, Y., and Sahinoglu, A., (2020). Reservoir-targeted oil and gas exploration in the Karaburun Peninsula (Western Turkey). International Journal of Energy and Engineering Sciences, 5(2), 115-145

[67] Bray, E.E., and Evans, E.D., (1961), Distribution of n-paraffins as a clue to recognition of source rocks. Geochim. Cosmochim, Acta. 22, 2-15

[68] Bray, E.E., and Evans, E.D., (1965), Hydrocarbons in non-reservoir-rock source beds: Part 1. American Association of Petroleum Geologists Bulletin, 49, 248-257

[69] Bourbonniere, RA., and Meyers, P.A., (1996), Sedimentary geolipid records of historical changes in the watersheds and productivities of lakes Ontario and Erie. Limn Ocean, 41, 352-359.

[70] Mille, G., Asia, L., Guiliano, M., Malleret, L., and Doumenq, P., (2007), Hydrocarbons in coastal sediments from the Mediterranean Sea (Gulf of Fos area, France). Marine Pollution Bulletin, 54, 566-575

[71] Peters, K.E, Walters, C.C., and Moldowan, J.M., (2005), The Biomarker Guide: Biomarkers and Isotopes in Petroleum Exploration and Earth History, Second Ed, Vol 2. Cambridge University Press, 1155 p.

[72] Cranwell, P. A., Eglinton G., and Robinson, N., (1987), Lipids of aquatic organisms as potential contributors to lacustrine sediments-2. Organic Geochemistry, 11, 513-527

[73] Goossens, H., Duren, C., De Leeuw, J. W., and Schenck, P. A., (1989), Lipids and their mode of occurrence in bacteria and sediments-2. Lipids in the sediment of a stratified, freshwater lake. Organic Geochemistry, 14, 27-41

[74] Meyers, P.A., and Ishiwatari, R., (1993), Lacustrine organic geochemistry-an overview of indicators of organic matter sources and diagenesis in lake sediments. Organic Geochemistry, 20, 867-900

[75] Kroon, J., (2011), Biomarkers in the Lower Huron Shale (Upper Devonian) As Indicators of Organic Matter Source, Depositional Environment, and Thermal Maturity. Clemson University, MSc. Thesis, 107 p.

[76] Forster, A., Sturt, H., and Meyers, P.A., (2004). Molecular biogeochemistry of Cretaceous black shales from the Demerara Rise: Preliminary shipboard results from sites 1257 and 1258, Leg 207. *in* Erbacher, J., Mosher, D.C., Malone, M.J., et al., Proceedings of the Ocean Drilling Program, Initial Reports: v. 207, p. 1-22.

[77] Sonel, N., Sari, A., and Demirel, İ.H., (2008), Petroleum source rock characteristics of the Lower Tertiary formations in the Ereğli-Ulukışla Basin, Southern Central Anatolia, Turkey. Petroleum Science and Technology, 26(4), 460-472

[78] Waples, D.W., (1985), Geochemistry in Petroleum Exploration. International Human Resources Development Corp., 232 p.

[79] Gülbay, K.R., Korkmaz, S., Erdoğan, M.S., and Kadınkız, G., (2019), Biomarker geochemistry of crude oils and Neogene bituminous shales in Yeniköy Area, Ereğli-Ulukışla Basin, Central Anatolia, Turkey. Journal of Petroleum Geology, 42, 173-192

[80] Shanmugam, G., (1985), Significance of coniferous rain forests and related oil, Gippsland Basin, Australia. AAPG Bulletin, 69, 1241-1254

[81] Sonel, N., Sari, A., and Demirel, İ.H., (2008), Petroleum source rock characteristics of the Lower Tertiary formations in the Ereğli-Ulukışla Basin, Southern Central Anatolia, Turkey. Petroleum Science and Technology, 26(4), 460-472

[82] Syaifudin, M., Eddy, A., Subroto, E.A., Noeradi, D., and Kesumajana, A.H.P., (2015), Characterızation and correlatıon study of source rocks and oils in Kuang area, South Sumatra basin: The potential of Lemat formation as hydrocarbon source rocks. Proceedings of Indonesian Petroleum Association, Thirty-Ninth Annual Convention & Exhibition, May 2015, IPA15-G-034

[83] Larasati, D., Suprayogi, K., and Akbar, A., (2016), Crude oil characterization of Tarakan basin: Application of biomarkers. The 9th International Conference on Petroleum Geochemistry in the Africa - Asia Region Bandung, Indonesia, 15 -17 November 2016

[84] Devi, E.A., Rachman, F., Satyana, A.H., Fahrudin, and Setyawan, R., (2018), Geochemistry of Mudi and Sukowati oils, East Java basin and their correlative source rocks: Biomarkers and isotopic characterisation. Procedings, Indonesian Petroleum Association, Forty-Second Annual Convention & Exhibition, May 2018

[85] Banga, T., Capuano, R.M., and Bissada, K.K., (2011), Petroleum generation in the southeast Texas basin: Implications for hydrocarbon occurrence at the South Liberty salt dome. AAPG Bulletin, 95(7), 1257-1291

[86] Hakimi, M.H., Al-Matary, A.M., and Ahmed, A., (2018), Bulk geochemical characteristics and carbon isotope composition of oils from the Sayhut sub-basin in the Gulf of Aden with emphasis on organic matter input, age and maturity. Egyptian Journal of Petroleum, 27(3), 361-370

[87] Viljoen, R.P., and İleri, S., (1973), The Geology and Mineralization of Partitions in the Pozantıdağı (Niğde) Massif of South Central Turkey. Johannesburg Consolidated Investments Co. Ltd. Geological Research Department, Rep. No. 39, 59 p (Unpublished).

[88] Dennis, R.A., (1970), The mineralisation st the mercury-antimony-tungsten mine near Niğde, South Central Turkey, University College of Swansea, Department of Geology, MTA Report No. 949

[89] [89] Kleyn, Van der P.H., (1970), Recommendation of Exploration for Mineralizations in the SW Part of Niğde-Çamardı Massif, MTA Report, No. 4345

[90] Gadirov, V.G., Kalkan, E., Ozdemir, A., Palabiyik, Y., and Gadirov, K.V., (2021). Use of gravity and magnetic methods in oil and gas exploration: Case studies from Azerbaijan. International Journal of Earth Sciences Knowledge and Applications (in press)

[91] Nettleton, L.L., (1976), Gravity and Magnetics in Oil Prospecting. McGraw-Hill, 464 p.

[92] Geist, E.L., Childs, J.R., and Scholl, D.W., (1987), Evolution and petroleum geology of Amlia and Amukta intra-arc summit basins, Aleutian Ridge. Marine and Petroleum Geology, 4, 334-352

[93] Lyatsky, H.V., Thurston, J.B., Brown, R.J., and Lyatsky, V.B., (1992), Hydrocarbon exploration applications of potential field horizontal gradient vector maps. Canadian Society of Exploration Geophysicists Recorder, 17(9), 10-15

[94] Eke, P.O., and Okeke, F.N., (2016), Identification of hydrocarbon regions in Southern Niger Delta Basin of Nigeria from potential field data. International Journal of Scientific and Technology Research, 5(11), 96-99

[95] Gadirov, V.G., Eppelbaum, L.V., Kuderavets, R.S., Menshov, O.I., and Gadirov, K.V., (2018), Indicative features of local magnetic anomalies from hydrocarbon deposits: examples from Azerbaijan and Ukraine, Acta Geophysica, doi: 10.1007/s11600-018-0224-0

[96] Gadirov, V.G., and Eppelbaum, L.V., (2012), Detailed gravity, magnetics successful in exploring Azerbaijan onshore areas. Oil and Gas Journal, 5, 60-73

[97] Gadirov, V.G., (1994), The physical-geological principles of ap

[98] plication of gravity and magnetic prospecting in searching oil and gas deposits. Proceed. of 10th Petroleum Congress and Exhibition of Turkey, Ankara, 197-203

[99] Piskarev, A.L., and Tchernyshev, M.Y., (1997), Magnetic and gravity anomaly patterns related to hydrocarbon fields in northern West Siberia. Geophysics, 62(3), 831-841

[100] Satyana, A.H., (2015), Subvolcanic hydrocarbon prospectivity of Java: Opportunities and challenges. Proceedings, Indonesian Petroleum Association. Thirty-Ninth Annual Convention & Exhibition, May 2015. IPA15-G-105

[101] Stephen, O.I., and Iduma, U., (2018), Hydrocarbon potential of Nigeria's Inland Basin: Case study of Afikpo basin. Journal of Applied Geology and Geophysics, 6(4), 1-24

[102] Whitney, D.L., and Dilek, Y., (1997), Core complex development in Central Anatolia. Turkey. Geology, 25(11), 1023-1026

[103] Ozdemir, A., and Palabiyik, Y., (2019), A review of Paleozoic - Miocene petroleum source rocks of Turkey by paleogeographic and paleotectonic data: New interpretations and major outcomes. 7th International Symposium on Academic Studies in Science, Engineering and Architecture Sciences, November 15-17, Ankara, Turkey, 689-725

[104] Ozdemir, A., and Palabiyik, Y., (2019), A new approach to petroleum source rock occurrence: The relationships between petroleum source rock, ophiolites, mantle plume, and mass extinction. IV. International Congress of Scientific and Professional Studies - Engineering (BILMES EN), November 07 - 10, Ankara, Turkey, 28-39

[105] Ozdemir, A., and Palabiyik, Y., (2019), A review of Paleozoic - Miocene petroleum source rocks of Turkey by paleogeographic and paleotectonic data: New interpretations and major outcomes. 7th International Symposium on Academic Studies in Science, Engineering and Architecture Sciences, November 15-17, Ankara, Turkey, 689-725

*RESEARCH ARTICLE*

# A NEW MOTOR DESIGN METHOD for INCREASING the AVERAGE TORQUE VALUE in SWITCHED RELUCTANCE MOTOR

Mehmet Murat TEZCAN[1], Asım Gökhan YETGİN[2,*]

[1]Kütahya Dumlupınar University, Faculty of Engineering, Department of Electrical Electronics Engineering, Kutahya, murat.tezcan@dpu.edu.tr, ORCID:0000-0002-5390-4527
[*2]Burdur Mehmet Akif Ersoy University, Faculty of Engineering and Architecture, Department of Electrical Electronics Engineering, Burdur, agyetgin@mehmetakif.edu.tr, ORCID: 0000-0003-3971-0504

## ABSTRACT

Switched reluctance motors have been widely used in industry in recent years. One of its most important advantages is its high-power density and its independence from rare magnet poles. In this study, a new motor design is proposed to increase the average and maximum torque values of a 2.2 kW switched reluctance motor. In the proposed design, slits are opened in the poles in the rotor core. Magnetic field and potential vector distributions, inductance, current and torque values are obtained for reference and slitted motor models. Analyzes were made using the Maxwell 2-D program. According to the results, it is determined that the proposed motor design for the same size and power values provides an improvement in the average and maximum torque values.

**Keywords:** *Switched Reluctance Motor, Slitted Motor, Torque Analysis*

## 1. INTRODUCTION

Many applications in the industry require the design and use of electrical machines with a large power-weight ratio. In most of these applications, while high efficiency is required, machines that provide high torque and operate at high speed are required. In this context, Switched Reluctance Motors (SRM) are known to operate at high torque or exceptionally high speeds, making them an ideal machine for such applications [1]. Switched reluctance motors have become one of the preferred electric motor types in industrial applications due to their simple structure, low cost and high torque density, high speed capacity [2], superior features such as robust structure and high reliability [3], high efficiency [4]. In recent years, with the use of SRM in various applications such as electric vehicles, aviation, ships, wind power generation and household appliances, improving motor driver and motor performance has become a priority for researchers [4]. Studies carried out in order to increase the performance of SRM can be grouped into two groups. The first of these is the work on the geometric structure of the motor. The second one is the studies on the motor driver circuit / control. On the basis of these studies, it is aimed to reduce the torque oscillations, one of the biggest disadvantages of SRMs, and to increase the average torque value.

Aydoun et al., in their studies, made a performance evaluation using grain-oriented electrical steel and non-oriented electrical steel in the rotor core of a switched reluctance motor. They have shown that

the grain-oriented electrical steel motor model provides a 16% improvement in the average torque value of the motor [1]. Han et al. evaluated the starting performance of a 12/8 pole switched reluctance motor in their study. According to their results, they showed that as the stator pole arc coefficient value increased, the starting torque of SRM increased and the starting torque of SRM could be improved by decreasing the air gap length appropriately [5]. Gondaliya and Tita carried out a new design of a new outer rotor switching reluctance motor and performed a performance comparison with an internal rotor SRM. According to their results, they stated that the torque value of outer rotor SRM is higher and this will result in a reduction in the size and cost of the motor [6]. Vattikuti et al. proposed a high torque and low loss reluctance machine design in their studies. They stated that the proposed segmented switched reluctance motor was 14% lighter than the variable switched reluctance motor (for the same frame) due to structural changes in geometry, and that an improvement in torque was achieved by 62% [7].

In this study, in order to increase the performance of the switched reluctance motor, slits were opened in the rotor poles. The purpose of these slits is to improve the magnetic flux value and to allow the flux lines to enter the inner parts of the rotor without dispersing. In addition, an additional air gap electromagnetic torque is provided thanks to the variable air gap reluctance thanks to the opened slits. In this context, three slits were opened on each of the rotor poles to create a variable reluctance effect. While the width of the slits is 0.1 mm, the depth is equal to the height of the pole. Magnetic field distribution, vector potential distribution, change of torque, current and inductance values for reference and slit motor models are analyzed.

The mathematical model and formulations of the switched reluctance motor is given in the second section of the study. The proposed slitted motor model is presented in the third section and the analysis results obtained from the models are given in the fourth section. In the last section, results and discussion are given.

## 2. SRM MATHEMATICAL MODEL

As with all electric motors, accurate determination of motor parameters is essential for simulation applications and motor control methods. This is particularly important in switched reluctance motors, which is a function of phase inductance and torque of the non-linear rotor position. These parameters can be obtained by analytical calculations, finite element method or measurements if the motor is produced [8].

In order to obtain the equivalent circuit of a switched reluctance motor, the mutual inductance between phases must be neglected due to it is too small [9]. The voltage applied to a phase is obtained by adding the voltage drop on the resistor and the flux linkage ratio and it is given in Eq. 1 [10].

$$V = R_s i + \frac{d\lambda(\theta, i)}{dt} \tag{1}$$

In the expression, $R_s$ is the resistance per phase, $i$ is the phase current, $\theta$ is the rotor position, and $\lambda$ is the flux linkage value per phase given in Eq. 2 [11].

$$\lambda = L(\theta, i) i \tag{2}$$

In the expression, L refers to the winding inductance depending on the rotor position and phase current. Phase voltage is given in Eq. 3 [10].

$$v = R_s i + \frac{d\{L(\theta,i)i\}}{dt} = R_s i + L(\theta,i)\frac{di}{dt} + i\frac{d\theta}{dt} \cdot \frac{dL(\theta,i)}{d\theta}$$
$$= R_s i + L(\theta,i)\frac{di}{dt} + \omega_m i\frac{dL(\theta,i)}{d\theta}$$

(3)

The three terms on the right side of this equation refer respectively to the voltage drop on the winding resistance, the inductive voltage drop on the phase winding and the electromotive force (emf) induced in the phase winding. The induced emf in the phase winding is given in Eq. 4 [10].

$$e = \omega_m i\frac{dL(\theta,i)}{d\theta} = K\omega_m i$$

(4)

Here K can be taken as an emf constant similar to a series excited DC machine. $\omega_m$ is the angular speed. From the voltage and induced emf expressions, the equivalent circuit for single phase of SRM is generated and is given in Figure 1.
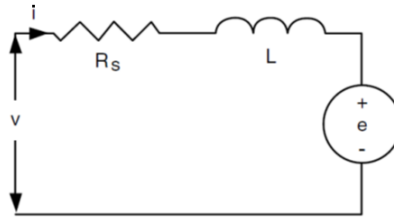


**Figure 1.** Single phase equivalent circuit model of SRM [10].

The motor's input power is obtained by multiplying the voltage value with the current, and it is given in Eq. 5 [11].

$$pi = vi = R_s i^2 + i^2\frac{dL(\theta,i)}{dt} + L(\theta,i)i\frac{di}{dt}$$

(5)

After the input power is obtained, the air gap power of the SRM is obtained. Air gap power can be written as in Eq. 6.

$$P_{airgap} = \omega_m T_e$$

(6)

The electromagnetic torque expression obtained in the air gap in the switched reluctance motor is given in Eq. 7. The expression can be thought as the value of the electromagnetic torque produced by deriving the co-energy stored in the magnetic core by the phase winding according to the rotor position [12]. It is assumed that the material used in the model is ideal, so there is no magnetic saturation.

$$T_e = \left. \frac{\partial W'(\mathrm{i},\theta)}{\partial \theta} \right|_i$$

$$W'(\mathrm{i},\theta) = \frac{1}{2} L(\theta) i^2 \qquad (7)$$

$$T_e = \frac{1}{2} i^2 \frac{dL(\theta)}{d\theta}$$

As can be understood from the statement, it is seen that the air gap electromagnetic torque in switched reluctance motors changes depending on the current, inductance and rotor position.

The winding inductance value is obtained by dividing the number of phase windings (N) by the total reluctance ($\mathfrak{R}$) value of the magnetic circuit of the motor and is given in Eq. 8 [12].

$$L = \frac{N^2}{\mathfrak{R}} \qquad (8)$$

Reluctance value is calculated separately for magnetic core and air gap parts and is given in Eq. 9 [12]. In the expression, $R_{core}$ and $R_{gap}$ represent the reluctance value of the magnetic core and the air gap length, respectively, l and $l_g$ are the length of the magnetic path and the air gap length, S is the area, $\mu_0$ and $\mu_r$, respectively, the permeability of free space and the magnetic material.

$$\mathfrak{R}_{core} = \frac{l}{\mu_0 \cdot \mu_r \cdot S} \; ; \quad \mathfrak{R}_{gap} = \frac{l_g}{\mu_0 \cdot S} \qquad (9)$$

In SRM, torque always tries to move the rotor to the highest inductance position. The inductance values obtained while the rotor is moving from the misaligned position to the aligned position are given in Figure 2 [13]. If the stator and rotor cores are aligned, a minimum air gap length occurs and naturally, minimum reluctance occurs. Thus, the inductance value is maximum. In the opposite case, it is seen that the inductance is at a minimum level.
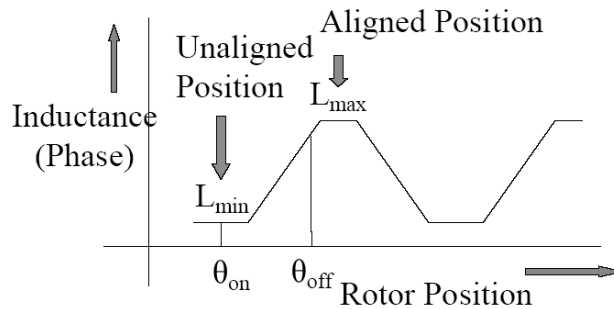


**Figure 2.** Change of inductance according to rotor position [13].

**3. PROPOSED MOTOR MODEL**

The stator of the SRM is made of silicon alloy steel material with inward protruding poles. The number of stator poles can be even or odd, but most of them are manufactured in even numbers. The rotor of SRM is made of silicon steel material, also silicon alloy with outward protruding poles. The number of rotor poles is also preferably even and less than the number of stator poles [14]. The features and dimensions of the reference motor used in the modeling are given in Table 1. The motor stator and rotor poles are determined as 8 and 6, respectively. 1008 steel was used as magnetic material. Stator pole winding number is 51.

**Table 1.** Specifications and dimensions of reference motor [15].

| Parameters | Values |
|---|---|
| Power [kW] | 2.2 |
| Voltage [V] | 230 |
| Stator Outer Diameter [mm] | 194 |
| Stator Inner Diameter [mm] | 99 |
| Rotor Outer Diameter [mm] | 98 |
| Number of Stator/Rotor Poles | 8/6 |
| Stator/Rotor Yoke Thickness [mm] | 15/15 |
| Stator/Rotor Embrace | 0.5/0.5 |
| Shaft Diameter [mm] | 36 |
| Length [mm] | 110 |

The cross-sectional images of the reference motor model and the proposed motor model are given in Figure 3.



(a)                                    (b)
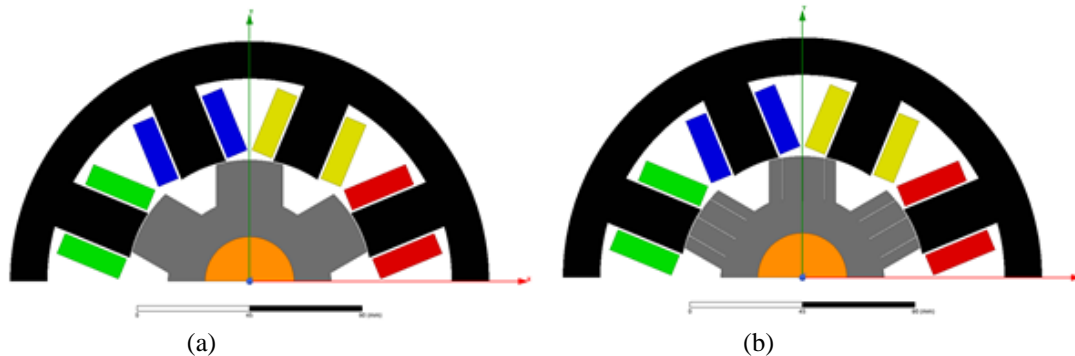
**Figure 3.** Cross-sectional view of motor models (a) Reference motor model (b) Slitted motor model

In the study, a slitted structure is proposed in order to increase the torque value of the switched reluctance motor. In the proposed slitted structure, slits are opened in the rotor poles. The depth of the slits is equal to the depth of the rotor pole. The width of the slits was chosen 0.1 mm in order to avoid saturation in the rotor poles. Choosing wide slits reduces the rotor pole tooth thickness, which causes saturation in the rotor poles. Likewise, if the number of slits in the rotor poles is high, saturation occurs in the rotor poles. Three slits are made on each rotor pole. The main purpose of opening the slits is to increase the length of the air gap between the stator and rotor poles and accordingly to

increase the reluctance value. The detailed section view of the proposed slitted motor model is given in Figure 4.
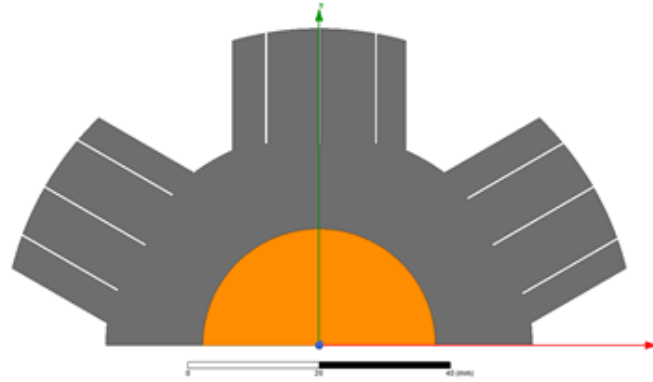


**Figure 4.** Detailed section of the slitted motor model.

## 4. OBTAINED RESULTS

RMxprt is an interactive software package used to design and analyze electrical machines. It is a template-based electrical machine design tool that provides fast and analytical calculations of machine performance. Various machines can be simulated and performance analysis can be performed using RMxprt. With the help of Maxwell, static electric fields, static magnetic fields, time varying magnetic fields and transient state analysis can be performed [14].

The analysis of reference and slitted motor models have been solved in Ansys Maxwell 2-D transient solver. The torque, current and inductance changes of each motor model are obtained. Torque changes for reference and slitted motor models are given in Figure 5. In Table 2, average and maximum torque values of both motor models are given.
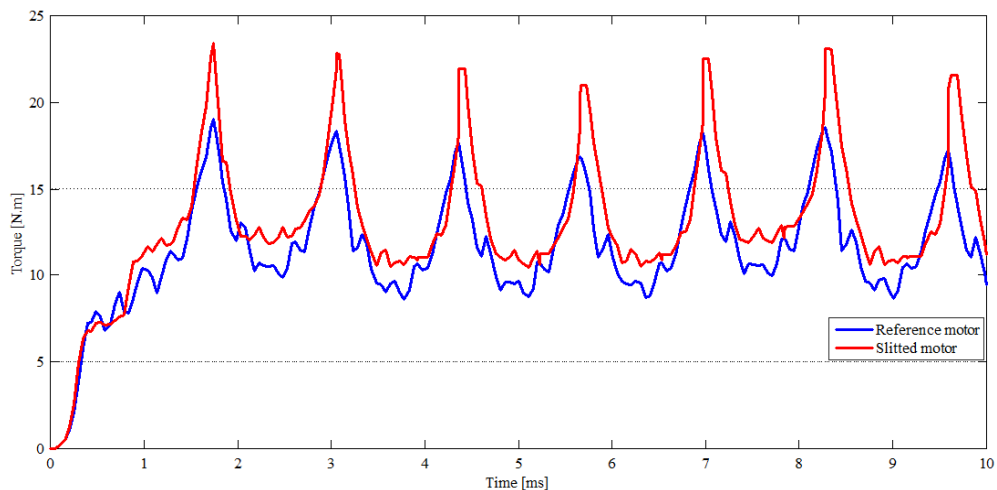


**Figure 5.** Torque variation for reference and slitted motor models.

**Table 2.** Maximum and average torque changes for reference and 3 slitted motor models.

| Torque | Reference Motor [N.m] | Slitted Motor [N.m] | Relative Difference [%] |
|---|---|---|---|
| Maximum | 19.0308 | 23.4392 | + 23.164 |
| Average | 11.5928 | 12.9987 | + 12.127 |

When Figure 5 and Table 2 are examined, it is seen that the torque values obtained from the slitted motor model increase. It was determined that the average torque increased by 12.127 % and the maximum torque by 23.164 %.

In addition, for making a healthy verify, a 5 slitted motor model has been solved in transient solver. The magnetic flux density distribution of the reference and different slitted motor models are given in Figure 6 (a), (b) and (c). When the figure is examined, it is seen that the flux density values are approximately the same.



(a)                                                                (b)



(c)
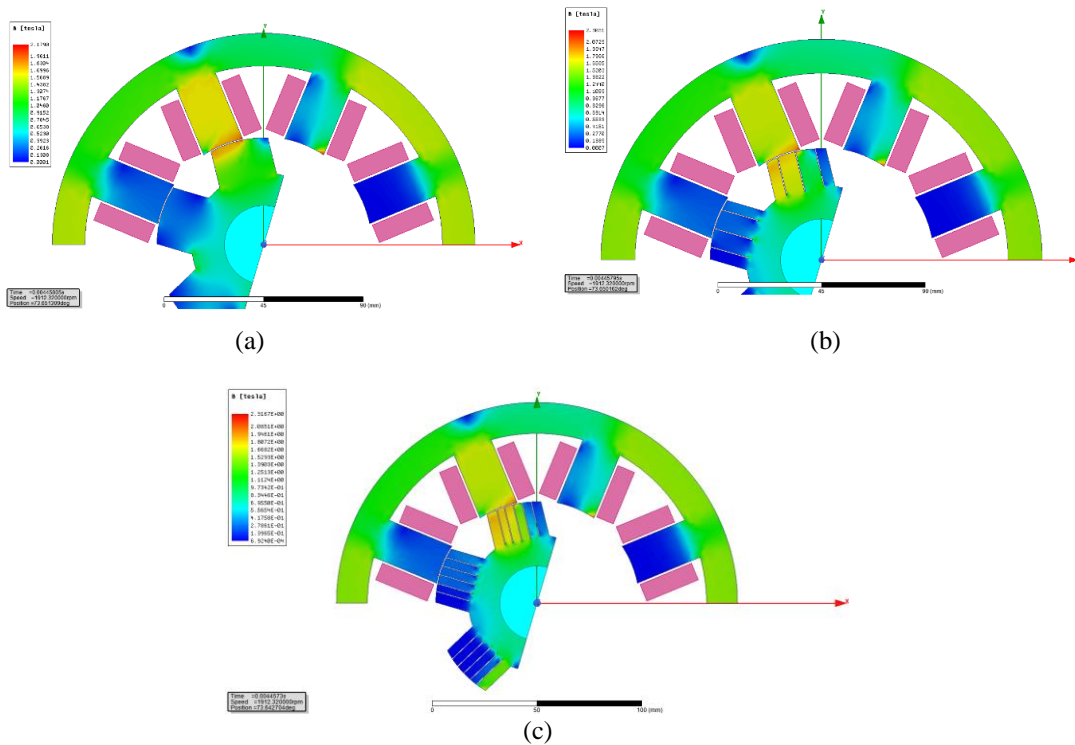
**Figure 6.** Magnetic flux density distribution (a) Reference motor model (b) 3 slitted motor model (c) 5 slitted motor model.

In Figure 7, the distribution of magnetic flux lines for reference and different slitted motor models are given. It is seen that flux lines can be directed by using slits.

(a)                                                      (b)



(c)
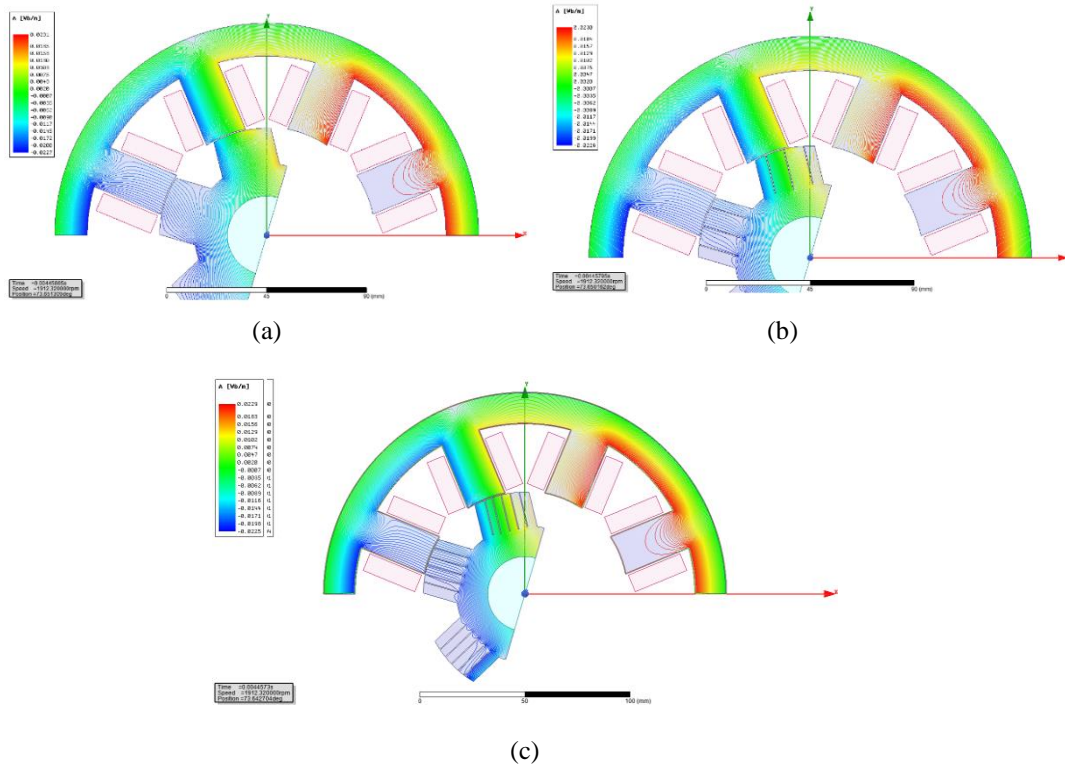
**Figure 7.** Magnetic vector potential distribution (a) Reference motor model (b) 3 slitted motor model (c) 5 slitted motor model.

Figure 8 shows the current values obtained from the reference and slitted motor models. A slight increase has been observed in the current values obtained from the 3 slitted motor model. There has no difference between the 3 slitted and 5 slitted motor current waveforms. For this reason, only 3 slitted motor current graph has been given in the text. This increase is the biggest factor in increasing the torque.
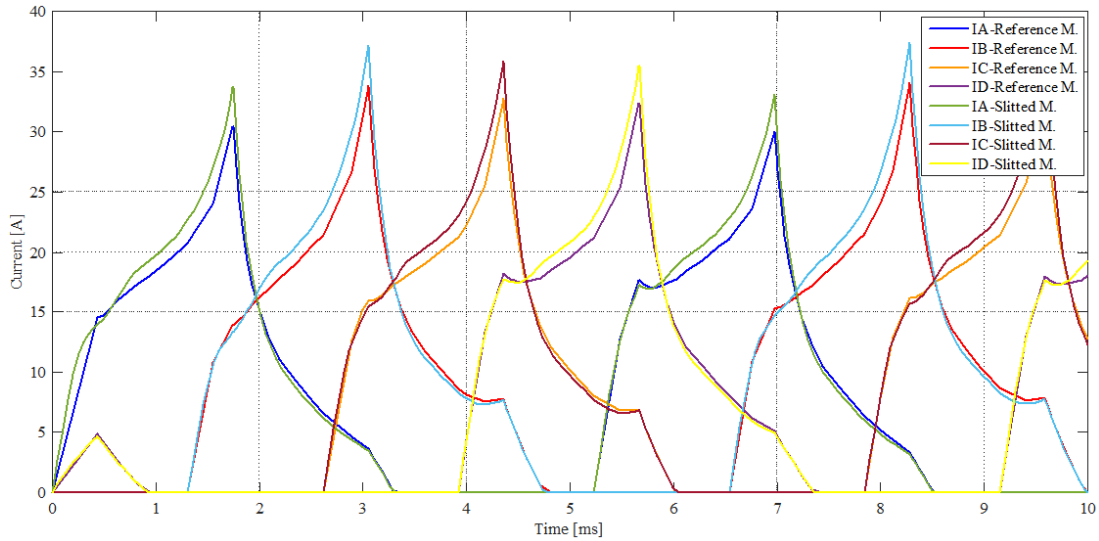
**Figure 8.** Current graph for reference and slitted motor models.

Inductance values obtained from both motor models are given in Figure 9. With the use of the 3 slitted structure, there has been a decrease in the inductance values due to the increase in reluctance in the rotor part. Also there has not been a significant inductance difference between 3 slitted and 5 slitted motor rotor models. For this reason, only 3 slitted motor graphs are given in the text. Although this situation seems to be a negative effect for the torque, it causes the voltage drop on the coils to decrease.
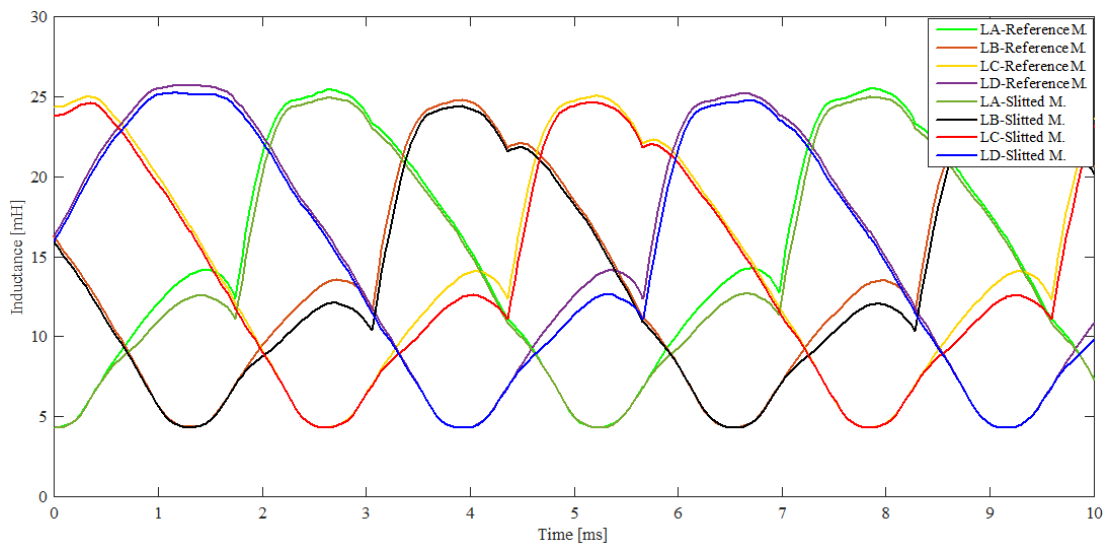


**Figure 9.** Inductance graph for reference and slitted motor models.

## 5. CONCLUSION

In this study, a new reluctance motor rotor structure design is proposed in order to increase the average and maximum torque values of the switched reluctance motor. In the proposed design, slits are opened in the rotor poles. The torque, current, inductance, magnetic flux density and magnetic vector potential changes of reference and slitted motor models are obtained.

Due to the increase in the reluctance value with the proposed motor model, a decrease has occurred in the inductance values. In the current values, it was determined that the values obtained from the slitted motor model increased by an average of 4% compared to the reference motor. This increase in current value resulted in an increase in torque values of the switched reluctance motor. Thanks to the proposed slitted structure, an increase of 12.127% in the average torque value and a 23.164% increase in the maximum torque value has been achieved. In terms of magnetic field distribution and magnetic vector potential values, it is seen that the changes obtained from both models coincide with each other.

The major objective of this study is, showing the booster effect of airgap reluctance on electromagnetic torque of slitted motor model. Only, if slot pole combinations are change, torque ripple effect can be controlled or modified on new designs. In this study, with same slot-pole configurations, only the booster effect of slit reluctances have been studied. Therefore, booster effect of airgap reluctance and inductances have been showed, how the average electromagnetic torque of proposed motor model has been increased.

A simple information can be given for stator and rotor structures material. Steel_1008 lamination has been used on transient solver while numerical modelling. Core loss model choice of the material has not been used while transient solver working. Reference and slitted models have been made from same lamination. Therefore, only average torque increasing effect with airgap reluctance has been observed. There will be a supplementary study about material effect can be conducted for future work. It has been shown that the average and maximum torque values can be increased for the same size and power values thanks to the proposed structure.

## ACKNOWLEDGMENT

## REFERENCES

[1]  Aydoun, R., Parent, G., Tounzi, A. and Lecointe, J. P., (2020), Performance comparison of axial-flux switched reluctance machines with non-oriented and grain-oriented electrical steel rotors, Open Physics, 18, 981–988.

[2]  Üstün, O. and Önder, M., (2020), An improved torque sharing function to minimize torque ripple and increase average torque for switched reluctance motor drives, Electric Power Components and Systems, 48(6-7), 667-681.

[3] Fan, J. and Lee, Y. K., (2020), A novel average torque control of switched reluctance motor based on flux–current locus control, Canadian Journal of Electrical and Computer Engineering, 43(4), 273-281.

[4] Hamouda, M. and Szamel, L., (2019), Optimum control parameters of switched reluctance motor for torque production improvement over the entire speed range, Acta Polytechnica Hungarica, 16(3), 79-99.

[5] Han, J., Ge, B., Zhang, K., Wang, Y. and Wang, C., (2020), Influence of control and structure parameters on the starting performance of a 12/8 pole switched reluctance motor, Energies, 13, 1-15.

[6] Gondaliya, B. and Tita, Y., (2016), Design of switched reluctance motor with exterior and interior rotor, International Journal for Innovative Research in Science & Technology, 2(11), 463-467.

[7] Vattikuti, N., Rallabandi, V. and Fernandes, B. G., (2008), A novel high torque and low weight segmented switched reluctance motor, 2008 IEEE Power Electronics Specialists Conference, 15-19 June, Rhodes, Greece, 1223-1228.

[8] Sovicka, P., Rafajdus, P. and Vavrus, V., (2020), Switched reluctance motor drive with low-speed performance improvement, Electrical Engineering, 102, 27–41.

[9] Polat, M., Öksüztepe, E. and Kürüm, H., (2011), Modeling and closed-loop speed and current control of submersible pump-type switched reluctance motor with 8/6 poles using inductance curves obtained from the finite element method, e-Journal of New World Sciences Academy Engineering Sciences, 6(1), 21-40.

[10] Krishnan, R., (2001), Switched reluctance motor drives, modeling, simulation, analysis, design, and applications, In J. D. Irwin (Ed.), CRC Press LLC, Blacksburg, Virginia.

[11] Öner, Y. and Öztürk, M., (2015), The magnetic analysis and design of new type axial flux switched reluctance motor, Gazi Üniversitesi Mühendislik Mimarlık Fakültesi Dergisi, 30(3), 461-474.

[12] Fitzgerald, A. E., Kingsley, C. and Umans S. D., (2002), Electric machinery 6th edition, Mc Graw Hill Series, USA.

[13] Bekkouche, B., Chaouch, A. and Mezari, Y., (2006), A switched reluctance motors analyse using permeance network method, International Journal of Applied Engineering Research, 1(2), 137-152.

[14] Allirani, S., Vidhya, H., Aishwarya, T., Kiruthika, T. and Kowsalya, V., (2018), Design and performance analysis of switched reluctance motor using ansys maxwell, Proceedings of the 2nd International Conference on Trends in Electronics and Informatics, 11-12 May, Tirunelveli, India, 1427-1432.

[15] Basha, S. N., Deepak, A., Raju, M. R. and Lavanya, K. S. L., (2020), Simulation of 8/6 switched reluctance motor using ansys - maxwell 2D, Compliance Engineering Journal, 11(5), 179-185.

*RESEARCH ARTICLE*

# OVERESTIMATION of DISPLACEMENT DUE to MISINTERPRETATION of EARTHQUAKE RUPTURE PARAMETERS

Cuneyt YAVUZ[1]

[1] Kütahya Dumlupınar University, Technical Sciences Vocational School, Department of Construction Technology, Kutahya, cuneyt.yavuz@dpu.edu.tr, ORCID: https://orcid.org/ 0000-0001-9767-7234

## ABSTRACT

Tsunamis that killed hundreds of thousands of people, especially in the last two decades, are one of the most devastating natural hazards. Throughout history, tsunamis caused by devastating earthquakes have resulted in the loss of life, property, and environmental damage on the coasts. Recently, however, extreme hazard possibilities have been suggested due to misinterpretation of earthquake parameters and the overestimation of displacements. The structure of the seismic moment equation commonly used by scientists allows some manipulation on the rupture area of the fault and the displacement. Because of this gap, scientists produce different displacement amounts for an earthquake of the same magnitude and therefore, different tsunami wave heights are estimated by decreasing the rupture area and also, increasing the displacement under the sea. In this study, earthquake parameters are calculated based on a comprehensive literature review and compared with previous studies. The difference between the displacements calculated using regression analysis in the study and other studies reveals that the assumptions and estimations regarding the rupture parameters differs according to expert knowledge. The article aims to shed light on a reliable method of rupture parameter calculation to avoid misinterpretation and randomness.

## 1. INTRODUCTION

The Mediterranean Sea coastlines have been densely populated in recent years. The utilization of the coastal regions has also been increased with critical infrastructures such as international ports, airports, industrial structures, and power plants. Therefore, reliable estimation of potential hazards is vital for the maximization of risk reduction along these coastlines. The reliable analysis of historical earthquakes and tsunamis is a method that has been used to determine the destructive effects of possible future hazards [1-4]. Ambraseys [5] stated that the 365 Crete earthquake and tsunami, which uplifted the western coast of the Crete island about 9 m and affecting almost all of the coastal cities of the Mediterranean, is the largest natural disaster recorded in the Mediterranean. Papadapoulos et al. [6] compiled evidence of the 365 Crete earthquake and tsunami. It has been recorded that up to 7 m tsunami waves hit the coasts of the Mediterranean Sea and resulted in nearly 5000 drowned people in Alexandria, countless affected people in Sicily, Crete, and other towns located along the

Mediterranean coastline. However, Papadopoulos et al. [6] also noted that the geological documentation of the 365 Crete earthquake and tsunami has still questionable. Yolsal et al. [7] also conducted a numerical investigation on the 365 Crete, the 1222 Paphos earthquake, and the 1303 Crete earthquake. Yolsal-Cevikbilen and Taymaz [8] conducted a study on earthquake source parameters along the Hellenic subduction zone and estimated the rupture parameters and displacement amounts for the same historical earthquakes in the Eastern Mediterranean Sea. Detailed rupture parameters were revealed, both historical earthquakes and tsunamis (Table 1).

**Table 1.** Rupture parameters the most known megathrust earthquakes in the Mediterranean Sea [7-8].

| Rupture Parameters | 365 Crete Earthquake | 1222 Paphos Earthquake | 1303 Crete Earthquake |
|---|---|---|---|
| Moment magnitude ($M_w$) | >8.0 | 7.0- 7.5 | $\approx 8.0$ |
| Focal Depth (km) | 20 | 15 | 20 |
| Displacement (D) (m) | 15 | 3 | 8 |
| Fault length (L) (km) | 200 | 50 | $\approx 100$ |
| Fault width (W) (km) | 50 | 25 | $\approx 30$ |
| Strike angle (°) | 295 | 305 | 115 |
| Dip angle (°) | 15 | 35 | 45 |
| Rake angle (°) | 90 | 110 | 110 |

Shaw et al. [9] estimated 20 m vertical displacement occurred in the 365 Crete earthquake. Necmioglu [10] also conducted a wide-ranging study on tsunami hazards in Turkey and connected seas. The study concluded by examining 2415 different tsunami scenarios that especially for the Aegean and Eastern Mediterranean regions. It was concluded that earthquakes with moment magnitude, $M_w \approx 6.5$-6.9, and focal depth $\leq 100$ km generate 0.5 m tsunami wave height along the coastlines of Aegean Sea, South-East Cyprus, and around the Hellenic Arc. For the earthquakes with a focal depth greater than 100 km, the Richter magnitude of the earthquake should be greater than $M_w 7.0$ for the same tsunami wave height along the coastline. In order to obtain a 0.5 tsunami wave height around the Levantine coasts, the northern parts of Egypt, the northeastern part of Libya, and the southern coasts of Turkey, the moment magnitude of the earthquake should be $M_w \approx 7.0$ to 7.4.

However, there are some recent studies mentioning misinterpretation and overestimation of historical earthquakes and tsunamis in the Mediterranean Sea. Underestimation of rupture parameters are comprehensively investigated for tsunami risk assessment and implementation of tsunami early warning issues considering the 2011 Tohoku Earthquake [11]. A specified Probabilistic Tsunami Hazard Analysis (PTHA) and risk assessment method was developed for the coastal urban areas [11]. Marriner et al. [12] mentioned that 90% of the inundation events observed throughout history along the Mediterranean coastlines might be due to storm activities instead of tsunamis. Therefore, it is claimed that scientists misinterpreted the evidence found in inland regions [12]. The support of this claim comes from the analysis of tsunami and storm data compiled in the EM-DAT (Emergency Events Database), which is an international data repository of disasters for the period 1900–2015. However, Papadopoulos et al. [13] stated that storm surge action does not explain the typical characteristics of tsunami deposition. Considering the literature survey, it is obvious that there is no consensus among scientists for a reliable calculation method of the earthquake rupture parameters. This difference of opinion creates a gap about the unreliable calculation of rapture parameters that can be the reason for overestimation of displacement and tsunami waves. Since the risk analyses are

conducted to estimate the most probable consequences of a natural hazard, a kind of misinterpretation of any data may have resulted in extraordinary risk evaluations and unnecessary precautions against an impossible hazard.

In this study, a comprehensive investigation has been conducted on the reliable estimation of earthquake rupture parameters, especially rupture area and displacement. Rupture parameters for the megathrust earthquakes are compiled from different scientific studies and compared with calculated ones. The source parameters (i.e. fault length ($L$), fault width ($W$), and displacement ($D$)) of 365 Crete, 1222 Paphos, and 1303 Crete earthquakes are re-evaluated using a specific calculation mean contrary to the revealed rupture parameters by some of the scientists (Figure 1).



**Figure 1.** Locations of the historical earthquakes.

A comprehensive investigation on empirical calculation means of rupture parameters is made and the most reliable empirical equations are revealed to end the debate on the vital issue. The performances of the selected equations are tested by calculating the rupture parameters of the megathrust historical earthquakes that occurred in the Mediterranean Sea. The difference between the results released by the previous studies and by this research is extremely erratic and presented in the results and discussion section.

## 2. MATERIALS AND METHODS

### 2.1. Calculation of Rupture Parameters
Commonly used seismic moment ($M_0$) equation was developed by Hanks and Kanamori [14]. The equation is derived as a function of the shear modulus of the crust ($\mu$), $L$, $W$, and $D$ to reveal the relationship between the source parameters and the magnitude of the earthquake. $M_0$ is calculated for crustal faults as [14]:

$$M_0 = \mu LWD \tag{1}$$

where $\mu$ is taken as $3*10^{11}$ dyne/cm$^2$.

Hanks and Kanamori [14] also developed a well-known relationship between $M_0$ and $M_w$ of a crustal earthquake as follows:

$$M_w = \frac{2}{3} * \log(M_0) - 10.7 \tag{2}$$

In this study, earthquake rupture parameters are calculated using Eq. 2 and Eq. 1, respectively. However, especially Eq.1 can easily be manipulated due to the proportional relationship between the essential parameters used in the equation. Therefore, some other empirical relationships are revealed by the scientists dealing with seismic analysis. [11,15-17]. Since the constituent parameters of the seismic moment equation are reversely proportional, an infinitesimal change of fault length or fault width value might end up within an extremely high displacement of the crust determines the size of tsunami wave height for the same moment magnitude. For instance, 2 m and 10 m displacement values can be obtained for $M_w 7.0$ by just manipulating the fault length or fault width value in $M_0$ equation. Thus, the correct determination of rupture parameters is significant to abstain from the overestimation of displacement of the earthquake.

The regression analysis proposed by some researchers are compared using the same historical earthquake data set (EDS) and shown as $M_w$-W, and $M_w$-L relationship in Figure 2 (a) and (b), respectively.
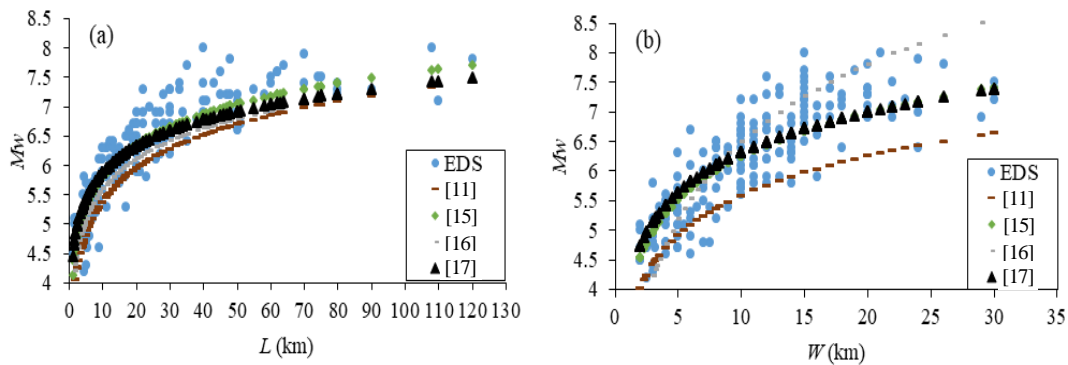


**Figure 2.** Comparison of (a) fault length and (b) fault width calculation from different sources.

Depending on the calculation results in Figure 2, the regressions provided by Wells and Coppersmith [17] are found as the most convenient equations and applied to calculate L and W of the historical earthquake's rupture parameters. Displacement occurred on the earth's crust due to earthquake can then be easily extracted from the seismic moment equation (Eq. 1) proposed by Hanks and Kanamori [14].

The empirical equation proposed by Wells and Coppersmith [17] shows the regression of L, on $M_w$ as follows;

$$M_w = 4.38 + 1.49 * \log(L) \tag{3}$$

The following equation shows the regression of W, on $M_w$ [17].

$$M_w = 4.06 + 2.25 * \log(W) \tag{4}$$

To preserve the similarity and ease of the comparison, the rest of the rupture parameters such as the location of the historical earthquake and the rupture angels are directly compiled from the literature [7-10]. This study shows that even making a small change among the rupture parameters in Eq. 1 by remaining the seismic moment value similar can be resulted in a high difference for the D value.

Misinterpretations of rupture parameters, especially for the rupture area, always resulted in high level of displacement estimation underneath the sea. That can cause extraordinary tsunami wave heights, which can be caused overestimated hazard assessments and unnecessary precautions against a hypothetical tsunami event throughout a coastline. If rapture area is correctly calculated, the overestimation of tsunami hazards might be prevented.

## 3. RESULTS

The assumed and estimated fault length, fault width, and displacement values revealed by the scientists are shown for the historical earthquakes are given in Table 2 with their references. To do this, L and W of the historical earthquakes are calculated using the equations proposed by Wells and Coppersmith [17]. Then displacement values can then be calculated using Eq. (1) and compared with the published studies. Displacement values are also calculated using the proposed method in this study, and given in Table 2, to show the misinterpretation of rupture parameters and their effects on the calculation of displacement.

**Table 2.** Comparison of the estimated and calculated displacement values for 365 Crete, 1222 Paphos and 1303 Crete Earthquakes.

| Earthquake ID | L (km) | W (km) | D (m) | Reference |
|---|---|---|---|---|
| 365 Crete | 100 | 90 | 20 | [18] |
| | 200 | 50 | 15.00 | [7,8] |
| | 100 | No data | 9.00 | [5], [19] |
| | 100 | No data | 10 | [20,21] |
| | **255** | **55** | **5.04** | **Calculated data** |
| 1222 Paphos | 50 | 25 | 3.00 | [7,8], [22,23] |
| | | | 3.00±1.00 | [24] |
| | **75** | **25** | **1.40** | **Calculated data** |
| 1303 Crete | 100 | 30 | 8.00 | [7,8] |
| | 60 | 30 | 4.00 | [25] |
| | No data | No data | 1.00-3.60 | [26] |
| | **230** | **50** | **3.75** | **Calculated data** |

All these data show that the displacement values released by the previous studies differ dramatically. This is because of the misinterpretation or manipulation of the commonly used seismic moment

equation proposed by Hanks and Kanamori [14]. Calculated rupture area using the Eqs. (3) and (4) gives lower displacement values comparing with the literature. Especially, Yolsal et al. [7] and Yolsal-Cevikbilen and Taymaz [8] misinterpreted the rupture areas and overestimated the tsunami risk for all three case studies in their research. Considering the 2004 Indian Ocean, 2011 Tohoku, and similar earthquakes and tsunami disasters experienced in the last two decades, the displacement values and tsunami wave heights coincide with the calculation mean proposed in this study.

## 4. CONCLUSION

Contrary to the magnitude of an earthquake, earthquake rupture area beneath the sea or ocean cannot be precisely recorded due to lack of scientific and technological deficiency. Because of this gap in the recorded data, fault length and fault width parameters are generally either estimated by the local authorities or based on expert options. Misinterpretation of the rupture area can generate a fatal error for the local authorities to take extraordinary precautions against a hypothetical tsunami event along the coastline. This can be resulted in wasting huge amounts of money and investment along the coastline. The structure of the seismic moment equation, commonly used by scientists, allows some manipulations on the rupture area and displacement. Due to this problem, scientists may generate different displacement values for the same magnitude of an earthquake by lowering the rupture area and increasing the displacement amount underneath the sea. Therefore, a reliable estimation of rupture area and displacement are vital for a pointed tsunami risk assessment not only for the Mediterranean coastline but also throughout the world. This study shows that the calculation characteristics of rupture parameters should be reconsidered and well-founded to obtain a good tsunami risk assessment.

## ACKNOWLEDGEMENTS

## REFERENCES

[1] Nazeri, S., Colombelli, S., & Zollo, A., (2019), Fast and accurate determination of earthquake moment, rupture length and stress release for the 2016–2017 Central Italy seismic sequence. Geophysical Journal International, 217(2), 1425-1432.

[2] Lin, J. T., Chang, W. L., Melgar, D., Thomas, A., & Chiu, C. Y., (2019), Quick determination of earthquake source parameters from GPS measurements: a study of suitability for Taiwan. Geophysical Journal International, 219(2), 1148-1162.

[3] Saadalla, H., Mohamed, A., & El-Faragawy, K., (2019), Determination of earthquake source parameters using the inversion of waveform data: A case of small earthquakes around High Dam Lake, Aswan region, Egypt. Journal of African Earth Sciences, 151, 403-416.

[4]  Prastowo, T., & Fahmi, M. N. (2020). Estimation of Rupture Directivity, CMT and Earthquake Tsunami Parameters and Their Correlation with the Main Source of the First Tsunami Wave, September 28, 2018. Science of Tsunami Hazards, 39(4).

[5]  Ambraseys, N., (2009), Earthquakes in the Mediterranean and Middle East. Cambridge, United Kingdom: Cambridge University Press, ISBN 978-0-521-87292-.

[6]  Papadopoulos, G.A., Daskalaki, E., Fokaefs, A., Giraleas, N., (2010), Tsunami hazard in the Eastern Mediterranean Sea: strong earthquakes and tsunamis in the west Hellenic arc and trench system, Journal of Earthquake and Tsunami, 4 (03): 145-179.

[7]  Yolsal, S., Taymaz, T., Yalciner, A.C., (2007), Understanding tsunamis, potential source regions and tsunami-prone mechanisms in the Eastern Mediterranean, Geological Society, 291 (1): 201-230.

[8]  Yolsal-Çevikbilen, S., Taymaz, T., (2012), Earthquake source parameters along the Hellenic subduction zone and numerical simulations of historical tsunamis in the Eastern Mediterranean, Tectonophysics, 536: 61-100.

[9]  Shaw, B., Ambraseys, N.N., England, P.C., Floyd, M.A., Gorman, G.J., Higham, T.F.G., Jackson, J.A., Nocquet, J.M., Pain, C.C., Piggott, M.D., (2008), Eastern Mediterranean tectonics and tsunami hazard inferred from the AD 365 earthquake, Nat. Geosci., 1: 268 – 276.

[10]  Necmioglu, O., (2014), Tsunami Hazard in Turkey and Surroundings, PhD, Istanbul Technical University, Istanbul, Turkey.

[11]  Goda, K., Abilova, K., (2016), Tsunami hazard warning and risk prediction based on inaccurate earthquake source parameters, Natural Hazards and Earth System Sciences, 16 (2): 577-593.

[12]  Marriner, N., Kaniewski, D., Morhange, C., Flaux, C., Giaime, M., Vacchi, M., Goff, J., (2017), Tsunamis in the geological record: Making waves with a cautionary tale from the Mediterranean, Science advances, 3 (10): e1700485.

[13]  Papadopoulos, G.A., Minoura, K., Imamura, F., Kuran, U., Yalciner, A.C., Fokaefs, A., Takahashi, T., (2012), Geological evidence of tsunamis and earthquakes at the Eastern Hellenic Arc: correlation with historical seismicity in the eastern Mediterranean Sea, Research in Geophysics, 2 (2): e12-e12.

[14]  Hanks, T.C., Kanamori, H., (1979), A moment-magnitude scale, J. Geophys. Res., 84: 2348-2350.

[15]  Blaser, L., Krüger, F., Ohrnberger, M., Scherbaum, F., (2010), Scaling relations of earthquake source parameter estimates with special focus on subduction environment, Bulletin of the Seismological Society of America, 100 (6): 2914-2926.

[16] Papazachos, B.C., Scordilis, E.M., Panagiotopoulos, D.G., Papazachos, C.B., Karakaisis, G.F., (2004), Global Relations between Seismic Fault Parameters and Moment Magnitude of Earthquakes, Bulletin of the Geological Society of Greece, 36.

[17] Wells, D.L., Coppersmith, K.J., (1994), New empirical relationships among magnitude, rupture length, rupture width, rupture area, and surface displacement, Bulletin of the seismological Society of America, 84 (4): 974-1002.

[18] Onat, Y., and Yalciner, A.C., (2013), Initial stage of database development for tsunami warning system along Turkish coasts, Ocean Engineering, 74: 141-154.

[19] Stiros, S.C., (2001), The AD 365 Crete earthquake and possible seismic clustering during the fourth to sixth centuries AD in the Eastern Mediterranean: a review of historical and archaeological data, Journal of Structural Geology, 23 (2-3): 545-562.

[20] Shaw, B., Ambraseys, N.N., England, P.C., Floyd, M.A., Gorman, G.J., Higham, T.F.G., Jackson, J.A., Nocquet, J.M., Pain, C.C., Piggott, M.D., (2008), Eastern Mediterranean tectonics and tsunami hazard inferred from the AD 365 earthquake, Nat. Geosci., 1: 268 – 276.

[21] England, P., Howell, A., Jackson, J., Synolakis, C., (2015), Palaeotsunamis and tsunami hazards in the Eastern Mediterranean, Philosophical Transactions of the Royal Society A: Mathematical, Physical and Engineering Sciences, 373 (2053), 20140374

[22] Periáñez, R., Abril, J.M., (2014), Modelling tsunamis in the Eastern Mediterranean Sea: Application to the Minoan Santorini tsunami sequence as a potential scenario for the biblical Exodus, Journal of Marine Systems, 139, 91-102.

[23] Hamouda, A.Z., (2010), Worst scenarios of tsunami effects along the Mediterranean coast of Egypt, Marine Geophysical Researches, 31 (3): 197-214.

[24] Altinok, Y., Alpar, B., Özer, N., Aykurt, H., (2011), Revision of the tsunami catalogue affecting Turkish coasts and surrounding regions, Natural Hazards and Earth System Sciences, 11 (2): 273-291.

[25] Hamouda, A.Z., (2006), Numerical computations of 1303 tsunamigenic propagation towards Alexandria, Egyptian Coast, Journal of African Earth Sciences, 44 (1): 37-44.

[26] El-Sayed, A., Romanelli, F., Panza, G., (2000), Recent seismicity and realistic waveforms modeling to reduce the ambiguities about the 1303 seismic activity in Egypt, Tectonophysics, 328 (3-4), 341-357.

*RESEARCH ARTICLE*

# INVESTIGATION OF FLOW CHARACTERISTICS FOR A MULTI-STAGE TESLA VALVE AT LAMINAR AND TURBULENT FLOW CONDITIONS

Ahmet Alper YONTAR[1]*, Duygu SOFUOĞLU[2], Hüseyin DEĞİRMENCİ[3], Mert Şevket BİÇER[4], Tahir AYAZ[5]

[1]Tarsus University, Mechanical Engineering Department Faculty of Engineering, Mersin, aayontar@tarsus.edu.tr, ORCID: 0000-0002-5453-5137
[2]Tarsus University, Manufacturing Engineering Department Graduate Education Institute, Mersin, duygu_sofuoglu@tarsus.edu.tr, ORCID: 0000-0001-5522-7331
[3]Tarsus University, Automotive Engineering Department Graduate Education Institute, Mersin, huseyin_degirmenci@tarsus.edu.tr, ORCID: 0000-0001-7585-8907
[4]Tarsus University, Mechanical Engineering Department Graduate Education Institute, Mersin, mert_bicer@tarsus.edu.tr, ORCID: 0000-0002-9215-6787
[5]Tarsus University, Automotive Engineering Department Graduate Education Institute, Mersin, tahir_ayaz@tarsus.edu.tr, ORCID: 0000-0002-1291-987X

## ABSTRACT

Tesla valve is a passive type check valve that empowers flow in one direction without moving parts used for flow control in mini or microchannel systems. It is a system that can be used for a long time with low fatigue and low wear due to the lack of moving parts in its structure. Besides the cost of production is cheap due to its simple geometry. Also, the Tesla valve differs from all other valves with these features. Allowing or preventing the movement of the fluid is due to the specific design of the profiles inside the valve. In addition, the fluid that encounters obstacles at high velocities continues on its way by gaining thermodynamic properties. The efficiency of the Tesla valve is measured by diodicity, which can be managed by small losses due to direction during forward or reverse flows, primarily along with the flow inlet speed and flow line design. In this study, the variation of the velocities of methane gas in the specially designed Tesla valve has been investigated in detail via numerical analysis. Tesla valve structure with eleven flow control segments was used in the analysis. Moreover, the fluid motion behaviors in both directions were investigated for laminar and turbulent velocities. As a result of the study, the turbulence kinetic energy change and diodicity were determined for methane use in the Tesla valve. Also, different characteristic features of laminar and turbulent flow have been revealed in the tesla valve.

**Keywords**: *Tesla Valve, Methane, Computational Fluid Dynamics, Diodicity, Turbulence Kinetic Energy.*

## 1. INTRODUCTION

Check valves without moving parts provide flow control in mini-micro channels [1-5] and the valves have a pressure drop based on the direction. As a consequence of the properties, the trend determines the progress of the flow direction. Small pressure losses occur depending on the flow direction owing

to their unique designs. Current flow in forwarding and reverse direction acquires diode feature to the fluid. Check valves have features that can be easily scaled and manufactured by separating them from micro-pumps containing moving parts. Besides, check valves can be used with colloidal suspensions. Check valves under the favor of these advantages; It has been used frequently in biotechnological devices, microelectromechanical systems, analytical chemistry, health, and engineering applications [1].

The Tesla valve was invented by Nikola Tesla, as it is well known. The Tesla valve was shown in Figure 1 consists of stationary parts that allow flow with low resistance in one direction but create high resistance to flow on the reverse. It is called reverse flow to the stream direction with high resistance and forward flow to the stream direction with low resistance. This difference in flow resistance causes a continuous directional flow velocity in the forward direction in oscillatory flows. The efficiency of a Tesla valve at constant velocities is measured by diodicity, which is the ratio of the pressure difference in the reverse and forward flow directions. The efficiency is frequently expressed as diodecity, which is the ratio of pressure drops for the same flow velocity. Small pressure losses in the Tesla valve; flow splitting is due to sudden expansion and jet impingement. The equation that can be seen below characterizes the ability to pass flow in the forward direction while inhibiting flow in the reverse direction. The differential pressure loss that forms the diodicity of a Tesla valve is due to inertial and viscous force.

$$Di = \left(\frac{\Delta P_r}{\Delta P_f}\right)_Q \tag{1}$$

$\Delta P_f$ represents the forward flow drop for flow rate Q and $\Delta P_r$ means that the pressure drop of the reverse flow. The literature on the use of Tesla valve, there are studies in various content and approaches. Some of these studies are briefly summarized in the following section.

Truong and Nguyen [6] conducted a numerical study to obtain the optimum geometry in the Tesla valve. They have been analyzed two-dimensional (2D) geometries with different flow rates and different channel angles (00-800) for the case of Reynolds number (Re <1000). As a result of the study, it was determined that the most suitable design is the Tesla valve with T45-R geometry with a canal angle of 450 in the range of 100 <Re <600.

Forster et al. [7] studied the efficiency of the diffuser valve and Tesla valve employing a piezo-operated pump. In the present study, they have been conducted an experimental study to develop efficient non-moving split valves and to provide optimum Tesla valve geometry. Consequently, it has been determined that Tesla valves have higher diodes than diffuser check valves. It has been found that the diodicity increases linearly with the flow rate when the Re number is below 300 for the T45-R valve.

Zhang et al. [8] investigated the relationship between diodicity, pressure drop, and flow rate in T45-R valve in three dimensions (3D) at Re = 2000. It has been observed that it gives maximum diodicity in low Re (Re <500) numbers. According to the results obtained for the same hydraulic diameter, valves having a higher aspect ratio have been found that better performance is obtained.

Gamboa et al. [9] examined the Tesla-type valve for micro pump applications with six independent and dimensionless parameters. They have been benefited from 2D numerical simulations in their

optimization studies. As a result of the study, it has been determined that the optimized design provides 25% higher diodicity in the range of 0-2000 Reynolds number compared to the commonly used Tesla-type valve shape. The resulting valve was adopted as the Gamboa, Marris, and Forster (GMF) Tesla valve.

Thompson et al. [10] investigated laminar and turbulent flow regimes up to Re = 2000 using 3D CFD in Tesla valve at inlet Reynolds numbers. It was based on the RANS-based flow modeling approach used to measure diodicity, various models including k-ε, k-ω, and SST k-ω models were used in the study. It has been determined that the k-ω model and SST k-ω models perform more accurate simulations than laminar two-dimensional CFD analysis for the case where Re> 500 is in the Tesla valve. It has been found that the k-ω model and SST k-ω models perform more accurate simulations compared to the laminar two-dimensional CFD analysis for the situation where there is Re>500 in the Tesla valve. The k-ω model has been found to provide the best performance and show 6% maximum relative error with available experimental data for up to Re = 1500.

Mohammadzadeh et al. [11] numerically investigated the effect of Reynolds number and Tesla valve stage on diodicity. The study was carried out in 2D and the results of the wide-angle multistage tesla valve (MSTV) and the diffuser type no-moving parts valve (NMPV) were compared. They have been found that the diodeicity of wide-angle MSTV is superior to diffuser type NMPV in high Reynolds numbers (Re> 200), and that the diodety of low Reynolds numbers is lower than NMPV. Besides, it was observed that the diodicity increased in direct proportion to the Tesla valve stage at the Re> 50.

Porwal et al. [12] examined the effect of different stages of the Tesla valve on flow properties and thermal improvement on CFD in three dimensions. They have been investigated in the simulation results that Tesla valve design can achieve efficiency in terms of Nusselt number, Darcy friction factor, diodicity, thermal diodicity. They have been monitored that the heat transfer increase with the number of stages in the reverse flow Tesla valve.

Thompson et al. [13] performed three-dimensional analyzes to examine the effect of Tesla valve stage on diodicity under laminar flow conditions. In the analyzes, the effect of the parameters of valve stage (up to 20), valve distance and Reynolds number (up to Re = 200) on diodicity was investigated. Consequently, it was determined that the diodicity was directly proportional to the number of Re and the number of stages and inversely proportional to the valve distance. It has been observed that the number of valves and the distance between the valves have little effect on the diodicity when the Re number is below 50.

Bardel [14] investigated experimentally and numerically the effect of different Tesla valve designs on diodicity at low Reynolds numbers. It has been found to be dependent on viscous forces, laminar flow of different location and size, recirculating flow mechanisms for the diodicity mechanism in Tesla valve. The results were gained from 2D numerical studies have been confirmed by experimental results.

Qian et al. [15] studied the flow of $Al_2O_3$-water nano-fluid through a micro-scale T45-R type Tesla valve numerically. The effects of nano-liquid flow rate, flow percentage, pressure drop in forwarding and backward flows, diodicity, temperature, and nanoparticle volume fraction on Tesla valve were investigated. They have been detected that nanofluids flowed towards the straight channel of the bifurcated section in forwarding flow and towards the arc channel in the opposite direction. It was determined that the diodicity changes linearly with the flow rate.

Jin et al. [16] quantified the use of Tesla valves in hydrogen fuel cell electric vehicles. They have been investigated a wide range of velocities using parameters such as hydraulic diameter, valve angle and radius of the inner curve to increase the pressure drop in the Tesla valve. It has been detected that the pressure drop decreases with increasing hydraulic diameter and increases with large velocity inputs. It has been observed with a numerical study that a multi-stage Tesla valve is needed to ensure sufficient pressure drop.

Wang et al. [17] made a series of numerical studies to optimize the design of new type Tesla valve micro-mixers. It was determined that a three-unit Tesla type micro mixer provides high flow mixing performance and observed that the optimal geometry provides a low pressure drop over the Tesla type micro mixer arrangement.

Although there are few studies conducted with Tesla valve in the literature, the working range has been limited. In this study, the behavior of methane fuel delivery velocity in the flow lines of a specially designed Tesla valve is examined in detail via the two-dimensional (2D) computational fluid dynamics (CFD) method.

## 2. METHODOLOGY

The effects of gas fluid delivery at different velocities in an eleven-wing Tesla valve with a low angle configuration were studied via 2D-CFD modeling in this study. The motion attitude of methane fuel was investigated between 1 m/s - 10 m/s in reverse and forward flows. The geometric design of the Tesla valve is shown in Figure 1.
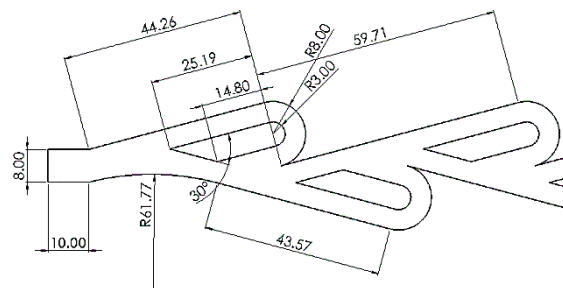


**Figure 1.** Tesla valve geometry.

As shown in Figure 2 that 10 lines other than the inlet and outlet line points were determined and evaluated for investigating the turbulence kinetic energy changes inside the Tesla valve. The lines were taken from the distance before 2 mm from the start of the point where the flow separates according to the reverse flow.
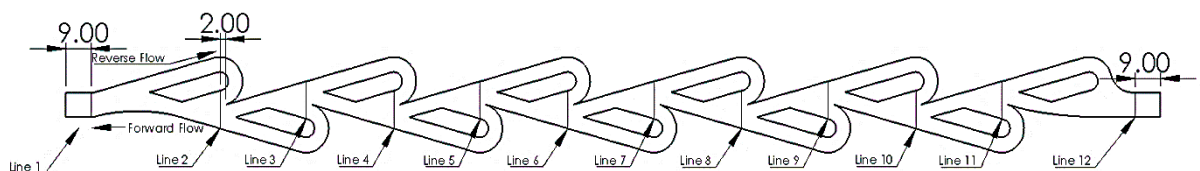


**Figure 2.** The positions of the lines.

Here, a very important detail should be taken into consideration while analyzing the study data. These are the flow from line 12 to line 1 in the forward flow where the reverse flow flows from line 1 to line 12.

$$Re_i = \frac{\rho u_i D_H}{\mu} \tag{2}$$

The Reynolds number is a unitless number that informant about the state of the fluid and it is described as the ratio of the inertia forces of the fluid to the viscosity forces. In the study; the changing Reynolds ($Re_i$) numbers with entry velocities were defined. Laminar and turbulent flow conditions were determined according to Reynolds numbers. At the equation; $u_i$ represents the input velocity with respect to the reverse or forward flow, $\rho$ represents the density of methane, $\mu$ represents the dynamic viscosity of methane, and $D_H$ represents the hydraulic diameter.

In order to ensure the mesh independent solution and make sure that the model is running correctly, turbulence kinetic energy analysis was run for the various meshes. Turbulence kinetic energy did not change beyond the mesh number of 2 million. Therefore, the number of meshes used in the flow analyses was set to approximately 2.25 million.
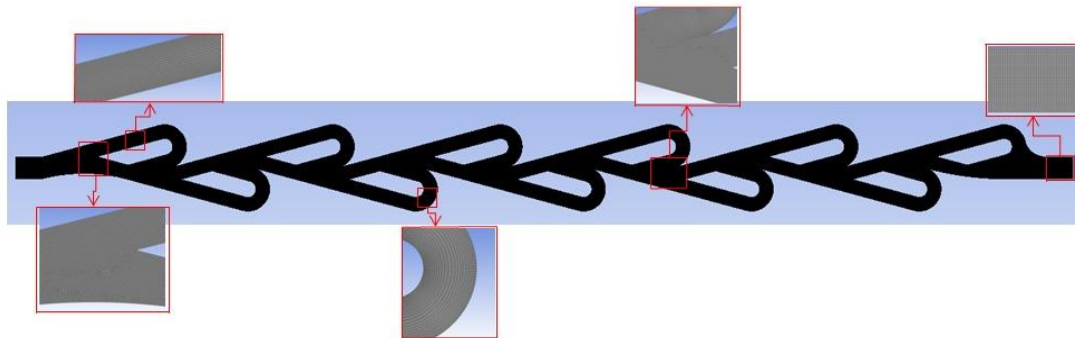


**Figure 3.** Tesla valve mesh structure.

The analyzes were performed using a 42 core parallel solver workstation. The Tesla valve mesh structure consists of regular rectangular mesh elements shown in Figure 3. The mesh model used has a total of 2249874 nodes, 2231746 cells, and 4481632 faces for simulations. The mesh structure was intensified in the boundary layer to capture the distinctive features of the flow process. Methane fuel was kept constant at 300 K for reverse and forward flows at all velocity inputs. Numerical solutions were gained for single-phase, incompressible Navier-Stokes equation sets with constant fluid properties. The analyzes for methane were carried out because the use of methane is widespread throughout the world, there is no study in this field for methane in the literature, and it is planned to examine the propagation of methane flame in the Tesla valve in the next study. For methane, whose flow behavior has been determined, the flame behavior in the Tesla valve will be examined in the next study.

$$\frac{\partial u_i}{\partial t} + \frac{\partial (u_i u_j)}{\partial x_j} = -\frac{1}{\rho}\frac{\partial P}{\partial x_i} + v\frac{\partial^2 u_i}{\partial x_i \partial x_j} \quad \frac{\partial u_j}{\partial x_j} = 0 \tag{3}$$

In the model, an iterative solution was realized with flowing pressure-based separated solvent under continuous flow conditions. The k-ε-Realizable model was used to simulate the average flow properties under turbulent flow conditions, and laminar model was used to laminar flow conditions. The k-ε realizable turbulence model becomes significant for the formulation of events occurring in the turbulent flow region. Besides, in the k-ε realizable turbulence model, the formation of turbulent kinetic energy provided depending on the average velocity values. The k-ε realizable turbulencemodel differs from the standard k−ε model in two ways. Firstly; it contains a new formulation for the turbulent viscosity. The second difference is a new transport equation for the dissipation rate. These features give improved predictions for the spreading rate of jets, a superior ability to capture the mean flow of complex structures, and forward flows involving rotation, boundary layers under strong adverse pressure gradients, separation, and recirculation. Consequently; turbulence kinetic energy change, diodicity, inlet, and outlet pressure changes for the use of methane at different velocities in the Tesla valve were determined and the flow behavior was investigated in detail.

## 3. RESULTS

The effects of gas fluid motion at different velocities in an eleven-stage Tesla valve with a low angle configuration on diodicity were investigated numerically. The fluid motion behavior of methane gas between 1m/s-10 m/s in reverse and forward directions was investigated. The effect of methane sent to the Tesla valve at different velocities on the diode is shown in Figure 4. The diodicity up to Re = 4915 and the relationship between pressure drop and flow velocity has been investigated numerically. The diodicity dimished until the Reynolds number was Re <1966. In the transition region from laminar flow to turbulent flow (1966≤ Re≤ 2457), the diodicity swells in absolute. After Re> 2457, a decrease in diodicity was observed. The maximum diodicity was determined as 0.110 at Re = 2457 and the minimum diodicity as 0.046 at Re = 1966. It has been detected that the diodicity decreases in inverse proportion to the Reynolds number in both the laminar and turbulent regions, and it reaches from minimum to maximum diodicity in the transition from laminar to turbulent region.
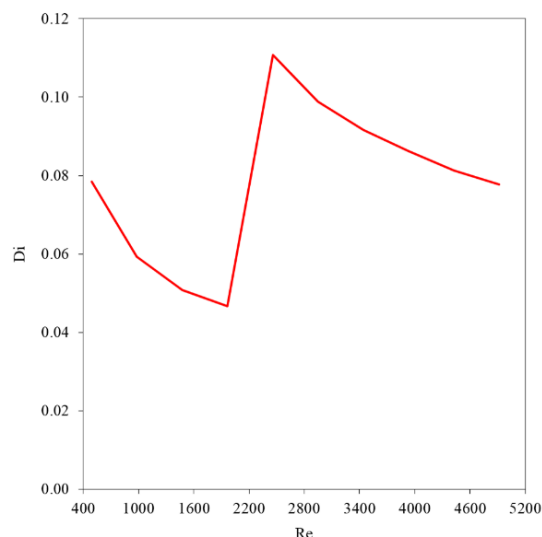


**Figure 4.** Di vs. Re trend.

The Tesla valve is a channel that changes resistance capability depending on the flow direction. The main flow line is divided into two and the flow collides when the flow comes from the reverse direction. In this case, the self-resistant flow appears inside the valve. Although there are no mechanical moving parts in the Tesla valve, the fluid behavior is restricted in the reverse flow or it is expected to slow down heavily because of its unique design. In forward flow, it is anticipated that the design will be able to flow without being exposed to any situation that may interfere with the flow.
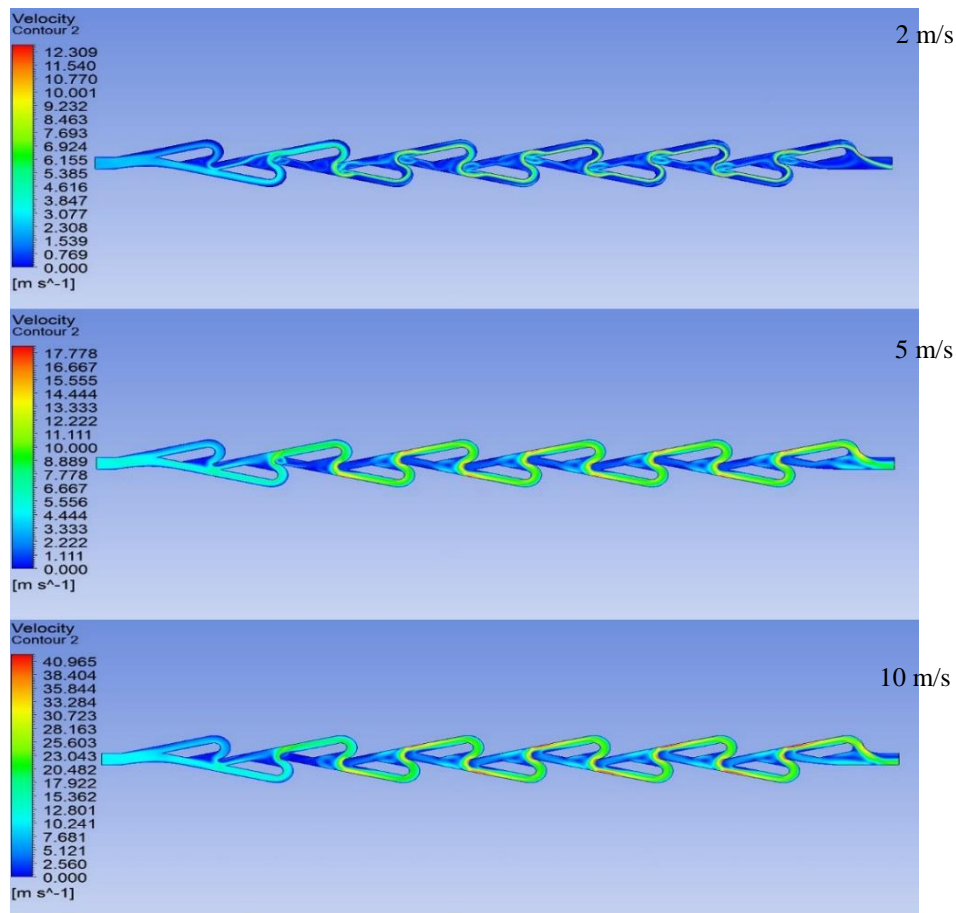


**Figure 5.** Reverse flow velocity.

The methane exhibits reverse flow from left to right as can be seen in Figure 5. In contour graphs, the display of the flow starts from the first step and progresses towards the fully developed flow up to the latest step and the red areas show where the fluid flows the fastest, while the blue areas represent the slowest flow. At the junction of discrete flow, vortices are occured, and these vortices increase the flow resistance, and it causes a gradual decrease in pressure. The eddies formed as a result of the collision are clearly visible on the contour graphs. The formed eddies direct most of the flow towards narrow wings. Therefore, a gradual decrease in pressure is provided.

In the study, it was observed that the lowest resistance was at a velocity of 1 m/s and the highest resistance occurred at a velocity of 10 m/s. In short, it is seen in reverse flow, when the resistance increases with the rise of velocity.
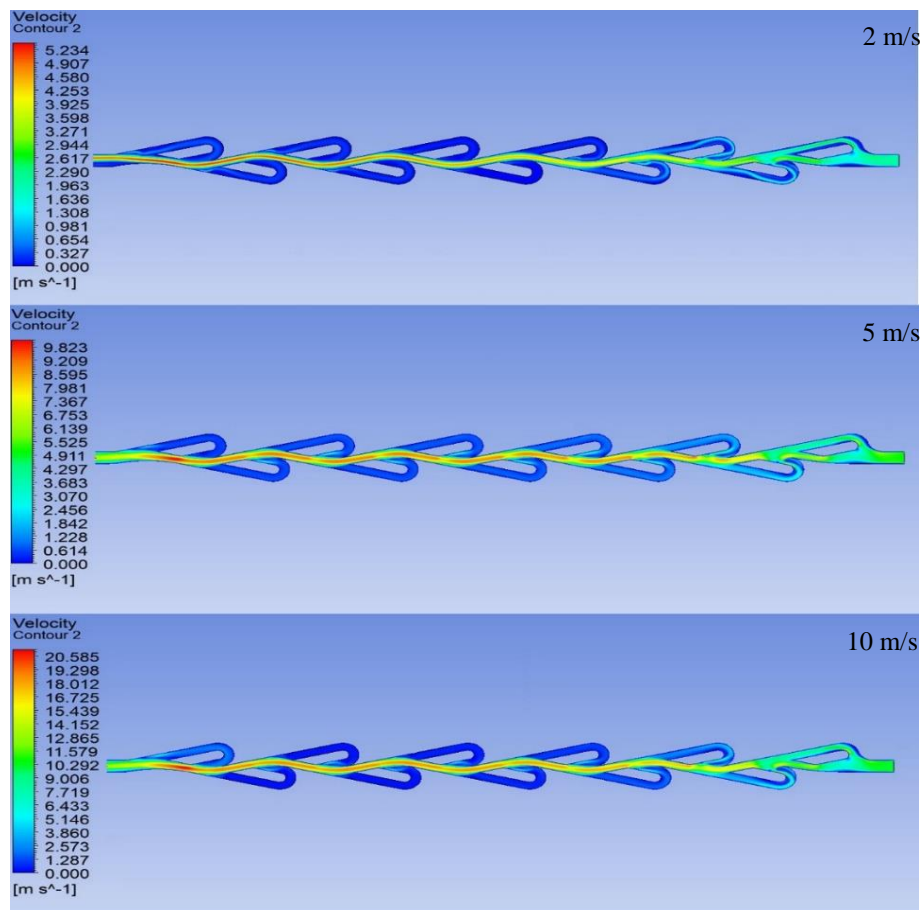


**Figure 6.** Flow velocity.

In Figure 6, the flow was sent from the opposite direction to the reverse flow. The contour graphs are also added as 2m/s, 5 m/s and 10 m/s respectively, from top to bottom. The evolution of forward flow from initial to fully developed flow is seen, and a few steps after the start of the flow, a smooth flow was created in the middle of the channel. The blue color was mostly observed in the wings, while the red color was observed in the regions where the flow moves from the middle to the forward. In this context, it is seen in the contour graph that the methane gas sent does not encounter much resistance along the channel.
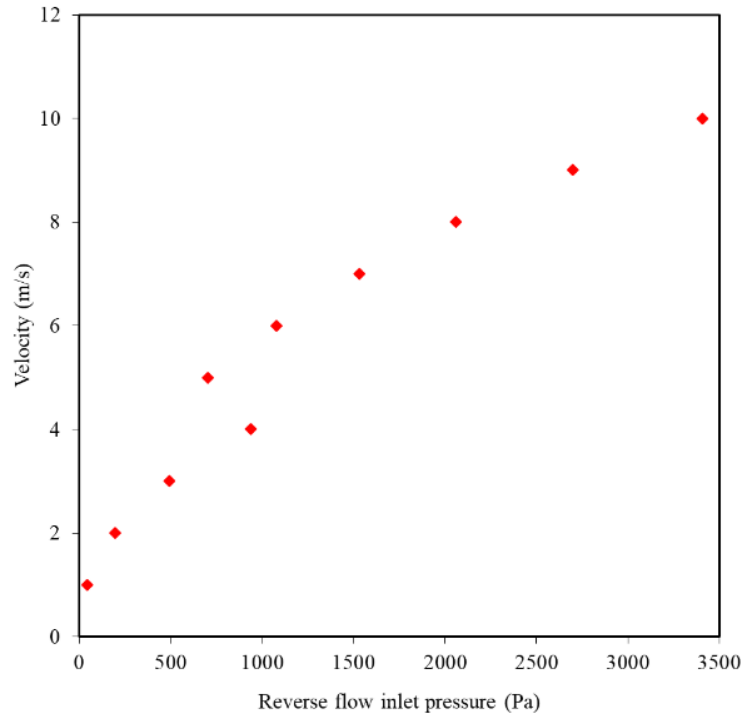
**Figure 7.** Velocity vs. Reverse flow inlet pressure.

The inlet pressure change depending on the velocity changes in reverse flow was given in Figure 7. The inlet pressure values shown in Figure 2 for reverse flow were obtained from line 1 data. The maximum inlet pressure was calculated at 3404 Pa when the inlet velocity was 10 m/s, and the minimum pressure value was calculated at 44 Pa at 1 m/s. It was observed that the pressure value increased with the increase of the velocity value in the laminar flow region. In the transition from laminar flow to turbulent flow region, it tended to instantaneous diminishes and then rises, similar to the diodicity chart. The trend of velocity-pressure variation in the turbulent flow region was similar to the change in the laminar region, showing a continuous upward trend.
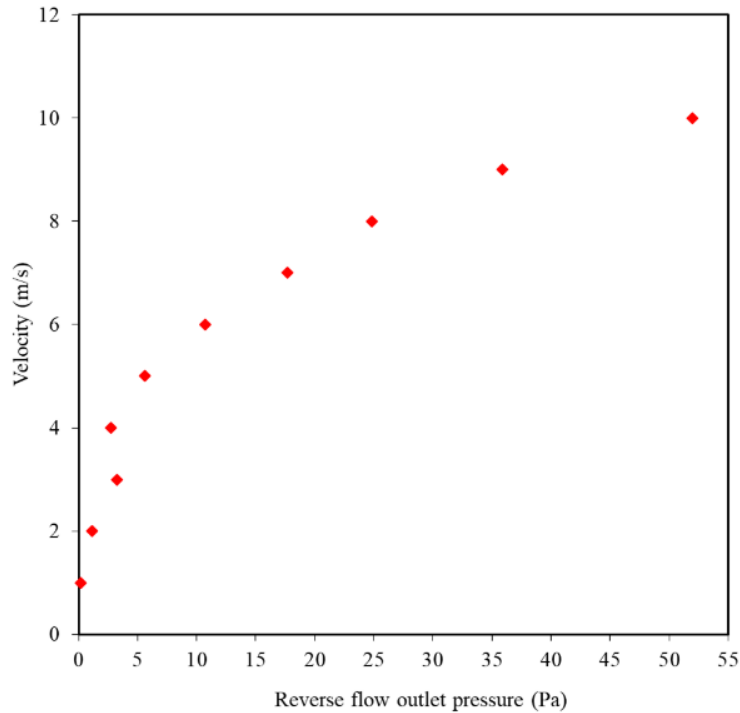
**Figure 8.** Velocity vs. Reverse flow outlet pressure.

Figure 8 shows that the output pressure change charts depending on the velocity changes in reverse flow. At the reverse flow, the outlet pressure of line 12 shown in Figure 2 was used. It is observed in Figure 8 that the maximum outlet pressure value increases depending on the velocity increase. While the maximum pressure is seen at 10 m/s velocity entry value, the lowest pressure is seen at the minimum velocity value of 1 m/s. On the other hand, the maximum pressure was about 51 Pa at an inlet velocity of 10 m/s, the minimum pressure value was calculated as 0.22 Pa in the analysis where the velocity was 1 m/s. Also, an exponential increment was observed in the laminar flow region, the exit pressure was continued to rise on the transition from the laminar region to the turbulent region.
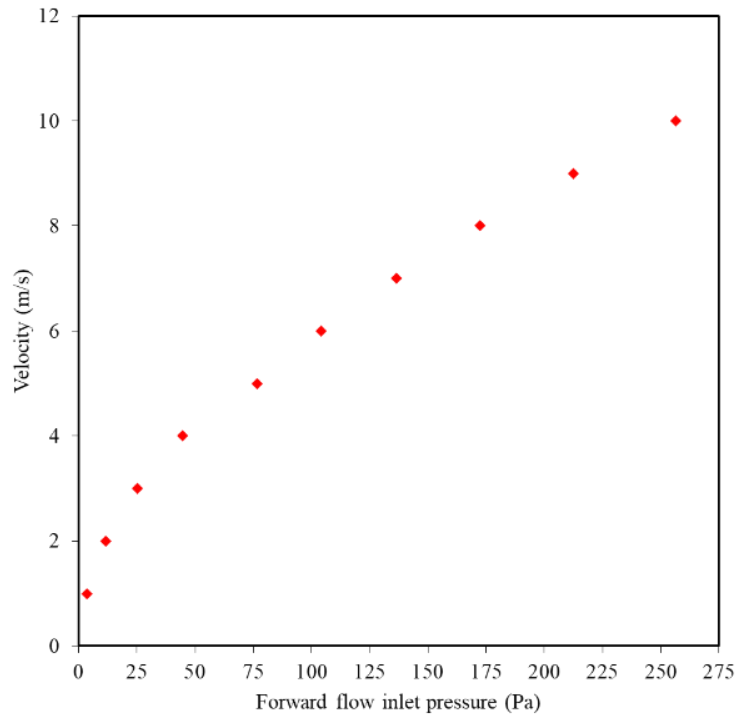
**Figure 9.** Velocity vs. Forward flow inlet pressure.

The inlet pressure change charts depending on the velocity changes for forward flow were shown in Figure 9. The inlet pressure values shown in Figure 2 for forward flow are taken from the data read on the line 12 position When Figure 9 is examined, it is observed that the maximum inlet pressure value is 256 Pa at 10 m/s velocity. It was determined that the minimum pressure was 3.46 Pa at the lowest velocity, ie 1 m/s. It was observed that the inlet pressure rised because of the increase in velocity for the forward flow.
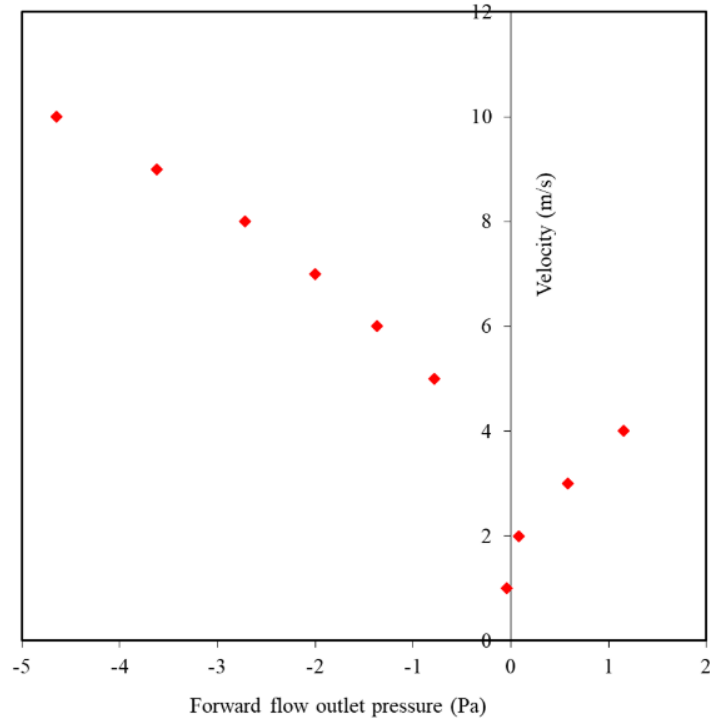
**Figure 10.** Velocity vs. Forward flow outlet pressure.

Figure 10 shows that the output pressure change charts depending on the forward flow velocity changes. Output pressure values shown in Figure 2 for forward flow are taken from line 1 data. It was observed that the outlet pressure rises during the laminar flow for the forward flow inlet pressure values. The maximum outlet pressure value was calculated as 1.15 Pa at 4 m/s. A sudden pressure drop was monitored during the transition from laminar flow to turbulent flow. Continuous decreasing pressure was detected from 5 m/s to 10 m/s in the turbulent region. There was a vacuum at the outlet pressure with the transition to turbulent flow. As the turbulent flow rate rises, the vacuum at the outlet pressure increases at the outlet pressure. It has been determined that the minimum pressure value is -4.645 Pa at 10 m/s. In this context, the laminar or turbulent flow regime in the Tesla valve affects the behavior of the flow.
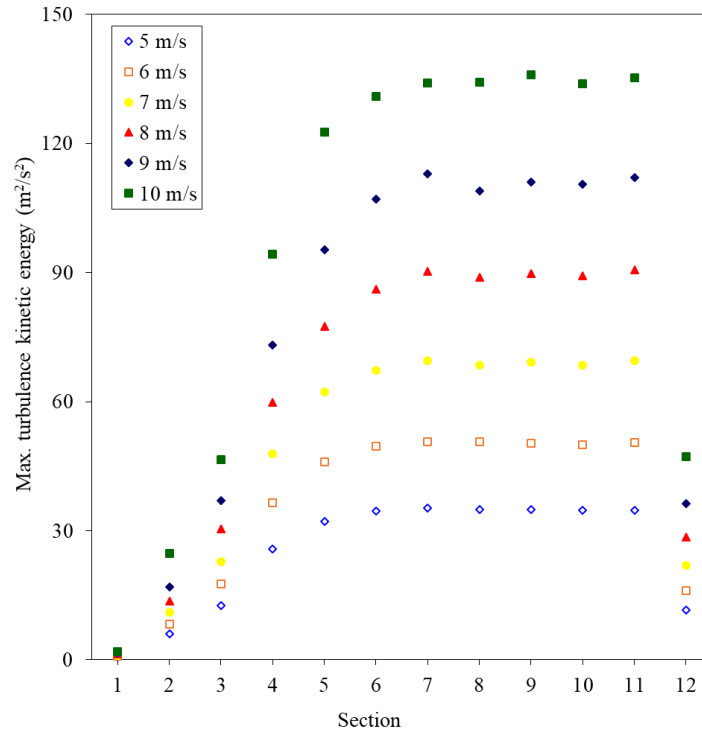
**Figure 11.** Maximum turbulence kinetic energy at reverse flow.

The maximum turbulence kinetic energy change depending on the velocity and position of the reverse flow was shown in Figure 11 and the flows displayed a linear increase in line 1, line 2, line 3, line 4 positions of the reverse flow depending on the turbulence kinetic energy. The flow development was considered to be completed after the line 5 position in reverse flow. It was detected that turbulence kinetic energy remained constant for all velocities after line 5. This trend is due to the tendency to slow down hereby collision of the flow. Turbulence kinetic energy kept constant after line 5 in reverse flow. Turbulence kinetic energies at line 6, line 7, line 8, line 9, line 10, and line 11 positions are almost the same. Turbulence kinetic energy has diminished at the line 12 point close to the exit.
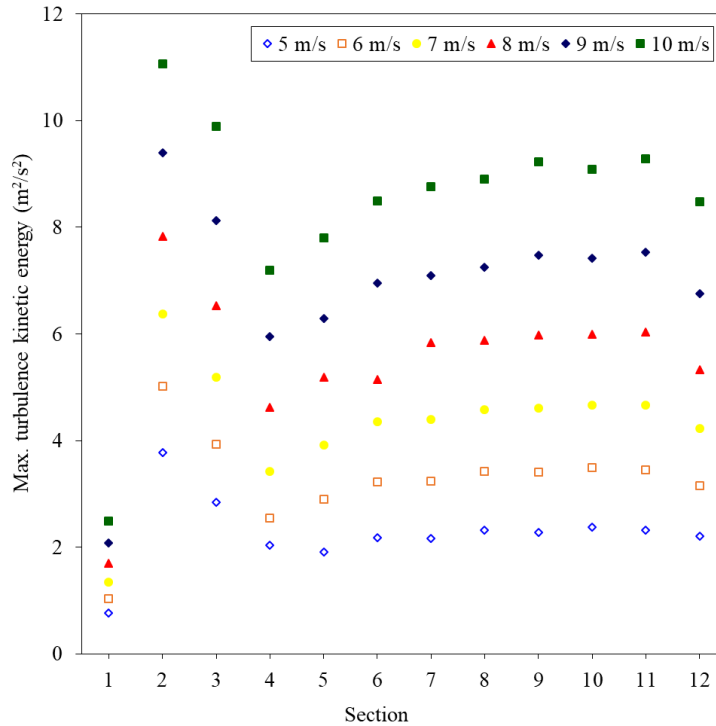
**Figure 12.** Maximum turbulence kinetic energy at forward flow.

Figure 12 shows that the maximum turbulence kinetic energy change depending on the velocity and position of the forward flow. The forward flow flows from line 12, which is the inlet port, to line 1. Since the flow from line 1 to line 2 is separated into two, turbulence kinetic energy has climbed the maximum points. Uniform flow towards line 3 was detected after line 2. Since an almost uniform flow forms after line 3, turbulence kinetic energy remained constant. The diminishes trend has been observed in the line 1 position, which is the outlet part.
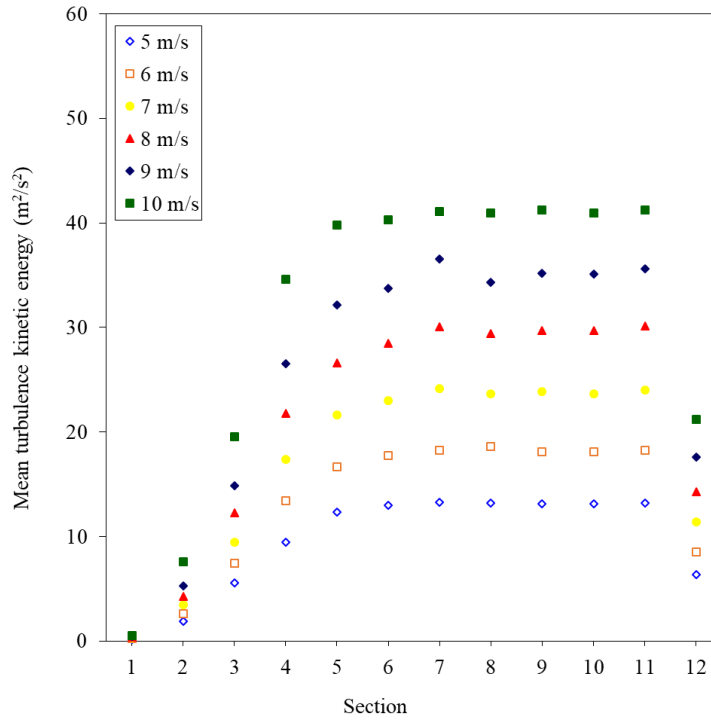
**Figure 13.** Mean turbulence kinetic energy at reverse flow.

The mean turbulence kinetic energy change depending on the velocity and position of the reverse flow was shown in Figure 13. Reverse flow average turbulence kinetic energy values are similar to Figure 11. The line 5 was observed an increase in both the maximum turbulence kinetic energy and the average kinetic energy. The flow that developed after line 5 showed almost uniform turbulence kinetic energy change in line 11. In the line 12, a decrease in turbulence kinetic energy change was observed while going towards the exit.
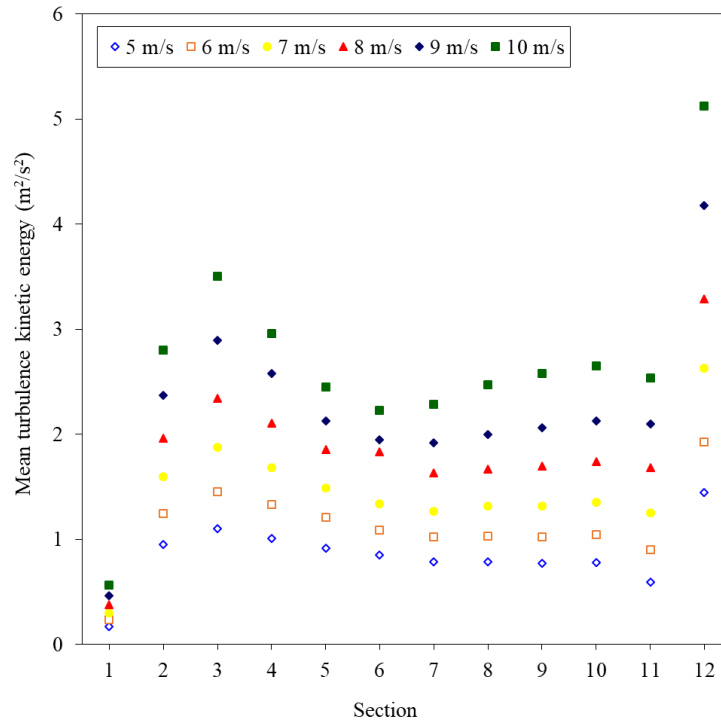
**Figure 14.** Mean turbulence kinetic energy at forward flow.

Figure 14 shows that the mean turbulence kinetic energy change depending on the velocity and position of the forward flow. Forward flow, average turbulence kinetic energy raised from line 12 to line 10. After line 10, the flow gathered in the center and continued on its way. The flows approaching a uniform structure after line 10 maintained constant turbulence kinetic energy at all velocities. The reason why the average turbulence kinetic energy climbs its maximum in line 1, which is the starting point, is thought to be due to the narrowing in the valve design. While there are sharp lines between positions in the chart of maximum turbulence kinetic energy change, it is seen a more gradual trend in the chart of average kinetic energy change.
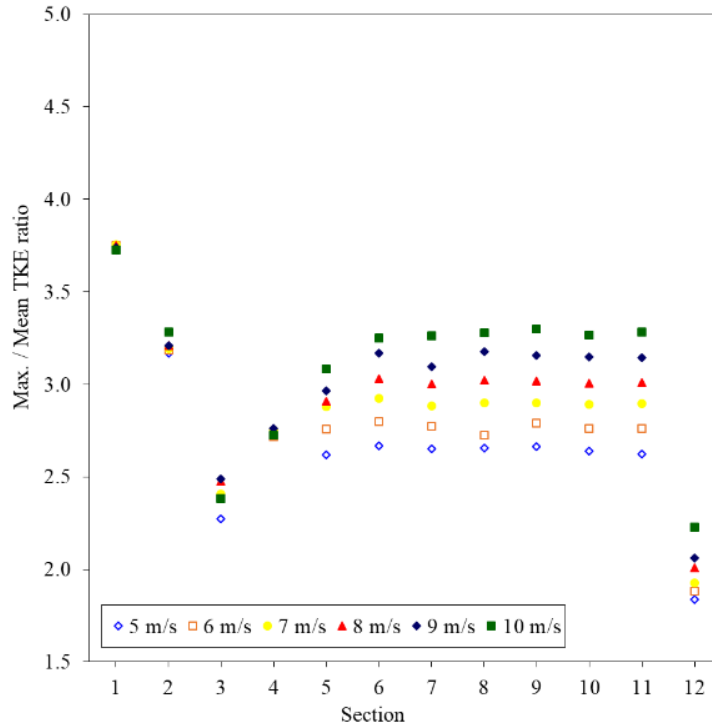
**Figure 15.** Max. / Mean TKE ratio at reverse flow.

In Figure 15, the chart is made from the division of the maximum turbulence kinetic energy of the reverse flow by the mean turbulence kinetic energy. This chart aims to see the relationship between maximum turbulence kinetic energy and mean turbulence kinetic and the flow development is seen more clearly. There is the same ratio as the flow is not fully developed until it reaches the line 4 point for all velocities. After line 5, the rates change according to the velocity distributions with the development of the flow. Each flow from line 5 to line 11 position achieves a fixed-rate at its own velocity rate.
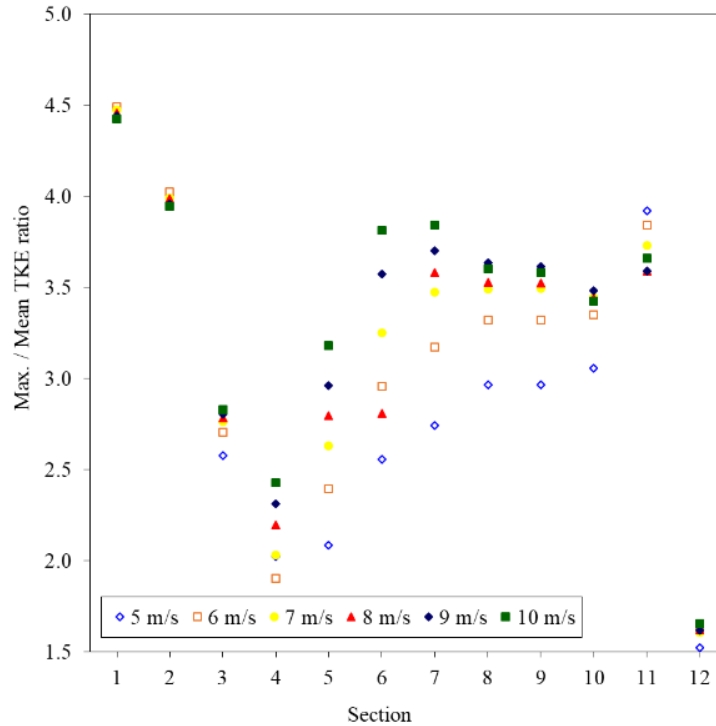
**Figure 16.** Max. / Mean TKE ratio at forward flow.

Figure 16 shows that the chart was obtained from the ratio of forward flow that maximum turbulence kinetic energy to mean turbulence kinetic energy. It has been observed that the ratios of maximum turbulence kinetic energy / mean turbulence kinetic energy at the inlet and outlet in forward flow are on coincident lines. Albeit these coincident lines are at different velocities, a fixed ratio is seen on the chart. The coincident lines at the entrance have begun to separate with the development of the flow at the entrance. The flow approaching the outlet leaves the system in coincident lines again. It has been observed that the rates at all velocities behave in the same direction as the direction changes along the flow. All positions for all velocities were parallel in directional motion.

## 4. CONCLUSION

In this study, the trends of the velocity of methane fuel in the specially designed Tesla valve have been investigated via computational fluid dynamics (CFD) methodology. Tesla valve structure with eleven flow control segments was used in the analyzes. The fluid motion behaviors in both directions were investigated for laminar and turbulent types. Two different directional analyzes were carried out as flow directions reverse and forward flow. Inlet and outlet pressures for flow from both directions were investigated separately. The diodicity up to Re = 4915 and the relationship between pressure drop and flow velocity has been investigated numerically. When the Reynolds number is Re <1966, the diodicity was decreased in the analyzes. In the transition region from laminar flow to turbulent flow (1966 ≤ Re ≤ 2457) the diodicity was risen in absolute. In the case of Re> 2457, a reduction in

diodicity was detected. The maximum diodicity was observed at 0.110 at Re = 2457 and the minimum diodicity was detected at Re = 1966 at 0.046.

It was seen that vortices occurred with the mutual collision of the flow for reverse flow. For the inlet pressure, it was observed that the pressure value soared up with the increase of the velocity in the laminar flow region. There was a partial dwell and then an increase in the transition from laminar flow to turbulent flow region. In the turbulent flow region, the velocity-pressure change has steadily swelled. While an exponential throw is detected in the laminar flow region for the outlet pressure, the pressure continued to increase in the transition from the laminar region to the turbulent region. A linear increase was seen in the maximum turbulence kinetic energy until the fully developed flow and after line 5, the flow was continued on its way, completing its development. Afterwards, it was seen that the turbulence kinetic energy remained almost the same for all velocities. A decrease in turbulence kinetic energy was observed at the line 12 point, which is close to the exit point. The average turbulence kinetic energy is similar to the maximum turbulence kinetic energy chart. In order to see the relation between maximum turbulence kinetic energy and average turbulence kinetic energy, a chart was created by dividing the maximum turbulence kinetic energy by the average turbulence kinetic energy. It remained at a constant rate after the development of flow until line 5. After that, the rates were changed according to the velocity distributions with the development of the flow.

It was seen that the flow continues over the main channel at pass the second stage in forward flow. Also, it was seen that the inlet pressure rise in direct proportion to the velocity in forward flow. The outlet pressure soared up with the increase of laminar flow, while the vacuum was observed in the turbulent flow. The vacuum trend was seen soared up even more as the velocity increased in the turbulent flow. The maximum turbulence kinetic energy has reached the maximum point since it flows in two directions in the first stage. Afterward, it turned towards a constant flow. There was a diminished in the exit positions. The average turbulence kinetic energy chart is similar to the maximum turbulence kinetic energy chart for analysis. Forward flow average turbulence kinetic energy increased from Line 12 to Line 10. After Line 10, the flow gathered in the center and continued on its way. Flows approaching a uniform state after Line 10 maintained constant turbulence kinetic energy at all velocities. The reason for the average turbulence kinetic energy to reach its maximum in line 1, which is the starting point, is thought to be because of the narrowing in the design of the valve. In the chart of maximum turbulence kinetic energy change, the lines between positions are sharp, while the average kinetic energy change chart is seen more gradually. The chart, which consists of the division of the maximum turbulence kinetic energy by the average turbulence kinetic energy, showed a development trend similar to the reverse flow chart.

## ACKNOWLEDGEMENT

## REFERENCES

[1]  Tesla, N., (1920), Valvular Conduit, U.S. Patent no. 1, 329-559.

[2]  Stemme, E. and Stemme, G., (1993), A valveless diffuser/nozzle-based fluid pump, Sensors and Actuators A: physical, 39, 159-167.

[3] Gerlach, T., (1998), Microdiffusers as dynamic passive valves for micropump applications, Sensors and Actuators A: Physical, 69, 181-191.

[4] Tsai, C.H., Lin, C.H., Fu, L.M. and Chen H.C., (2012), High-performance microfluidic rectifier based on sudden expansion channel with embedded block structure, Biomicrofluidics, 6, 24108-241089.

[5] Fadl, A., Zhang, Z., Geller, S., Tölke, J., Krafczyk, M. and Meyer, D., (2009), The effect of the microfluidic diodicity on the efficiency of valve-less rectification micropumps using Lattice Boltzmann Method, Microsystem Technologies, 15, 1379-1387.

[6] Truong, T. Q. and Nguyen, N.T., (2003), Simulation and optimization of tesla valves, Nanotech Nanotechnology Conference and Trade Show, San Francisco,178-181.

[7] Forster, F. K., Bardell, R.L., Afromowitz, M.A. and Sharma, N.R., (1995), Design, fabrication and testing of fixed-valve micro-pumps, Asme-Publications-Fed, 234,39-44.

[8] Zhang, S., Winoto, S.H. and Low, H.T., (2007), Performance simulations of Tesla microfluidic valves, International Conference on Integration and Commercialization of Micro and Nanosystems, Sanya, China, The American Society of Mechanical Engineers, New York,15-19.

[9] Gamboa, A.R., Morris, C. J. and Forster, F.K., (2005), Improvements in fixed-valve micropump performance through shape optimization of valves, 127, 339-346.

[10] Thompson, S.M., Jamal, T., Paudel, B. J. and Walters, K.D., (2013), Transitional and turbulent flow modeling in a tesla valve, ASME International Mechanical Engineering Congress and Exposition, American Society of Mechanical Engineers 56321.

[11] Mohammadzadeh, K., Kolahdouz, E. M., Shirani, E. and Shafii, M. B., (2013), Numerical Investigation on the effect of the size and number of stages on the Tesla microvalve efficiency, Journal of Mechanics, 29, 527-534.

[12] Porwal, P.R., Thompson, S. M. and Walterss, K.D. & Jamal, T., (2018), Heat transfer and fluid flow characteristics in multistaged Tesla valves, Numerical Heat Transfer, Part A: Applications, 73, 347-365.

[13] Thompson, S. M., Ma, H. and Wilson, C., (2011),  Investigation of a flat-plate oscillating heat pipe with Tesla-type check valves, Experimental Thermal and Fluid Science, 35,1265-1273.

[14] Bardell, R. L., (2000), The diodicity mechanism of tesla-type no-moving-parts valves, Ph.D. dissertation, University of Washington, Seattle, WA.

[15] Qian, J.Y., Chen, M.R. and Liu, X.L.& Jin, Z. J., (2019), A numerical investigation of the flow of nanofluids through a micro Tesla valve, Journal of Zhejiang University-SCIENCE A, 20, 50-60.

[16] Jin, Z.J., Gao, Z.X., Chen, M.R. and Qian, J.Y., (2018), Parametric study on Tesla valve with reverse flow for hydrogen decompression, International Journal of Hydrogen Energy, 43, 8888-8896.

[17] Wang, C.T., Chen, Y.M., Hong, P.A. and Wang, Y.T., (2014), Tesla valves in micromixers, International Journal of Chemical Reactor Engineering 1.open-issue.

*RESEARCH ARTICLE*

# INVESTIGATION of MECHANICAL PROPERTIES of CARBON FIBRE REINFORCED POLYESTER MATRIX COMPOSITE

Deniz GÜNEŞ[1], Murat ÇANLI [2], Levent URTEKİN[3*]

[1]Bandırma Onyedi Eylül University, Maritime Vocational School, Bandırma, Balıkesir, dgunes@bandirma.edu.tr, ORCID: 0000-0003-0056-3789
[2]Kırşehir Ahi Evran University, Mucur Vocational School, Chemistry and Chemical Processing Technologies, Kırşehir, murat.canli@ahievran.edu.tr. ORCID:0000-0002-5275-861X
[3]Kırşehir Ahi Evran University, Mechanical Engineering Department, Kırşehir, levent.urtekin@ahievran.edu.tr , ORCID: 0000-0003-4348-4749

## ABSTRACT

This study aimed to administer hand lay-up method for designing composite materials in which unidirectional and biaxial carbon fiber reinforcements are placed in a polyester matrix to generate one, two and three layers at room temperature. The samples were laid up from composite plates with the help of a mold in accordance with the fiber direction angle in accordance with the standards. In order to determine the mechanical properties of the samples, tensile, bending and drop weight low velocity impact tests were performed. The tensile test results in composite materials with the same layer number, pointed out that $0^0$ unidirectional fiber reinforced composite materials performed the highest tensile strength values. On the other hand, the biaxial carbon fiber reinforced composite materials had the highest elasticity values of $\pm 45^0$. The highest elasticity values have been found in the unidirectional carbon fiber reinforcements of composite materials with $0^0$ fiber direction angle in terms of bending test results. The biaxial composite materials with a $\pm 45^0$ fiber direction angle showed the highest values of impact tensile strength in drop weight low velocity impact tests. $0^0$ unidirectional fiber reinforced composite materials, which showed the highest elasticity values in tensile and bending tests, were found to be the composite materials with the highest deformation values in the falling weight low velocity impact tests. It appears that increasing the number of layers caused an increase in the impact strength. They can be an alternative to aluminum and glass fiber reinforced polyester matrix composite materials due to their lightness and strength at the same thickness, which is valuable in boats, caravans and design cars.

**Keywords:** *Carbon fiber, Composite, Mechanical properties, Polyester resin*

## 1. INTRODUCTION

Composite materials are used to reduce the energy consumption caused by weight, especially in vehicles. The use of composite materials increased this gain between 60-80% instead of iron and its alloys, while it was possible between 20-50% instead of aluminum and its alloys.[1] In addition, the polymer composite materials give strength, flexibility, lightness to any material.[2-5] In such, aramid reinforced polymer composites are used in the production of sports equipment, ropes, tires, vehicle

brake systems, gaskets, armor and missile sheaths with high strength, temperature, and friction resistance.[3] Another polymer is epoxy resin which can form a good bond with many types of fibers and thus composite products can be produced with the desired properties. As a result of the reactions with amines at high temperatures during ripening, it can form very good cross-links and a product with high chemical resistance, strength and hardness can be obtained. Its shrinkage values are very low during freezing and hardening. Epoxies have a more fragile structure.6-9 During the reaction, the epoxy rings, also called ring cleavage, are opened, taking a hydrogen from the amine group or hydroxyl group and reacting with the oxygen atoms of the epoxide group to form a crosslink.[6,10-11]

The most used reinforcing elements in fiber reinforced polymer composites are glass fiber, carbon fiber and Kevlar type fibers.[12-15] Glass fibers are the oldest fiber type preferred to be used in many composite studies. Carbon, boron, silicon carbide and aramid fibers are types of fibers that have been gradually used increasingly later to obtain the desired properties.[16, 17] In addition, polyethylene fibers, which have a chemically stable structure, easily shaped, and produced in film and layer. On the other hand, chemical resistance might decrease, and it softens at high temperatures.[18, 19]

Carbon fibers are bundles consisting of 6-15 μm diameters and 500-2000 filaments obtained at the application stage.[20, 21] These bundles can be used on their own or as a fabric by weaving.[22] Beside the carbon fibers to adhere well with the resin, their surfaces are also treated. This process is to obtain a threadlike structure by opening a pit on its surface by gas and liquid oxidation process or by forming silicon nitride crystals on its surface.[23-26] Carbon fibers are also marketed as continuous fibers and chopped fibers. Chopped fibers are used in pressure vessels, injection molding, machine manufacturing and chemical environments. [17, 27] Polyester-carbon composite materials are still being in the center of research focus. [28-30]

This study is part of master thesis and designed as part I. [31] In this study, composite materials have been designed using Uni-Directional Carbon Fiber and Double Axis Carbon Fiber as reinforcement materials having different number of layers and fiber orientation angles into the polyester matrix. The mechanical properties of composite materials were compared by performing tensile, three-point bending and falling weight low speed impact tests of the composite materials. The mechanical, structural, and thermal properties of carbon fiber reinforced composite materials produced in the studies were examined.

## 2. EXPERIMENTAL METHOD

The composite material was produced at room temperature using hand lay-up method at Bandırma Vocational School-Shipbuilding Program Workshop in Bandırma Onyedi Eylül University. In the experimental part, two different knitted carbon fiber fabrics were combined with polyester matrix, and then, the mechanical properties of composites consisting of one, two and three layers were compared. [32, 33]
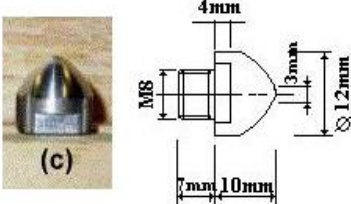
In the samples, carbon fiber fabric with two different weaves, polyester as matrix material, freezer, and accelerator and solid (Polivaks SV-6) and liquid separators (Polivaks PVA) were used as additives. The carbon fiber fabrics were supplied from Telateks as unidirectional woven CW400 B-Carbon 12K Plain Weave Fabric and biaxial woven CX300 E05A-45/45 Biaxial carbon fabric. The matrix material was directly provided from the company of "Yücel Kompozit A.Ş". CAMELYAF brand CE 92 N8 general purpose polyester resin is used as matrix material. It is one of the most

preferred polyester types in hand lay-up methods. Methyl ethyl ketone peroxide (MEK-P) and cobalt were used for fast freezing of the matrix material.

Tensile and three-point compression tests were carried out in the test training laboratory of Zwick Avrasya firm. The falling weight-low speed impact test was carried out in Dumlupınar University Mechanical Engineering Department Laboratory. For the tensile test, Zwick / Roell brand Allround Line Z250 SrR test device was used with the samples produced according to ISO 527-1 standard. Four samples were tested for each sample batch. For the three-point compression test, Zwick / Roell branded ProLine table-top testing machines Z005 up to Z100 test device was used with samples produced according to ISO 178 standard.

The low-speed impact test of the falling weight was achieved in Kütahya Dumlupınar University Engineering Faculty Mechanical Engineering Department Laboratory. The samples of 10x10 cm were prepared for the test and five samples were tested for each group. The speed of the falling weight and the energy at the time of impact were calculated after necessary assumptioms made, and the numbers were presented in Table 1.

**Table 1.** Falling weight low speed impact test data entry values.

| Property | Unit | Value |
|---|---|---|
| Fallen weight | Kg | 3.10 |
| Falling Distance | m | 1.00 |
| Gravitational Acceleration (g) | m/s2 | 9.81 |
| Velocity | m/s | 4.43 |
| Impact Energy | J | 30.41 |
| Friction force | N | 0 |
| Tip Used | |  |

### 3.1. RESULTS AND DISCUSSION

The composite samples were prepared and named differently. The abbreviations of BCF for biaxial carbon fibers, angle 0- ± 45 values of the samples according to the fiber-fiber direction, B for tensile test, E for flexure test, K for drop test and 1,2,3 for layer numbers are given according to the test type.

### 3.1. Tensile Test
The grouped test samples were tested according to the number of layers from low to high (Table 2). The tensile test results of the Biaxial Carbon $0^0$ single layer composite (BCF 0 B 1) group with an angle of fiber orientation showed that the values are close to each other except for the last sample. There is a difference of 44.06% between the highest and the lowest values in tensile test and a 17.63% difference in the breaking strength value. The tensile test results of the Biaxial Carbon $0^0$ fiber orientation angle two-layer composite (BCF 0 B 2) group show a 13.16% difference between the highest and the lowest values in elasticity and a 5.95% difference in the breaking strength value.

These results showed that two-layer samples had closer properties than single-layer samples. As a result of the breakings, the carbon fibers are separated from the sample in some cases. It was found that there was less dispersion in single-layer samples, and two-layer samples were more durable. On the other hand, the tensile test results of the Biaxial Carbon $0^0$ three-layer composite (BCF 0 B 3) group with an angle of fiber orientation showed close values to each other. It is seen that there is a 19.24% difference between the highest and lowest values of tensile test results, and a 22.93% difference in the breaking strength value.

The tensile test results of the Biaxial Carbon ± 450 fiber orientation angle single layer composite (BCF 45 B 1) group pointed out that there is a difference of 30.04% between the highest and the lowest values in the elasticity value and an 11.68% difference in the tensile strength values. The reason for the low values was the capillary fractures on the surfaces. Those fractures might be caused by the hand lay-up method or during sample preparation. The tensile test values of the two-layer (BCF 45 B 2) group are quite similar. It is seen that there is a difference of 12.40% between the highest and lowest values and a difference of 34.27% in the breaking strength value. Comparison of them with single-layer samples points out that the values are closer to each other which makes them more durable but more flexible. There is a 26.68% difference between the highest and the lowest values and a 12.83% difference in the breaking strength value of the three-layer composite (BCF 45 B 3) group.

**Table 2.** Comparison of average tensile test results of the samples.

| Sample | Elasticity ($E_t$) MPa | Tensile Strength ($\sigma_m$) MPa | Percent of Elongation at Break ($\varepsilon_m$) % |
|---|---|---|---|
| BCF 0 B 1 | 27000 | 417 | 1.6 |
| BCF 45 B 1 | 2690 | 24.3 | 1.8 |
| BCF 0 B 2 | 43300 | 601 | 1.5 |
| BCF 45 B 2 | 4680 | 42.8 | 3.9 |
| BCF 0 B 3 | 36900 | 468 | 1.6 |
| BCF 45 B 3 | 4080 | 56.4 | 6.5 |

**3.2. Three Point Bend Test**
The sample values were different from each other in the three point bending test results of the composite (BCF 0 E 1) group consisting of Double Axis Carbon 00 fiber orientation angle and single layer. These changes might occur because the matrix material does not cover the carbon fiber reinforcement at the same rate everywhere during the sample preparations. There is a 52.72% difference between the highest and the lowest values and a 25.37% difference in the bending strength value.

The composite (BCF 0 E 2) group consisting of double axis carbon $0^0$ fiber orientation angle and two layers have close values to each other except for the first sample. The two-layer sample values have reached better values as the number of layers increased. Besides, there is a difference of 57.67% between the highest and lowest values and a 58.88% difference in the bending strength value.

Considering the three-point bending test results of the Double Axis Carbon $0^0$ fiber orientation angle composite (BCF 0 E 3) group consisting of three layers, the sample values were found closer to each

other than the other layer numbers. There is a 21.84% difference between the highest and the lowest values in the elasticity value and a 21.30% difference in the bending strength value.

In the Biaxial Carbon ± 45$^0$ single layer composite (BCF 45 E 1) group with an angle of orientation, the first sample has higher values than the other samples, and the other sample values are close to each other. The reason is that the matrix material was more than the other samples. There is a 49.45% difference between the highest and the lowest values in the elasticity value and a 27.51% difference in the bending strength value.

The two-layer composite (BCF 45 E 2) group with double axis carbon ± 45$^0$ fiber orientation angle test values are close. It was observed that the samples were stronger than a single layer. There is a 23.11% difference between the highest and the lowest values in the elasticity value and a 30.68% difference in the bending strength value. While the elasticity values of the ratios between the samples decreased, the bending strength ratio increased.

Examining the bending test results of the Biaxial Carbon ± 45$^0$ fiber orientation three-layer composite (BCF 45 E 3) group showed close sample values to each other, but they were lower than the two-layer samples. There is a 21.02% difference between the highest and the lowest values in the elasticity value and an 11.76% difference in the bending strength value.

The average elasticity (Ef), bending strength ($\sigma$fM) and bending elongation percentage values ($\epsilon$fM) of the samples were compared according to the layer numbers. The average values of the three-point bending test data belonging to the sample groups consisting of a single layer are presented in Table 3.

**Table 3.** Average three-point bending test results of the single layer samples**.**

| Sample | Elasticity ($E_f$) MPa | Bending strength ($\sigma_{fM}$) MPa | Bending elongation percentage value ($\epsilon_{fM}$) % |
|---|---|---|---|
| BCF 0 E 1 | 4480 | 174 | 4.0 |
| BCF 45 E 1 | 1940 | 66 | 4.2 |
| BCF 0 E 2 | 14000 | 218 | 1.3 |
| BCF 45 E 2 | 4650 | 104 | 3.4 |
| BCF 0 E 3 | 23400 | 293 | 1.4 |
| BCF 45 E 3 | 4250 | 94.1 | 6.1 |

The biaxial carbon ± 450 fiber orientation angle single layer (BCF 45 E 1) composite group, which has the lowest elasticity and bending strength value, was the most ductile material. BCF 0 E 1 group have a higher elasticity value of 230.92%. Similarly, in terms of bending strength, BCF 0 E 1 group has higher values by 263.64% compared to BCF 45 E 1 group. Looking at the breaking elongation percentage values, the BCF 0 E 1 group was brittle at a rate of 95.24% compared to the BCF 45 E 1 group.

The best bending strength values of a single layer belonged to the two-layer composite group (BCF 0 E 2) with biaxial 0$^0$ fiber orientation angle. The most ductile material was a two-layer (BCF 45 E 2) composite group with a biaxial carbon ± 45$^0$ fiber orientation angle as in a single layer. When the values of BCF 45 E 2 group are accepted as 100%; BCF 0 E 2 group is seen to have 301.08% higher elasticity value. Similarly, it was seen that the bending strength of the BCF 0 E 2 group was 209.62%

higher than the BCF 45 E 2 group. The breaking elongation percentage values point out that the BCF 0 E 2 group was 38.24% brittle compared to the BCF 45 E 2 group.

In terms of bending strength values, the best average result belonged to the biaxial $0^0$ fiber orientation angle three-layer (BCF 0 E 3) composite group, as in the two-layer samples. The most ductile material was the three-layer composite group (BCF 45 E 3) with a biaxial carbon ± 450 fiber orientation angle compared to the other groups. BCF 0 E 3 group has 550.59% higher elasticity value. Similarly, in terms of bending strength, BCF 0 E 3 group has 311.37% higher values than BCF 45 E 3 group. The breaking elongation percentage values show that the BCF 0 E 3 group was brittle at a rate of 22.95% compared to the BCF 45 E 3 group.

The most ductile material belonged to the single layer three (BCF 0 E 1-3) composite sample with biaxial carbon ± $45^0$ fiber orientation angle as in the average value. The BCF 0 E 1-3 sample has a higher elasticity value of 230.99%. Likewise, in terms of flexural strength, BCF 0 E 1-3 sample has higher values by 254.03% compared to BCF 45 E 1-1 sample. The elongation at break percentage values presents that the BCF 0 E 1-3 sample was 103,125% brittle compared to the BCF 45 E 1-1 sample. It was determined that the highest values and average values showed similar properties.

The best bending strength values belonged to the two-layer composite sample (BCF 0 E 2-2) with biaxial carbon 00 fiber orientation angle. In the samples with the highest value of BCF 0 E 2 group, the most brittle material belonged to the two-layer composite sample (BCF 0 E 2-2) with biaxial carbon 00 fiber orientation angle. As with the average values, the most ductile material belongs to a two-layer (BCF 0 E 2-1) composite sample with biaxial carbon ± 450 fiber orientation angle. The BCF 0 E 2-2 sample has a higher elasticity value of 317.30%. Likewise, in the bending strength, the BCF 0 E 2-2 sample has 262.07% higher values than the BCF 45 E 2-1 sample. The breaking elongation percentage values show that the BCF 0 E 2-2 sample was 38.24% brittle compared to the BCF 45 E 2-1 sample. The comparison of the mean with maximum values of the samples showed a slight difference from each other.

The three-point bending test with the highest value of the samples consisting of three layers showed similar properties with the other layers. The best bending strength values were found to be the biaxial carbon $0^0$ fiber orientation angle three-layer composite sample with four (BCF 0 E 3-4). The most ductile material was found to belong to the three-layer composite sample. The BCF 0 E 3-4 sample has a higher elasticity value of 512.77%. Similarly, in the bending strength, the BCF 0 E 3-4 sample has 317.65% higher values than the BCF 45 E 3-4 sample. The breaking elongation percentage values point out that the BCF 0 E 3-4 sample was brittle at a rate of 22.81% compared to the BCF 45 E 3-4 sample.

### 3.3. Dropped Weight Impact Test at Low Speed
Considering the biaxial Carbon $0^0$ composite group samples with an angle of orientation, all samples are pierced because of the breakage of the fibers at the contact point due to the energy generated by the weight. All the samples showed same results that there is a deformation at the point where the weight falls on the sample surface and its close vicinity, but the deformation on the back of the sample is greater.

The two-layer (BCF 0 D 2) composite group samples with Biaxial Carbon $0^0$ fiber orientation angle were drilled because of the breaking of all the fibers at the contact point of the samples with the

energy generated due to the weight used. In the three-layer (BCF 0 D 3) composite group samples with Biaxial Carbon 00 fiber orientation angle, some of the samples were pierced because of the breaking of the fibers at the contact point due to the energy.

**Table 4.** The falling weight low speed impact test results of the two-layer composite group with biaxial carbon $0^0$ fiber orientation angle (Fall height is 1.00 meter, and Velocity is accepted as 4.43 (m/s), and Impact energy 30.41 J)

| Sample No | Average Thickness (mm) | Dimension (mm-mm) | Hole diameter (mm) | Hole depth (mm) | Rear surface deformation height (mm) |
|---|---|---|---|---|---|
| BCF 0 D 1-1 | 1.43 | 99.26x99.43 | 16.98 | 3.19 | 4.14 |
| BCF 0 D 1-2 | 1.37 | 99.60x99.52 | 17.04 | 5.55 | 5.79 |
| BCF 0 D 1-3 | 1.46 | 99.52x99.35 | 16.23 | 3.75 | 3.98 |
| BCF 0 D 1-4 | 1.36 | 99.82x99.74 | 16.32 | 4.63 | 4.87 |
| BCF 0 D 1-5 | 1.49 | 99.74x99.63 | 16.26 | 4.89 | 5.38 |
| BCF 0 D 2-2 | 1.92 | 99.26x99.12 | 16.38 | 5.33 | 6.95 |
| BCF 0 D 2-3 | 1.89 | 99.50x99.92 | 16.07 | 5.78 | 7.49 |
| BCF 0 D 2-4 | 1.95 | 99.67x99.29 | 15.94 | 5.17 | 6.64 |
| BCF 0 D 2-5 | 1.93 | 99.67x99.52 | 15.64 | 5.23 | 6.18 |
| BCF 0 D 3-1 | 2.83 | 99.12x99.16 | 11.3 | 4.36 | 4.67 |
| BCF 0 D 3-2 | 2.89 | 99.18x99.09 | 11.02 | 4.19 | 5.03 |
| BCF 0 D 3-3 | 2.92 | 99.20x99.16 | 10.96 | 3.67 | 5.12 |
| BCF 0 D 3-4 | 2.78 | 99.50x99.38 | 10.67 | 4.27 | 4.44 |
| BCF 0 D 3-5 | 2.82 | 99.40x99.06 | 10.76 | 4.48 | 5.08 |

In the composite group samples with Biaxial Carbon ± $45^0$ fiber orientation angle, all samples are pierced by the breakage of the fibers at the contact point due to the energy generated by the weight. At the two-layer (BCF 45 D 2) composite group samples with Biaxial Carbon ± 450 fiber orientation angle, we see that all samples are pierced by the breakage of the fibers at the contact point due to the energy generated by the weight. Some of the three-layered (BCF 45 D 3) composite group samples

with biaxial carbon $\pm 45^0$ fiber orientation angle were pierced because of the breakage of the fibers at the contact point.

**Table 5.** The falling weight low speed impact test results of the composite groups with biaxial carbon $\pm 45^0$ fiber orientation angle. (Falling height is 1.00 meter, and Velocity is accepted as 4.43 (m/s), and Impact energy is 30.41 J).

| Sample No | Average Thickness (mm) | Dimension (mm-mm) | Hole diameter (mm) | Hole depth (mm) | Rear surface deformation height (mm) |
|---|---|---|---|---|---|
| BCF 45 D 1-1 | 1.02 | 99.67x99.68 | 16.04 | 3.06 | 3.8 |
| BCF 45 D 1-2 | 0.93 | 99.62x99.58 | 16.43 | 4.42 | 3.56 |
| BCF 45 D 1-3 | 0.92 | 99.72x99.47 | 16.15 | 3.02 | 3.49 |
| BCF 45 D 1-4 | 0.98 | 99.40x99.27 | 16.86 | 2.84 | 4.25 |
| BCF 45 D 1-5 | 0.99 | 99.58x99.79 | - | 3.07 | 3.58 |
| BCF 45 D 2-1 | 1.51 | 99.25x99.30 | 15.05 | 6.9 | 5.23 |
| BCF 45 D 2-2 | 1.54 | 99.23x99.30 | 14.95 | 6.89 | 4.94 |
| BCF 45 D 2-3 | 1.56 | 99.21x99.46 | 15.48 | 6.64 | 3.2 |
| BCF 45 D 2-4 | 1.52 | 99.13x99.43 | 16.3 | 6.22 | 3.18 |
| BCF 45 D 2-5 | 1.5 | 99.30x99.44 | 16.45 | 6.74 | 4.35 |
| BCF 45 D 3-1 | 2.47 | 99.54x99.63 | 10.23 | 5.01 | 3.46 |
| BCF 45 D 3-2 | 2.51 | 98.64x98.59 | 9.85 | 5.23 | 4.09 |
| BCF 45 D 3-3 | 2.58 | 98.74x98.92 | 9.82 | 4.83 | 3.81 |
| BCF 45 D 3-4 | 2.56 | 99.85x99.43 | 10.77 | 5.51 | 4.57 |
| BCF 45 D 3-5 | 2.53 | 99.50x99.45 | 10.84 | 5.7 | 4.52 |

Examination of the falling weight low speed impact test results showed that all sample groups undergo deformation (Table 4 and 5). The best resistant group to impact energy of 30.41 J is the composite materials with biaxial $\pm 450$ fiber orientation angle (BCF 45 D), followed by the composite material group with Biaxial $\pm 450$ fiber orientation angle (BCF 0 D). Besides, the samples of BCF 45 D 3 group had the best tensile strength. The deformation on the surface of the samples in the BCF 45 D and BCF 0 D groups occurred in the direction of the fiber orientation angles or circularly. It was

also found that the deformation on the sample lower surface was caused by the fiber orientation and separation of the fibers.

## 4. CONCLUSIONS

The mechanical test results have shown that the reinforcement element, the number of layers, the fiber orientation direction, angle, matrix material and the selected production method during production have great importance according to the place and purpose of use of composite materials. In the production of carbon fiber composites, the high cost of carbon fiber materials has led to the selection of matrices with higher mechanical values and the use of more technological methods.

In further studies, the composite production method can be changed and compared with the hand lay-up method. The falling weight can be compared with the work made in the low-velocity impact test that has been selected for the deformation that can occur by changing the weight and drop height. It is thought to be an alternative to composite materials with aluminum and glass fiber reinforced polyester matrix due to its lightness and strength at the same thickness values in boats, caravans, and design cars. Moreover, by using these unidirectional carbon fibers and different fiber orientation angles, lower-cost products can be obtained.

## ACKNOWLEDGEMENT

## REFERENCES

[1] Wonderly, C., Grenestedt, J., Fernlund, G. and Cepus, E. (2005). Comparison of mechanical properties of glass fiber/vinyl ester and carbon fiber/vinyl ester composites, *Composites: Part B*, 36(5), 417-426

[2] Cohades, A., Branfoot, C., Rae, S., Bond, I. and Michaud, V. (2018). Progress in self- healing fiber- reinforced polymer composites. *Advanced Materials Interfaces*, 5(17), 1800177

[3] Meng, M., Chua, Y.J., Wouterson, E. and Ong, C.P.K. (2017). Ultrasonic signal classification and imaging system for composite materials via deep convolutional neural networks. *Neurocomputing*, 257, 128-135

[4] Sanjay, M.R., Madhu, P., Jawaid, M., Senthamaraikannan, P., Senthil, S. and Pradeep, S. (2018). Characterization and properties of natural fiber polymer composites: A comprehensive review. *Journal of Cleaner Production*, 172, 566-581

[5] Sprenger, S. (2015). Improving mechanical properties of fiber-reinforced composites based on epoxy resins containing industrial surface-modified silica nanoparticles: review and outlook. *Journal of composite materials*, 49(1), 53-63

[6] Bush, M.A., Bush, P.J. and Miller, R.G. (2006). Detection and classification of composite resins in incinerated teeth for forensic purposes. *Journal of forensic sciences*, 51(3), 636-642

[7] Nissila, T., Hietala, M. and Oksman, K. (2019). A method for preparing epoxy-cellulose nanofiber composites with an oriented structure. *Composites Part A: Applied Science and Manufacturing*, 125, 105515

[8] Reis, A.K.D., Monticelli, F.M., Neves, R.M., de Paula Santos, L.F., Botelho, E.C. and Luis Ornaghi Jr H. (2020). Creep behavior of polyetherimide semipreg and epoxy prepreg composites: Structure vs. property relationship. *Journal of Composite Materials,* 54(27), 4121-4131

[9] Şahin, Y. (2006). Introduction to composite materials (In Turkish), Seçkin Publishing, Ankara

[10] Elarabi S.M. and Weidong, Y. (2005). The effect of transversely aligned fibers on the axial tensile strength of carbon epoxy composites. *Journal of industrial textiles*, 35, 39-45

[11] Murugan, R., Ramesh, R. and Padmanabhan, K. (2014). Investigation on static and dynamic mechanical properties of epoxy based woven fabric glass/carbon hybrid composite laminates. *Procedia Engineering*, 97, 459-468

[12] Botelho E.C. and Rezende, M.C. (2006). Monitoring of carbon fiber/polyamide composites processing by rheological and thermal analyses. *Polymer-Plastics Technology and Engineering*, 45, 61-69

[13] Yağmur, S., Kurt, A. and Şeker, U. (2018). Karbon Fiber Takviyeli Kompozit Malzemelerinin Frezelenmesinde Meydana Gelen Yüzey Pürüzlüğünün Değerlendirilmesi ve Matematiksel Modellenmesi (In Turkish). *Gazi Üniversitesi Fen Bilimleri Dergisi Part C: Tasarım ve Teknoloji*, 6(3), 705-714

[14] Yetgin, S. H., Ünal, H. and Hatipoğlu, G. (2016). Poli-Fital-Amid (PPA) Polimerinin Tribolojik Özelliklerine Karbon Fiber ve Kayma Hızı'nın Etkisinin İncelenmesi (In Turkish). *Düzce Üniversitesi Bilim ve Teknoloji Dergisi*, 4(1), 167-175

[15] Zhang, X., Fan, X., Yan, C., Li, H., Zhu, Y., Li, X. and Yu, L. (2012). Interfacial microstructure and properties of carbon fiber composites modified with graphene oxide. *ACS applied materials & interfaces*, 4(3), 1543-1552

[16] Das, T.K., Ghosh, P. and Das, N.C. (2019). Preparation, development, outcomes, and application versatility of carbon fiber-based polymer composites: a review. *Advanced Composites and Hybrid Materials*, 1-20

[17] Eray, S. (2020). In: Metal Oxide Powder Technologies, , Elsevier, Amsterdam, 101-119

[18] Shin, S.E., Ko, Y.J. and Bae, D. (2016). Mechanical and thermal properties of nanocarbon-reinforced aluminum matrix composites at elevated temperatures. *Composites Part B: Engineering*, 106, 66-73

[19] Xu, Z., Zhang, Y., Zhou, J., Qi, M., Shi, J. and Zhang, J. (2020). Study on high- temperature composite properties of fluorosilicone rubber with nano- Sb2O3. *Journal of Applied Polymer Science*, 137(42), 49302

[20] Djordjevic, I., Sekulic, D.P. and Stevanovic, M. (2007). Carbon fiber composites, main engineering elastic constants and macromechanical characterization. *Journal of reinforced plastics and composites*, 26, 1193-1199

[21] Karataş M.A. and Gökkaya, H. (2018). A review on machinability of carbon fiber reinforced polymer (CFRP) and glass fiber reinforced polymer (GFRP) composite materials. *Defence Technology*, 14(4), 318-326

[22] Karslı N.G. and Aytac, A. (2013). Tensile and thermomechanical properties of short carbon fiber reinforced polyamide 6 composites. *Composites Part B: Engineering*, 51, 270-275

[23] Dong, F., Hou, G., Cao, F., Yan, F., Liu, L. and Wang, J. (2016) The lubricity and reinforcement of carbon fibers in polyimide at high temperatures. *Tribology International*, 101, 291–300

[24] Engin, K., Koyuncu, T. and Lüle, F. (2015). Farklı kompozit malzemelerin üretilmesi ve bazı teknik özelliklerinin belirlenmesi. Anadolu Journal of Agricultural Science, 30(1), 43-50

[25] Henerichs, M., Voss, R., Kuster, F. and Wegener, K. (2015). Machining of carbon fiber reinforced plastics: Influence of tool geometry and fiber orientation on the machining forces. *CIRP Journal of Manufacturing Science and Technology*, 9, 136-145

[26] Song, H. (2015). Pairing effect and tensile properties of laminated high-performance hybrid composites prepared using carbon/glass and carbon/aramid fibers. *Composites Part B: Engineering*, 79, 61-66

[27] Akbar, İ. and Liew, K.M. (2020). Assessing recycling potential of carbon fiber reinforced plastic waste in production of eco-efficient cement-based materials. *Journal of Cleaner Production*, 274, 123001

[28] Demir, M.E., Çelik, Y.H. and Kılıçkap, E. (2019). Cam ve Karbon Elyaf Takviyeli Kompozitlerde Elyaf Cinsinin, Yükün, Kayma Hızı ve Mesafesinin Abrazif Aşınmaya Etkisi (In Turkish). *Politeknik Dergisi*, 22(4), 811-817

[29] Knoblauch R. and Geddes C.D. (2020). Carbon nanodots in photodynamic antimicrobial therapy: A review. *Materials*, 13(18), 4004

[30] Yue Z. and Economy. J. (2017). Carbonization and activation for production of activated carbon fibers. *Activated Carbon Fiber and Textiles*, 61-139

[31] Güneş. D. (2019). Comparison of Mechanical Properties of Composite Materials with One Way And Biaxial Carbon Fiber Reinforced Polyester Resin Matrix. (In Turkish) Master Thesis. Kütahya Dumlupınar University, Kütahya,

[32] Baral, N., Guezenoc, H., Davies, P. and Baley, C. (2008). High modulus carbon fibre composites: Correlation between transverse tensile and mode I interlaminar fracture properties. *Materials letters*, 62, 1096–1099

[33] Bergmann, T., Heimbs, S., and Maier, M. (2015). Mechanical properties and energy absorption capability of woven fabric composites under±45 off-axis tension. *Composite Structures*, 125, 362-373

[34] Shi, Y., Swait, T. and Soutis, C. (2012). Modelling damage evolution in composite laminates subjected to low velocity impact. *Composite Structures,* 94(9), 2902-2913

[35] Arslan, G., Fidan, S. and Sınmazçelik, T. (2018). Solid particle erosion behavior of carbon fiber-metal wire hybrid reinforced polymer composites. *Journal of Science and Engineering*, 5(1), 182-190

*RESEARCH ARTICLE*

# INVESTIGATION OF PRODUCTION PARAMETERS FOR FUNCTIONALLY GRADED Al-Al₂O₃ and Cu-Steatite

Levent URTEKİN[1], Serkan SEVDA[2], Fatih BOZKURT[3] , İbrahim USLAN[4]

[1]Ahi Evran University, Department of Mechanical Engineering, Kırşehir, levent.urtekin@ahievran.edu.tr, ORCID:0000-0003 4348-4749
[2]Gazi University, Department of Mechanical Engineering, Ankara. ssevda@gazi.edu.tr, ORCID: 0000-0002-1497-1030
[3] Eskişehir Technical University, Vocational School of Transportation, Eskişehir, fatihbozkurt@eskisehir.edu.tr, ORCID: 0000-0001-9897-1558
[4]Gazi University, Department of Mechanical Engineering, Ankara. iuslan@gazi.edu.tr,ORCID: 0000-0003-1486-4865

## ABSTRACT

In this study, determined amount of powder (Al-Al2O3 and Cu-Steatite) by weight are mixed homogeneously with 3-D shaker and then pressed to obtain FGM. Mixture ratios by weight vary from 80 % Al - 20 % $Al_2O_3$ to 20 % Al - 80 % Al2O3. Same mixture ratios are also prepaired for Cu-Steatite. For both of the mixtures, maximum ratio of metal (Aluminum and Copper) stay in the core while maximum ratio of ceramics (Al2O3 and Steatite) at the outer. Powder mixtures are passed through Hall funnel and appearant densities of them are calculated. Appearant density of Al-Al2O3 mixtures varies from 1.184 gr/cm3 to 1.344 gr/cm3 while it varies from 1.04 gr/cm3 to 2.352 gr/cm3 for Cu-Steatite mixtures. Aluminum tubes at successive diameters are placed into the cylindirical die of 32 mm diameter to seperate the different regions in the die before pressing. Each layer between the tubes corresponce to a different ratio of homogeneous mixture. Zinc stearate lubricant at the amount of 1% of each mixture by weight is added into each mixture before pressing. Pressing pressure varies from 700 MPa to 750 MPa. FGM specimen prepared from $Al-Al_2O_3$ mixture is sintered at 630 0C for 90 min and the one from Cu-Steatite 1030 0C for 60 min.

**Keywords:** *Functionally graded materials, Powder Mettalurgy, Sintering*

## 1. INTRODUCTION

The concept of FGM was first mentioned in 1984 for a science project. In this project, a combination of materials has been used for creating a thermal barrier with enduring a surface temperature of 2000 K and a temperature gradient of 1000 K across a 10 mm section.

FGM aims to make a composite material by varying the microstructure from one material to another material with a specific gradient in order to have the best of both materials. Both strengths of the material may be used to avoid corrosion, fatigue, fracture, and stress corrosion cracking when considering thermal, corrosive resistance or malleability and toughness.

Powder metallurgy is widely used to produce FGMs. Some of the material couples to produce FGM by means of the powder metallurgy are ZrO2-Ni, Hydroxyapatite-Ti (biomaterial), $ZrO_2$-NiCr, Ti-$ZrO_2$, $Al_2O_3$-$Ti_3SiC_2$, Mullite/Mo, SiC/C, Al-SiC and Ni-$Al_2O_3$. In this study, Al-$Al_2O_3$ and Cu-Steatite couples are used to produce FGM by means of the powder metallurgy. Powder metallurgical processing is one of method for manufacturing of FGM [1]. This method required by powder metallurgical (PM) processing involves rapid solidification that offers unique advantages for the ductility of the material. For example, segregation in the powdered material can be minimized, very fine grains can be produced, and solid solubility of alloying elements can be increased [1-3]. Biomaterial implants [4], thermal barriers [5], energy conversion materials [6], cutting and rock drilling tools [7], mechanical elements as gears, and optical and optoelectronic materials [8] are some of the fields for application. FGM development procedures also include powder metallurgy (PM), centrifugal casting, thermal or plasma spraying, electrochemical processing, and chemical vapor deposition (CVD) and physical vapor deposition (PVD). Cast blanking, frictional mixing machining (FSP) and laser-controlled web formation are state-of-the-art processes to produce such hybrid material. FGMs have a growing role due to their custom-made properties and the lack of well-defined restrictions or interfaces among their different sections unlike conventional composites. As a result of the high sectional laminar stresses in classical composites, the layers split, leading to the breakdown of the load transfer mechanism between the matrix and the reinforcement, loss of rigidity and structural integrity, which ultimately leads to failure. functionality and structure. FGM has a good opportunity for diminishing mechanical and thermal stress concentrations in several structural materials to develop specific tools [9]. For example, the optimized formation gradient of a cutting tool can increase tool life and abrasion resistance [10]. Likewise, dental implants are improved by optimized constituent gradients and gradient thicknesses in terms of implant duration and convenience [11].

J.R.Cho and J.Tinseley [12], in their studies, express material properties in terms of the volume fractions of the ceramic and metal components in the composition. In this study, FGM is considered as a multilayered composite structure. Each layer is assumed to be isotropic so that stress and strain components are calculated as shown below:

$$\sigma = V_s\sigma_s + V_m\sigma_m$$
$$\varepsilon = V_s\varepsilon_s + V_m\varepsilon_m$$

Where;
$V_s$ : Volume fraction of the ceramic, $V_m$ : Volume fraction of the metal
$\sigma_s$ : Stress of the ceramic , $\sigma_m$ : Stress of the metal
$\varepsilon_s$ : Strain of the ceramic , $\varepsilon_m$ : Strain of the metal

So, modulus of elasticity of the FGM is determined as shown below [13]:
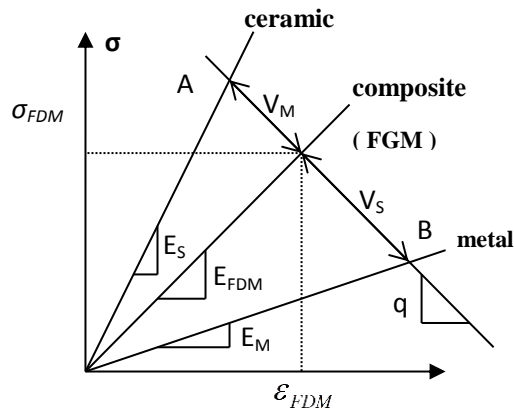
**Figure 1.** Stress-Strain relationship in FGM due to volume fractions.

As shown in the figure;

$$q = (\sigma_A - \sigma_B)/(\varepsilon_A - \varepsilon_B)$$

Values of q are determined experimentally for various volume fractions. So that, modulus of elasticity is calculated along the FGM layers in the material. Modulus of elasticity is defined in terms of q, $V_m$, $V_s$, $E_m$ and $E_s$ due to the experimental results.

## 2. EXPERIMENTAL METHOD

**Materials:**
Production of the FGM is achieved by using metal and ceramic powders. Properties of these powders are tabulated in Table 1. Metal powder is composed from aluminum and copper whereas ceramic powder is composed from aluminum oxide and steatite.

**Table 1.** Powders used to produce FGM.

| Powder Material | Al | $Al_2O_3$ | Cu | Steatite |
|---|---|---|---|---|
| Density (g/cm$^3$) | 2.7 | 3.89 | 8.96 | 2.7 |
| Melting Temperature ($^0$C) | 660 | 2054 | 1084 | 1450 |
| Mean Particle Size (μm) | 60 | 12.15 | 72 | 15.12 |

**Particle Sizer:**
Particle size is determined by means of the Malvern Mastersizer Laser Particle Sizer Unit in the powder metallurgy laboratory of Gazi University, Department of Mechanical Engineering. This unit contains a laser beam source to emit monochrome, intensive and parallel beams, in addition to the beam expander, measurement chamber, Fourier lense and detector. Mechanical shaker, centrifugal pump and ultrasonic energy application facilities are available in the sample preparing unit. Ultrasonic energy is applied to dissipate the lumps. Mechanical mixer is used to make the suspension stay homogenous during analyzing. Finally centrifugal pump is used to make the suspension be sprayed towards the laser beam. The sample in the reservoir, prepared with one liter of water, is maintained to

circulate continuously in front of the laser beams. Laser beams which collide with the particles refract with definite angles, pass through the Fourier lens and then land on the detector. These beams which land on the detector are digitized by means of an analog-digital converter. Then these converted data are entered into the computer. Refracting angles of the beams help to calculate the particle size besides intensity of the beams help to calculate the particle percentage by volume. A general view and installation of the "particle sizer" is shown in figure 2.
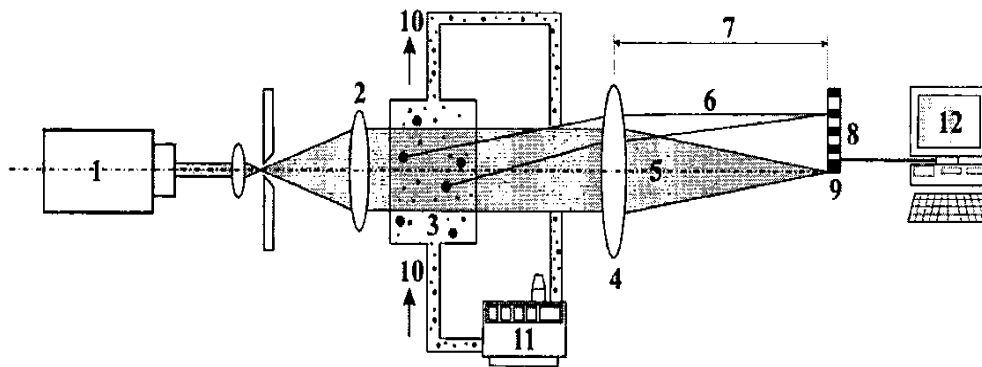


**Figure 2.** Installation of Particle Sizer. (1. Laser beam source, 2. Beam expander, 3. Measurement chamber, 4. Fourier lens, 5. Laser beam cluster which didn't collide with any particle, 6. Refracted beams which collided with the same-sized particles, 7. Lens focus length, 8. Detector, 9. Central detector, 10. Suspension flow direction, 11. Sample preparing unit (reservoir), 12. Computer.

**Turbula Shaker:**
Shaking process is achieved in the Powder Metallurgy Laboratory of Mechanical Engineering Department of Gazi University by means of a three dimensional shaker which is called "Turbula Shaker". Powders with definite percentages (Table 2) are shaked in a dry medium during approximately 45 minutes and it is observed that this period is sufficient for a homogenous mixture.

**Table 2.** Powder percentages used for FGM.

| Mixture Numbers | Mixture Percentages by weight | | | |
|---|---|---|---|---|
| | Al | $Al_2O_3$ | Cu | Steatit |
| 1 | 80 | 20 | 80 | 20 |
| 2 | 60 | 40 | 60 | 40 |
| 3 | 20 | 80 | 20 | 80 |

**Hall Funel:**
Mixture powders are passed through hall funel and apparent densities are determined. The powders which pass through the holes diameter of 1 inch, flow into the cylinder that has a volume of 25 cm³. Apparent density is calculated by means of the fraction of the weight of the powder mixture to the volume. It is observed that apparent density varies between 1.184-1.344 gr/cm³ for $Al_2O_3$-Al and 1.04-

2.352 gr/cm$^3$ for Cu-Steatite. Increasing of ceramic content decreases the apparent density of both mixtures.

**Molding:**

Pressing of the powders are achieved by means of "Dartec Tensile Testing Machine" which has a capacity of 60 tons. The powders are pressed between the loads of 570-600 kN. Applied pressures are between 709.1 MPa for Al$_2$O$_3$-Al and 746.42 MPa for Cu-Steatite. Zinc stearate lubricant at the amount of 1% of each mixture by weight is added into each mixture before pressing in order to minimize the friction. Two hollow cylinders each of which has a thickness of 1 mm are placed into the die in order to create three cylindirical regions and powder mixtures are poured into the each region. The diameters of these hollow cylinders are 23 mm and 9 mm whereas the diameter of the die is 32 mm which consists of upper and lower punches. Into the outer region of the die, Al$_2$O$_3$-Al powder mixture 80% by weight is poured and then into the inner regions 40% and 20% by weight of the same mixture respectively. Similarly for the Cu-Steatite, into the outer region Cu-Steatite powder mixture 80% by weight is poured and then into the inner regions 60% and 20% by weight of the same mixture respectively. Pressing pressure and the amount of powder to be poured into the die are determined due to the apparent density of the powder mixture. The die, upper and lower punches are shown in the figure 3a besides the regions are shown schematically in the figure 3b.



|        (a)         |        (b)         |        (c)         |
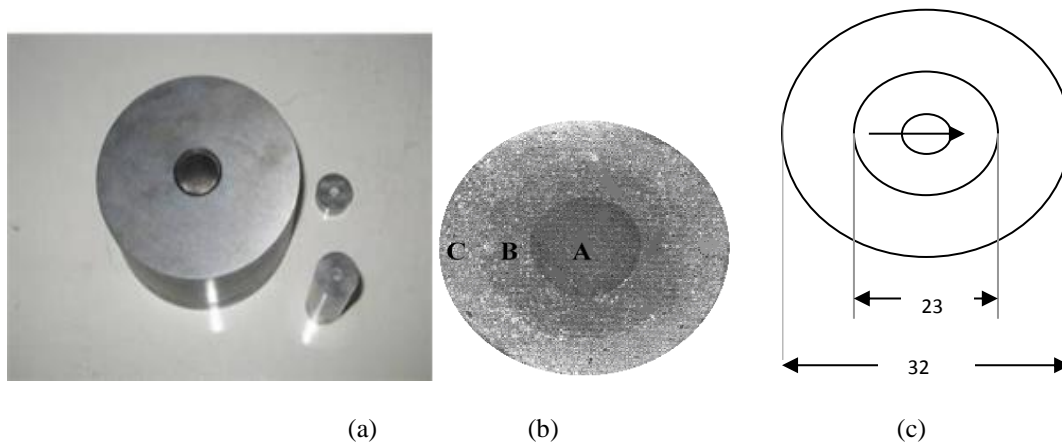
**Figure 3.** (a) The die, upper and lower punches (b) Schematical regions (c) FGM.

**Sintering Properties:**

Sintering temperature for Al$_2$O$_3$-Al is 630 $^0$C where sintering period is 90 min. This temperature is above the sintering temperature but below the melting temperature of aliminum. Sintering temperature for Cu-Steatite is 1030 $^0$C where sintering period is 60 min. Similarly, this temperature is above the sintering temperature but below the melting temperature of copper. Applied pressure for Al$_2$O$_3$-Al is 709.1 MPa whereas 746.42 MPa for Cu-Steatite. Sintering graph is given in figure 4 for both materials. In figüre 5 and 6 raw and sintered views of Cu-Steatite are given.
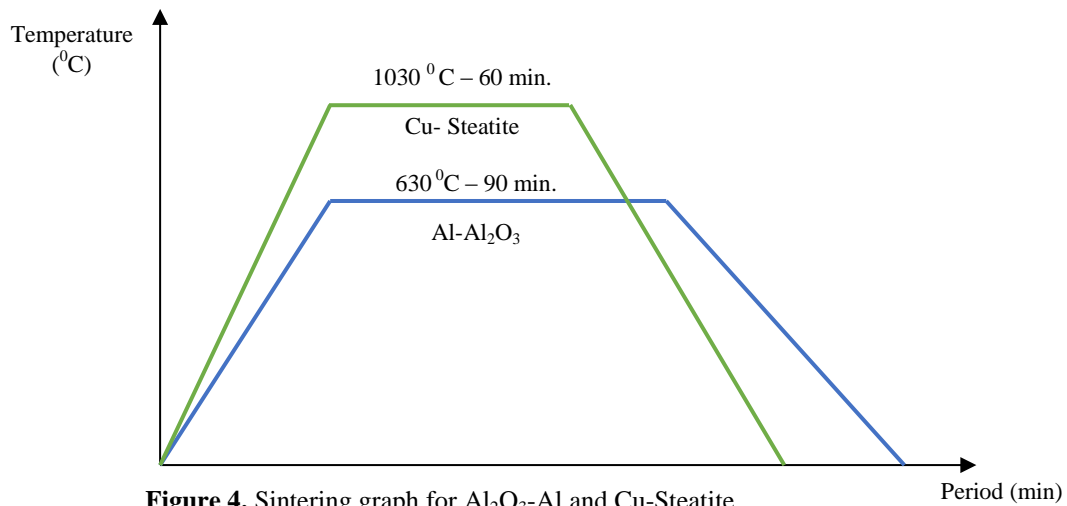
**Figure 4.** Sintering graph for $Al_2O_3$-Al and Cu-Steatite.



(a)                                  (b)
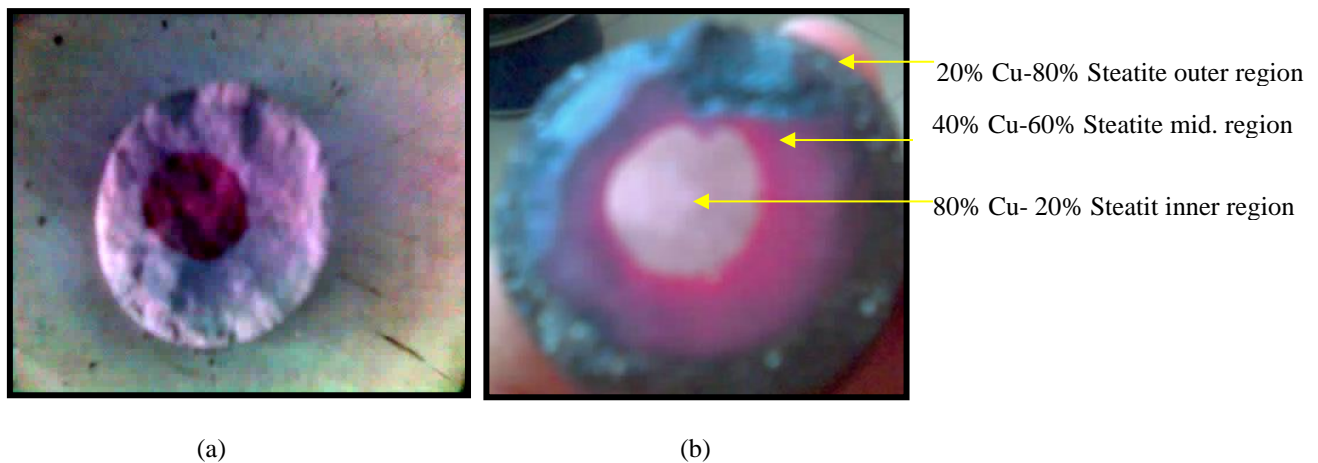
**Figure 5.** (a) Sintering Cu-Steatite FGM (b) Sintering Cu-Steatite FGM.

## 3. RESULTS and DISCUSSION

It is observed that Cu-Steatite specimen has higher strength than the raw material. However some cracks are visible around the specimen. Sintering conditions must be improved in order to avoid from the cracks. Strength of the pressed Al-$Al_2O_3$ specimen increases after sintering but not as much as the increase of the Cu-Steatite specimen. Appropriate sintering conditions must be determined by means of DSC and sintering must be achieved under a protective atmosphere. Apparent densities of both mixtures decrease when ceramic content increases. Appearant density of Al-$Al_2O_3$ mixtures varies from 1.184 $gr/cm^3$ to 1.344 $gr/cm^3$ while it varies from 1.04 $gr/cm^3$ to 2.352 $gr/cm^3$ for Cu-Steatite mixtures depending on the mixture pertentages. Powders are pressed between the loads of 570-600 kN. Pressing pressure is 709.1 MPa for $Al_2O_3$-Al where 746.42 MPa for Cu-Steatite.

**ACKNOWLOEDGEMENT**

## REFERENCES

[1] Watanabe R. and A. Kawaski, (1987), "Powder Metallurgical Fabrication of the Thermal Stress Relief Type of Functionally Gradient Materials," Sintering, Elsevier, Tokyo, Vol. 2, pp. 1197-1202.

[2] Schubert T., Weibgarber T., Kieback B., Balzer H., Neubing H. C., Baum U. and Braum R., (2005), "Aluminum PM is a Challenge That Industry Can Overcome," Metal Powder Report, Vol. 60, No. 3, pp. 32-37.

[3] Mahmoud M. Nemat-Alla, Moataz H. Ata, Mohamed R. Bayoumi, Wael Khair-Eldeen, (2011), Powder Metallurgical Fabrication and Microstructural Investigations of Aluminum/Steel Functionally Graded Material, Materials Sciences and Applications, 2, 1708-1718.

[4] Mehboob H, Chang SH., (2014), Evaluation of the development of tissue phenotypes: Bone fracture healing using functionally graded material composite bone plates, *Compos. Struct.* 117, 105–113.

[5] Koizumi M. (1997), FGM activities in Japan, *Compos. Pt. B Eng.* 28, 1–4.

[6] Muller E, Drasar D, Schilz J, Kaysser WA., (2003), Functionally graded materials for sensor and energy applications, *Mater. Sci. Eng. A* 362, 17–39.

[7] Ilschner B., (1993), Structural and compositional gradients: basic idea, preparation, applications, *Le J. Phys. IV,* 03, C7-763–C7-772.

[8] Bharti I, Gupta N, Gupta KM., (2013), Novel Applications of Functionally Graded Nano, Optoelectronic and Thermoelectric Materials, *Int. J. Mater. Mech. Manuf.* 1, 221–224.

[9] Jha DK, Kant T, Singh RK., (2013), Free vibration response of functionally graded thick plates with shear and normal deformations effects, 96, 833–849.

[10] Xu CH, Wu GY, Xiao GC, Fang B., (2014), Al2O3/(W,Ti)C/CaF2 multi-component graded self-lubricating ceramic cutting tool material, *Int. J. Refract. Metals Hard Mater.* 45, 125–129.

[11] Ichim PI, Hu X, Bazen JJ, Yi W., (2016), Design optimization of a radial functionally graded dental implant, *J. Biomed. Mater. Res. – Pt. B Appl. Biomater.* 104, 58–66.

[12] J.R. Cho, J. Tinsley Oden, (2000), Functionally graded material: a parametric study on thermal-stress characteristics using the Crank±Nicolson±Galerkin scheme, Comput. Methods Appl. Mech. Engrg., 17-38.

[13]  K.S. Ravichandran, (1994), Elastic properties of two-phase composites, J. Am. Ceram. Soc. 77 (5) 1178-1184.

*RESEARCH ARTICLE*

## An APPLICATION of A MODIFIED CAMEL TRAVELING BEHAVIOR ALGORITHM for TRAVELING SALESMAN PROBLEM

Mehmet Fatih DEMİRAL[1]

[1]Burdur Mehmet Akif Ersoy University, Faculty of Engineering and Architecture, Department of Industrial Engineering,
mfdemiral@mehmetakif.edu.tr, ORCID:0000-0003-0742-0633

## ABSTRACT

Camel Traveling Behavior Algorithm (CA) is a fairly new algorithm developed in 2016 by Mohammed Khalid Ibrahim and Ramzy Salim Ali. Scientists have put forward a few publications on CA. CA was applied to continuous optimization problems and engineering problems in the literature. It has been shown that CA has comparable performance with Particle Swarm Optimization (PSO) and Genetic Algorithm (GA). Besides, a modified camel algorithm (MCA) has been implemented in the field of engineering and was showed that it has competitive performance with Cuckoo Search (CS), PSO, and CA. In this work, an application of MCA has been done in the traveling salesman problem. A set of classical datasets which have cities scale ranged from 51 to 150 was used in the application. The results show that the MCA is superior to Simulated Annealing (SA), Tabu Search (TS), GA, and CA for 60% of all datasets. Also, it was given that a detailed analysis presents the number of best, worst, average solutions, standard deviation, and the average CPU time concerning meta-heuristics. The metrics stress that MCA demonstrates a performance rate over 50% in finding optimal solutions. Finally, MCA solves the discrete problem in reasonable times in comparison to other algorithms for all datasets.

**Keywords:** *Modified Camel Algorithm, Meta-heuristic Algorithms, Traveling Salesman Problem*

## 1. INTRODUCTION

Combinatorial optimization is a popular research area in the last decades. Besides, solving combinatorial problems with meta-heuristic approaches and comparing them in popular problems are also interesting research of field [1-3]. Meta-heuristics are nature-inspired algorithms that simulate natural phenomena and put forth solutions to mathematical problems. In general, meta-heuristics are investigated in classical and modern meta-heuristics [4, 5]. Classical meta-heuristics are simulated annealing (SA), tabu search (TS), genetic algorithm (GA), particle swarm optimization (PSO), and ant colony optimization (ACO). Artificial Bee Colony algorithm (ABC), Black Hole algorithm (BH), Sine-Cosine algorithm (SCA), Lion Optimization algorithm (LOA), Water-Wave optimization (WWA), Artificial Atom algorithm ($A^3$), and Physarum-Energy optimization algorithm (PEO) are popular examples of modern meta-heuristics [6-12].

Modern meta-heuristics generally start with an initial population and evolving this population with the algorithm mechanism in every iteration. Algorithms mostly have two features in their structures: intensification and diversification. Diversification means that the algorithm searches new areas and has the chance of finding many solutions in the solution space. On the other hand, intensification helps the algorithm to focus on optimal solutions and escape from local solutions. To converge optimality efficiently, meta-heuristics may hybridize with other algorithms or be improved with new mechanisms. Nature-inspired meta-heuristics have been often implemented in business administration, industrial engineering, computer engineering, technology, and other fields of science [13-15].

Camel algorithm mimics the traveling behavior of camels in the desert under several factors. The algorithm explores solution space at a certain level of endurance, supply, and temperature. Even if CA has several parameters, it is a simple and assertive approach to many optimization problems [16-18]. MCA is an approach that was proposed for engineering applications in previous research. It was successfully applied to the anti-jamming smart antenna optimization and the optimization of the proportional-integral-derivative (PID) controller parameters. It is concluded that MCA is a good candidate for online optimization systems [17].

In this study, the MCA is applied to solve the traveling salesman problem (TSP). The traveling salesman problem is a popular test problem for evaluating the efficiency and effectiveness of the optimization algorithms. The discrete problem aims to find an optimal tour, visiting each city exactly once and returning to the starting city where the total length of the tour is optimized [19].

The rest of the paper is organized as follows: In Sect. 2, the traveling salesman problem is widely discussed. The MCA is given in Sect. 3. In Sect. 4, the experimental results of the performance analysis of the MCA are described, and finally, Sect. 5 contains a conclusion and future expectations of this work.

## 2. TRAVELING SALESMAN PROBLEM

The traveling salesman problem (TSP) is a widely studied and well-known benchmark problem in the field of engineering and optimization. Many scientists have been working on that problem to solve it optimally in reasonable times [20]. To solve the problem, many approaches have been applied to solve TSP and its variants. A traveling salesman problem is a problem in which a salesman travels all the cities exactly once and returns to the initial city in optimal distance. The salesman can complete its tour in optimal distance, optimal time, optimal budget, and other objectives. TSP is generally investigated in symmetric and asymmetric types in many studies [21-24]. In symmetric type (s-TSP), the cost of an edge $\left(d_{ij} = d_{ji}\right)$ is valid for all points. Otherwise, if $\left(d_{ij} \neq d_{ji}\right)$ for at least one, then the TSP becomes asymmetric TSP (a-TSP). The TSP is also classified as the number of tours or salesmen. Double TSP (d-TSP) and multiple TSP (m-TSP) are the well-known types of traveling salesman problems. Besides, many researchers are still working on the generalizations of TSP, which are the traveling purchaser problem and the vehicle routing problem.

The traveling salesman problem (TSP) is an NP-hard problem, so finding an optimal solution to the problem in a reasonable time with linear programming requires exponential time. If a large size of data is used, the number of solutions becomes n! When n gets large, it will be impossible to find all of the solutions in a polynomial time. Thus, many exact, heuristic, and meta-heuristic methods are used

to solve the TSP problem [25, 26]. Especially, classical and modern meta-heuristics are the highly potential solution algorithms for the TSP problem.

To define TSP in a short form, the problem can be described as: *N* is the set of *n* cities, *E* is the set of the edges, and $D_{ij} = (d_{ij})$ is the distance matrix between city *i* and city *j*. $P_{ij} = \{1, 2, \ldots, n, 1\}$ is the permutation of the constructed tours. 1 represents the first city; n represents the nth city of all the permutations. Then, the model of the problem is briefly given in Eq. 1.

$$Min. \sum_{i=1}^{n-1}\left(d_{i,i+1}\right) + d_{n,1} \tag{1}$$

The Euclidean distance is applied to calculate the distance between cities using Eq. 2.

$$d_{i,j} = \sqrt{\left(x_i - x_j\right)^2 + \left(y_i - y_j\right)^2} \tag{2}$$

## 3. MODIFIED CAMEL ALGORITHM

The camel algorithm (CA) is one of the exciting meta-heuristic algorithms in the literature. It is based on the camel traveling behavior in the desert under strict conditions. In the MCA, the camels (camel caravan) are searching for the best positions and looking randomly for the food supply [17]. Therefore, they try to survive and live for a long time in the desert. In the camel algorithm, each camel has its initial supply (*S*) at the beginning, and then both temperature (*T*) and journey duration affect camel endurance (*E*). The temperature *T* of a camel varies randomly between $T_{min}$ and $T_{max}$ using Eq. 3.

$$T_d^{i,iter} = \left(T_{max} - T_{min}\right) * Rand + T_{min} \tag{3}$$

However, the temperature is the primary factor that affects the camel endurance; the endurance is redefined in the modified camel algorithm using Eq. 4 [17].

$$E_d^{i,iter} = 1 - \left(\frac{T_d^{i,iter} - T_{min}}{T_{max} - T_{min}}\right) \tag{4}$$

In the MCA, there are two options for producing new solutions or updating the new locations. When the camel visibility v is less than a specific probability, the first alternative occurs using Eq. 5.

$$x_d^{i,iter} = x_d^{i,iter-1} + E_d^{i,iter} * \left(x_d^{best} - x_d^{i,iter-1}\right) \tag{5}$$

On the other hand, when the camel visibility v is larger than a specific probability, the second alternative is realized using Eq. 6.

$$x_d^{i,iter} = \left(x_{max} - x_{min}\right) * Rand + X_{min} \tag{6}$$

In the light of Eq. 3-6, the pseudo-code of the MCA with oasis condition is shown in Fig. 1 [17].

| |
|---|
| **Algorithm: Modified CA** |
| **Begin** |
| **Step 1: Initialization:** Set the min. and max. temperature $T_{min}$ and $T_{max}$; set the camel caravan size and the dimensions; set the visibility threshold; Initialize the camel caravan using the Eq. (6). |
| **Step 2:** Subject the locations to a certain fitness function; determine the current best location; randomly assign a visibility ($v$) for each camel. |
| **Step 3: While** (iter < itermax) **do** |
| **for** i=1: Camel Caravan size |
| Compute the temperature T from Eq. (3) |
| Compute the endurance E from Eq. (4) |
| **If** $v$ < *visibility threshold* **then** |
| Update the camel location from Eq. (5) |
| **Else** |
| Update the camel location from Eq. (6) |
| **End If** |
| **If** (oasis condition occur) |
| Replenish Endurance |
| **End If** |
| **End for** |
| Subject the new locations to the fitness function |
| **If** the new best location is better than the older one |
| The new best is the global best |
| **End If** |
| Assign new visibility for each camel |
| **Step 4: End While** |
| **Step 5:** Output the best solution |
| **End** |

**Figure 1.** Pseudo-code of the MCA.

The neighborhood operators are used to obtain the new solutions from the current solution. A neighborhood operator or the combination of operators may generate new solutions [27, 28]. In this study, four basic neighborhood operators are chosen randomly and applied once in each iteration. The selected operators for the optimization process are swap, insert, reverse, and swap_reverse. As previous papers indicate, the use of a single structure can be divergent and cannot search optimal regions of the search space [28, 29]. Thus, instead of using a single structure, it would hopefully give better results when multiple combinations are used. Then, the neighborhood selection is defined by the minimum of four operators using Eq. 7.

$$NH(x) = \min(swap(x), insert(x), reverse(x), swap\_reverse(x)) \qquad (7)$$

However, the MCA converges at a later stage by using multiple combinations. It will be needed more iteration and computation time to find near-optimal solutions [27-29]. On the other hand, the use of the four investigated structures would give better solutions: swapping, insertion, reversing, and swapping of reversed subsequences than others at 1000-2000 iterations.

**4. EXPERIMENTAL ANALYSIS**

The ten datasets ranged from 51 to 150 cities were selected from the TSPLIB library in the implementation. In this section, all the experiments were run on Intel® Core™ i7 3520-M CPU 2.9 GHz speed with 8 GB RAM by using Matlab. The algorithms which are MCA, CA, GA, TS, and SA are compared to demonstrate the performance of the MCA. All the algorithms were run 10 times independently for optimal parameters and 1000-2000 iterations for each run. There are many parameters for the used meta-heuristics. However, it is mentioned the fundamentals for algorithms. In the SA algorithm, initial temperature ($T_0$ =40000), cooling rate (r=0.80), and the iteration limit for temperature change (L=10) are sufficient for optimization. In the TS algorithm, the tabu length (L=30) is the adequate parameter. In GA, the crossover rate is 0.80, the mutation rate is 0.02 and the population size is 100. In CA and MCA, the dimension of space (dim=10), min. and max. temperature ($T_{min}$=0, $T_{max}$ =100), initial endurance (Init_End=1), visibility threshold (Vis=0.5), dying rate (dye_rate=0) are taken as optimal parameters. In CA, initial supply (Init_Supp=1) is available.

**Table 1.** Computational results of algorithms on the medium-scale TSP instances.

| TSP | Measure | SA | TS | GA | CA | MCA |
|---|---|---|---|---|---|---|
| eil51 | Best | 478.97 | 488.49 | 478.73 | 489.7 | 471.43 |
| (426) | Worst | 591.41 | 577.43 | 525.4 | 569.24 | 495.75 |
| | Avg | 541.57 | 527.14 | 499.14 | 514.6 | 478.79 |
| | Std. | 36.85 | 26.94 | 18.16 | 28.77 | 8.18 |
| | Time | 0.2 | 0.35 | 46.63 | 18.29 | 15.95 |
| | Number | 1000 | 1000 | 1000 | 1000 | 1000 |
| berlin52 | Best | 8591.18 | 8466.93 | 8104.65 | 8373.08 | 8357.37 |
| (7542) | Worst | 10329.7 | 9825.44 | 8883.47 | 10481 | 9011.83 |
| | Avg | 9415.69 | 9452.24 | 8451.47 | 9194.62 | 8659.57 |
| | Std. | 546.37 | 413.04 | 225.23 | 561.6 | 213.12 |
| | Time | 0.25 | 0.33 | 48.62 | 18.96 | 16.46 |
| | Number | 1000 | 1000 | 1000 | 1000 | 1000 |
| st70 | Best | 952.37 | 920.14 | 930.31 | 892.84 | 898.43 |
| (675) | Worst | 1206.55 | 1212.84 | 1057.09 | 1120.32 | 987.66 |
| | Avg | 1064.81 | 1011.57 | 1001.24 | 1021.07 | 953.59 |
| | Std. | 92.9 | 81.2 | 45.24 | 67.11 | 36.79 |
| | Time | 0.49 | 0.30 | 69.81 | 21.38 | 18.78 |
| | Number | 1000 | 1000 | 1000 | 1000 | 1000 |
| eil76 | Best | 744.43 | 745.62 | 781.92 | 698.83 | 676.74 |
| (538) | Worst | 897.59 | 908.12 | 886.94 | 815.02 | 787.58 |
| | Avg | 805.4 | 789.54 | 827.71 | 773.3 | 746.38 |
| | Std. | 53.49 | 47.5 | 35.87 | 35.85 | 31.62 |
| | Time | 0.27 | 0.32 | 81.84 | 21.25 | 19.6 |
| | Number | 1000 | 1000 | 1000 | 1000 | 1000 |
| pr76 | Best | 144562 | 138357 | 128068 | 147348 | 146743 |
| (108159) | Worst | 162619 | 148753 | 149040 | 178085 | 162307 |
| | Avg | 155394 | 142024 | 135946 | 164720 | 157814 |
| | Std. | 5059.64 | 3623.74 | 5544.75 | 9510.72 | 4688.28 |
| | Time | 0.24 | 0.33 | 65.33 | 22.05 | 19.12 |
| | Number | 1000 | 1000 | 1000 | 1000 | 1000 |

**Table 1.** continued.

| TSP | Measure | SA | TS | GA | CA | MCA |
|---|---|---|---|---|---|---|
| rat99 | Best | 2024.28 | 1566.22 | 1521.5 | 1993.3 | 1937.49 |
| (1211) | Worst | 2214.42 | 1758.13 | 1836.3 | 2399.76 | 2370.5 |
| | Avg | 2142.83 | 1666.17 | 1655.32 | 2222.23 | 2172.74 |
| | Std. | 66.64 | 63.25 | 81.33 | 121.06 | 146.47 |
| | Time | 0.30 | 0.42 | 101.5 | 24.94 | 21.52 |
| | Number | 1000 | 1000 | 1000 | 1000 | 1000 |
| kroa100 | Best | 34383.6 | 35136.1 | 32865.5 | 33863.5 | 29816.7 |
| (21282) | Worst | 39483.7 | 43265.7 | 37832.2 | 43562.7 | 35823 |
| | Avg | 37055.2 | 38186.5 | 35417.8 | 37895.5 | 33721.5 |
| | Std. | 1649.85 | 3080.13 | 1446.68 | 2974.65 | 1746.97 |

| | | | | | | |
|---|---|---|---|---|---|---|
| | Time | 0.64 | 0.63 | 191.92 | 51.01 | 43.95 |
| | Number | 2000 | 2000 | 2000 | 2000 | 2000 |
| eil101 | Best | 864.99 | 862.19 | 855.68 | 870.06 | 843.11 |
| (629) | Worst | 1007.91 | 998.82 | 970.2 | 1043.86 | 943.08 |
| | Avg | 938.98 | 921.97 | 904.38 | 939.7 | 892.74 |
| | Std. | 46.19 | 43.93 | 33.63 | 54.01 | 31.93 |
| | Time | 0.77 | 0.66 | 196.15 | 50.7 | 50.58 |
| | Number | 2000 | 2000 | 2000 | 2000 | 2000 |
| bier127 | Best | 175583 | 175733 | 170334 | 186581 | 181965 |
| (118282) | Worst | 201548 | 203137 | 189736 | 213526 | 200309 |
| | Avg | 192011 | 187255 | 179673 | 197687 | 191837 |
| | Std. | 7596.82 | 7756.69 | 5897.25 | 9587.58 | 6177 |
| | Time | 0.81 | 0.78 | 262.47 | 57.51 | 50.45 |
| | Number | 2000 | 2000 | 2000 | 2000 | 2000 |
| kroa150 | Best | 54469.6 | 56795.3 | 59429.8 | 53625.4 | 54587.5 |
| (26524) | Worst | 66400.4 | 64183.5 | 66014.5 | 65501.6 | 63608.6 |
| | Avg | 60349.3 | 60694.1 | 62526.7 | 58669.9 | 58616.2 |
| | Std. | 3571.35 | 2803.79 | 1808.7 | 3654.78 | 2691.54 |
| | Time | 0.72 | 0.85 | 349.21 | 64.88 | 57.24 |
| | Number | 2000 | 2000 | 2000 | 2000 | 2000 |

**Table 2.** The #of optimal solutions and average CPU time.

| Alg. | Best | Worst | Avg. | Std. | Avg. Time |
|---|---|---|---|---|---|
| **MCA** | 4 | 6 | 6 | 5 | 31.37 |
| **CA** | 2 | 0 | 0 | 0 | 35.10 |
| **GA** | 4 | 2 | 4 | 3 | 141.35 |
| **TS** | 0 | 2 | 0 | 2 | 0.5 |
| **SA** | 0 | 0 | 0 | 0 | 0.47 |

Table 1 shows the experimental results and comparison between MCA, CA, GA, TS, and SA. In this table, the results are given as best, worst, average solution, standard deviation, and CPU Time.
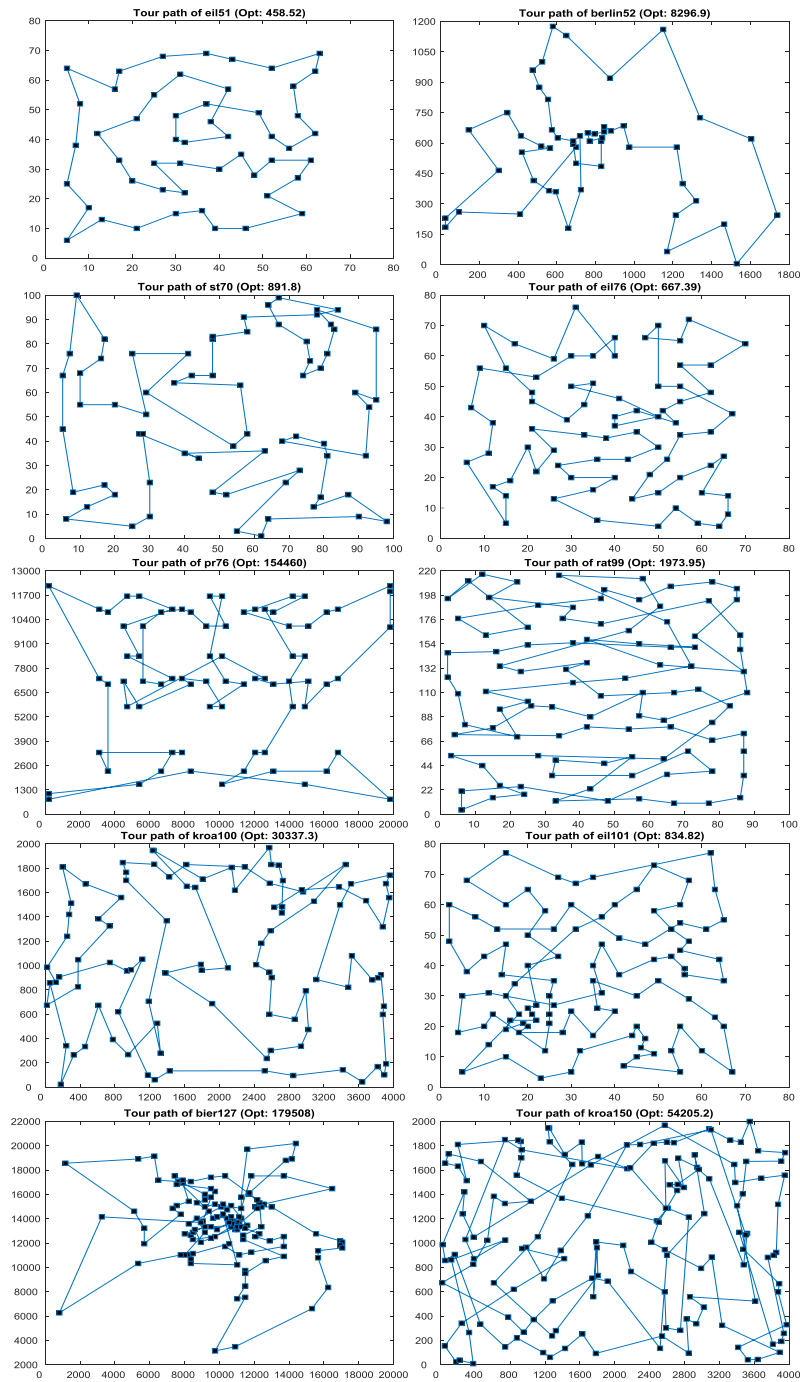
**Figure 2.** A set of optimal results found by the modified CA (MCA).

As inferred from Table 1, it can be observed that the quality of the MCA solutions is better compared to CA, GA, TS, and SA for 60% of all datasets. Besides, in Table 2, MCA finds 21 optimal, CA finds 2 optimal, GA finds 13 optimal, TS finds 4 optimal and SA finds never optimal solutions among 40 best results. Table 2 summarizes that MCA is superior to CA, GA algorithm, TS, and SA for 53% of all optimal solutions. MCA has low standard deviations among other algorithms. A low standard deviation specifies that the MCA is a more reliable and certain approach to find the optimal results. Lastly, MCA solves the TSP problem in reasonable times in comparison to other algorithms for all datasets.

In general, the experimental analysis shows that the MCA is a reliable and certain approach for solving the traveling salesman problem. This modified meta-heuristic gives better results and reasonable standard deviation as compared to the test meta-heuristics. Figure 2 shows a set of optimal results found by the MCA on the benchmark datasets.

## 5. CONCLUSION

In recent decades, solving discrete problems via modern meta-heuristics is a popular research area. In this paper, the MCA is applied to the symmetric TSP instances. To evaluate the performance of MCA, it has been tested on ten benchmark test datasets. The experimental results show that the MCA can find better solutions compared to the camel algorithm (CA), genetic algorithm (GA), simulated annealing (SA), and tabu search (TS) for 60% of all datasets and 53% of all optimal solutions. As CPU time is considered, MCA is considerably fast (31.37 secs.) to find optimal solutions. In future works, MCA can be compared with other meta-heuristics to evaluate performance analysis in scheduling, assignment, timetabling, routing, and many other combinatorial problems.

## ACKNOWLEDGEMENTS

## REFERENCES

[1] Parejo, J.A., Ruiz-Cortés, A., Lozano, S., and Fernandez, P., (2012). Metaheuristic optimization frameworks: a survey and benchmarking. Soft Computing, 16, 527–561. https://doi.org/10.1007/s00500-011-0754-8.

[2] Cárdenas-Montes, M., (2018). Creating hard-to-solve instances of travelling salesman problem. Applied Soft Computing, 71, 268-276. https://doi.org/10.1016/j.asoc.2018.07.010.

[3] Yang, XS., (2010). Nature-inspired metaheuristic algorithms. United Kingdom (Bristol): Luniver Press.

[4] Gogna, A. and Tayal, A., (2013). Metaheuristics: review and application. Journal of Experimental & Theoretical Artificial Intelligence, 25(4), 503–526. http://doi.org/10.1080/0952813X.2013.782347.

[5] Rajpurohit, J., Sharma, T.K., Abraham, A., and Vaishali, (2017). Glossary of metaheuristic algorithms. International Journal of Computer Information Systems and Industrial Management Applications, 9, 181-205.

[6] Karaboga, D. and Basturk, B., (2007). A powerful and efficient algorithm for numerical function optimization: artificial bee colony (ABC) algorithm. Journal of Global Optimization, 39(3), 459–471.

[7] Hatamlou, A., (2018). Solving travelling salesman problem using black hole algorithm. Soft Computing, 22(24), 8167-8175. https://doi.org/10.1007/s00500-017-2760-y.

[8] Mirjalili, S., (2016). A sine cosine algorithm for solving optimization problems. Knowledge-Based Systems, 96, 120-133.

[9] Yazdani, M. and Jolai, F., (2016). Lion optimization algorithm (LOA): A nature-inspired metaheuristic algorithm. Journal of Computational Design and Engineering, 3(1), 24-36.

[10] Zheng, Y.J., (2015). Water wave optimization: a new nature-inspired metaheuristic. Computers & Operations Research, 55:1–11.

[11] Yildirim, A.E. and Karci A., (2018). Applications of artificial atom algorithm to small-scale traveling salesman problems. Soft Computing, 22(22), 7619-7631. https://doi.org/10.1007/s00500-017-2735-z.

[12] Feng, X., Liu, Y., Yu, H., and Luo, F. (2019). Physarum-energy optimization algorithm. Soft Computing, 23, 871–888. https://doi.org/10.1007/s00500-017-2796-z.

[13] Dorigo, M., Birattari, M., and Stutzle, T., (2006, Nov). Ant colony optimization. IEEE Computational Intelligence Magazine, 1(4), 28-39.

[14] Akça, M.R. (2011). Yapay arı kolonisi algoritması kullanılarak gezgin satıcı probleminin Türkiye'deki il ve ilçe merkezlerine uygulanması, Selçuk Üniversitesi Fen Bilimleri Enstitüsü, Konya.

[15] Bektas, T., (2006). The multiple traveling salesman problem: an overview of formulations and solution procedures. Omega, 34(3), 209-219.

[16] Ibrahim, M.K. and Ali, R.S., (2016). Novel optimization algorithm inspired by camel traveling behavior. Iraqi Journal for Electrical and Electronic Engineering, 12(2), 167-177.

[17] Ali, R.S., Alnahwi, F.M., and Abdullah, A.S., (2019). A modified camel travelling behavior algorithm for engineering applications. Australian Journal of Electrical and Electronics Engineering, 16(3), 176-186. https://doi.org/10.1080/1448837X.2019.1640010.

[18] Hassan, K.H, Abdulmuttalib, T.R., and Jasim, B.H., (2021, Feb). Parameters estimation of solar photovoltaic module using camel behavior search algorithm. International Journal of Electrical and Computer Engineering (IJECE), 11(1), 788-793.

[19] Burkard, R.E., Deineko, V.G., van Dal, R., van, J.A.A., Veen, der, and Woeginger, G.J., (1998). Well-solvable special cases of the traveling salesman problem: a survey. Society for Industrial and Applied Mathematics, 40(3), 496-546. https://doi.org/10.1137/S0036144596297514.

[20] Sahana, S.K., (2019). Hybrid optimizer for the travelling salesman problem. Evolutionary Intelligence, 12, 179–188. https://doi.org/10.1007/s12065-019-00208-7.

[21] Nagata, Y. and Soler, D., (2012). A new genetic algorithm for the asymmetric traveling salesman problem. Expert Systems with Applications, 39(10), 8947-8953. https://doi.org/10.1016/j.eswa.2012.02.029.

[22] Osaba, E., Yang, XS., Diaz, F., Lopez-Garcia, P., and Carballedo, R., (2016). An improved discrete bat algorithm for symmetric and asymmetric traveling salesman problems. Engineering Applications of Artificial Intelligence, 48, 59-71. https://doi.org/10.1016/j.engappai.2015.10.006

[23] Öncan, T., Altınel, İ.K., and Laporte, G., (2009). A comparative analysis of several asymmetric traveling salesman problem formulations. Computers & Operations Research, 36(9), 637-654.https://doi.org/10.1016/j.cor.2007.11.008.

[24] Malik, W., Rathinam, S., and Darbha, S., (2007). An approximation algorithm for a symmetric generalized multiple depot, multiple travelling salesman problem. Operations Research Letters, 35(6), 747-753. https://doi.org/10.1016/j.orl.2007.02.001.

[25] Asih, A.M.S., Sopha, B.M., and Kriptaniadewa, G., (2017). Comparison study of metaheuristics: empirical application of delivery problems. International Journal of Engineering Business Management, 9, 1-12. https://doi.org/10.1177/1847979017743603.

[26] Khanra, A., Maiti, M.K., and Maiti, M., (2015). Profit maximization of tsp through a hybrid algorithm. Computers & Industrial Engineering, 88, 229-236. https://doi.org/10.1016/j.cie.2015.06.018.

[27] Halim, A.H. and Ismail, I., (2019). Combinatorial optimization: comparison of heuristic algorithms in travelling salesman problem. Archives of Computational Methods in Engineering, 26, 367–380. https://doi.org/10.1007/s11831-017-9247-y.

[28] Szeto, W.Y., Yongzhong, W. and Ho, S.C., (2011). An artificial bee colony algorithm for the capacitated vehicle routing problem. European Journal of Operational Research, 215(1), 126-135. https://doi.org/10.1016/j.ejor.2011.06.006.

[29] Demiral, M.F. and Işik, A.H., (2020). Simulated annealing algorithm for a medium-sized tsp data. In: D. J. Hemanth and U. Kose (Eds), Artificial Intelligence and Applied Mathematics in Engineering Problems. ICAIAME 2019. Lecture Notes on Data Engineering and Communications Technologies, 43. Springer, Cham, pp. 457-465. https://doi.org/10.1007/978-3-030-36178-5_35.

*RESEARCH ARTICLE*

# THE EFFECTS of PH and HYDROGEN PEROXIDE CONCENTRATION on CHEMICAL OXYGEN DEMAND (COD) and COLOR REMOVAL FROM LEACHATE by ELECTRO-FENTON METHOD

Kasım ATMACA[1,], Nevzat BEYAZIT[2*]

[1]Ondokuz Mayıs University, Faculty of Engineering, Department of Enviromental Engineering, Samsun, kasim.atmaca@omu.edu.tr, ORCID: 0000-0002-6570-4127
[2]Ondokuz Mayıs University, Faculty of Engineering, Department of Enviromental Engineering, Samsun, nbeyazit@omu.edu.tr, ORCID: 0000-0002-8396-5996

## ABSTRACT

This study investigated how COD and color removal efficiencies from leachate changed with pH (2.5-4) and $H_2O_2$ (1000-3000 mg/L) by electro-Fenton method. Maximum COD and color removals were 68% and 69%, respectively, with electrical energy consumptions of 0.79 and 0.108 kWh/m$^3$. Since the removal efficiencies obtained could not meet the discharge limits in Turkey, it would be more appropriate to apply electro-Fenton together with other treatment methods to achieve higher COD and color removal efficiencies.

**Keywords:** *COD, Color, Electro-Fenton, Leachate, pH, Hydrogen peroxide*

## 1. INTRODUCTION

The leachate contains various toxic organic pollutants, ammonia nitrogen compounds, heavy metals due to the decomposition of solid wastes during their disposal in landfills and the effect of rainwater. Therefore, landfill leachate can cause severe hazards to the environment and public health in surface and groundwater. Although the characterization of leachate varies according to the amount of solid waste, its composition, humidity, age and climate of the landfill, seasonal weather changes, they are mostly characterized by high concentrations of dissolved organic carbon, chloride, conductivity and low heavy metal contents [1,2]. Because it contains high levels of pollutant components, leachate must be treated with economical and efficient methods before it is released into the environment.

Physical-chemical treatment processes such as chemical oxidation, membrane treatment, adsorption, coagulation-flocculation and adsorption are used individually or together with biological treatment processes [1]. Depending on treatment objectives, combinations of these methods can also be used. Most easily degradable organic substances in leachate can be efficiently removed by conventional biological treatment processes. Advanced oxidation processes (AOPs) such as Fenton ($Fe^{2+}/H_2O_2$), hydrogen peroxide with UV radiation ($UV/H_2O_2$), photo-Fenton ($Fe^{2+}/H_2O_2/UV$), ultraviolet (UV) are more efficient treatment technologies for removing degradation-resistant pollutants and colours [3]. Fenton technology is preferred because of its advantages, such as applicability and high efficiency [2]. Fenton processes, which are defined as the reactions of hydrogen peroxide ($H_2O_2$) with iron ions, can

effectively oxide organic or inorganic compounds [4]. Classical Fenton reactions occur as follows. In Fenton processes, $OH^\bullet$ radicals are generated by Equation 1 and serve as the first step for other Fenton reactions (Equations 1-6).

$$H_2O_2 + Fe^{2+} \rightarrow Fe^{2+} + OH^\bullet + OH^- \tag{1}$$

$$OH^\bullet + H_2O_2 \rightarrow HO_2^\bullet + H_2O \tag{2}$$

$$Fe^{3+} + HO_2^\bullet \rightarrow Fe^{2+} + H^+ + O_2 \tag{3}$$

$$Fe^{2+} + HO_2^\bullet \rightarrow Fe^{3+} + HO_2^- \tag{4}$$

$$Fe^{2+} + OH^\bullet \rightarrow Fe^{3+} + OH^- \tag{5}$$

$$Fe^{3+} + H_2O_2 \rightarrow Fe^{2+} + HO_2^\bullet + H^+ \tag{6}$$

Equations (1-3) form the cycle in which $O_2$ oscillates and Equations. Equations (4) and (5) serve as termination reactions. $OH^\bullet$ radicals, which have a standard potential of 2.80 V, can effectively take electrons from other materials and oxidize them. The pH range in which the Fenton process is effective is 2.8-3. Compared to $OH^\bullet$, $HO_2^\bullet$ radicals produced by the Fenton-like reaction are less effective at breaking down organic compounds [5]. Some disadvantages of Fenton processes are as follows: (i) Relatively high costs and risks associated with the storage, transportation, and transportation of $H_2O_2$ (ii) High amount of chemical to acidify effects to pH 2-4 and neutralize processed solutions before disposal (iii) Iron sludge accumulation the end of treatment, and (iv) General mineralization does not occur due to the formation of Fe (III) complexes via produced carboxylic acids, which $OH^\bullet$ radicals can not destroy [6].

The electro-Fenton method extends the Fenton process and is developing the traditional Fenton method [7,8]. Four types of Fenton processes can be performed. In Type 1, ferrous ions and hydrogen peroxide are generated by sacrificial electrodes. In Type 2, while ferrous ion is produced from the sacrificial anode, hydrogen peroxide is added externally (Eq. (7)).

$$Fe \rightarrow Fe^{2+} + 2e^- \tag{7}$$

In Type 3, hydrogen peroxide is produced using oxygen scattering cathodes, and ferrous ions are added externally. In Type 4, the hydroxyl radical is generated in an electrolytic cell using Fenton's reagent, and the ferrous ion is regenerated by reducing ferric ions on the cathode. Even if Type 4 seems attractive, $H_2O_2$ production is relatively slow because the solubility of oxygen in water is low, and the process efficiency is low at low pH (pH <3) values in the $H_2O_2$ production process dominated by acidic conditions [9].

Literature data indicate that advanced oxidation processes are effective methods for removing pollutants from leachate. For example, Altin [10] removed 94% of COD and 97% of color removal from leachate using the photo-electro-Fenton method. (COD: 2350 mg/L; pH: 3; $H_2O_2$: 3000 mg/L; current: 2.5 A; UV source: 4 watts time: 20 min). Sruthi et al. [11] obtained 88.6% COD removal from leachate with heterogeneous Fenton process (COD: 6160 mg/L; pH:3; $H_2O_2$: 0.03 molar and catalyst ($Fe^{2+}/Fe^{3+}$): 700 mg/L, leading a molar ratio $[H_2O_2]/[Fe^{2+}]$ of 2.64; pH: 3; time: 90 min), a

COD removal of 87.5% was achieved by heterogeneous EF process in the same study (pH: 3, Catalyst: 25 mg/L, Voltage: 4 V). Also, these research results showed that catalyst dosage, input pH and voltage values significantly affect the heterogeneous EF process efficiency. Also, the $BOD_5/COD$ ratio of the leachate increased from 0.03 to 0.52 after the Fenton treatment, indicating biodegradability increases [11]. In another study, 70% COD removal from the leachate was obtained by the Fenton process (COD: 2500 mg/L, pH: 2, $H_2O_2$: 0.187 mol/L and catalyst: 1745 mg/L, leading a molar ratio $[H_2O_2]/[Fe^{2+}]$ of 6; current density: 206 $A/m^2$ and inter-electrode gap: 1.8 cm, time: 150 min) [12]. Using the same method as Altin [10], Asaithambi et al. [2] achieved 100% color and 97% COD from leachate.

The present study constitutes the second stage of two-stage research conducted by us before [13]. Under optimum experimental conditions determined in the first stage, the effects of initial pH and $H_2O_2$ concentration on COD and color removal were revealed.

## 2. MATERIALS AND METHODS

### 2.1. Characteristics of Leachate

The leachate samples were taken from the landfill in Samsun. An average of 300 $m^3$ of leachate is produced daily at the site, and a waste of about 800-900 tons collected every day is discharged to the landfill. A representative analysis of the leachate used in the experiments was as follows: pH: 7.50-7.90, COD: 7150-9000 mg/L, conductivity: 20-40 mS/cm, and color: 2102-3596 Pt-Co.

### 2.2. Experimental Set-Up

EF experiments were done in a volume Plexiglass reactor of 860 $cm^3$ for EF times of 0-45 minutes. The experiments used two anodes (iron) and two cathodes (steel) (4.5 cm x 5.5 cm in dimension). The total activated anode surface area of the anodes was 94.64 $cm^2$. The anode and cathode materials were mounted with a monopolar connection before connecting to the power supply (30V, 6A). The electrochemical set-up is shown in Figure 1.
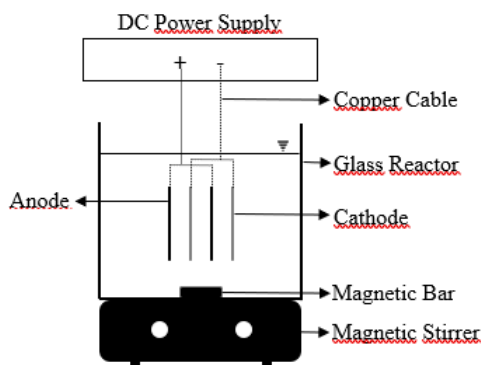


**Figure 1.** Schematic of the electrochemical set-up.

Experiments were carried out with 750 ml of wastewater at 250 rpm mixing speed. For Fenton reactions, hydrogen peroxide (35%) was added externally, while iron ions were obtained by dissolving the iron used as the anode in wastewater with the effect of current. Before each experiment, the oxide layers formed on the electrode surfaces were kept in concentrated hydrochloric acid (37% HCl) and

then rinsed with distilled water as required. NaOH and $H_2SO_4$ were used to adjust the wastewater pH to the desired values, and pH values were measured by an Orion 4 Star pH meter. Samples needed for COD and color measurements were taken at periodic intervals of 2.5, 5, 7.5, 10, 15, 20, 25, 30, 35, 40, and 45 minutes and centrifuged before necessary measurements were made. COD and color analyses were carried out with a Merck Spectroquant Nova 60A photometer.

## 2.3. Analytical System

The closed reflux colorimetric method was used to measure the chemical oxygen demand with a Merck Spectroquant Nova 60A model photometer. The Pt-Co method was used for color analysis [14]. COD removal efficiencies (Eq. 8) were calculated using:

$$\text{Removal efficiency (\%)} = \frac{C_0 - C_t}{C_0} \times 100 \tag{8}$$

Where $C_0$ represents the initial COD concentration (mg/L), $C_t$ represents the concentration of COD corresponding time (mg/L).

## 2.4. Calculations

Electrical energy consumptions were calculated by Eq. 9 [15].

$$E = \frac{U x I x t}{V} \tag{9}$$

Where E represents energy consumption ($kWh/m^3$), U denotes the voltage (V), I denotes current (A), t represents time (second), V represents wastewater volume (litre).

## 3. RESULTS AND DISCUSSION

### 3.1. Influence of pH

The initial pH is one of the main factors affecting the performance of electro-Fenton systems [4]. It is known that the optimum pH value is around 3 for these processes [16,17,18]. The effects of pH values ranging from 2.5 to 4 were investigated on COD and color removal efficiencies. COD removal was not obtained during the first 7.5 minutes (Figure 2a). At the end of the 10th minute, the COD removals were 19.7%, 27.7%, 18%, and 16% for pH values ranging from 2.5 to 4. Relatively high removal efficiencies were achieved for all pH values between the 10th and 30th minutes, indicating that hydroxyl radicals increased in the reactor with time. For pH: 3, a maximum COD removal efficiency of 68% was reached at the end of the 25th minute. At this minute, electrical energy consumption was 0.79 $kWh/m^3$. After the 30th minute, the removal efficiencies for all pHs decreased to zero. This case is an indication of the depletion of hydroxyl radicals in the reactor. The maximum removal efficiency was obtained at pH: 3, which was considered as optimum pH. Asaithambi et al. [2] reached a maximum COD removal efficiency of 97% with pH: 3, which was on the leachate treatment by the electro-Fenton. In another study by Atmaca [19], the maximum COD removal efficiency in the treatment of leachate by the electro-Fenton method was reached at pH: 3 and 30 minutes treatment time. Figure 2b shows the effect of different pH on color removal. As shown in Figure 2b, color removal at the end of the 5th minute reached a maximum for all pH. At the end of the 5th minute, the colour removals were 52%, 61%, 60%, 57% for pH ranging from 2.5 to 4. At this minute, energy consumptions were 0.120, 0.126, 0.116 and 0.126 $kWh/m^3$ for pH values ranging from 2.5 to 4. Color removal efficiencies decreased rapidly between the 5th and 10th minutes, indicating that hydroxyl

radicals in the reactor rapidly decreased. Figure 2a and Figure 2b show that the maximum COD and color removal efficiencies were acheved at pH 3, which was considered optimum.
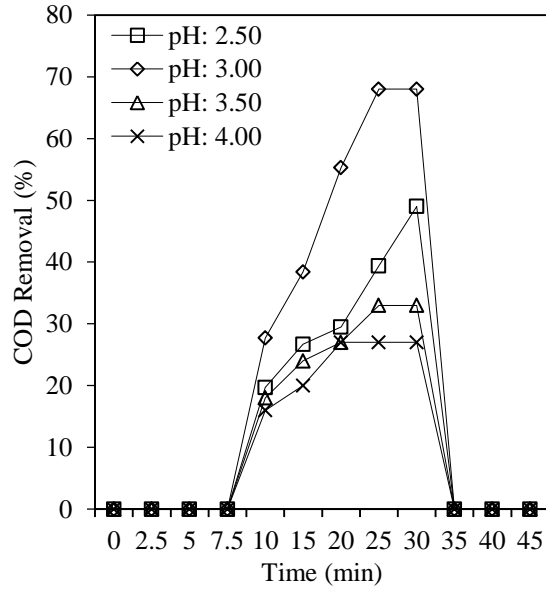


**Figure 2a.** The effect of pH on COD removal (Conditions: current density: 100 A/m$^2$, H$_2$O$_2$: 2000 mg/L, stirring rate: 250 rpm, inter-electrode gap: 1.5 cm).
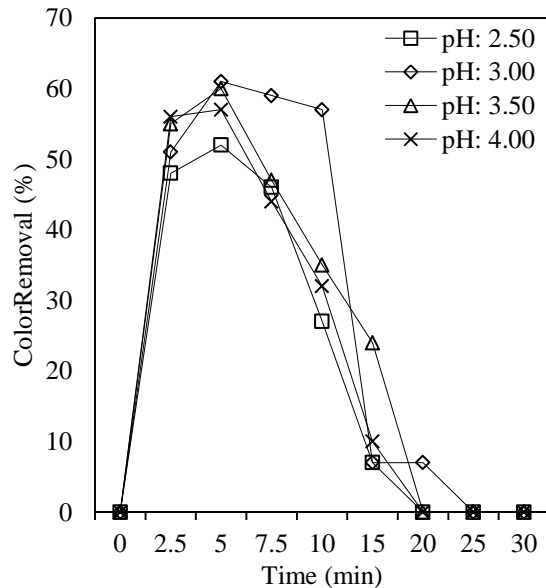


**Figure 2b.** The effect of pH on color removal (Conditions: current density: 100 A/m$^2$, H$_2$O$_2$: 2000 mg/L, stirring rate: 250 rpm, inter-electrode gap: 1.5 cm).

### 3.2. Influence of $H_2O_2$

The primary source for the generation of $OH^\bullet$ radicals is $H_2O_2$, and this chemical is critical in Fenton processes [5]. The effects of $H_2O_2$ concentrations ranging from 1000 to 3000 mg/L on COD and color removal were investigated. Figure 3a shows that a maximum COD removal efficiency of 68% was reached at the end of the 25th minute. At this minute, electricity consumption was 0.79 kWh/m$^3$. Figure 3a also shows a rapid increase in COD removals between the 10th and 25th minutes at optimum $H_2O_2$ concentration (2000 mg/L). At other concentrations, a slight increase or decrease in removal efficiencies was observed between these minutes. The reason for this is the increasing hydroxyl radicals over time. At $H_2O_2$ concentrations above 2000 mg/L, the removal efficiencies decreased. This case can be explained by the fact that the excess $H_2O_2$ chemical converts the hydroxyl radicals to the less reactive $HO_2^\bullet$ radicals (Eq. (2)). After the 25th minute, removal efficiencies decreased for all concentrations of hydrogen peroxide. As shown in Figure 3b, color removals increased for all concentrations during the first 5 minutes. At the end of the 7.5th minute, color removal efficiency reached a maximum of 69% for 2000 mg/L $H_2O_2$ with an energy consumption of 0.108 kWh/m$^3$. After 7.5th minutes, removal efficiencies decreased for all $H_2O_2$ concentrations.
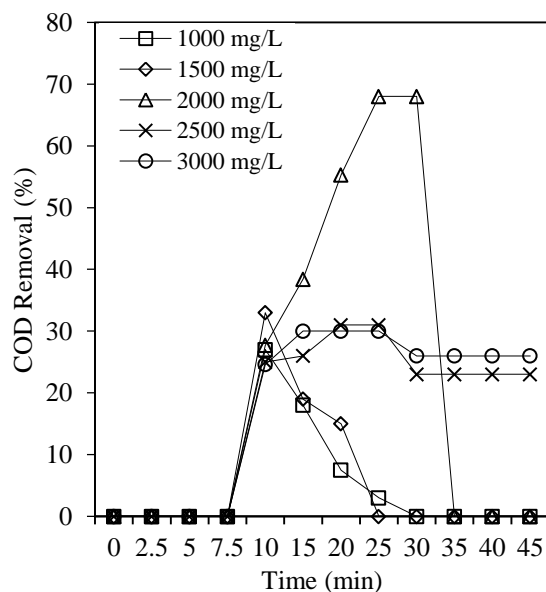


**Figure 3a.** The effect of $H_2O_2$ concentration on COD removal (Conditions: pH: 3, current density: 100 A/m$^2$, stirring rate: 250 rpm, inter-electrode gap: 1.5 cm).
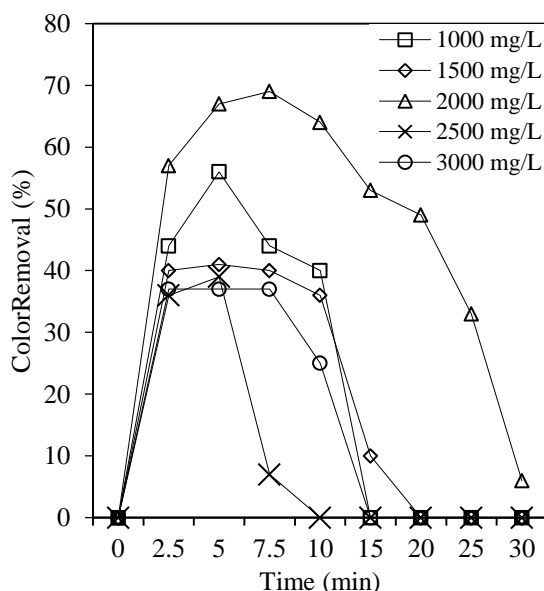
**Figure 3b.** The effect of $H_2O_2$ concentration on color removal (Conditions: pH: 3, current density: 75 A/m$^2$, stirring rate: 250 rpm, inter-electrode gap: 1.5 cm).

## 4. CONCLUSIONS

The results achieved can be summarized as follows:

$[H_2O_2]/[Fe^{2+}]$ molar ratios were 5.97 and 26.27 for maximum COD (68%) and color (69%) removal, respectively. These values show that relatively more $H_2O_2$ was consumed for color removal, and a total treatment cost of 71 USD/m$^3$ was calculated.

It is expected that COD will be removed with lower efficiency than color removal due to the breakdown of intermediate and by-products generated in wastewater treatment processes. However, this difference was not observed in this study, indicating that the color components in the leachate used in this study are resistant to removal such as COD. Physical removal of possible colloidal elements in the leachate before the electro-Fenton process should be considered a fundamental approach.

Higher color removal efficiencies were obtained in the first minutes, as the increase in the dissolved iron ions from the anode over time caused the wastewater to become colored.

The relatively high $H_2O_2$ concentrations consumed may limit the use of this method for the treatment of leachate consisting of high levels of organic compounds. Therefore, evaluating the electro-Fenton method as a pre-treatment process, especially before the biological treatment of large volume leachate, would be more beneficial and economical than using it alone.

## ACKNOWLEDGEMENTS

## REFERENCES

[1] Oulego, P., Collado, S., Laca, A. and Diaz, M. (2016), Impact of leachate composition on the advanced oxidation treatment, Water Research, 88, 389-402.

[2] Asaithambi, P., Govindarajan, R., Yesuf, M.B. and Alemayehu, E. (2020), Removal of color, COD and determination of power consumption from landfill leachate wastewater using an electrochemical advanced oxidation processes, Separation and Purification Technology, 233, 115935.

[3] Solmaz, S.K.A., Birgul, A., Ustun, G.E and Yonar, T. (2006), Color and COD removal from textile effluent by coagulation and advanced oxidation process, Coloration Technology, 122, 102-109.

[4] Nidheesh, P.V and Gandhimathi, R. (2012), Trends in electro-Fenton process for water and wastewater treatment: An overview, Desalination, 299, 1-15

[5] He, H and Zhou, Z. (2017), Electro-Fenton process for water and wastewater treatment, Critical Reviews in Environmental Science and Technology, 47(21), 2100-2131.

[6] Sires, I and Brillas, E. (2018), Laboratori d'Electroquı´mica dels Materials i del Medi Ambient, Departament de Quı´mica Fı´sica, Facultat de Quı´mica, Universitat de Barcelona, Martı´ i Franque`s. Barcelona, Spain, 1-11.

[7] Liu, X., Zhou, Y., Zhang, J., Luo, L., Yang, Y., Huang, H., Peng, H., Tang, L. and Mu, Y. (2018), Insight into electro-Fenton and photo-Fenton for the degradation of antibiotics: Mechanism study and research gaps, Chemical Engineering Journal, 347, 379-397.

[8] Martinez-Huitle, C.A. and Brillas, E. (2009), Decontamination of wastewaters containing synthetic organic dyes by electrochemical methods: A general review, Applied Catalysis B: Environmental, 87(3-4), 105-145.

[9] Babuponnusami, A. and Muthukumar, K. (2014), A review on Fenton and improvements to the Fenton process for wastewater treatment, Journal of Environmental Chemical Engineering, 2(1), 557-572.

[10] Altin, A. (2008), An alternative type of photo-electro-Fenton process for the treatment of landfill leachate, Separation and Purification Technology, 61(3), 391-397.

[11] Sruthi, T., Gandhimathi, R., Ramesh, S.T. and Nidheesh, P.V. (2018), Stabilized landfill leachate treatment using heterogeneous Fenton and electro-Fenton processes, Chemosphere, 210, 38-43.

[12] Wang, Z., Li, J., Tan, W., Wu, X., Lin, H. and Zhang, H. (2019), Removal of COD from landfill leachate by advanced Fenton process combined with electrolysis, Separation and Purification Technology, 208, 3-11.

[13] Atmaca, K. and Beyazit, N. (2020), The effect of cathode material, current density and anode-cathode gap on the COD and color removal from leachate by electro-Fenton method, Desalination and Water Treatment, 201, 431-437.

[14] APHA, AWWA, WEF. (2017), Standard Methods for the examination of water and wastewater, 23rd ed., American Public Health Association, American Water Works Association and Water Environment Federation, Washington DC.

[15] Alaton, I., Kabdaslı, I., Hanbaba, D. and Kuybu, E. (2008), Electrocoagulation of a real reactive dyebath effluent using aluminum and stainless steel electrodes, Journal of Hazardous Materials, 150(1), 166-173.

[16] Hammami, S., Oturan, N., Bellakhal, N., Dachraoui, M. and Oturan, M.A. (2007), Oxidative degradation of direct orange 61 by electro-Fenton process using a carbon felt electrode: Application of the experimental design methodology, Journal of Electroanalytical Chemistry, 610(1), 75-84.

[17] Ma, L., Zhou, M., Ren, G., Yang, W. and Liang, L. (2016), A highly energy-efficient flow-through electro-Fenton process for organic pollutants degradation, Electrochimica Acta, 200, 222-230.

[18] Hsueh, C.L., Huang, Y.H., Wang, C.C. and Chen, C.Y. (2005), Degradation of azo dyes using low iron concentration of Fenton and Fenton-like system, Chemosphere, 58(10), 1409-1414.

[19] Atmaca, E. (2009), Treatment of landfill leachate by using electro-Fenton method, Journal of Hazardous Materials, 163(1), 109-114.

RESEARCH ARTICLE

# INVESTIGATION of the THICKNESS THINNING for THE PORCELAIN TILES and THEIR APPLICABILITY

Ahmet VURAL[1], Nihal DERİN COŞKUN[2], C. Eren IŞIK[3], Fuat ÇELİK[4], İskender IŞIK[5]

[1] Kaleseramik R&D Center, Çanakkale, ahmetvural@kale.com.tr, ORCID:0000-0003-1282-371x
[2] Ordu University, Faculty of Fine Arts, Department of Ceramic and Glass, Ordu, nihal.dcoskun@dpu.edu.tr, ORCID: 0000-0002-3024-9443
[3] Kütahya Dumlupınar University Faculty of Fine Arts, Department of Handicraft Design and Production, Kütahya, eren.isik@dpu.edu.tr, ORCID:0000-0002-1129-2497
[4] Kütahya Dumlupınar University, Faculty of Engineering, Department of Metallurgical and Material Engineering, Kütahya, fuat.celik@dpu.edu.tr, ORCID:0000-0002-8892-080x
[5] Kütahya Dumlupınar University, Faculty of Engineering, Department of Metallurgical and Material Engineering, Kütahya, iskender.isik@dpu.edu.tr, ORCID:0000-0002-9523-2837

## ABSTRACT

Porcelain tiles are building materials that offer aesthetics and advantages to the user by using ceramic raw materials and additives at high pressure. Energy and labor are spent on raw materials used for production, raw material transportation and transportation until they reach the customer after they become finished products. These high costs reduce competitiveness in the market. In this study, it has been studied on the thinning of porcelain tiles to reduce the cost and to take advantage of transportation. Two different size tiles, which are the most preferred in the market, were selected. In the study, the possibilities of making thinner and environmentally friendly tiles were investigated by characterizing the selected porcelain tile bodies. Çanakkale Saribeyli Region bentonite was used in the body instead of Istanbul clay at the rates of 0.5%, 1%, 1.5%, 2% and 2.5% by weight, respectively. The body recipes, which were prepared in standard thickness and thinned by 0.5 mm, were fired at 1185 °C temperature. Shrinkage, water absorption, color and mechanical tests of the studied compositions were carried out. As a result of the study, the tile thickness thinning process was carried out in industrial trials in accordance with TSE standards, supported by laboratory test results, and the advantages it provides for transportation cost, environment and human health were demonstrated.

**Keywords:** *Porcelain Tile, Bentonite, Thin Tile*

## 1. INTRODUCTION

Based on the data from the report published by T.R. Ministry of Industry and Technology in 2020 for the ceramic sector, Turkey exports ceramic flooring materials to 113 countries and is ranked at number 9 in the world [1]. Products that are classified as ceramic flooring materials can be divided into three sub-categories of floor tile, wall tile and porcelain tile [2]. In 2021, about ~48 million $m^2$ of products have been exported in this large sector in which porcelain tiles provide an advantage with regard to water absorption, colour, surface texture and dimension and are also preferred from an

aesthetic standpoint [3]. The facts that they are especially resistant against seasonal changes especially for outdoor surfaces and that they have high strength, resistance to wear, chemicals and staining are among the primary reasons for this preference. Porcelain tiles that are defined as strong tiles with water absorption of below 0,5 % are comprised of raw materials such as clay (%30-40), feldspar (%45-50), quartz sand (%10-15) and glass-ceramic, frit and pigments [4-5].

The raw materials used in porcelain tiles should contain minimum amount of iron oxide since the impact of the colouring pigment on the body is subject to the whiteness of the body. Clays provide wet and dry strength to the bodies by providing plasticity to ceramic bodies while also giving colour to the fired product based on the impurities they contain [6]. Feldspars used as fluxing agents generate a reaction at low temperatures thus reducing the sintering temperatures. Quartz is added to the body as an actual component or as an addition component coming from clay and feldspar. The wide particle size provides resistance against cracks during drying and prevents pyro plastic deformation by generating a skeleton web during firing. It reduces dry shrinkage of the body thus controlling the thermal expansion in addition to the viscosity of the melt at high temperatures [7].

The necessity to manufacture the products based on the design recipe in the ceramic sector along with the requirement for the continuity of raw material procurement limits competitive strength. Thus, working on alternative raw materials gives an edge to the manufacturer. When the compositions of the recipes and ceramic production processes are taken into consideration, clays are the primary raw materials used in the production of ceramic coating flooring products. And it also significantly affects the end product characteristics. These raw materials mostly arrive via road transport and hence make an impact on production costs [8].

In the present study, bentonites of the Çanakkale Sarıbeyli Region were used at the facility in the Çanakkale Region instead of Şile clays. Bentonite is a raw material that increases plasticity and dry strength due to its alumina silicate structure, its binding characteristic in ceramic as well as temperature resistance [9]. This high water absorption characteristic of bentonites lead to high plasticity and it is observed that clays lose their plasticity at moisture levels of below 5 % [10-11]. In the light of all this data, Çanakkale bentonites were used as an alternative to the clay group of materials in the recipe for the thinning of porcelain tiles. It was aimed in the study to reduce transportation and raw material costs in addition to providing market advantage in export and import. In addition, it is known that carbonates which enter the ceramic body with the raw materials disintegrate at different temperatures based on the type of the metal oxide they are bound to leading to the transformation to metal oxide and $CO_2$ [12]. The reduction of $CO_2$ release during porcelain tile production also provided an advantage with regard to environmental friendliness in the present study.

## 2. GENERAL

### 2.1. Identification of the Properties of Clays Used in Porcelain Tile Production

Çanakkale region Sarıbeyli bentonite which is closer to Istanbul clays with regard to alternative production was used during the study with the aim of thinning the porcelain tiles and reducing costs. Bentonite tile was preferred since it has become an in-demand material used in production recipes due to its high-water absorption property and strength increasing effect. Chemical, mineralogical and physical tests were carried out. The bentonite used in the study was formed as a result of the decomposition of the volcanic ash, tuff and lava rich in calcium and magnesium and clays predominant in montmorillonite [13]. The characteristics of clays were examined in order to identify

the amount of bentonite in the recipe and chemical analyses were conducted on the clays for this purpose the results of which are presented in Table 1. XRF analyses were carried out via X-ray fluorescence spectrometer using the Panalytical Axios brand device.

**Table 1.** XRF chemical analysis results for Sarıbeyli Bentonite and Clay 2 (By weight %).

| SAMPLE NAME-INFORMATION | SARIBEYLI BENTONITE | CLAY 2 |
|---|---|---|
| L.O. I | 5,67 | 5,26 |
| $SiO_2$ | 71,3 | 70,11 |
| $Al_2O_3$ | 14,18 | 17,17 |
| $TiO_2$ | 0,3 | 0,8 |
| $Fe_2O_3$ | 1,55 | 2,48 |
| CaO | 2,18 | 0,36 |
| MgO | 2,14 | 0,6 |
| $Na_2O$ | 1,43 | 0,26 |
| $K_2O$ | 1,03 | 2,8 |
| TOTAL | 99,78 | 99,84 |

L.O.I: Lost on ignition

Rheological measurements were made following the chemical analyses which are presented in Table 2. The density, viscosity and over sieve properties were examined for the Çanakkale region Sarıbeyli bentonite in sludge form prior to granulation. The litre weight of the sludge affects the energy consumed by the spray dryer while the over sieve particle size is observed to change the particle size of the granule. Fine particle size distribution of the granule provides ease of operation during shaping. It makes an impact on the transportation of the sludge mixture prepared by taking into consideration the flow behaviour and the energy at the time of granulation.

**Table 2.** Rheological Properties of Sarıbeyli Bentonite and Clay 2.

| RHEOLOGICAL PROPERTY | SARIBEYLİ BENTONITE | CLAY 2 |
|---|---|---|
| Sludge Litre Weight (gr/lt) | 1282 | 1486 |
| Viscosity/ T $^0$C(sn) | YOK | 21 |
| Over Sieve (63 μm) (%) | 1,81 | 2,19 |
| Grinding Time (min) (dk) | 44 | 17 |

The mineralogical analysis of Sarıbeyli Bentonite was performed using a diffractometer device while the CuKα 1.5406$^o$A while Celerator detector was used for radiation and X'. It can be observed when Tables 3 and 4 are examined that the primary phase in Sarıbeyli bentonite is montmorillonite. In addition, the main structure is comprised of cristobalite, feldspar and quarts at various ratios [14]. High montmorillonite affects the pouring characteristic, and these values support the properties provided in Table 2.

**Table 3.** Quantitative XRD mineralogical results for Sarıbeyli Bentonite.

| PHASE | (%) |
|---|---|
| MONTMORILLONITE | 58 |
| CRISTOBALITE | 21 |
| FELDSPAR | 9 |
| CALCIDE | 5 |
| ZEOLITE | 2 |
| QUARTZ | 2 |
| OTHER | 3 |
| TOTAL | 100 |

The XRD analysis results indicate that montmorillonite ratio is 5 times greater in bentonite compared with clay. Montmorillonite phase provides strength. The feldspar amount of Sarıbeyli Bentonite was observed to be about 3 times greater compared with Clay 2. The feldspar pgase helps in reducing water absorption thanks to its fluxing property. It was determined based on the phase ratios presented in Table 4 that this clay has an illitic and caolinitic with a mixed clustered structure and a 3 layered structure. These characteristics may result in the formation of anorthite at high temperatures in addition to suitability for tile production.

**Table 4.** Minerological Results for Clay 2 via Quantitative XRD (By weight %).

| PHASE | % | PHASE | % |
|---|---|---|---|
| MONTMORILLONITE | 10,38 | ILLITE | 9,76 |
| CAOLENITE | 36,28 | QUARTZ | 36,43 |
| FELDSPAR | 2,55 | OTHER | 4,6 |
| | | TOTAL | 100 |

## 2.2. Porcelain tile recipe studies prepared using Sarıbeyli Bentonite

Çanakkale region Sarıbeyli Bentonite was used in place of the Istanbul clay used in porcelain tile recipes at the Çanakkale Ceramic tile factories at ratios of 0,5-1-1,5-2 and 2,5 % by weight. Table 5 shows the raw materials used by weight % and their ratios.

**Table 5.** Porcelain tile recipes prepared using Sarıbeyli Bentonite (by weight %).

| Recipe Name-Information | STANDART RECIPE % | RECIPE 1 (R1) % | RECIPE 2 (R2) % | RECIPE 3 (R3) % | RECIPE 4 (R4) % | RECIPE5 (R5) % |
|---|---|---|---|---|---|---|
| FIRED GROG | 6,20 | 6,20 | 6,20 | 6,20 | 6,20 | 6,20 |
| KAOLINE 1 | 7,00 | 7,00 | 7,00 | 7,00 | 7,00 | 7,00 |
| CLAY 1 | 0,80 | 0,80 | 0,80 | 0,80 | 0,80 | 0,80 |
| KAOLINE 2 | 10,00 | 10,00 | 10,00 | 10,00 | 10,00 | 10,00 |
| FELDSPAR | 30,00 | 30,00 | 30,00 | 30,00 | 30,00 | 30,00 |
| KAOLINE 3 | 7,00 | 7,00 | 7,00 | 7,00 | 7,00 | 7,00 |
| CLAY 2 | 18,00 | 17,50 | 17,00 | 16,50 | 16,00 | 15,50 |
| CLAY 3 | 21,00 | 21,00 | 21,00 | 21,00 | 21,00 | 21,00 |
| SARIBEYLİ BENTONITE | 0 | 0,50 | 1,00 | 1,50 | 2,00 | 2,50 |

| TOTAL | 100 | 100 | 100 | 100 | 100 | 100 |
|---|---|---|---|---|---|---|

**Table 6.** Rheological properties of the porcelain tile recipe prepared using Sarıbeyli Bentonite.

| Recipe Name-Information | UNIT | STANDART RECIPE | R 1 | R 2 | R 3 | R 4 | R 5 |
|---|---|---|---|---|---|---|---|
| Sieve Balance (+ 45 μm) | (%) | 4,37 | 4,31 | 4,31 | 4,32 | 4,3 | 3,28 |
| Density | (gr/lt) | 1685 | 1685 | 1685 | 1678 | 1670 | 1665 |
| Flow Time | (sec) | 20 | 45 | 45 | 58 | 62 | 69 |
| Grinding Time | (min) | 28 | 31 | 32 | 34 | 36 | 38 |

The mixtures were prepared by grinding in ball mills with at laboratory scale with a 45 μm over sieve balance of 4-4,5 %. Sludges close to the standard recipe with a density of ~1685 g/lt were dried at 120ºC in the stove and after which they were reground in agate mortar with the granule having a humidity ratio of 5 % shaped in laboratory presses under a pressure of 450 kg/cm$^2$. All samples were sintered at the Çanakkale Ceramic tile factories for a period of 45 minutes in ovens working with dimensions of 45x45 at 1185ºC. As can be seen in Figure 1, the prepared samples were obtained in the laboratory environment, however Recipe 2 with 1 % additive that had the best result was manufactured in two dimensions of 60x60 cm and 15x60 cm which have the greatest customer demand and the cost and thickness calculations were made for these samples.



**Figure 1** Fired porcelain tile tablets at 1185ºC

Konika Minolta brand device for CIALab colour system and colour identification was used in the study in addition to the Gabrielli brand vacuum device used in water absorption vacuum method. The properties that the porcelain tile bodies should have in accordance with ISO 10545 standards were used and the values were measured based on these standards [15].

## 3. RESULTS AND DISCUSSION

Adverse impacts on rheology were observed in the recipe behaviours of the montmorillonite structure in the quantitative XRD results of bentonite. Since montmorillonite structure which has an adverse impact on rheology displays a positive behaviour with regard to strength in construction, it enables tile thinning and the reduction of clay use in the recipes.

Water absorption test was conducted for these composition studies using the vacuumed water

absorption test method. It was observed when bentonite was used at ratios of 0,5 % and 1 % that the maximum 0,5 % water absorption target is reached for glazed granite porcelain tiles. It was also observed that the shrinkage is increased due to its magnesium content when used at ratios of above 1,5 %.

**Table 7.** Tablet shrinkage, size, water absorption characteristics of the prepared porcelain tile recipes.

| Recipe Name-Information | UNIT | STANDART RECIPE | R 1 | R 2 | R 3 | R 4 | R 5 |
|---|---|---|---|---|---|---|---|
| Tablet Biscuit Size average | mm | 46,36 | 46,32 | 46,32 | 46,25 | 46,23 | 46,19 |
| Shrinkage average | % | 7,63 | 7,71 | 7,71 | 7,85 | 7,89 | 7,97 |
| Vacuum method Biscuit Water Absorption | % | 0,02 | 0 | 0 | 0,02 | 0 | 0 |

As is shown in Table 8, bentonite was added to the glazed granite recipes at various different ratios and firing process was carried out. Afterwards, colour value measurements were taken for the fired tablets and the L*, a*, b* values were compared. Based on the colour value results for the Standard Recipe and the recipes including bentonite, it can be seen from Table 8 and Figure 1 that ; (L+) whiteness values changed at very small ratios such as <%0,4, (a+) redness value increased slightly, that the highest change was observed in the shift from yellowness (b+) to blueness (b-) but that these changes did not reach 1 % and hence they cannot affect production.

**Table 8.** L*, a*, b* measurement values for the prepared porcelain tile tablet samples .

| | SG STD | R 1 | R 2 | R 3 | R 4 | R 5 |
|---|---|---|---|---|---|---|
| L | 49,77 | 49,72 | 49,57 | 49,41 | 49,36 | 49,34 |
| a | 4,05 | 4,09 | 4,13 | 4,24 | 4,25 | 4,31 |
| b | 14,17 | 13,37 | 13,38 | 13,65 | 13,59 | 13,57 |

Bentonite was tested at different ratios in glazed granite recipes under laboratory conditions. It was observed based on the acquired results that 1 % Bentonite results were positive for the glazed granite masse Recipe. Operation with 1 % bentonite was continued based on the evaluation of the shrinkage, water absorption and colour results. Glazed granite masse mixture was prepared with 1 % bentonite.

**Table 9.** Thinning goals for 60x60 and 15x60 tiles.

| DIMENSION (cm) | 60 x 60 | | 15 x 60 | |
|---|---|---|---|---|
| WORKING GOAL | STANDARD THICKNESS | AIMED THICKNESS | STANDARD THICKNESS | AIMED THICKNESS |
| THICKNESS (mm) | 9,1 | 8,6 | 9 | 8,5 |

**Table 10.** Dry and fired strength values for the prepared recipes.

| | STANDARD 60 x 60 | R 2 60 x 60 | STANDARD 15 x 60 | R 2 15 x 60 |
|---|---|---|---|---|
| **DRY STRENGTH (kg/cm$^2$)** | 16,22 | 15,12 | 18,12 | 17,95 |
| **FIRED STRENGTH (kg/cm$^2$)** | 549,36 | 578,79 | 598,00 | 597,9 |

The dry and fired strength measurements were conducted for the prepared 1 % bentonite containing masse tiles and the standard tiles. While dry strength was measured as 16,22 kg/cm$^2$ at 60 x 60 dimension and standard thickness, fired strength was measured as 549,36 kg/cm$^2$. Dry strength decreased to 15,12 compared with the standard for the 1 % bentonite containing tile at 60 x 60 dimension subject to thinning. Fired strength increased in comparison with the standard fired strength reaching a value of 578,79 kg/cm$^2$. While dry strength was measured as 18,12 kg/cm$^2$ for 15 x 60 dimension at standard thickness, fired strength was measured as 598 kg/cm$^2$. Dry strength was measured as 17.95 kg/cm$^2$ for 15 x 60 dimension with 1 % bentonite whereas fired strength was measured as 597,9.

**Table 11.** Water absorption results for the prepared 1 % bentonite Recipe 2 and standard recipes.

| | 60X60 Standard | 60X60 R 2 | 15X60 Standard | 15X60 R 2 |
|---|---|---|---|---|
| **VACUUM WATER ABS. AVERAGE (%)** | 0,43 | 0,29 | 0,23 | 0,08 |

The vacuum water absorption results are presented for the tile samples of 1 % bentonite masse at dimensions of 60 x 60 and 15 x 60 after firing with the standard masse. Vacuum water absorption for 60 x 60 dimension was measured for the standard tile as 0,43. Vacuum water absorption for thinned 1 % bentonite 60 x 60 tile was measured as 0,29 which is lower than that of the standard. Whereas standard vacuum water absorption value was measured as 0,23 for the tile with dimensions of 15 x 60. Vacuum water absorption was measured as 0,08 for the 15 x 60 tile with 1 % bentonite.

Figures 2 and 3 show the phase analyses for the standard porcelain tile and the samples with the best results with regard to thickness, water absorption, strength, shrinkage, colour values and cost. These results indicated that there is illite, kaolinite, albite, quartz, orthoclase and bentonite in the structure. The quartz, albite and anorthite phase formations differ in the structure, while a slight decrease takes place in the quartz ratio intensity, it is observed in Recipe 2 that the formation of multiple phases has increased [16].
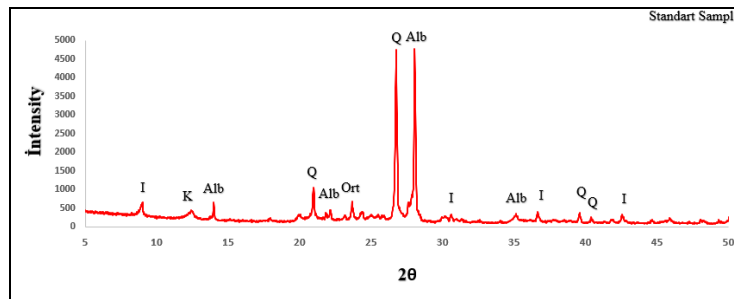
**Figure 2.** Standard porcelain tile masse XRD results (I: Illite, K: Kaolinite, Alb: Albite, Q: Quartz, Ort: Orthoclase B: Bentonite).
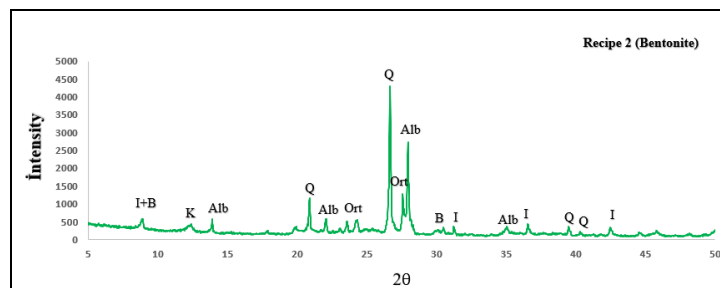


**Figure 3.** XRD results for Recipe 2 prepared using Sarıbeyli bentonite (I: Illite, K: Kaolinite, Alb: Albite, Q: Quartz, Ort: Orthoclase B: Bentonite).

Table 12 presents the thermal expansion analysis results which indicates that the data obtained from the XRD analyses have been met and that thermal changes have occurred in the structure following the formation of the change in the feldspars and multiple albite, orthoclase and quartz peaks. Moreover, it can also be seen from Table 12 that thermal expansion has decreased subject to the increase in the anorthite formation at high temperatures due to the greater montmorillonite ratio compared with clay 2 in bentonite use [17-18].

**Table 12.** Thermal expansion results for the prepared 1 % bentonite Recipe 2 and the standard recipes.

|  | STD | R 2 |
|---|---|---|
| DLM$\alpha$400(kg/cm$^2$) | 75,14 | 74,83 |
| DLM$\alpha$500(kg/cm$^2$) | 78,31 | 77,81 |
| DLM$\alpha$600(kg/cm$^2$) | 86,15 | 85,56 |

## 4. CONCLUSION

It was determined in the present study that tile thinning can be conducted in glazed porcelain tiles using bentonite. It was observed that the use of bentonite at ratios of over 1 % have various adverse impacts on flow and shrinkage behaviours. Whereas it was observed for bentonite use of 1 % and

below that values such as strength and water absorption have been met.

A total of 120 tiles of 60 x 60 and 43,2 $m^2$ can be carried in one palette whereas this number increased up to 128 tiles of 46,08 $m^2$ after the present study. Carrying about 22-25 palette tiles in an average transportation vehicle, it thus provides an opportunity to carry 72 $m^2$ more tiles which correspond to 6 % on average. Sales advantage is thus attained by reducing costs per $m^2$ through transporting more tiles. By increasing the quantity shipped at one time, the goods will reach the consumer more quickly and in a timely manner. 6 % less masse is required by reducing the masse amount through decreasing thickness and thus reducing the amount of masse used per 1 $m^2$. By using in the Sarıbeyli Bentonite Recipe instead of 1%, Clay 2 the distance will be reduced by about 8 times. In addition, transportation labour will decrease as well as the exhaust gases from the vehicles thereby reducing pollution. It was determined that it is possible to reduce the porcelain tile thickness by 5 % through the utilization of 1 % by weight bentonite instead of Istanbul clays. A decrease of about 8,1 % obtained for the recipe prepared using Sarıbeyli bentonite instead of Istanbul clay through the reduction of tile-thickness by 5 %.

Savings in both transportation and raw material cost will provide significant market advantages to the manufacturing company. Moreover, the fact that bentonite raw material is transported from a distance that is about ten times shorter will reduce $CO_2$ emissions thus providing a more superior contribution for human health compared with the reduction in costs.

## ACKNOWLEDGMENTS

## REFERENCES

[1]  [T.C. Sanayi ve Teknoloji Bakanlığı Seramik Sektörü Raporu, Sanayi Genel Müdürlüğü, Sektörel Raporlar ve Analizler Serisi. 2020.

[2]  Tarhan M., Tarhan B., (2019), Sırlı Porselen Karo Üretimi için Alternatif Hammadde Olarak Eşme/Uşak Feldspatı, AKU J. Sci. Eng. 19. 2019. 025702 (429-438),

[3]  https://www.serfed.com/istatistik

[4]  Biffi, G. (1999), Porcelain stoneware - production manual and methods of use, Gruppo Editoriale Faenza Editrice S.p.A., Faenza.

[5]  Zanelli, C., Raimondo, M., Dondi, M., Guarini, G. ve Tenorio Cavalcante, P. M. (2004), "Sintering mechanisms of porcelain stoneware tiles", Qualicer, 247-259.

[6]  Sanchez, E., Orts, M. J., Garcıa-Ten, K., Cantavella, V., (2001), Porcelain tile composition effect on phase formation and end product, Am. Ceram. Soc. Bull., 80 (6), 43-49.

[7]    Carty W. M. Senapatı U., (1998), Porcelain-raw materials, processing, phase evolution, and mechanical behaviour, J. Am. Ceram. Soc., 81 (1), 3- 20.

[8]    https://www.serfed.com/upload/ihracatrakamlari/SERAM%C4%B0K%20SEKT%C3%96R%C3%9C%20MAKRO%20PAZAR%20ARA%C5%9ETIRMASI%20RAPORU-2017-03.pdf

[9]    Akar, A. (1987), Endüstriyel Hammaddeler ve Zenginleştirme Yöntemleri, Dokuz Eylül Üniversitesi Yayın No: 142, İzmir, 145-163. 1987.

[10]   https://www.esan.com.tr/tr/uretim-urunleri/bentonit

[11]   İpekoğlu, B., Kurşun, İ., (1997). Türkiye Bentonit Potansiyeline Genel Bir Bakış.

[12]   2.Endüstriyel Hammaddeler Sempozyumu, (s. 51-57). İzmir

[13]   Çetin, B., (2015), Tokat-Reşadiye Bölgesi Bentonitinin Duvar Karosu Bünyelerinde Kullanılabilirliğinin Araştırılması, İstanbul Teknik Üniversitesi FBE, Metalurji ve Malzeme Mühendisliği Anabilim Dalı, Yüksek Lisans Tezi

[14]   https://www.mta.gov.tr/v3.0/bilgi-merkezi/bentonit

[15]   Çoban, F., (1999), Ayvacık (Çanakkale) bentonit yataklarındaki baydellit oluşumu, Türkiye Jeoloji Bülteni, Cilt. 425 Sayı 1,47-55

[16]   Anonim (2002), Applied ceramic technology, Volume I, SACMI IMOLA Italy.

[17]   Kuzvart, M. (1984), Industriel minerals and rocks. Elsevier, New York.

[18]   Murray, H. H. (1996), Common Clay: Industrial Mıneral and Rocks, 6.Edition (Senior Editor carr, D. D), p.p.: 247-248.

[19]   Reed, J. S. (2000), "From batch to pressed tile-mechanics and system microstructural changes", Qualicer, 23-42.

RESEARCH ARTICLE

# EFFECT of MICROWAVE and CONVEYOR DRYING on the DRYING CHARACTERISTICS, MODELING, and THERMAL PROPERTIES of MUNICIPAL WASTEWATER SLUDGE

Tuğçe EKİCİ[1], Esra TINMAZ TÖRE[2], Soner ÇELEN[3],*

[1] Tekirdağ Namık Kemal University, Çorlu Faculty of Engineering, Department of Environmental Engineering, Tekirdağ, Turkey, tugcekici@gmail.com, ORCID: 0000-0002-4049-7811
[2] Tekirdağ Namık Kemal University, Çorlu Faculty of Engineering, Department of Environmental Engineering, Tekirdağ, Turkey, etinmaz@nku.edu.tr, ORCID: 0000-0001-9877-305X
[3],* Tekirdağ Namık Kemal University, Çorlu Faculty of Engineering, Department of Mechanical Engineering, Tekirdağ, Turkey, scelen@nku.edu.tr, ORCID: 0000-0001-5254-4411

## ABSTRACT

Wastewater treatment plant sludges are high moisture content sludges that during their storage and transport can cause various different problems. Therefore, a significant process is to dry these sludges. Based on drying times and energy consumption, microwave and conveyor drying methods for drying wastewater treatment plant sludge were examined in this study. Sludge weights of 20 g, 40 g and 60 g were used in the drying experiments carried out using two separate dryers. Microwave drying trials were performed at 360 W, 600 W and 800 W power, conveyor drying trials at temperatures of $60 \pm 1$ $^oC$, $70 \pm 1$ $^oC$ and $90 \pm 1$ $^oC$, at a fixed belt speed of 0,2 m/min. Energy consumption increased with the rise in microwave power as a consequence of the experiments. At 800 W and 60 g, the least energy consumption is measured as 0,015 kWh. In conveyor drying, on the other hand, drying time decreased with the rise in drying temperature, and energy consumption decreased. At 90 $^oC$ and 20 g, the least energy consumption was measured as 4,1 kWh. In terms of time and energy, the most appropriate of both drying systems was determined at 800 W. Furthermore, as a result of the statistical analysis, the most suitable model among five drying models was determined according to the $\chi2$, $e_s$, and r criteria as Logarithmic and Henderson and Pabis.

**Keywords:** *Sewage Sludge, Microwave Drying System, Conveyor Drying System, Energy Consumption, Modeling*

## 1. INTRODUCTION

The number of wastewater treatment facilities is growing increasingly in parallel with population growth, leading to a significant rise in the amount of sewage sludge [1]. In terms of substance, sludge treatment is rich in heavy metals, pathogenic bacteria, viruses and toxic chemicals. In order to remove tons of treatment sludge generated every year in a way that does not affect human and environmental health, various treatment methods are implemented. The need to establish new methods of disposal has emerged in sustainable environmental management in order to allow effective and profitable use of sewage sludge.

Every year in Turkey, around 1.38 million tons of sewage sludge are manufactured [1]. According to TÜİK (Turkish Statistical Institute) 2018 data, there are 16 Metropolitan Municipalities and 1399 Municipalities in our country with a population of 82.003.882. The population rate that provides sewerage service in these settlements is 91 percent. As of 2018, 88.3 percent of 4,795,130 thousand m³ of waste water discharged from the network to the receiving environment has been treated. Taking into account the 2018 TÜİK results, the ratio of the population served by wastewater treatment facilities to the total population is 79 percent. 1,226,767,920 billion tons of sewage sludge are expected to be generated annually when 3,361,008 tons of domestic / urban sewage sludge is produced per day, assuming 60 g of solid matter per person per day. Most of these treatment sludges are sent to the municipalities' controlled solid waste landfills as they are seen as an simple and inexpensive disposal process. It is a raw material that has beneficial usage alternatives considering the rich content of nutrients, calorific value etc. in domestic sewage sludge [2]. Sending treatment sludge to landfill sites both prevents them from being used as alternative raw materials and causes the capacity of storage sites that already have limited space, to fill up earlier. It is important to give the country's economy maximum benefit by correctly and properly using this substance, which has thermal and nutritional value.

The variety of disposal systems to be applied to reduce the wastewater sludge in volume and mass, and to result in a reduction in costs are of key importance in terms of correct management of waste. In order to treat wastewater sludge in the most efficient way, it is necessary to establish a uniform structure that includes public health and environmental safety elements simultaneously with low-cost alternatives by being evaluated within the management system. While evaluating the use in agriculture, incineration or storage alternatives in the selection of treatment sludge treatment systems or in their final disposal, the issue should be handled as a whole, and choices should be made by evaluating sludge characteristics, country conditions, the country's economy, as well as the conditions specific to the region being talked about [2]. It can be used as fertilizer in agriculture because of its (domestic) dry sludge content. Furthermore, its calorific value increases as the sludge dries, so it can be considered as a strong alternate source of energy.

The treatment sludge must first be stabilized in order to be discharged into the receiving environment; deodorized with reduced pathogen and organic material content must be generated. Principal methods of sludge stabilization; anaerobic digestion, aerobic digestion, lime stabilization, composting and drying [3]. By evaporating the water in the sewage sludge, Both the volumetric/ weight reduction of the sludge is done and the pathogens in it are eliminated. Two different processes take place during drying; first, energy is transferred to evaporate surface moisture from the surrounding atmosphere. Here according to temperature, air moisture flow, and pressure levels, water moves away from the solid surface. Second, after evaporation, the moisture in the sludge is transferred to the surface. The physical structure, temperature and initial humidity are dependent on moisture away from the solid. The drying process is a complex process in which heat and mass transmission occur simultaneously in physico-chemical transformations [4]. Among the applied sludge drying techniques are mechanical drying, solar drying and thermal drying. Moreover, evaporation and filtration are among the methods of natural drying used.

85% of industrial dryers are convection type. However, conduction dryers are more economically efficient and environmentally more advantageous [5]. Due to the increasing energy costs, the legal requirements to be met and the need to create safe working conditions, it is necessary not only to choose the dryer process, but also to design the plant. The chosen method of sludge drying varies

according to the size of the plant, the content of the waste processed, and the physical and economic capability of the facility.

Different thermal drying techniques (microwave and conveyor belt dryers) were applied to sludge obtained from the domestic waste water treatment plant in this study.

Since the realization of heating by activating the water molecules in the substances and the evaporation of water in a little while during the processes performed in microwave ovens, many studies have been carried out on microwave drying [6].

The domestic wastewater treatment sludge to be used in the study was taken according to the sampling conditions and the characterization of the treatment sludge was determined in the first stage, the first and last moisture content of the samples was measured with the conveyor belt drying system and microwave methods, which have two different thermal drying methods in the next stages, and the amount of power consumed and thermal changes of the samples were measured by imaging method and the calorific value of the treatment sludge was examined. Furthermore the findings obtained were evaluated according to various models of drying.

## 2. MATERIAL AND METHOD

The sample of sewage sludge was drawn from the domestic wastewater treatment facility. The sample of sewage sludge, 20 kg, was taken with an industrial type thick black three-layer garbage bag over the belt system where the dried treatment sludge was poured, and it was taken and stored in accordance with the sampling and storage standards so that it would not contact with air. The findings of the research carried out on 2 kg of sewage sludge taken from a sterile plastic bottle are shown in Table 1 below [7].

**Table 1.** Characterization of waste water treatment plant sewage sludge.

| Parameter | Unit | Analysis Results | Regular Storage Criteria of Inert Wastes | Regular Storage Criteria of Non-Hazardous Wastes | Hazardous Waste Storage Criteria |
|---|---|---|---|---|---|
| Eluat Criteria | | | | | |
| Antimony | mg L$^{-1}$ | <0,001 | 0,06 | 0,07 | 0,5 |
| Arsenic | mg L$^{-1}$ | <0,01 | 0,05 | 0,2 | 2,5 |
| Copper | mg L$^{-1}$ | <0,01 | 0,2 | 5 | 10 |
| Barium | mg L$^{-1}$ | <0,01 | 2 | 10 | 30 |
| Mercury | mg L$^{-1}$ | <0,0001 | 0,001 | 0,02 | 0,2 |
| Zinc | mg L$^{-1}$ | <0,01 | 0,4 | 5 | 20 |
| DOC (Dissolved Organic Carbon) | mg L$^{-1}$ | 18,9 | 50 | 80 | 100 |
| Phenol Index | mg L$^{-1}$ | 0,092 | 0,1 | - | - |
| Fluoride | mg L$^{-1}$ | <1 | 1 | 15 | 50 |
| Cadmium | mg L$^{-1}$ | <0,001 | 0,004 | 0,1 | 0,5 |

| | | | | | |
|---|---|---|---|---|---|
| Chloride | mg L$^{-1}$ | 40,03 | 80 | 1500 | 2500 |
| Bullet | mg L$^{-1}$ | <0,01 | 0,05 | 1 | 5 |
| Molybdenum | mg L$^{-1}$ | <0,01 | 0,05 | 1 | 3 |
| Nickel | mg L$^{-1}$ | <0,01 | 0,04 | 1 | 4 |
| pH | - | 7,26 | - | ≥6 | - |
| Selenium | mg L$^{-1}$ | <0,01 | 0,01 | 0,05 | 0,7 |
| Sulfate | mg L$^{-1}$ | 6,7 | 100 | 2000 | 5000 |
| TDS (Total Soluble Solids) | mg L$^{-1}$ | 400 | 400 | 6000 | 10000 |
| Total Chrome | mg L$^{-1}$ | <0,01 | 0,05 | 1 | 7 |
| Criteria to Look for in Original Waste | | | | | |
| BTEX (Benzene, Toluene, Ethylbenzene, Xylene) | mg kg$^{-1}$ | 0,06 | 6 | - | - |
| Loss on Glow (LOI) | % | 76,6 | - | - | 10 |
| Mineral Oil | mg kg$^{-1}$ | 105,63 | 500 | - | - |
| Moisture | % | 34,88 | - | - | - |
| PCBs | mg kg$^{-1}$ | 0,07 | 1 | - | - |
| Total Organic Carbon (TOC) | mg kg$^{-1}$ | 24650 | 30000 | 50000 | 60000 |
| Polychlorinated biphenyls (PCBs) | mg kg$^{-1}$ | 0,07 | | | |

### 2.1. Conveyor Drying System

Conveyor drying tests were performed at 1,8 m belt length, at 60 ± 1 °C, 70 ± 1 °C and 90 ± 1 °C temperatures, at a fixed belt speed of 0.2 m / min and at an air speed of 1 m / s. In order to calculate the temperature in the conveyor belt dryer, two thermometers are mounted in the system (as shown Fig.1).
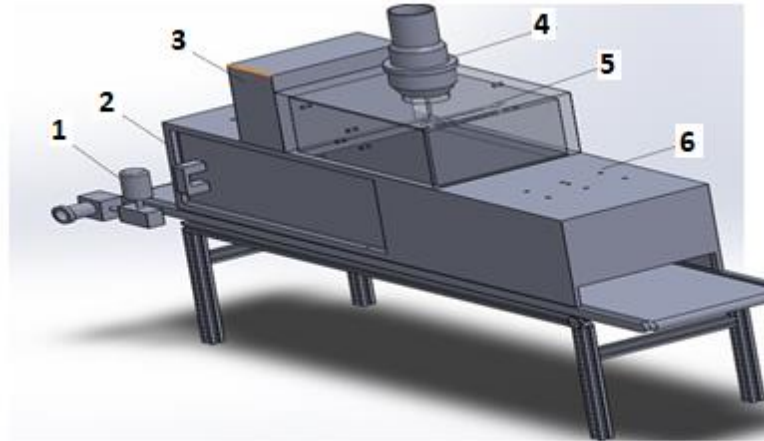
**Figure 1**. Conveyor drying system (1. Electric Motor, 2. Drying room, 3. Control Panel, 4. Fan, 5. Heater, 6. Ventilation holes) [7].

### 2.2. Microwave Drying System

Microwave dryer (Arçelik MD554, Turkey) with maximum of 1200 W at 2450 MHz was used for the drying (as shown Fig.2). Furthermore, microwave-resistant 9 cm diameter containers in which the product will be put during drying are suspended in the microwave. Weight losses were measured with a balance with a sensitivity of 0,001 g (Presica XB 620 M, Precisa Instruments AG, Dietikon, Switzerland). In the microwave drying system, the sensitive balance is placed on the microwave oven and the weight loss is recorded by measuring from the bottom.



**Figure 2.** Microwave Drying System (1: Microwave Oven, 2: Ventilation Gap, 3: Glass Container, 4: Timer, 5: Magnetron, 6: Fan, 7: Computer, 8: Power Switch, 9: Precision Balance) [6].

### 2.3. Energy and thermal analysis

In both the conveyor belt and microwave drying systems, a digital electricity meter was used with an accuracy of 0,01 kW. When the sludge is wet and after cooling, prior to the experiment, temperature changes of the samples were measured and photographs were taken with the imaging device (Flir Ex E6, Estonia). The regions where the sample is heated t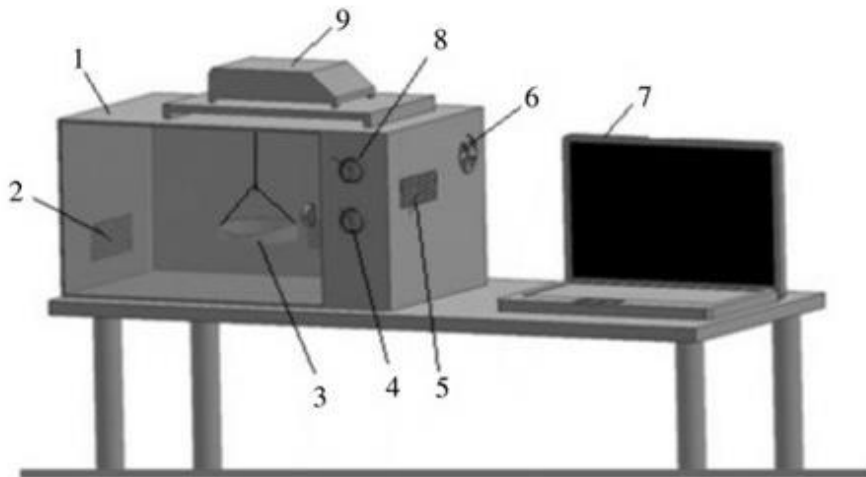he most and if the heat is distributed homogeneously are analyzed with thermal imaging. For all power levels and drying temperatures in both drying systems, thermal images of all samples were taken.

### 2.4. Preparation and Drying of Samples

Sewage sludge was put in glass petri dishes 9 cm in diameter in the form of samples of 20 g, 40 g and 60 g. The initial sludge moisture values used in the dry weight trials were determined at 105 °C for 24 hours in the MINGDA KIT-35A brand oven. The initial moisture content of the productswas estimated to be $97 \pm 0.8$ percent (wet base) as a consequence of the dry weight determination. As shown in Figure 3, glass containers were taken one by one and treatment sludge was placed so that all surfaces were coated. No external physical compression was applied to the sewage sludge during the preparation of the samples. Before the experiment, the temperatures of each container were measured and imaged while wet with a thermal imager.
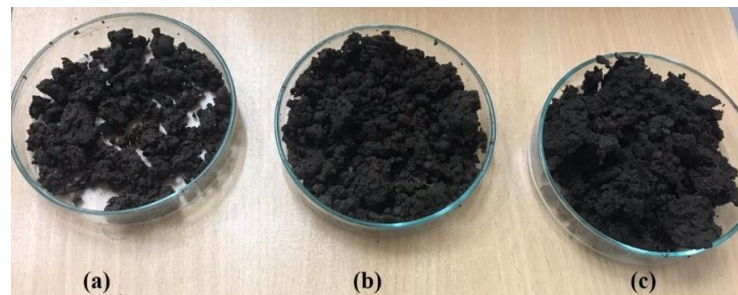


**Figure 3.** Wet sewage sludge samples (a) 20 g, (b) 40 g and (c) 60 g.

In the microwave drying system, first 360 W, 600 W and 800 W power was applied to the glass container connected to the bottom of the precision scale as 20 g, 40 g, 60 g respectively. The weight data was processed into the device every 10 seconds during the software used on a computer connected to a microwave oven. In the process with conveyor belt dryer, samples were placed one after another on the conveyor belt. The power of the conveyor belt used in the experiment is 2000 W and the dimensions are 2370×50×40 mm. The test system was set to be performed at 0.2 m / min and 1 m / s air speed, and it was studied at $60 \pm 1$ °C, $70 \pm 1$ °C and $90 \pm 1$ °C.

The microwave drying trials were completed when it reached $86 \pm 0.5$ percent (w.b) and the conveyor trials reached $79 \pm 0.5$ percent (w.b) with respect to the wet base (w.b). Drying took place in the drying trials until the final moisture value stabilized. The energy consumed during the process was measured by the energy meter.

The temperature changes of the specimens were measured with a thermal imager after each drying phase and their photographs were taken. Trials were repeated three times for each parameter. The means of the data are used.

After the moisture content of the products was calculated according to the wet base as in Equation 1, the dimensionless moisture ratio was calculated using equation 2 in conveyor drying trials and equation 3 in microwave drying trials. It is assumed that the equilibrium moisture content in the microwave oven is zero [8, 9].

$$m_w = \frac{M_w - M_d}{M_w} \tag{1}$$

$$m_R = \frac{m - m_e}{m_o - m_e} \tag{2}$$

In these equations;
$M_d$: dry mass of the product (g), $M_w$: wet mass (g) of the product, $m_R$: dimensionless moisture content, $m_w$: moisture content of the product at a given time (g.water / g. wet matter), $m_e$: equilibrium moisture content (g water / g.wet matter), $m_o$: initial moisture content (g.water / g.wet matter)

## 2.5. Mathematical Modeling
In the simulation of the drying phase of complex compounds such as sewage sludge, empirical and semi-empirical models are used. Nonlinear regression analysis was used when modeling in this study and the moisture reduction obtained as a result of the experiment was analyzed and modeled. According to the value of the correlation coefficient (r), the suitability of the model in the expression of experimental data was determined. Standard error ($e_s$) and chi-square ($\chi 2$) values were used to measure the fit of the model. These sizes are defined in equation 3-6 [6].

$$r = \sqrt{\frac{S_t - S_r}{S_t}} \tag{3}$$

$$e_s = \sqrt{\frac{\sum_{i=1}^{n_0}(mr_{pre,i} - mr_{exp,i})^2}{n_0}} \tag{4}$$

$$x^2 = \frac{\sum_{i=1}^{n_0}(mr_{pre,i} - mr_{exp,i})^2}{n_0 - n_c} \tag{5}$$

$$S_t = \sum(mr_{exp,i} - mr_{ave})^2 \tag{6}$$

$$S_r = \sum(mr_{exp,i} - mr_{pre,i})^2 \tag{7}$$

where; $mr_{pre,i}$ is the i*th* predicted moisture ratio, $mr_{exp,i}$ is the i*th* experimental moisture ratio, $n_o$ is the number of observations and $n_c$ is the number of coefficients in the drying model. $S_t$ and $S_r$ are the sum of squared error values, which were calculated using average moisture rate ($mr_{ave}$).

**Table 2.** Models used to express experimental results.

| Model | Model Equation | Referance |
|:---:|:---:|:---:|
| Page | $m_R = \exp(-kt^n)$ | [10] |

| Henderson&Pabis | $m_R = a\exp(-kt)$ | [11] |
|:---:|:---:|:---:|
| Wang&Singh | $m_R = 1 + at + bt^2$ | [12] |
| Logarithmic | $m_R = a\exp(-kt) + b$ | [13] |
| Newton | $m_R = \exp(-kt)$ | [14] |

## 2.6. Calorific Value Analysis

The calorific value of a substance is determined by various methods such as analysis based on the composition of the waste, predictive analysis, calorimetry measurement or elemental analysis. It is obtained by making some improvements to the method of measurement used in the method of elemental analysis in the method of analysis based on the composition of the waste. In the estimated method of study, the mass loss suffered by volatile and inert substances at elevated temperatures is measured using volatile and inert waste material detail. One of the most widely used approaches is calorimeter measurement. The bomb is measured with a calorimeter. In elemental analysis, by means of the DuLong equation, the amounts of carbon, hydrogen, oxygen and sulfur are determined in the chemical structure of the sample [15]. The calorific value of the sample was calculated in Leco AC-350 after the crude purified sludge was dried in an oven at 100 $^o$C for 2 hours.

## 3. RESEARCH FINDINGS

### 3.1. Moisture Change Findings

In the microwave drying system, as seen in Figure 5, the initial and final moisture of 20 g, 40 g and 60 g samples at 360 W power, respectively, according to the wet base, is 0,9629 to 0,8650 in 509 seconds, from 0,9713 to 0,8701 in 200 seconds and dried from 0.9769 to 0.8615 in 180 seconds. Dried from 0.9635 to 0.8656 at 600 W of power in 249 seconds, 110 seconds from 0.9720 to 0.8524 and 120 seconds from 0.9768 to 0.8576. Dried in 190 seconds at 800 W of power from 0.9639 to 0.8650, in 80 seconds from 0.9711 to 0.8629, and in 78 seconds from 0.9773 to 0.8598. With the increase of microwave power, drying time declined [16].
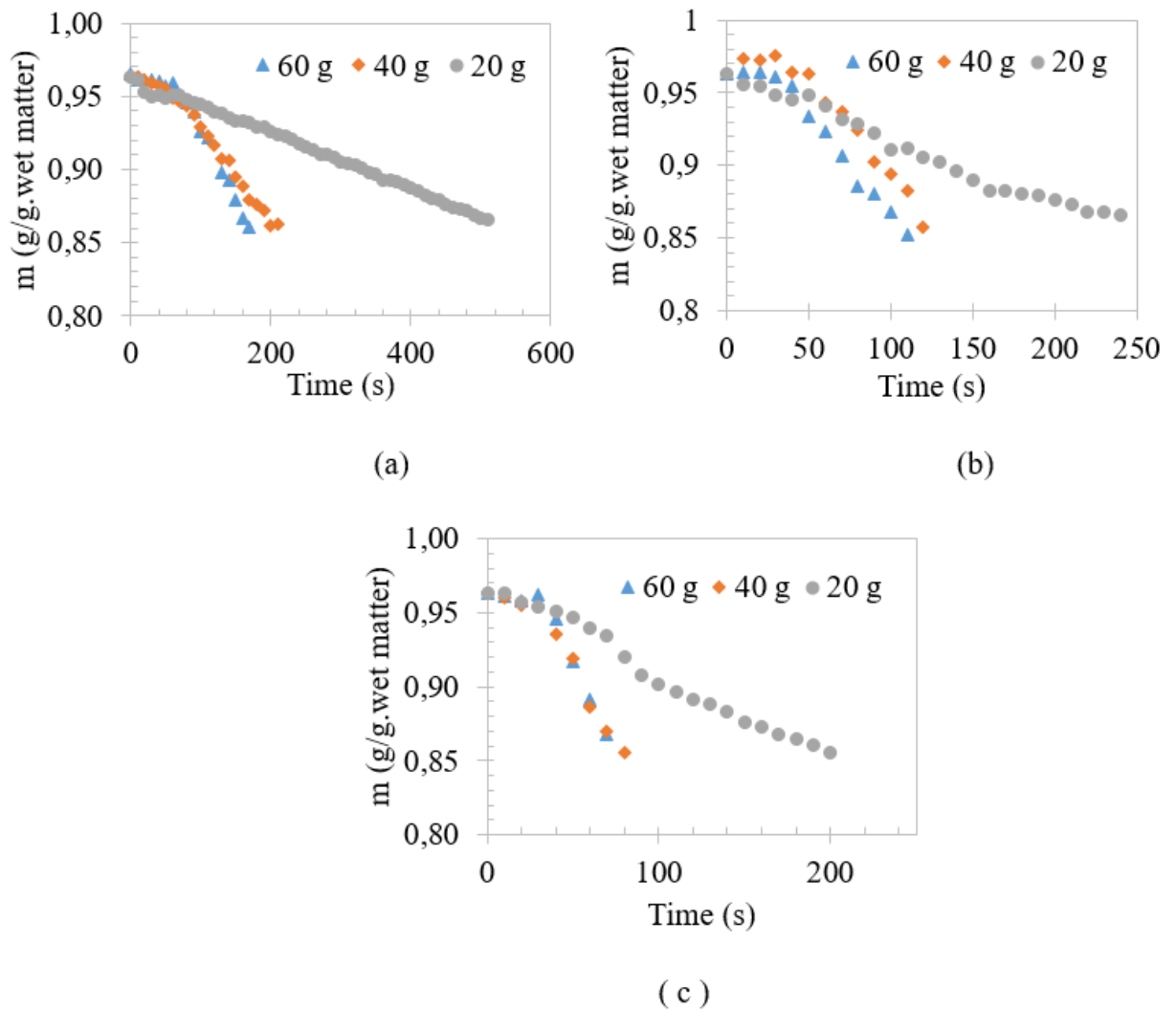
**Figure 4.** a) Moisture change of sludge dried at 360 W microwave power b) 600 W microwave power c) 800 W microwave power.

In the conveyor drying method, as shown in Figure6, the initial and final moisture of 20 g, 40 g and 60 g samples at 60 $^o$C, respectively, according to the wet foundation, from 0.9632 to 0.7880 and 255 minutes, from 0.9713 to 0.7896, 300 minutes and It was dried from 0.9770 to 0.7898 for 345 minutes. It was dried at 70 $^o$C for 225 minutes from 0.9632 to 0.7936, 255 minutes from 0.9714 to 0.7989 and 285 minutes from 0.9770 to 0.7960. Dried at 90 $^o$C for 165 minutes from 0.9632 to 0.7956, 195 minutes from 0.9714 to 0.7914 and 225 minutes from 0.9770 to 0.7834 The results showed that it is consistent with previous literature [17].

126
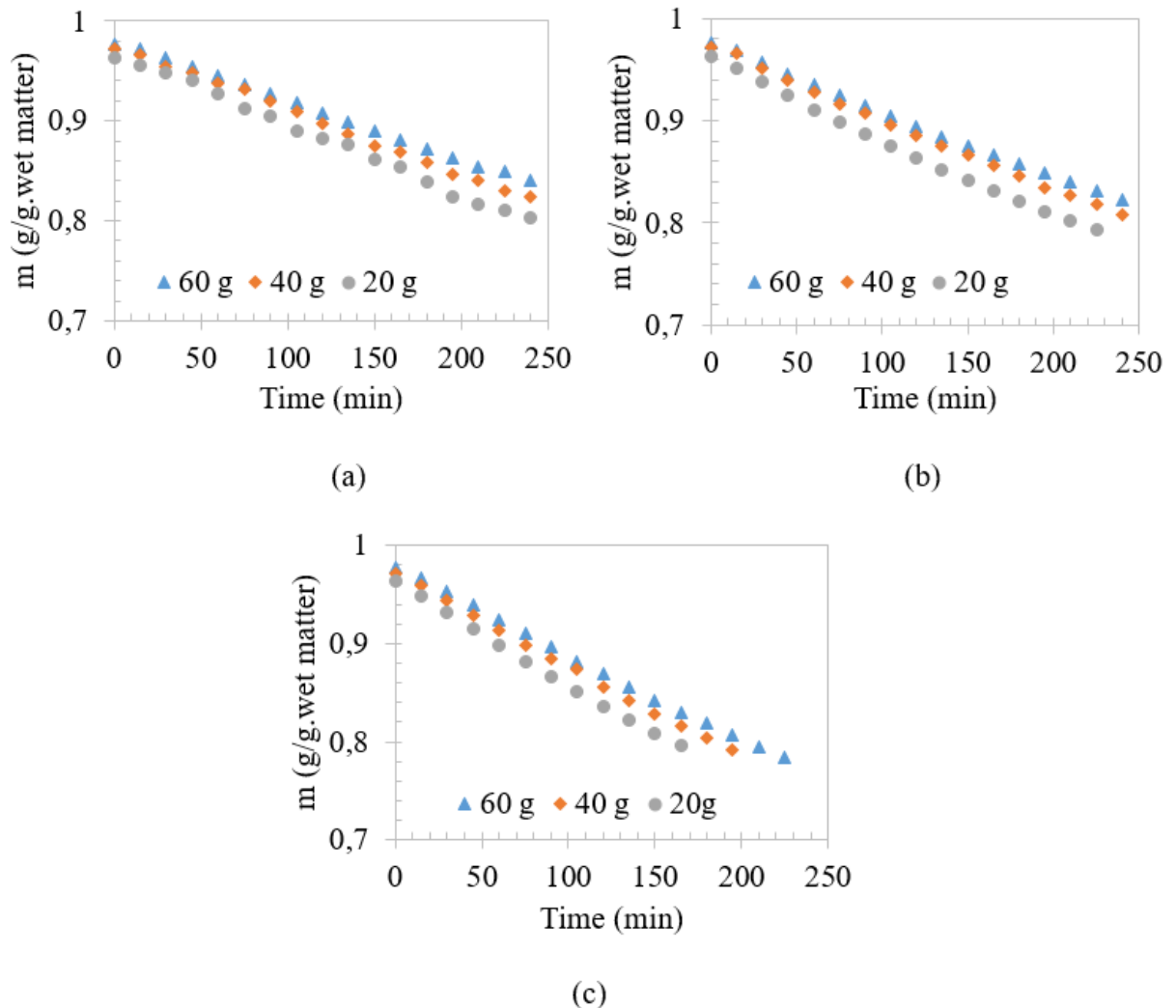
**Figure 5.** a) Moisture change of sludge dried at 60 °C drying temperature b) 70 °C drying temperature c) 90 °C drying temperature.

In addition to increasing drying power, drying time is influenced by microwave power, moisture loss accelerates, and drying time decreases. Owing to the reduction of the sample mass, there are variations in drying time as well. The reason for this phenomenon is that the moisture in the sample is not homogeneous, the heat energy is formed in the interiors and the interaction of microwave energy with the product due to the band speed causes variation in drying times. Since both drying processes are different from each other, different drying times have occurred. Drying occurred more rapidly than conveyor drying due to volumetric heating in microwave drying [5].

### 3.2. Mathematical Modeling Findings

Among the models given in Table 2, correlation coefficient calculated for 60 g for microwave drying (0,902-0,986), standard error (0,014-0,05) and $\chi2$ (2 $x10^{-5}$-2,1×$10^{-4}$) for 40 g calculated correlation coefficient (0.937-0.978), standard error (0.012-0.005) and $\chi2$ (3×$10^{-5}$-1.2×$10^{-4}$) and the correlation coefficient calculated for 20 g (0.985-0.996), standard error (0.002-0.004) and It is concluded that the logarithmic model is suitable for the values of 3,2 (3,1×$10^{-6}$-1,6×$10^{-5}$). As shown in Figure 7, an appropriate correspondence is between model results and experimental data. The best compatibility between microwave powers is at 800 W, where the fastest drying takes place.
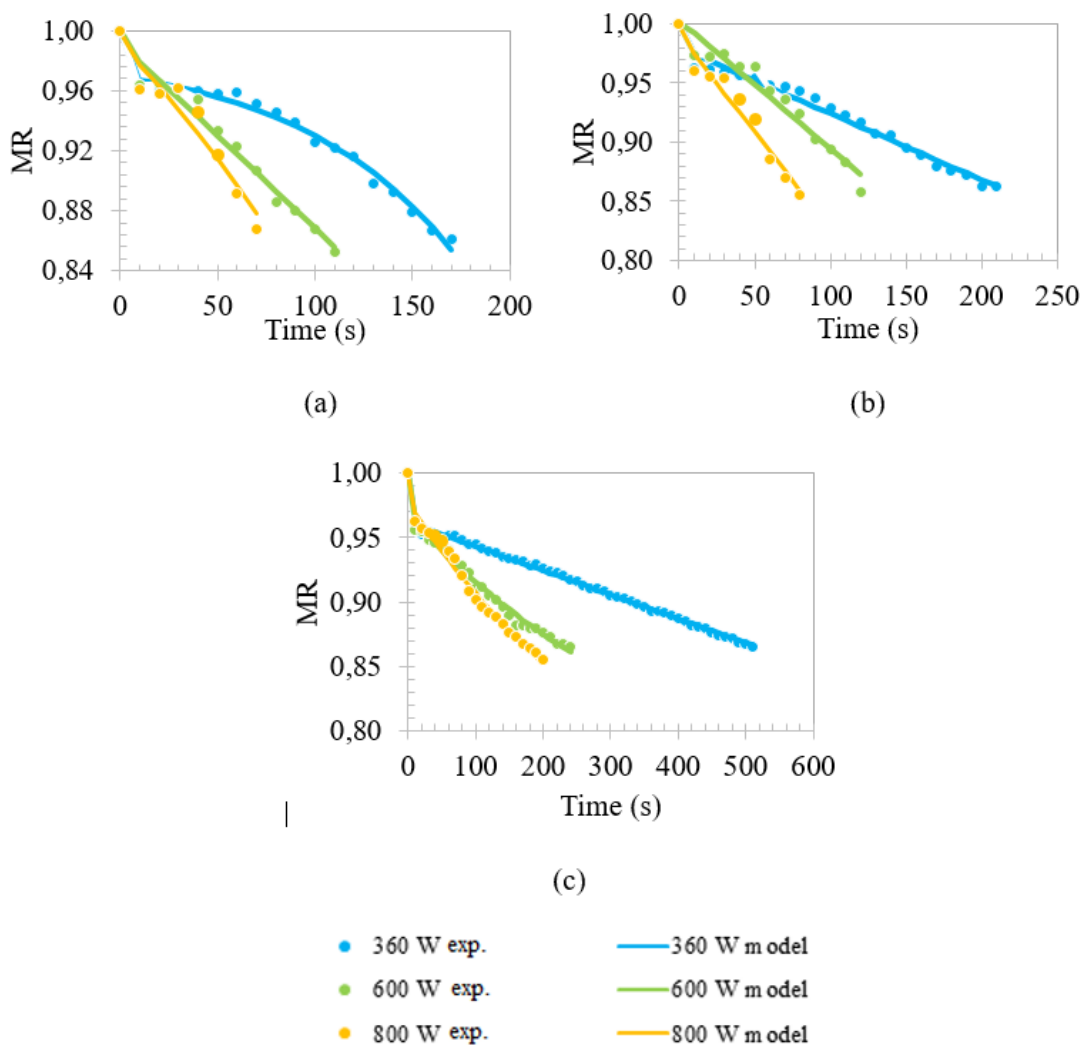


**Figure 6.** Compliance of a) 60 g, b) 40 g and c) 20 g samples in microwave drying to the logarithmic model.

Correlation calculated for 60 g (0.999-1), standard error (0.002-0.001) and $\chi2$ ($6.1\times10^{-7}$; $2.7\times10^{-6}$) for conveyor drying, correlation coefficient calculated for 40 g (0.998-1), the standard error (0.003-0.001) and the correlation coefficient calculated for $\chi2$ ($6.38\times10^{-6}$-$1.63 \times 10^{-6}$) and 20 g (0.997-1), standard error (0.003-0.001) and It was concluded that the Henderson and Pabis model was suitable for 2 ($4.63\times10^{-6}$- $8.68\times10^{-6}$) values. As shown in Figure 8, an acceptable correspondence is between model outcomes and experimental results. The greatest compatibility between the drying conditions of the conveyor is at 90 $^{o}$C, where the quickest drying occurs.
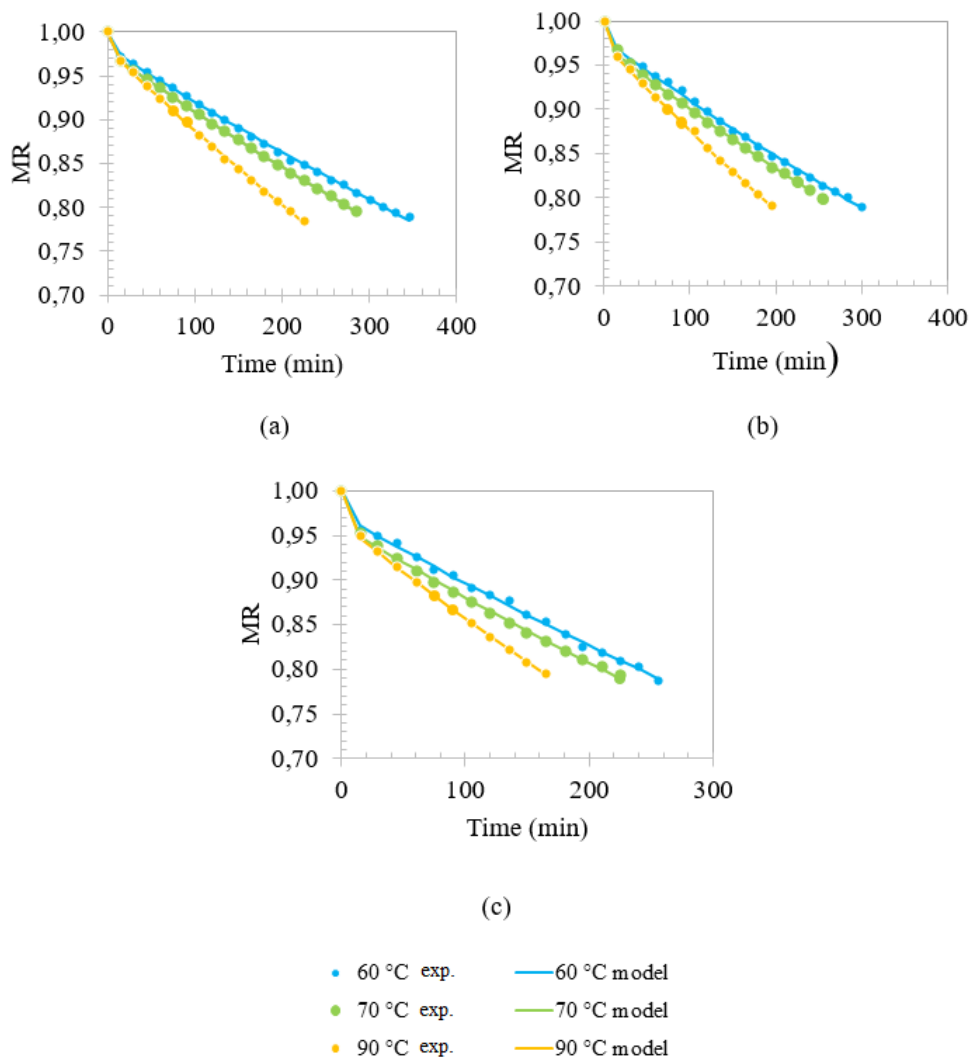


**Figure 7.** Conformity of samples a) 60 g, b) 40 g and c) 20 g in conveyor drying for Henderson and Pabis models.

### 3.3. Thermal Analysis Findings

For all the drying conditions, Figure 9-14 shows the lowest and highest temperatures of the thermal images. Temperatures for microwave drying system; measured between 23,8 $^{o}$C - 130 $^{o}$C / 22,9 $^{o}$C - 128 $^{o}$C / 23,6 $^{o}$C - 145 $^{o}$C. Local overheating is caused by high energy absorption and drying rates. Excessive localization is triggered by overheating and becomes difficult to manage. The temperature of the end product grew as the microwave power increased. In certain areas, the color is shown as yellow; these points are where the substance begins to heat. Microwave energy acts on water molecules and by vibrating water molecules, allows heat to be emitted. As a result, increasing temperature was detected, especially in the middle of the sample. The red color on the sides shows that the slurry's liquid component is discharged sideways and this is due to unnecessary loading of energy. According to the thermal images taken in the microwave drying system, the drying process is homogeneous. Temperatures for the conveyor belt dryer system have been measured between 22,4 $^{o}$C – 51,5 $^{o}$C / 19,7 $^{o}$C - 53 $^{o}$C / 21,7 $^{o}$C – 65,5 $^{o}$C. The temperature stays on the surface in the conveyor belt drying system, so it does not go far, so the temperature is not homogeneous, as shown in Figure 12-14. The inhomogeneity of the treatment sludge is related to the differences found in temperatures. In order to obtain a homogeneous composition, the sample has to be mixed.
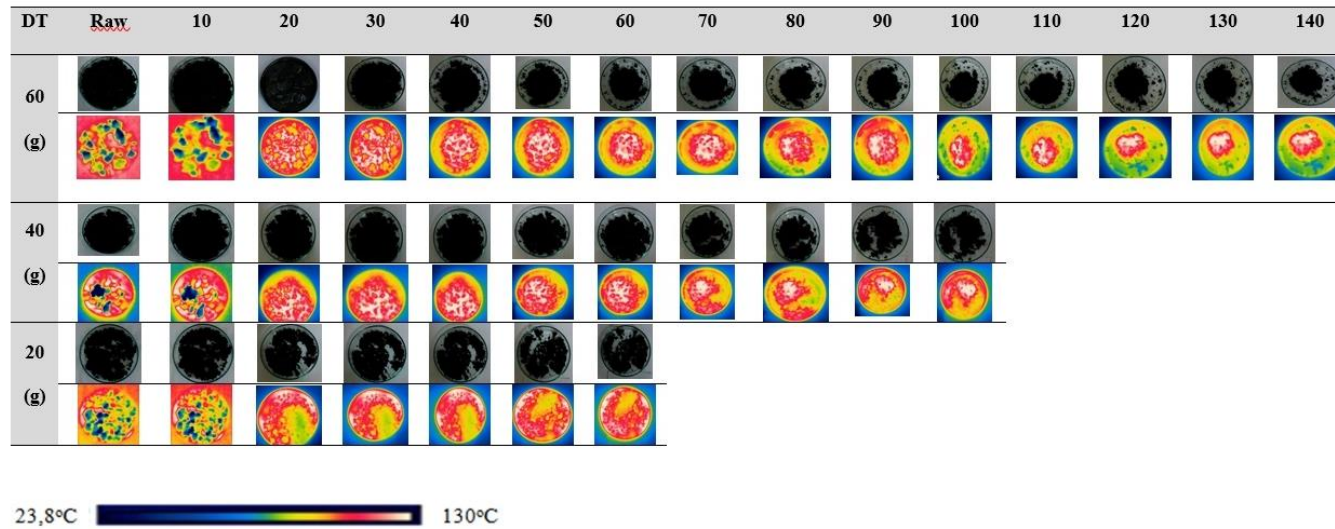
**Figure 8**. Thermal images of raw and dried treatment sludge under 360 W in microwave drying system (DT: Drying Time, minute.).

**Figure 9.** Thermal images of raw and dried sewage sludge under 600 W in microwave drying system.

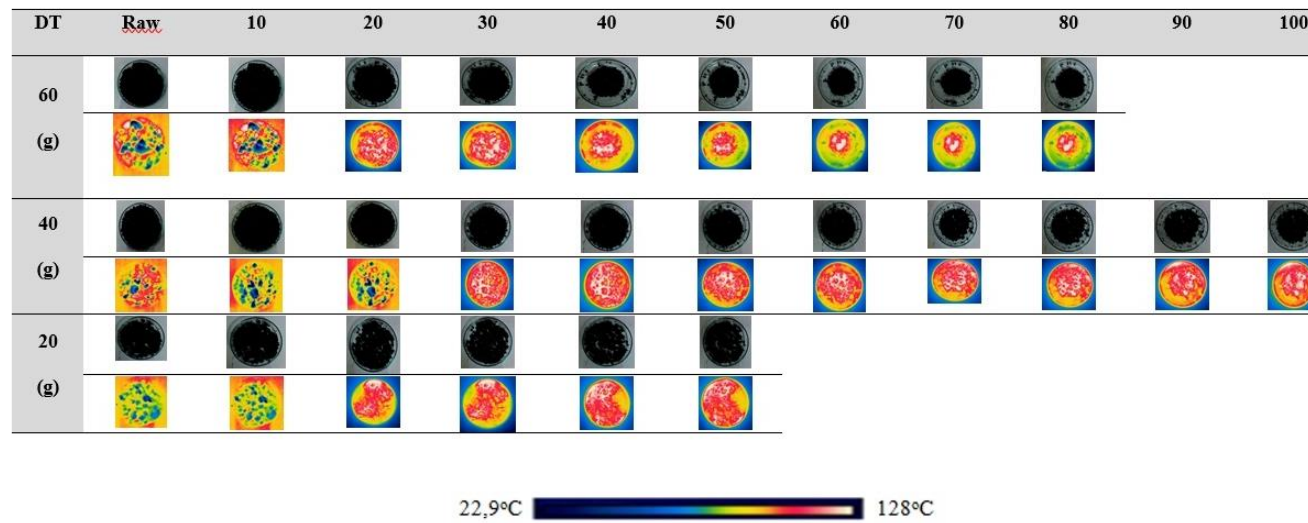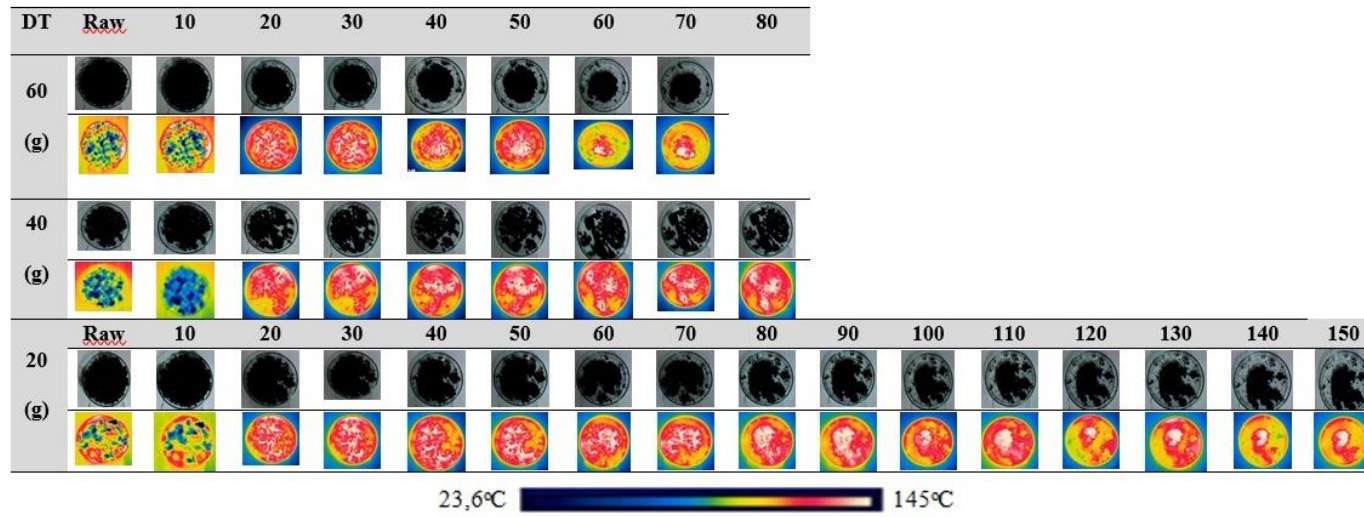**Figure 10.** Thermal images of raw and dried sewage sludge under 800 W in microwave drying system.
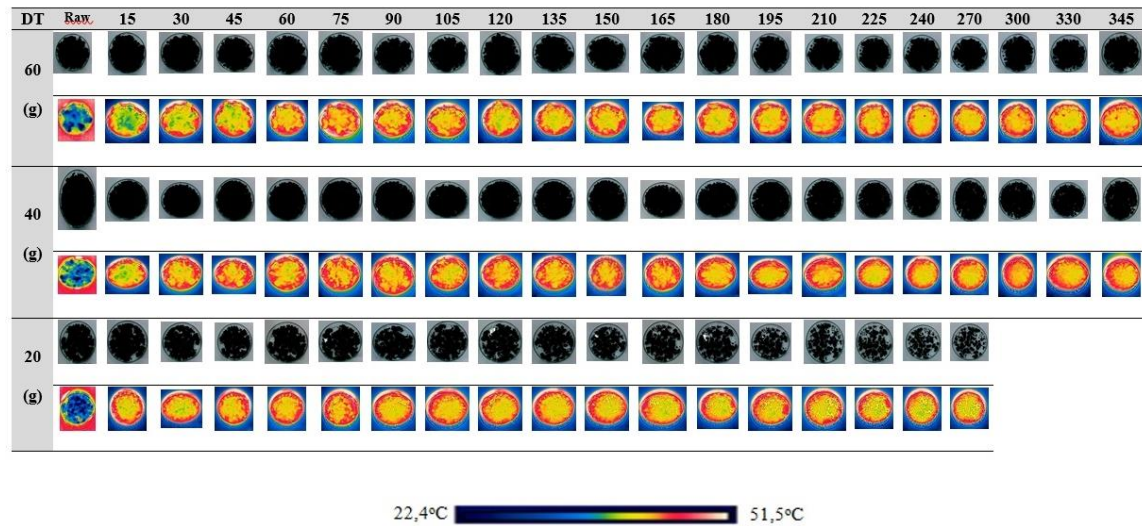
**Figure 11.** Thermal images of raw and dried sewage sludge below 60 °C in conveyor belt drying system.
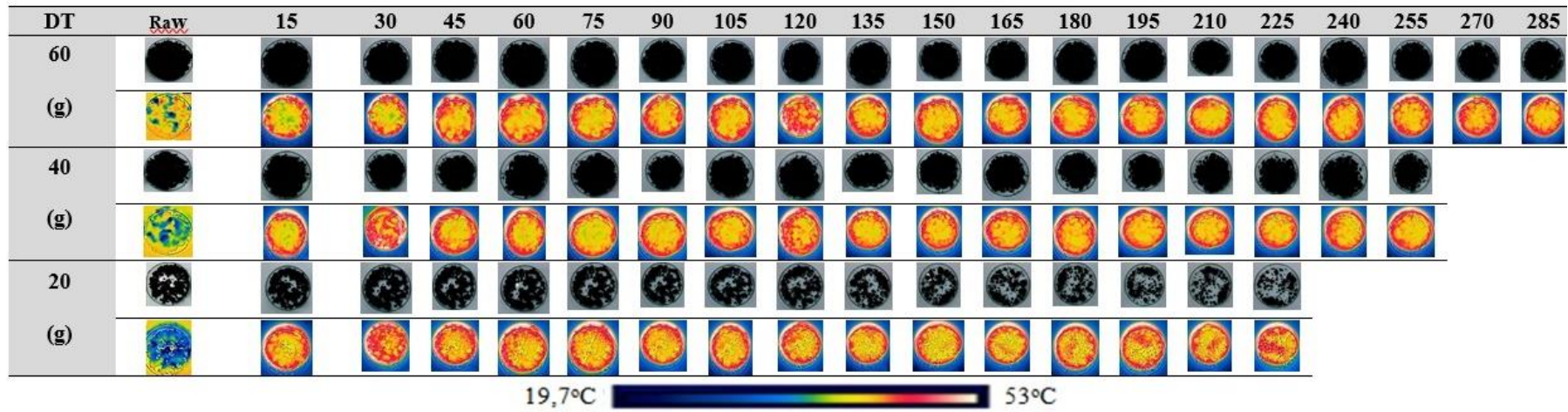
**Figure 12.** Thermal images of raw and dried sewage sludge below 70 °C in conveyor belt drying system.
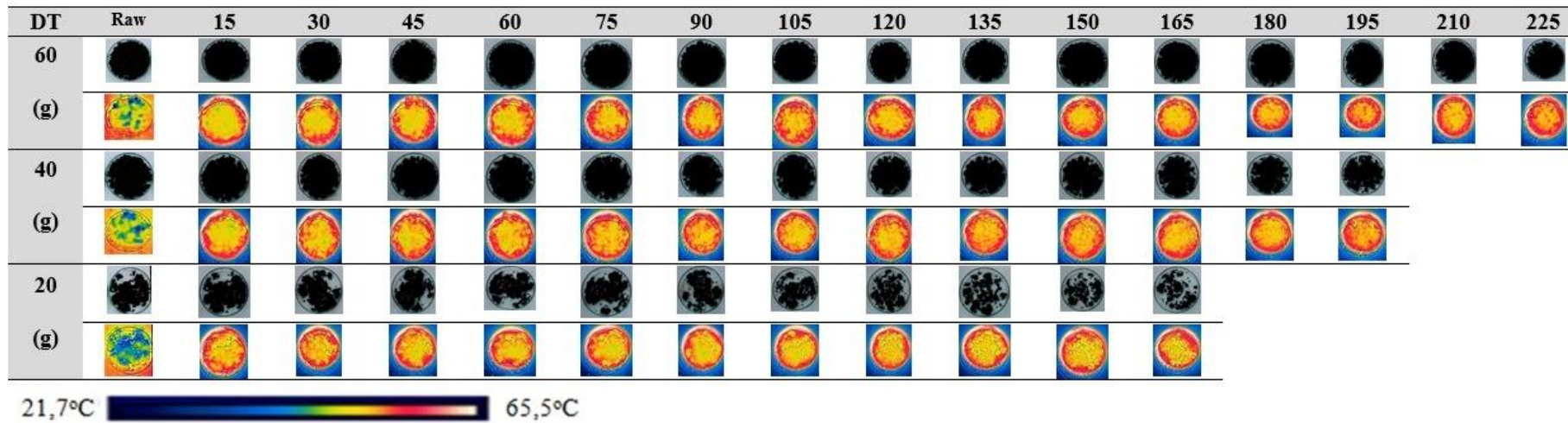
**Figure 13.** Thermal images of raw and dried sewage sludge below 90 °C in conveyor belt drying system.

**3.4. Energy Analysis Findings**

In the study of the analysis, the electrical energy consumption values of the microwave sludge system were between 0,03-0,15 kWh by weight for microwave power of 360 W, 0,02-0,06 kWh for microwave power of 600 W and 0,015-0,07 kWh for microwave power of 800 W. As the drying power enhanced the drying time, energy values increased. With the rise in microwave capacity, energy consumption has increased. At 800 W and 60 g, the least energy consumption is calculated as 0,015 kWh.

In conveyor drying, it was between 4,75-6,32 kWh for 60 $^o$C drying temperature, 4,55-5,78 kWh for 70 $^o$C drying temperature and 4,1-5,46 kWh for 90 $^o$C drying temperature, respectively. As the drying time increased, energy consumption increased as the drying temperature decreased. Drying time decreased and the consumption of energy decreased as the drying temperature increased [17]. At 90 $^o$C and 20 g, the least energy consumption is calculated as 4.1 kWh.

Since the heat generated at low microwave power is lower, the transfer of heat within the material and the transfer of heat from the product to the environment takes longer. Thus the time needed to achieve the evaporation temperature for the water in the product extends and the energy used for evaporation is decreased. In this situation, efficient drying is prevented.

**4. CONCLUSIONS**

For the drying of sewage sludge, the microwave drying system and the conveyor belt drying system were contrasted. It has been found that compared to the microwave drying system, the conveyor belt drying system has a longer drying time. It has been found that the microwave drying system is more favorable than the conveyor belt drying system when it comes to energy consumption. In terms of time and energy, the most appropriate of both drying systems was calculated at 800 W level. When the product is placed in a larger plate, more drying can be done. When the results of the study were evaluated, it was revealed that different drying times were observed because the drying mechanisms of both dryers were different, and microwave drying was faster than conveyor belt drying. It has been found that the higher the output power of the microwave and the smaller the mass of dried material, the quicker the drying takes place.

According to the thermal analysis performed on the sewage sludge, the drying process in the microwave drying system is more homogeneous, the drying process in the conveyor belt drying system is not homogeneous. In the calorific value analysis, it was shown that drying could increase the calorific value of the sewage sludge. With the calorific value of the waste, 3503.8 cal / g was concluded.

For predicting separable humidity rate (mr), Logarithmic and Henderson and Pabis model was chosen as the most predictive drying kinetics model with the comparisons made depending on the coefficients of the examined drying models with the highest r value based on microwave power, drying temperature and sludge weights in all experiment conditions.

Drying of treatment sludges due to their high moisture content and increasing amount each day; It is an effective method for reducing transportation and management costs, storing and recycling these wastes. When selecting the right drying process, drying time and energy consumption are a restricting factor.

As the drying process is carried out in the microwave drying system at high temperatures, it is assumed that pathogenic microorganisms in the sewage sludge can be more effectively eliminated.

It was observed that the samples dried in the conveyor belt drying system could not be dried homogeneously and some regions in the sample had different temperatures, and it was seen that the drying process was more homogeneous, which was not seen in the microwave drying system. If a uniform distribution of heat is required, it is assessed that the sample should be mixed.

While a very effective method for drying thin layer materials is microwave drying, it is not ideal for drying high volume and bulk materials. A conveyor belt drying scheme should be used if mass drying is needed. It is concluded, because of these differences, that an integrated structure should be developed in which the two systems can operate together.

## ACKNOWLEDGEMENTS

## REFERENCES

[1]  Uzun, P. and Bilgili, U. (2011). Possibilities of using sewage sludge in agriculture, Journal of Agricultural Faculty of Uludag University, 25(2), 135-146.

[2]  Anonymous (2015). Management project final report of municipal sewage sludge-accession address: https://cygm.csb.gov.tr/evsel-kentsel-aritma-camurlarinin-yonetimi-projesi-duyuru-33959, Turkey (in Turkish).

[3]  Göçmez, S., (2006). Effects of İZSU municipal waste treatment sludge on microbial biomass and activity, some physical and chemical properties of soils in Menemen Plain. Ph.D Thesis, Ege University, İzmir, Turkey.

[4]  Dinçer, E. A. and Erbaş, M. (2019). Quality properties of dried meat products. The Journal of Food, 44 (3), 472-482.

[5]  Tınmaz Köse, E. (2019). Drying of drilling cutting: emphasis on energy consumption and thermal analysis. Processes, 46(3), 43-53.

[6]  Çelen, S. (2010). Modeling and drying of some food products in microwave and vacuum dryer. Ph.D Thesis, Trakya University, Edirne, 152p.

[7]  Ekici, T. (2019). Investigation of drying parameters of municipal wastewater sludge. MSc. Thesis, Tekirdağ Namık Kemal University. Tekirdağ, 114p.

[8]  Çelen, S., Haksever, A. and Moralar, A. (2017). The Effect of microwave energy to the drying of apple (gala) slices, Karaelmas Science and Engineering Journal, 7 (1), 228-236.

[9]  Çelen, S., Aktaş, T., Karabeyoğlu, S. S. and Akyıldız, A. (2015). Drying of prina using microwave energy and determination of appropriate thin layer drying model. Jotaf. 12(2), 21-31.

[10] Omolola, A. O., Kapila, P. F. and Silungwe, H. M. (2019). Mathematical modeling of drying characteristics of Jew's mallow (Corchorus olitorius) leaves, Informatıon Processing In Agriculture 6, 109–115.

[11] Younis, M., Abdelkarim, D. and El-Abdein, A. Z. (2018). Kinetics and mathematical modeling of infrared thin-layer drying of garlic slices, Saudi Journal of Biological Sciences, 25(2), 332-338.

[12] Miranda, M., Maureira, H., Rodriguez, K., Vega-Galvez, A. (2009). Influence of temperature on the drying kinetics, physicochemical properties, and antioxidant capacity of Aleo vera gel. Journal Food Engineering. 91(2), 297–304.

[13] Ashtiani, S. M., Salarikia, A., Golzarian, M. R. (2017). Analyzing drying characteristics and modeling of thin layers of peppermint leaves under hot-air and infrared treatments. Inf Processing Agri. 4(2):128–39.

[14] Zhu, X., Zhang, Z., Hinds, L. M., Sun, D. and Tiwari, B. K. (2021). Applications of ultrasound to enhance fluidized bed drying of Ascophyllum Nodosum: Drying kinetics and product quality assessment, Ultrasonics – Sonochemistry, 70, 105298.

[15] Öztürk, İ. (2015). Katı Atık Yönetimi ve AB Uyumlu Uygulamaları, İSTAÇ Yayınları, Teknik Kitaplar Serisi. (Turkey). pp. 456. (in Turkish).

[16] Tınmaz Köse, E., Çelen, S., Çelik, S. Ö., Akın, G. And Akyıldız, A. (2019). Drying of drilling sludge: Conventional and microwave drying. Hittite Journal of Science & Engineering. 6 (2), 119-122.

[17] Tınmaz Köse, E., Çelen, S. and Çelik, S. Ö. (2019). Conventional and microwave drying of hydrocarbon cutting sludge. Environmental Progress & Sustainable Energy 38(4), 13104.

*RESEARCH ARTICLE*

# PID CONTROL IMPLEMENTATION of AN INVERTED PENDULUM SYSTEM

Yunus SERT[1,*], Ayhan GÜN[2]

[1] Kütahya Dumlupınar University, Faculty of Engineering, Department of Electrical-Electronical Engineering, Kütahya,
yunus.sert@dpu.edu.tr, ORCID: 0000-0003-1286-1257
[2] Kütahya Dumlupınar University, Faculty of Engineering, Department of Electrical-Electronical Engineering, Kütahya,
ayhan.gun@dpu.edu.tr, ORCID: 0000-0002-4223-2518

## ABSTRACT

Inverted pendulum which consists of a straight pole and a horizontally moving cart has been one of the most widely researched systems and is considered a classical problem in the area of control engineering. Main objective of the system is to control and stabilize both the angle of the pendulum and position of the cart. In this study, an example of such type of system was designed, implemented and controlled. Stabilization and control objective of the system was successfully achieved by using a Proportional-integral-derivative (PID) controller and graphs of input and outputs of the system was obtained in MATLAB environment.

**Keywords:** *Nonlinear systems, PID controller, Inverted pendulum*

## 1. INTRODUCTION

Inverted pendulums are non-linear systems which have a stable, and an unstable equilibrium states. They are regarded as underactuated systems because pendulum motion is provided by cart motion, not by the pendulum shaft itself. One of the two main objectives of the system is to bring the pendulum to the upper unstable position from the lower/stable position. Other objective is to keep the system stable in that state by controlling the pendulum angle and the cart position within the desired reference points.

Literature shows that many researches have shown great interest in inverted pendulum and its varieties and suggested various linear and non-linear control algorithms for the non-linear inverted pendulum systems. According to studies, PID as a linear algorithm proved to be useful and effective on controlling non-linear under-actuated systems such as inverted pendulum despite its simplicity.

Lozano et al. [1] proposed a control system design that takes the displacement of the vehicle underneath, while bringing the pendulum to upper unstable equilibrium point. The control strategy they suggested is based on the control of the total energy of the system. In the study, a Lyapunov function was obtained using the total energy of the system and the movement of the vehicle was realized using LaSalle's invariance principle. They have shown that the control system they have obtained can be used in practice by testing in a real pendulum system.

Huang and Huang [2] aimed to solve the problem of inverted pendulum using gray theory analysis in their work. Dynamic model of underactuated mechanical system was obtained by using Lagrange equation. Based on the dynamic model and the sliding mode control, the speed and braking system of the vehicle were controlled. Simulation and experimental results had shown that the system works effectively.

Gani et al. [3] proposed a fuzzy logic-based control algorithm for the control of the inverted pendulum system. The researchers simulated the control algorithms via MATLAB/Simulink and observed that it takes 25 seconds for the system to be stable.

Elibol [4] used an energy-based control method to study the problem of lifting the pendulum to the upper equilibrium position and then keeping it in that point by using Linear Quadratic Regulator (LQR).

Kajita et al. [5] have studied a three-dimensional inverse pendulum problem for controlling a plane of arbitrary motion of a two-legged robot motion. In the study, they proposed a 3D linear inverted pendulum mode for the control of robot walk. The walking motion of the humanoid robot was analyzed in a dynamic simulator and a stable walking on a circle motion was obtained.

Sugihara et al. [6] proposed a real-time motion generator for the movement of humanoid robots in their work. They have reduced the computation time for real-time applications by using the dynamics of the inverted pendulum in their work.

Pathak et al. [7] examined the dynamic model of a wheeled inverted pendulum in terms of feedback linearity and controllability. First, they derived a dynamic model that takes the moment of the motors as the input value and then compared the results with the models proposed in previous studies.

Gun [8] designed a practical application of a non-linear and underactuated inverted pendulum system. He used Adaptive Neuro Fuzzy Inference System (ANFIS) and Proportional-Integral-Derivative (PID) controller to control the two outputs against a single input. The results of the system which performed successfully were interpreted graphically and the video visual of the experimental work was also presented.

Grasser et al. [9] built a two-wheeled vehicle named JOE with the solution of the inverse pendulum problem. The vehicle consisting of two coaxial wheels controlled by DC motors was an example of mobile inverted pendulum which showed a successful performance against external disturbances.

Sharif [10] preferred to use the sliding mode control in the analysis of the non-linear inverted pendulum and designed the sliding mode control algorithm using the Ackerman formula and linear matrix equations to stabilize the system.

Kharola et al. [11] approached the inverse pendulum problem in a different way and aimed to control the system on a sloping surface. The proposed system was controlled by PID and fuzzy logic controllers and simulated in MATLAB/Simulink environment.

Studies show that the inverted pendulum system is an important test environment in the analysis of underactuated non-linear systems. Many algorithms have been proposed and their performances have been examined both in simulations and experimental setups.

In this study, a two degree-of-freedom inverted pendulum control system with single input and two outputs was designed and implemented. While the input of the system is the speed of the cart carrying the pendulum in the horizontal axis, its outputs are the pendulum angle and the cart position which are changed by the cart movements. Movement of the cart on a 2m long track is provided by a brushless servomotor connected to the track, while the pendulum angle and cart position are measured by incremental optical encoders. Digital signal processor (DSP) used in the system computes the current error by processing angle and position information provided by the encoders. The speed of the cart which stabilizes the system by correcting the calculated errors is determined by the PWM signals generated by the DSP. The PID controller used in the system calculates at what speed and in which direction the cart must change its position on track in relation to angle and position errors. Thus, both outputs of the system are being controlled simultaneously.

## 2. MECHANICAL AND ELECTRICAL HARDWARE

Components of the main mechanical hardware of the system as illustrated in Fig. 1 consists of a 2m long track, a pendulum with a length of 0.5m and weight of 180g and a cart with a weight of 230g which carries the pendulum along the track.
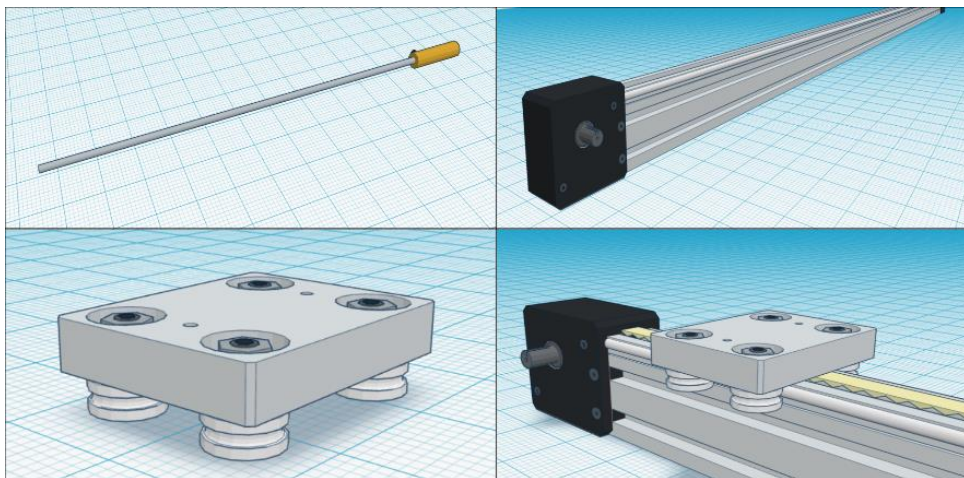


**Figure 1.** Mechanical hardware of the system.

The mechanical hardware used in the physical implementation of the system were chosen to allow the system to operate efficiently, allow experimental work, application of different control methods and algorithms, and to minimize exposure to physical factors that could negatively affect the system such as friction, wear and oxidation. In addition, limit switches are connected to both ends of the track as shown in Fig. 2. With the use of limit switches, the rail length available for vehicle movement has been reduced to 1.86 m.
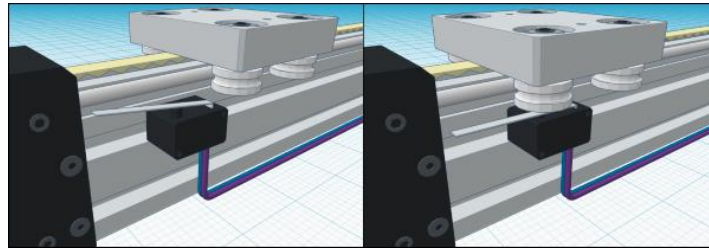
**Figure 2.** Limit switches.

Actuator of the system which provides cart movement is a 3-phase brushless servomotor. Its nameplate ratings are as given in Table 1. A compatible motor drive was also used to control the motor efficiently. Connections of the motor to the track and the drive is as shown in Fig.3.

**Table 1.** Nameplate ratings of the motor.

| Nominal | | | |
|---|---|---|---|
| **Torque** | **Speed** | **Current** | **Voltage** |
| 2 Nm | 3000 rpm | 4A | 220V |
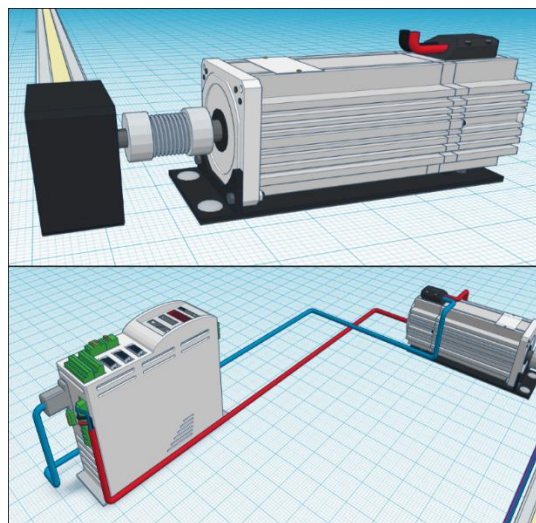


**Figure 3.** Connections of the motor with the track and the motor drive.

## 3. ELECTRONIC HARDWARE

Electronic hardware of the system consists of two rotary encoders which are used for measurement of pendulum angle and cart position, and a DSP. While the pendulum is connected to an optical and incremental encoder for angle measurement, cart position is measured by the internal encoder of the

motor. Pendulum encoder and its connections between the pendulum and the cart are as shown in Fig. 4.
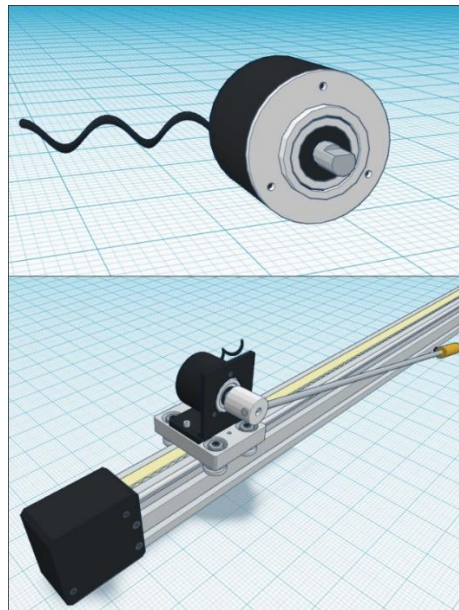


**Figure 4.** Connections between the pendulum, pendulum encoder and the cart.

Incremental encoders used in the system generate sequential two-bit logic signals using two channels separated by 90 degrees of phase shift. Direction and displacement information is obtained by interpreting the signal sequences composed of these signals as in Fig. 5.
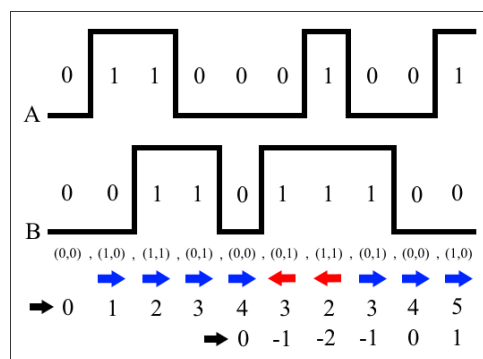


**Figure 5.** Counting of encoder signal sequences.

As seen in Fig. 5, obtaining the direction and displacement information from the encoder signals is not sufficient for detecting the position of the encoder shaft. Because counting of the signals generated by the encoder starts at zero whatever the position of the encoder shaft is when the system is started. For the cart, regardless of its position on the track when the system is started, the two-bit signal sequence

generated by the motor encoder will not be sufficient to determine the position information. As for the pendulum, regardless of its angle at the start of the system, counting of the signals generated by the pendulum encoder starts at zero. Therefore, if the pendulum is already in motion when the system is started, it will cause a shift in angle information. If all these are taken into consideration, it is clear that reference points are required for both encoders. In this study, preferred reference points are the direction of gravity for the pendulum angle and the midpoint of the track for the cart position.

Digital signal processor which is used to control the system in this study is a       TMDSDOCK28335 Experimenter Kit (manufactured by Texas Instruments) which has a TMS320F28335 microprocessor. It has two Enhanced Quadratic Encoder Pulse (eQEP) modules which are both used for reading and processing the encoder signals. Pulse Width Modulation (PWM) required to control the motor speed are generated by the ePWM module. All DSP inputs and outputs used in the system are as shown in Fig. 6 below.



1-) GND
2-) 3.3V
3-) 5V
4-) eQEP1A (GPIO20)
5-) eQEP1B (GPIO21)
6-) eQEP1I (GPIO23)
7-) eQEP2A (GPIO24)
8-) eQEP2B (GPIO25)
9-) eQEP2I (GPIO26)
10-) Limit Switch-1 (GPIO33)
11-) Limit Switch-2 (GPIO34)
12-) ePWM1A (GPIO00)
13-) Activate analog ref. input (GPIO58)
14-) Motor direction (GPIO59)
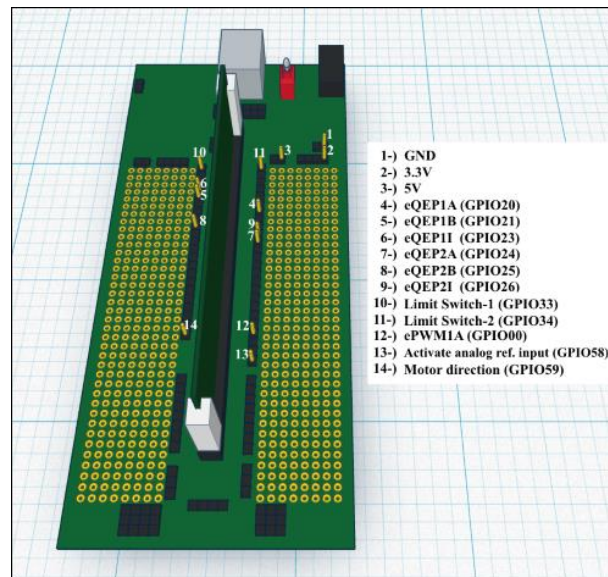
**Figure 6.** DSP inputs and outputs used in the system.

Motion control of the servomotor which is the only actuator of the system is provided by a motor drive [12]. Used analogue and logic inputs of the motor drive are as seen in Fig. 7.
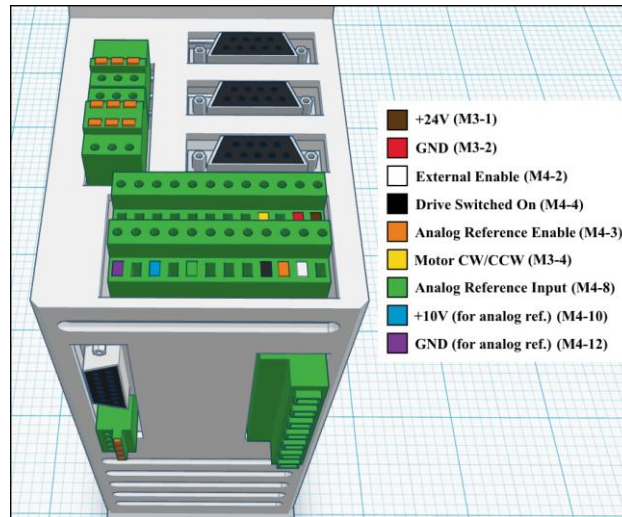
**Figure 7.** Motor drive inputs and outputs used in the system.

For a more compact connection between system components, another board was designed to be placed under the DSP as a dock, as shown in Fig. 8. It has two 5V/3.3V logic level converters for dropping voltage levels of encoder channels (5V) to DSP's input/output voltage level (3.3V).
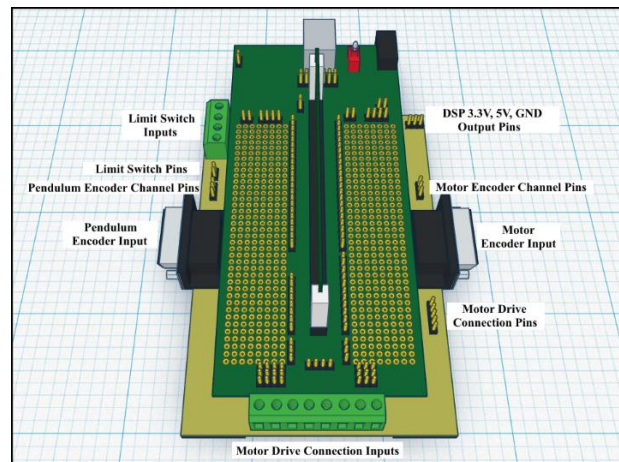


**Figure 8.** Dock design and its connectors.

Designed dock also includes optocoupler circuits for controlling the motor drive inputs which have 10V and 24V voltage levels with DSP output voltage level, which is 3.3V. Connection between analog reference input (M4-8) and +10V reference output (M4-10) of motor drive is being switched using the PWM output of DSP (GPIO00) via a high speed optocoupler. Two more optocouplers are used for controlling logic inputs of the motor drive (M4-3, M3-4). Using optocouplers between DSP and motor drive also provides electrical isolation. Diagram of the mentioned optocoupler circuits is given in Fig. 9.
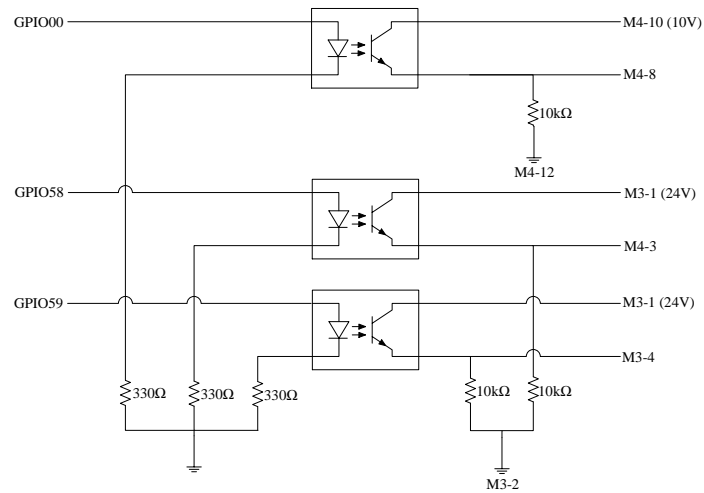
**Figure 9.** Diagram of optocoupler circuits used between DSP and motor drive.

An overview of the system used in the study with all its mechanical, electrical and electronic hardware is shown in Fig. 10.
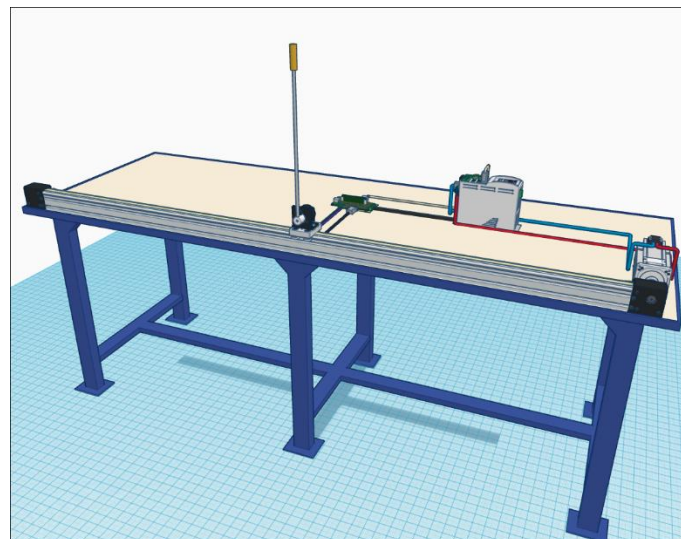


Figure 10. An overview of the inverted pendulum system.

## 4. READING AND CONVERSION OF ENCODER SIGNALS

Two outputs of the system, which are pendulum angle and cart position, are measured by incremental, optical rotary encoders. PPR (pulses per revolution) values are 5000 for pendulum and 2500 for motor

encoder, which means total counts per revolution are 20000 and 10000 for pendulum and motor encoders respectively.

Encoder channel outputs are connected to the DSP's eQEP1 and eQEP2 module inputs. Since these modules count the encoder signals one by one, these counts must be converted to units of angle and length, which are radians and centimetres for this study. For conversion to radians, signal count of pendulum encoder is multiplied by the angle ratio, which is calculated as seen in Eq. 1.

$$r_\theta = \frac{RPR}{CPR} = \frac{2\pi \; rad}{20000} = 0,000314 \; rad \tag{1}$$

$r_\theta$    : *Angle ratio*

*RPR* : *Radians per revolution*

*CPR* : *Counts per revolution*

In order to convert the motor encoder counts to centimetres, it is examined how many encoder signals are generated in the 1 meter movement of the cart on the rail. The length ratio is then calculated as shown in Eq. 2 using the number of counts which is found to be about 27400.

$$r_x = \frac{LPM}{CPM} = \frac{100 \; cm}{27400} \cong 0,00365 \; cm \tag{2}$$

$r_x$    : *Length ratio*

*LPM* : *Length per meter*

*CPM* : *Counts per meter*

## 5. ADJUSTMENT OF ANGLE AND POSITION REFERENCES

Since incremental encoders are used in angle and position measurement in the system, the pendulum angle and cart position at the start of the system take the value of 0. This leads to offsets in the angle and position references, for example, if the pendulum is swinging at the start or the cart is not at the midpoint of the track. For correction of these offsets, a number of conditions have been used.

For the pendulum, the encoder value is desired to be zero at the lower/stable equilibrium point. Since the pendulum is naturally held at this point by gravity while it is still, no reference adjustment is required. However, if the pendulum is already in motion when the system is started, a shift in the angle reference is inevitable. In order to prevent this, first thing the system does as soon as it is started is to check if the pendulum speed is zero or not. If it is zero, then the pendulum is stationary at the lower equilibrium point with the angle value of zero as desired. If not, the system waits for the pendulum to stop at the lower equilibrium point by losing its energy due to frictions and then resets the encoder signal count. Thus, the angle value is set to zero, as seen on Fig. 11.
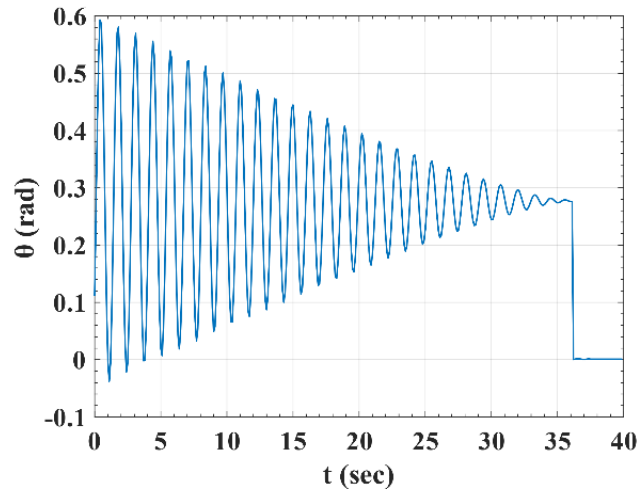
**Figure 11.** Adjustment of angle reference.

For adjustment of position reference, the limit switch on the right end of the track is used. At the start of the system, the cart always goes to that limit switch, no matter where it was in the beginning. When the limit switch gets in contact with the cart and closes, it is obtained that the cart is at the right end of the track. After that, the position value is set to zero and then the cart immediately turns to the other direction and starts moving to the left. When it travels exactly half the length of the track, which is 0.93 m, it immediately stops, and then the position value is set to zero again. At this point, it is ensured that the cart is at the midpoint of the track, with the position value of zero as desired. Fig. 12 shows the adjustment of the position reference after the system is started with the cart is at the left end, midpoint and right end of the track.
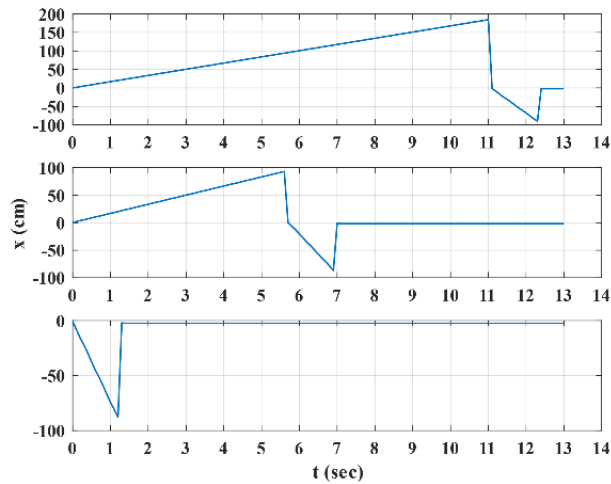


**Figure 12.** Adjustment of position reference.

## 6. SWING-UP METHOD FOR THE PENDULUM

When the angle and position references of the system are adjusted, the cart is in the middle of the track while the pendulum is in the lower/stable equilibrium point. In this state, the position and angle values are both zero as desired. This can be considered as the default state of the system in stable equilibrium.

However, the system is desired to be kept in the state of unstable equilibrium. For this to happen, the pendulum must first be lifted to the upper/unstable equilibrium point. This can be achieved by transferring energy to the pendulum with cart movements. When left-to-right and right-to-left movements of the cart are made at the right times, the pendulum can be given a little more height each time, until it finally reaches the upper/unstable equilibrium point. This is achieved by moving the cart in the opposite direction to the direction from which the swinging pendulum comes, as shown in Fig. 13.
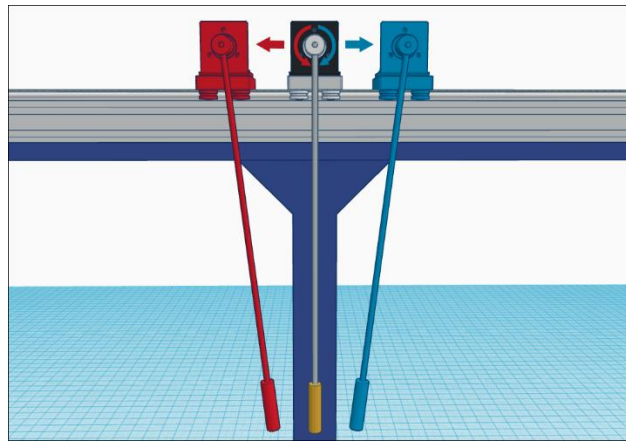


**Figure 13.** Directions of motion during the swing-up process.

For maximum energy transfer from the cart to the pendulum during a swing, left-to-right and right-to-left movements of the cart starts at the moment the pendulum has maximum kinetic energy, which is the lower equilibrium point. Cart movement continues until the pendulum has maximum potential energy, which is the moment the pendulum comes to a stop before it changes direction. Cart motions follow this rule until the angle value of the pendulum is $\pm\pi/2$ rad where it is parallel with the ground. When the pendulum hits those limits during a swing, the cart stops its motion and waits for the next swing. To summarize, the cart moves left-to-right when the pendulum is swinging clockwise and its angle is between the $[-\pi/2$ rad, $0$ rad$]$ range. Similarly, it moves right-to-left for counterclockwise swing in the range of $[0$ rad, $\pi/2$ rad$]$.

Following the method described above, the pendulum gains a little more height with each swing, eventually reaching the upper equilibrium point. However, when the pendulum reaches its peak, it is desired to have a reasonable speed so that it can be easily caught and stabilized by the controller. For this purpose, speed of the cart is gradually decreased in relation to the maximum height the pendulum has reached. In this way, it can be said that the swing-up process starts fast and ends slowly. The

pendulum angle and cart position during the swing-up process with gradually decreasing cart speed can be seen in Fig. 14.
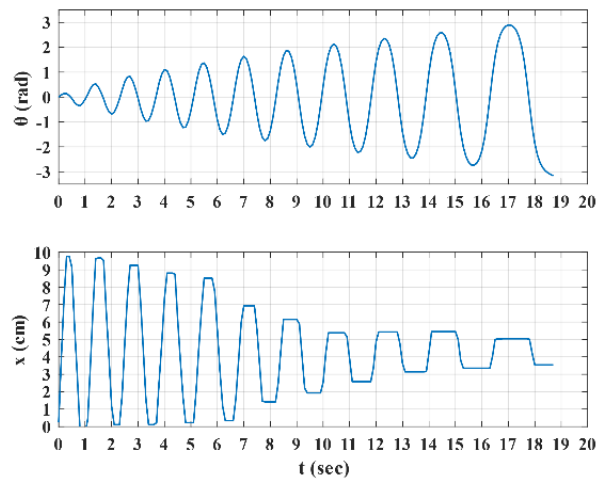


**Figure 14.** The pendulum angle and cart position during the swing-up process.

At the end of the swing-up process, the angle of the pendulum becomes π or -π at the upper equilibrium point, depending on the direction of the last swing. Therefore, at the end of the swing-up process, the angle reference is set to either of those, right before the control process begins and catches the pendulum at the top.

## 7. PID CONTROL OF THE SYSTEM

For the stabilizing of the system at the upper/unstable equilibrium point, a classical PID controller is used. As soon as the swing-up process raises the pendulum to the top, it is caught by the controller and held there, while keeping the cart in the midpoint of the track. As a single input and two outputs control system, angle error of the pendulum and position error of the cart are both eliminated by the algorithm. As seen in Fig. 15, two separate PID controllers are used for pendulum angle and cart position.
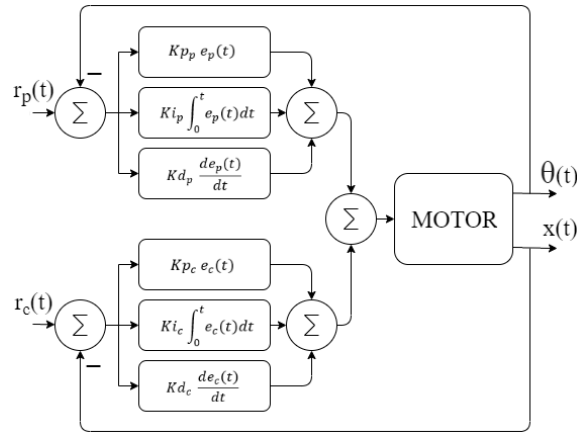
**Figure 15.** Block diagram of the control system.

As digital signal processors work in discrete time, approximate values of the integral and derivative terms are calculated with a discrete approach. Discrete time equivalents of the analog expressions in the controller blocks in Fig. 15 are calculated as follows [8]. $T_s$ terms seen in Eq. 4 and Eq. 5 represent the sampling period, which is 10 ms.

$$K_p e(t) = K_p e[\text{n}] \tag{3}$$

$$K_i \int_0^t e(t)dt \cong K_i T_s \sum_0^n e[n] \tag{4}$$

$$K_d \frac{de(t)}{dt} \cong K_d \frac{e[n] - e[n-1]}{T_s} \tag{5}$$

After the angle and position errors are processed in their dedicated controllers and two separate controller outputs are produced, they are added together to become a single control output which is used as the duty cycle value of the PWM signal generated by the DSP. Since the output voltage level of the DSP is 3.3V, it gets converted to 10V using the optocoupler circuit shown in Fig. 9. This PWM signal with the 0-10V voltage range can be seen as the ultimate controller output, since it is applied to the analog reference input of the motor drive, which determines the motor speed. A flowchart of the system with all its processes is given in Fig.16 below.
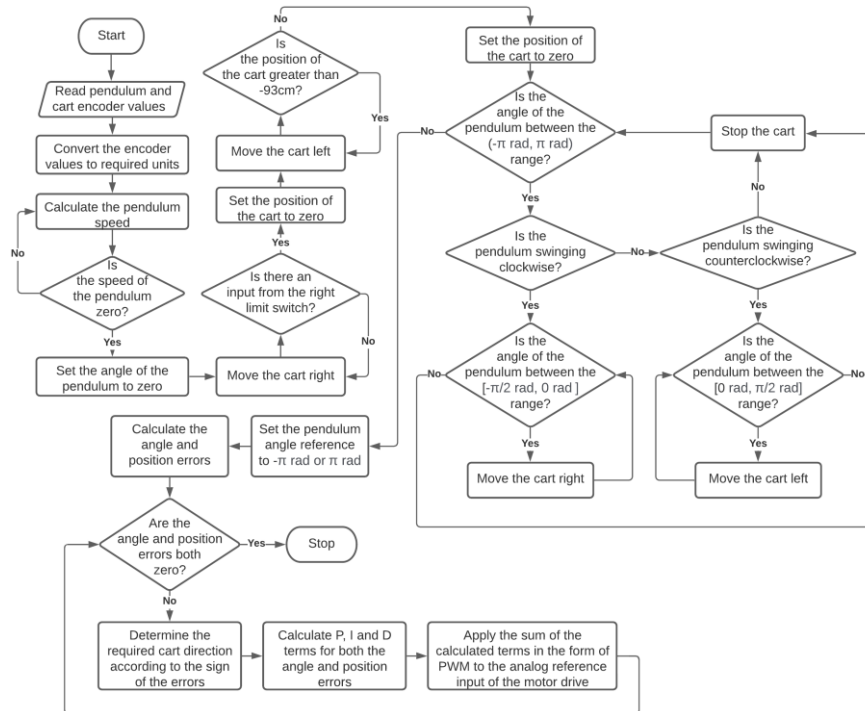
**Fig. 16** A flowchart of the system with all its processes.

$K_p$, $K_i$ and $K_d$ parameters for the pendulum and the cart are determined heuristically by making small changes and observing the system behavior. By eventually setting the appropriate values, system could be stabilized as shown in Fig. 17. From the figure, it can be deduced that when the system was started, the cart was already around the midpoint of the track. However, the system did not yet have this information. Therefore, it adjusted the position reference by moving the cart to the limit switch at the right end of the track, and then bringing it back to the midpoint again. After immediately starting and ending the swing-up process, it is seen that the system is stabilized around 35th second.
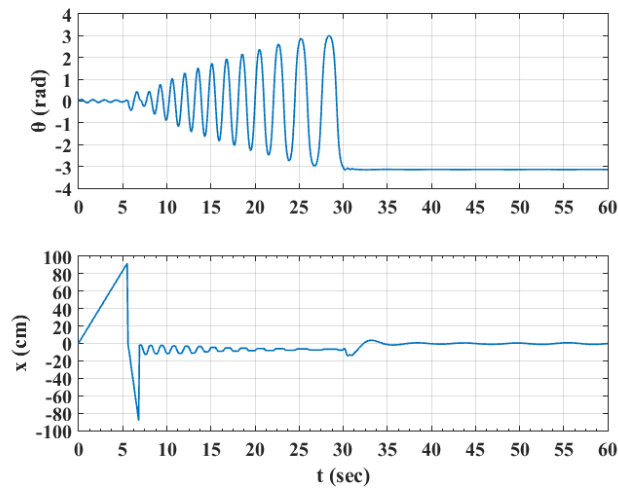
**Figure 17.** PID control of the inverted pendulum system.

After stabilizing the system with corrected angle and position references, a new feature has been added to the system by making the position reference variable. By pressing the limit switches at both ends of the track, position reference of the cart can be increased or decreased. Therefore, the cart can be moved along the track while still keeping the pendulum at the equilibrium point. In Fig. 18, it is seen that the position reference was increased up to around 50 cm by pressing the limit switch at the right end of the track at around $50^{th}$ second. Then it was decreased down to around -50 cm using the other limit switch. Finally it was brought back to the midpoint of the track. It is seen that the stability of the system was maintained throughout these processes. Also, at around $40^{th}$ second, a disturbance was applied to the system by poking the tip of the pendulum. This shows that the system resists external disturbances by stabilizing itself again.
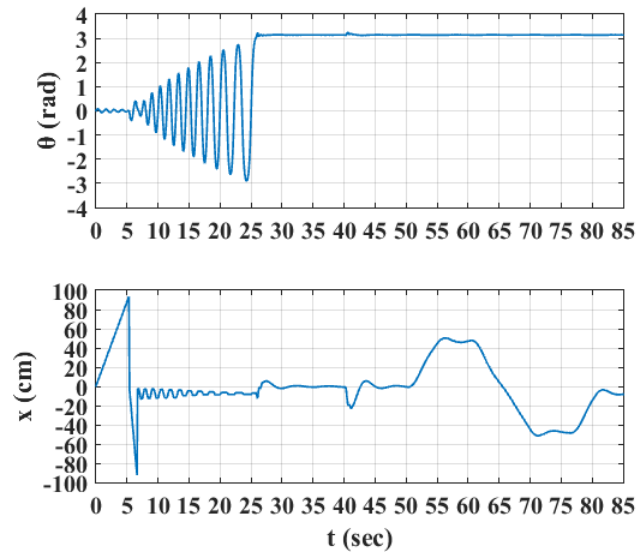
**Figure 18.** PID control of the system with variable position reference.

## 8. SUMMARY AND CONCLUSION

In this study, a PID controlled inverted pendulum system shown in Fig. 19 was designed and implemented. Controller parameters were tuned by hand heuristically. It was acknowledged that even for highly unstable, underactuated, single input and multiple output systems, the PID algorithm still proves its efficiency, reliability and convenience. It was seen that in the worst case, where the initial conditions of the system are pendulum being dropped from the highest point and the cart being at the left end of the track, it takes approximately 78 seconds for the system to reach steady state. In further studies, performance, stability and robustness of the system can be further improved by fine tuning the control parameters.
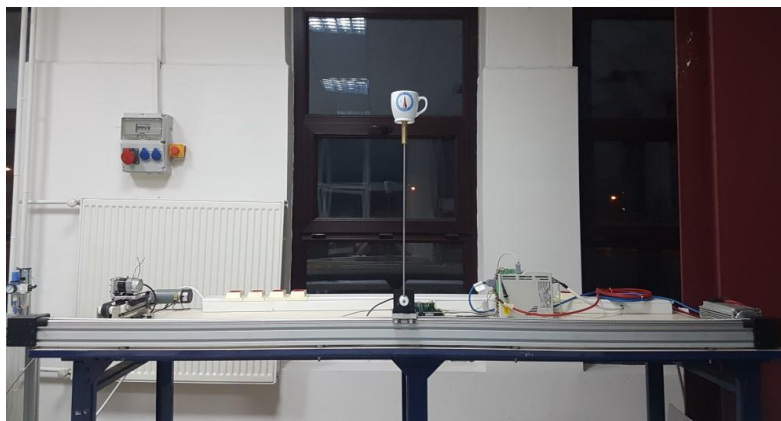


**Figure 19.** Inverted pendulum system.

155

**ACKNOWLEDGEMENTS**

**REFERENCES**

[1] Lozano, R., Fantoni, I., Block, D.J., (2000), Stabilization of the inverted pendulum around its homoclinic orbit, System & Control Letters 40, s.197-204.

[2] Huang, S.J., Huang, C.L., (2000), Control of an inverted pendulum using grey prediction model, IEEE Transactions on Industry App. 36(2), s.452-458.

[3] Gani, A., Açıkgöz, H., Kılıç, E., Şit, S., (2014), Ters sarkacın bulanık mantık esaslı denetimi, Elektrik-Elektronik-Bilgisayar ve Biyomedikal Mühendisliği Sempozyumu ELECO'14, s.347-350.

[4] Elibol, G., (2015), Bir Ters Sarkaç Denetimi Gerçeklenmesi, Yüksek Lisans Tezi, Eskişehir Osmangazi Üniversitesi Fen Bilimleri Enstitüsü, Eskişehir.

[5] Kajita, S., Kanehiro, F., Kaneko, K., Yokoi, K., Hirukawa, H., (2001), The 3D linear inverted pendulum mode: A simple modeling for a biped walking pattern generation, International Conference on Intelligent Robots and Systems, s.239-246.

[6] Sugihara, T., Nakamura, Y., Inoue, H., (2002), Realtime humanoid motion generation through ZMP manipulation based on inverted pendulum control, International Conference on Robotics & Automation, s.1404-1409.

[7] Pathak, K., Franch, J., Agrawal, S.K., (2005), Velocity and position control of a wheeled inverted pendulum by a partial feedback linearization, IEEE Transactions on Robotics 21(3), s.505-513.

[8] Gün, A., (2007), Yetersiz Uyarımlı Bir Elektromekanik Sistem Gerçeklenmesi ve Denetimi, Doktora Tezi, Eskişehir Osmangazi Üniversitesi Fen Bilimleri Enstitüsü, Eskişehir.

[9] Grasser, F., D'Arrigo, A., Colombi, S., Rufer, A.C., (2002), JOE: A mobile, inverted pendulum, IEEE Transactions on Industrial Electronics 49(1), s.107-114.

[10] Sharif, B.A., (2013), A Sliding Mode Control For Inverted Pendulum System, Yüksek Lisans Tezi, Gaziantep Üniversitesi Fen Bilimleri Enstitüsü, Gaziantep.

[11] Kharola, A., Patin, P., Raiwani, S., Rajput, D., (2016), A comparison study for control and stabilisation of inverted pendulum on inclined surface (IPIS) using PID and fuzzy controllers, Recent Trends in Engineering and Material Sciences 8, s.187-190.

[12]  http://www.bdfdigital.com/PDF_ITA/BROCHURE/BDF_DIGITAL_OPDE.pdf

*RESEARCH ARTICLE*

## INNOVATIVE METHOD FOR THE DIAGNOSIS of DISEASES: E NOSE

Cihat TAŞALTIN[1*]

[1] TUBITAK Marmara Research Center Materials Institute 3B Excellent Center P.O. Box 21, Kocaeli,
cihat.tasaltin@tubitak.gov.tr, ORCID: /0000-0002-8978-802X

**ABSTRACT**

E-nose systems can be used in different applications which are varying from explosive and chemical hazardous detection to health applications using breath analysis such as lung cancer, and Covid -19 diagnosis. One of the best practices of the E-nose application is breath analysis for disease diagnosis. Exhaled breath is a mixture of water and Volatile Organic Compounds (VOCs) in very low concentration which was shown via Gas Chromatography(GC) or other possible technologies. Electronic Nose (E-Nose) seems to be the best solution to the development of analyzing system for diagnosis using breath. Conventional E-nose incorporates non-selective gas sensors that are called sensor array and data recognition part which having artificial intelligence algorithm. Due to the performance of gas sensors is negativily effected by the humidity in the environment, the most important problem encountered in practice is the negative effects of uncontrollable external effects such as humidity on the E-nose system.

In this study, a $CaCl_2$ tube was equipped to the gas inlet of the E Nose system to reduce the effect of variable humidity in environments. The tube enabled that only the gas of interest passes onto the sensors and trap the ambient humidity. Positive results on sensor responses are shown by using PCA method. It is assumed that this approach will make significant contributions to the development of methods based on breath analysis.

**Keywords:** *Gas Sensor, Disease Diagnosis, VOC Detection, SAW Sensor, E-Nose*

## 1. INTRODUCTION

Humans release to the environment complex molecules which of them volatile and nonvolatile by the effect of an individual's genetics, health, diet, and stress during their life. Many body odors include being olfactory messengers, which convey information about health and physiological status between individuals. Measuring the changes in the breath profile is a recommended method for the easy diagnosis of diseases. However, technological impossibilities in terms of the changes in the breath profile. In modern life, the scents have been taken into account for disease detection again because it is a non-invasive technique. Gas sensors could provide ideal platforms to solve this problem for realizing portable, hand-held breath. Exhaled breath is a mixture of water and Volatile Organic Compounds (VOCs) in very low concentration which was shown via Gas Chromatography(GC) or other possible technologies. [1-3].

Since the 1970s,  most researchers were focused to explain the composition of the human breath. It has been shown that exhaled breath includes some chemicals such as ethanol, phenol, benzene, propanol, acetone, and their derivatives. In the following years, research activities were carried out to reveal the relationship between the disease and these chemicals [4-6]. The main reason for the evolution of the studies is VOCs that originate from organs that are transported by the bloodstream, to the alveoli, where diffusion into the exhaled breath takes place[7].

VOCs present in exhaled breath as result of part of the metabolic process such as fractioning of larger molecules. The major fractions of saturated hydrocarbons in exhaled breath are from oxidative stress and resulting in extensive cellular damage. On the other hand, saturated hydrocarbons such as Isoprene and derivatives could be from the chemical reaction for cholesterol biosynthesis or bacterial origin in the human body. The decreases in isoprene levels have reported as the effect of acute respiratory distress syndrome, cystic fibrosis, and asthma [8-10]. Also, isoprene levels can change in physiological and pathophysiological conditions (including hemodialysis, general anesthesia, liver disease and cancer). Breaths which include sulphur-containing were reported for incomplete metabolism of methionine via the transamination pathway[11] and ammonia level is also influenced by cigarette smoking [12] in the range of 245–2935 ppb in breath for normal healthy humans[13]. This level may be related to bacterial production in the oral cavity [7].

Using the breath analysis for the diagnosis of disease, several factors and parameters should be taken into consideration. Because, the biological mechanism of the human body is a complex and non-linear process thus, exhaled breath includes a complex composition. Therefore, the correct relationship must be established between the markers which are indicating the disease. This process must be completed with the cooperation of clinical study and instrumental chemistry unit using GC-MS and other functional devices. In practice, Chromatography (GC) and Mass Spectrometry (MS) are commonly used as devices with solid-phase extraction (SPE) and solid-phase microextraction (SPME) for the analysis of breath. Via help of the unique spectrum and retention time of each molecule can be separated from another's and/or derivatives. Although GC-MS produces high accuracy results, it is quite expensive and requires expert staff to use. For this reason, research and development activities are carried out on alternative, inexpensive, and easy-to-use devices. Electronic Nose (E-Nose) seems to be the best candidate as an alternative technology to obtain highly accurate data for the diagnosis. Conventional E-nose incorporates non-selective gas sensors[14] that are called sensor array and data recognition part which having artificial intelligence algorithm. The working methods of E-nose were mimicked from the mammalian olfactory system for the discrimination of odors. In the E-Nose system; odor receptor cells and neural processing are represented by the gas sensors and microprocessor as a respectively[15]. Utilizing sensor arrays, an E-nose detects patterns in complex mixtures which may have include water vapor of exhaled breath VOCs [7].

One of the challenges of the practical application of electronic noses is that the interested gases are a small part of the whole ambient atmosphere and shadowing of water vapor to all signals. Technically, sensors may also be sensitive to water vapor which can be call background gases thus, the sensor signals cannot represent the analyzed atmosphere[16]. Therefore, the E-nose must be highly selective against only interested gases. This is why sensor development studies will increasingly continue to

obtain the perfect solution to the interesting problem. Many researchers all over the world have been working development of sensors using different sensing materials and methods.

The gas sensing mechanism of a Surface Acoustic Wave (SAW) sensor is based on the absorption of gas molecules by the sensing film, then changing of velocity and attenuation of the wave. These changes can be measured by the oscillator circuit with high accuracy and sensor responses occur via frequency shift. Film conductivity is one of the parameters of wave attenuations. The frequency shift of the SAW sensor's in terms of wave propagation $(\frac{\Delta v}{v_0})$ and attenuation $(\frac{\Delta \alpha}{k})$ can be given in equation 1 and 2.

$$\frac{\Delta \alpha}{k} = \frac{K^2}{2} \frac{v_0 C_s \sigma_s^2}{\sigma_s^2 + (v_0 C_s)^2} + 4C_e \frac{f_0}{v_0^2} (\Delta h G'') \tag{1}$$

$$\frac{\Delta v}{v_0} = -C_m f_0 \rho_s + 4C_e \frac{f_0}{v_0^2} (\Delta h G') - \frac{K^2}{2} \frac{\sigma_s^2}{\sigma_s^2 + (v_0 C_s)^2} \tag{2}$$

Where, $K^2$ is the electromechanical coefficient, $\sigma_s = \sigma h$ is surface conductivity, $G'$ and $G''$ is a constant number which is realted to elasticity properties of sensing film, $\sigma$ is bulk conductivity, $C_s$ is the total dielectric permittivity of the substrate and sensitive film. The electrical charge of the sensitive film is one of the reasons for the frequency shift of SAW. When the analyte is absorbed by the sensing film, the surface electric charge changes and causes a change in wave velocity[17, 18]. This process is one of the important mechanisms of SAW in frequency shift and $K^2$ is an important factor determining the perturbation of the SAW.

This study is focused on establishing the right relationship between the exhaled breath and gas sensor systems. In general, a gas sensor is consisting of two components; a transducer and sensing materials. The role of these components is transferring chemical signals to the electronic signals without knowledge loss in the sensor system. The size of the sensor system should decrease according to modern device requirements such as the More Law postulate. Therefore, the fabrication of transduction systems benefits from the help of microfabrication techniques and it has become possible to produce functional structures with small dimensions. The other component, sensing material determines the features of the sensor such as stability, accuracy. Metal oxides [19], macrocyclic organic molecules, and metal-organic-frames are often used materials in gas sensors. In this article, we are not considering the interaction between the sensing materials and measured because our sensors had been prepared before analyzed and published in a different journal. We are considering to avid dominant background gases shadow effect on sensor response during the designing of the device for health or any other application.

## 2. MATERIALS AND METHOD

### 2.1. Sensors
In this study, the dual-port resonator SAW transducers having 433 MHz frequency (SAW Components Dresden GmbH, Germany) located on a TO-39 socket were used. Metal oxide nanoparticles that are mixed with polymers and macrocyclic organic molecules were used as sensitive materials. Our sensors were prepared before for the determination of lung cancer diagnosis inbreathe

and published in different journals. Therefore, in this study, we are not mentioning sensor preparation, sensing materials, sensitivity, selectivity, and sensing mechanism of our used sensor.

**Table 1.** Sensor list and sensitive materials.

| Sensor Number | Coating Materials |
|---|---|
| Sensor 1 | Compound Number 11 at [20] |
| Sensor 2 | Compound Number 12 at [20] |
| Sensor 3 | S1 at [2] |
| Sensor 4 | S2 at [2] |
| Sensor 5 | S3 at [2] |
| Sensor 6 | S4 at [2] |

### 2.2. Sensor Measurements in Controlled Atmosphere

Sensors were tested against VOCs using two different test systems. First of all (Fig. 1a,1b), it is a conventional test system having a thermally controlled bath that can generate gas using bubblers with synthetic air as the carrier gas and generated gas concentration is changing range of 500-5000 ppm. The desired gas concentration was adjusted by mixing pure dry air and gas stream saturated with the analyte in a different ratio. Total gas flow was kept at 300 sccm (ml/min) and all flows were adjusted by using Mass Flow Controller (MFC, MKS Instruments Inc., USA) with computer-driven. Sensors were exposed to the desired concentration and/or binary mixed gases and also were kept at 22°C during the measurement to avoid the negative effect of temperature and environmental conditions. All measurements were carried out sequentially in dry air and gas (figure 6 in section 3.1).
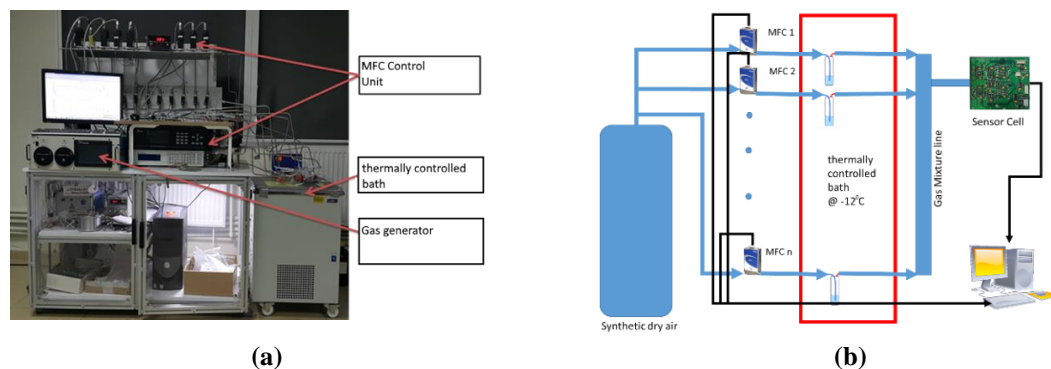


**Figure 1.** a) Photo, and b) Schematic representation of conventional sensor test system.

The second test system has two temperature-controlled chambers with mass flow controller which were used for dilution and carrier. Each chamber can be adjusted from 30°C to 110°C, regulated to ±0.01°C to provide accurate, precise results. The carrier stream mixes with the calibration gas in the chamber and is then fed forward to the mixing tee (Fig. 2a). This system contains a permeation tube to the regeneration of low concentration gas. The generated gas concentration depends on the chamber temperature.

The sensors were kept in temperature-controlled chambers of 4 ml volume and frequencies of each SAW sensor were read out respectively using a multiplexing technique. To avoid high frequencies of the operation frequency difference between reference and sensor SAWs were processed and the seventh uncoated device was used as a reference.

Prepared sensors were performed using the first system against VOCs such as toluene, hexane, ethanol, isoprene, and a binary mixture of water vapor. The concentrations of each gas were varied in the range of 100–5,000 ppm and water vapor was varied in the range of 20-80 %. The performance of the sensors against VOCs in low concentration was determined via the used gas generation device with permeation tubes (Fig. 2b). Gas generation device generated the gases which concentration was varied between 0.14 ppb and 4.2 ppb at 100 sccm synthetic dry air gas flow (Table 2).

The reason for generation low concentration wherein the real application trace gas concentration is very low such as varying 1-5 ppb in lung cancer patient breathing.



| (a) | (b) |
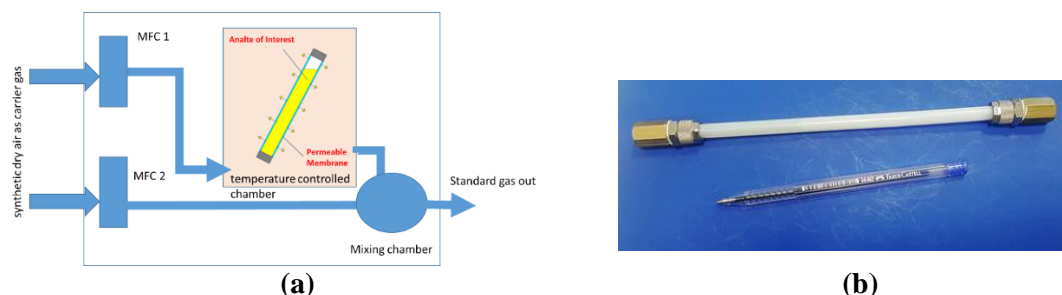
**Figure 2**. a) Schematic representation of gas generation system, and b) homemade permeation tube.

**Table 2.** Considered VOCs and concentration of in 100 sccm gas flow for the homemade permeation tube.(1 mg/ml = 1000 ppb).

| VOCs | The amount of Total Mass before(mg) | The amount of Total Mass After(mg) | Duration (min) | Evaporated Mass(mg) | The amount of mass evaporating per minute in 100 sccm gas flow(mg) | Concentration (ppb) |
|---|---|---|---|---|---|---|
| Toluene | 75.5804 | 75.2987 | 8580 | 0.2817 | 0.00032 | 0.32 |
| Hexane | 87.0454 | 86.8156 | 6720 | 0.22970 | 0.00034 | 0.34 |
| Ethanol | 87.707 | 87.6070 | 6720 | 0.100 | 0.000149 | 0.14 |
| Isoprene | 76.626 | 76.1722 | 1080 | 0.4538 | 0.00420 | 4.20 |

**2.3. Sensor Measurements in Uncontrolled Atmosphere**

One of the challenges for medical application which based on the gas sensor (E-Nose) is the interference effect and resulting in decreasing sensitivity and selectivity. The best way to reduce this negative situation is to include effective solutions to eliminate these effects in the system. The water vapor has a negative effect on gas sensors because of having high polarity and gets adhere to the

surface of the sensor. It is necessary to carry out some pre-processing steps in order to remove analytes from the sample that may have negative effects on the measurement setup or sensors to obtain high accuracy data with minimum error. The best known of these processes is the addition of kind of solid-phase extraction (SPE) solutions. SPE works as a separator to remove interferences constituents in the sample from collected health and the environment[21].

It is necessary to carry out some pre-processing steps in order to remove analytes from the sample that may have negative effects on the measurement setup or sensors to obtain high accuracy data with minimum error. The best known of these processes is the addition of kind of solid-phase extraction (SPE) solutions. SPE plays a crucial role in sample pretreatment, removal of interferences, and elimination of sample constituents in health and environmental analyzes [21]. Kind of solid-phase extraction (SPE) solutions. SPE plays a crucial role in sample pretreatment, removal of interferences, and elimination of sample constituents.

In this study, SPE columns (Agilent catalog number: GT-C-AT010C) were used to enrich total analytes up to detectable levels and elimination of undesired molecules in breath samples. Water vapor was trapped by the using $CaCl_2$ column located before SPE columns. Thus, water molecules were removed from the samples without changing the quantity of interested gas.
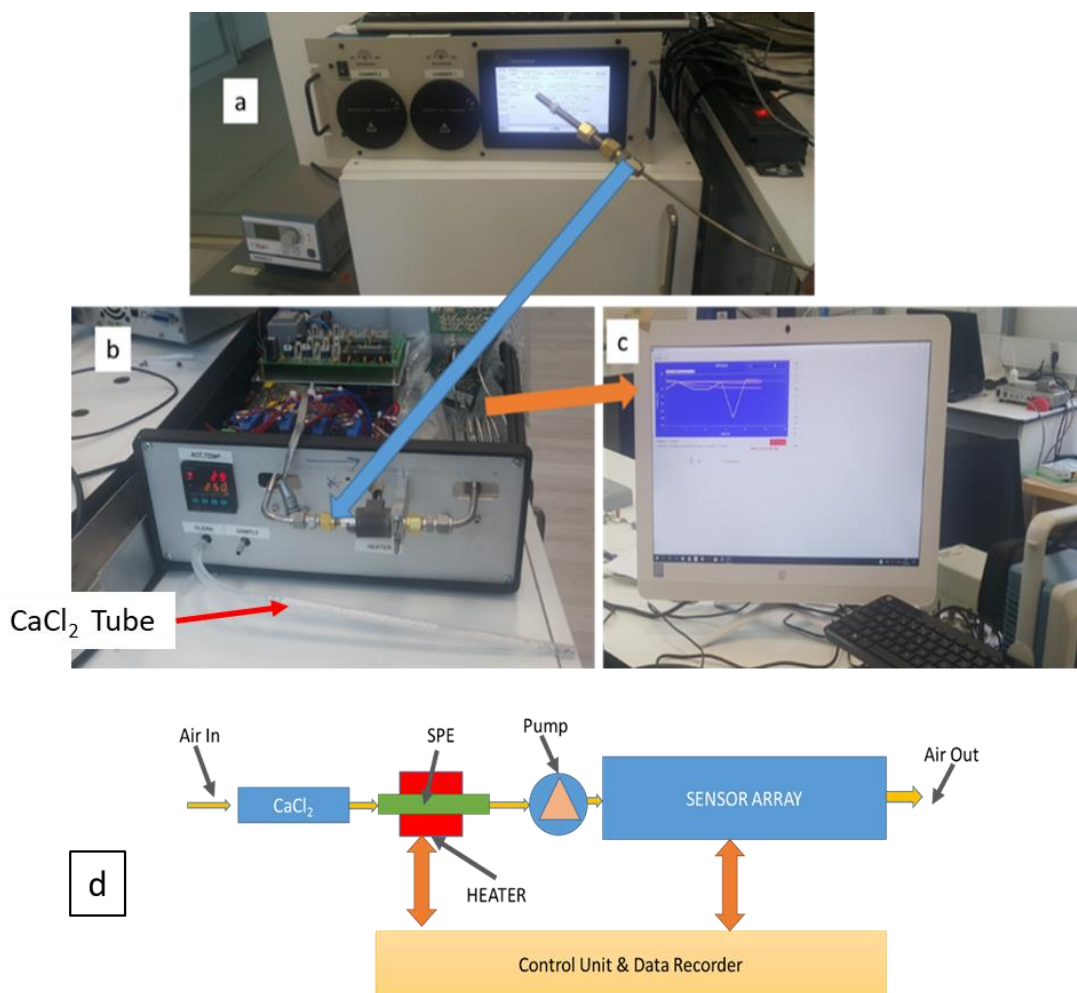
**Figure 3.** a) Gas generator (at the gas collecting stage)  b) E-Nose mesurement system and $CaCl_2$ tube c) Data collection software interface d) Schematic representation of E-nose system. SPE columns were marked between Fig. 3a to 3b with blue arrow.  The raw sensor data was transferred to the PC via RS 232 interface in each 2 s. Data transfer line was marked with orange arrow.

In the real application, humidity levels in the test ambient cannot be under control, and analytes concentrations varying as well as 1-5 ppb. To obtain performance data in real ambient of E-nose, SPE tubes were exposed to analytes using the gas generator at 100 sccm flow for the accumulation at three different times (30, 60, and 120 min). After the collection procedure than, the SPE column was placed into the E-nose system and flash heated for the fast desorption in a few seconds, and the sensor was exposed to desorbed gases to obtain responses (Fig. 3).  Arranging the application in this way is the copy from the standard GC-MS procedure with the thermal desorption system.  Measurement environment temperature was at room temperature and humidity was varying 45-60 % RH.  Despite this change in humidity resulting from the measurement ambient, the humidity sensor (SHT 75) that

was placed in the sensor array did not read more change and the readings were around 15%. This value is at the border of the region where humidity sensors are linear and for this reason, it may not be able to measure with high accuracy at a very low humidity value. So, it is possible that the actual moisture value was lower than the measured. The temperature of the air was also not increased during the gas flowing into the sensor chamber and temperature changes were lower than 2-3°C at RT.

## 3. RESULTS and DISCUSSION

Using conventional test systems that are shown in Fig. 1, toluene, hexane, ethanol, and isoprene were exposed to sensors with single gas and mixture background humidity at 80 %. The reason for measurement configuration is to observe the effect of moisture on sensor responses. The second evaluation was performed using gas generation to getting sensor performance at the low-level concentration ambient.

### 3.1. Sensor Performance at in Controlled Atmosphere

The obtained response of sensors to VOC's vapor in dry air and with the %80 humidity background are depicted in Fig. 4,5, respectively. The sensor responses are linearly increasing or decreasing with concentration. A linear fit to the response data (frequency shifts during analyte exposure from baseline) vs. concentration was made and the slope is the sensitivity (Hz/ppm). The response of each sensor is different from the others for each gas, theses case is a desired event for the E-Nose application. Even if simple Artificial Intelligence (AI) algorithms can be sufficient to distinguish these different situations and identification of gas ambient.
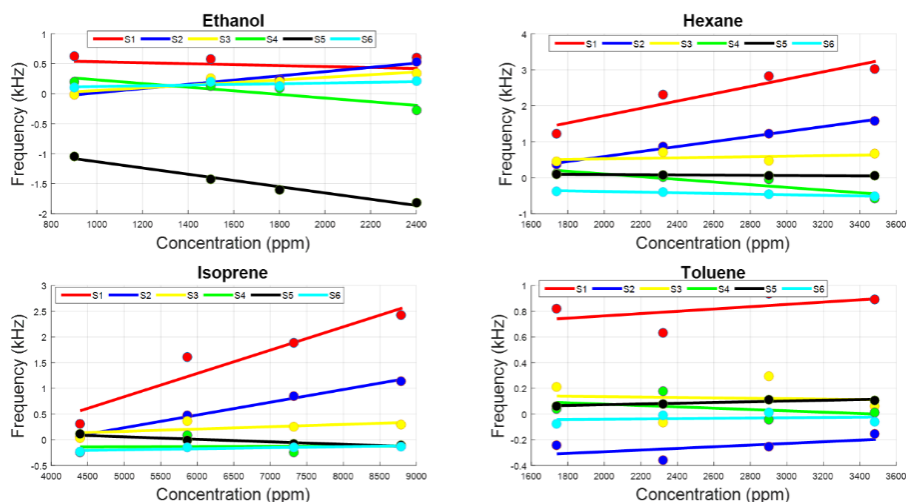


**Figure 4.** Sensor responses against the considered VOCs at 0 % Rh condition.

The characteristics of the sensors varied depending on the acoustoelectric effect formulated in Equation 2. Sensor 4 and 5 have an opposite response for ethanol and isoprene at 0 % Rh while they sensed the toluene sharply. In 0 % Rh gas ambient (Fig. 4, Toluene) the sensors have lower responses in positive direction on the contrary to the other sensors. Furthermore, in the 80 % Rh gas ambient the sensors have higher responses in negative direction, and also sensor 4 has a low response in positive

direction (Fig. 4 and Fig. 5). The results reveal that the adsorbed gas by the sensitive materials is changed surface mass, conductivity, and elasticity.

The generated acoustic wave propagates onto the surface of the transducer and inside of the sensing film. In any change of characteristics due to the absorption or adsorption step is affected from the amplitude and velocity of the wave. This acoustoelectric effect has been discussed before and how the sensor response changes with under these effects [17].
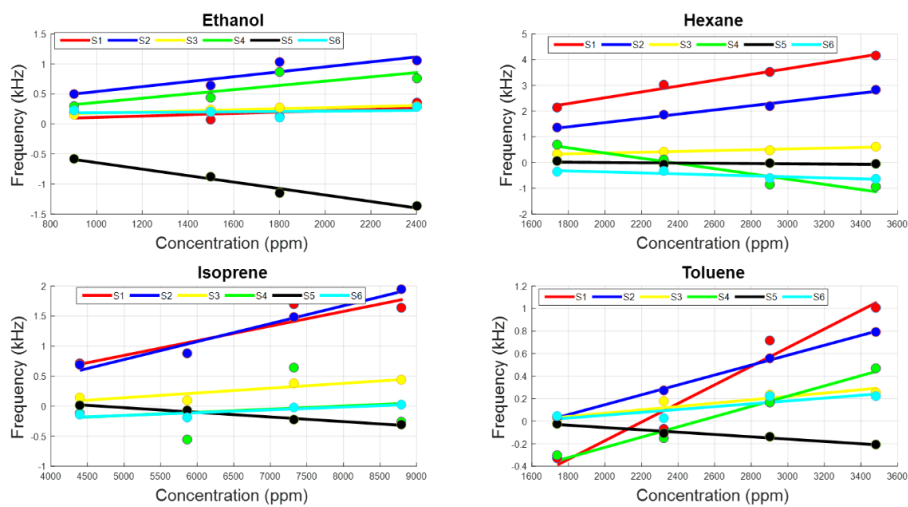


**Figure 5.** Sensor responses against the considered VOCs at 80 % Rh condition.

Besides this, background humidity is having a negative or positive effect on the sensor responses thus response characteristics are change depends on humidity level (Fig. 6). In this case, it will not be easy to discriminate each gas medium from each other with high accuracy using AI that is the main part of E-Nose.



| (a) | (b) |
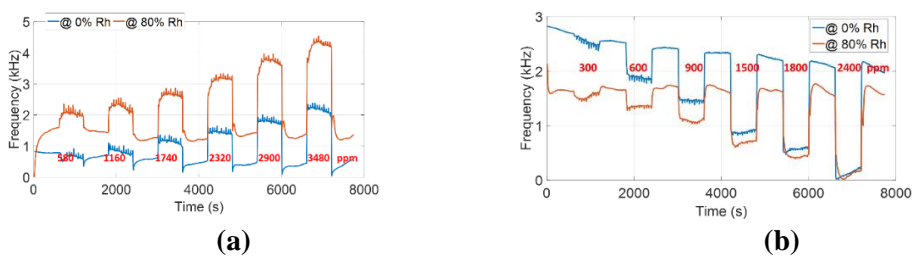
**Figure 6.** a) Responses of Sensor2 against hexane and b) Responses of Sensor5 against ethanol at 0 % and 80 % Rh ambient.

The gas media becomes complex with the including of humidity to the gas environment. This situation has a negative or positive effect on the sensor response decrease and increase (Fig. 6a , 6b). Since this interaction will occur at every humidity level, it will necessitate the addition of a new

dimension to the data during the processing. For this reason, all negative parameters on the system must be removed such as humidity. The best solution to prevent humid from reaching the sensors but not retaining other gases is to add $CaCl_2$ in front of the sensors.

### 3.2. Sensor Performance at in Uncontrolled Atmosphere

Up to now, the effect of humidity change on the sensor response is discussed. The algorithms for the analysis of data will never be sufficient to understand and determine the real environment. The complexity of the real atmosphere is seen in Fig. 7-10. During the measurement, periodicity could not be performed because uncontrolled atmosphere tests were carried out manually. Therefore, the gas on and off times for each measurement have minor differences, and to make a clear, duration of "gas on" is marked on the graphs as shown in Fig. 7-10. Sensors were tested against ethanol, isoprene, hexane and toluene with three different concentrations. Gas concentrations were adjusted via gas collecting by using SPE in 30, 60, 120 min. Typical experiments were performed in approximately 300 s gas exposure and purging with environmental air which is passing through $CaCl_2$, respectively. "Gas On" in Fig. 7-10 in all graphs depicts the gas exposure time which marked with red, blue, and black for 30, 60, and 120 min gas collecting duration respectively.
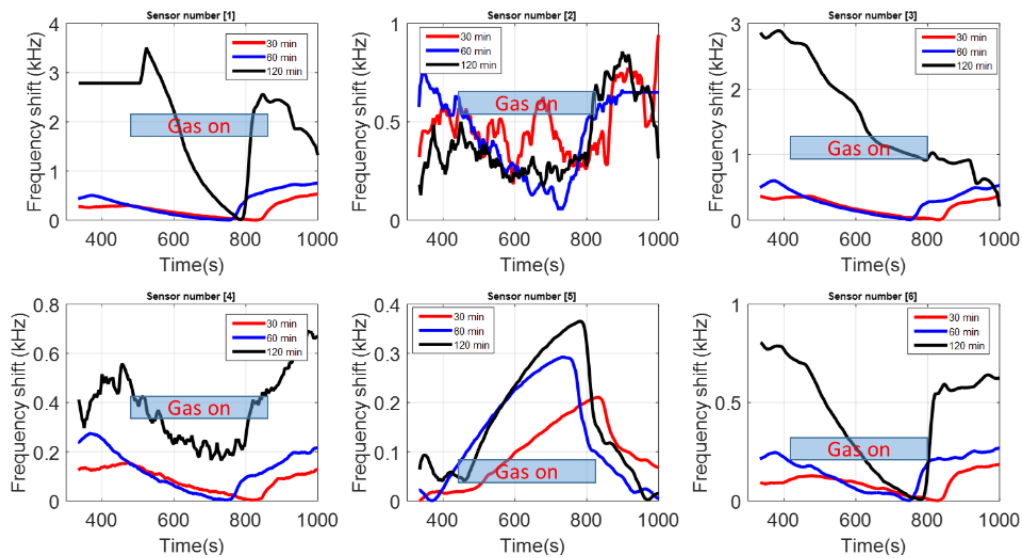


**Figure 7.** Responses of the sensors against ethanol with three different concentrations.
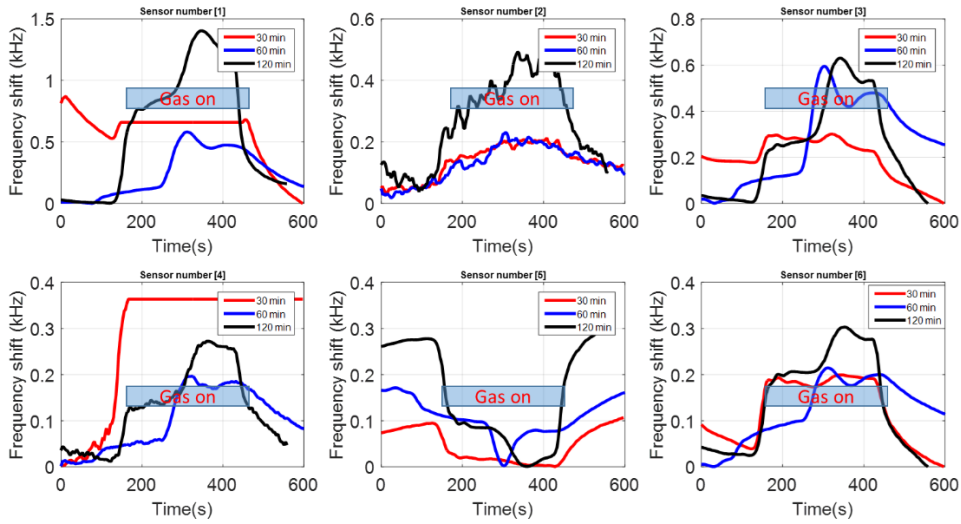
**Figure 8.** Responses of the sensors against isoprene with three different concentrations.
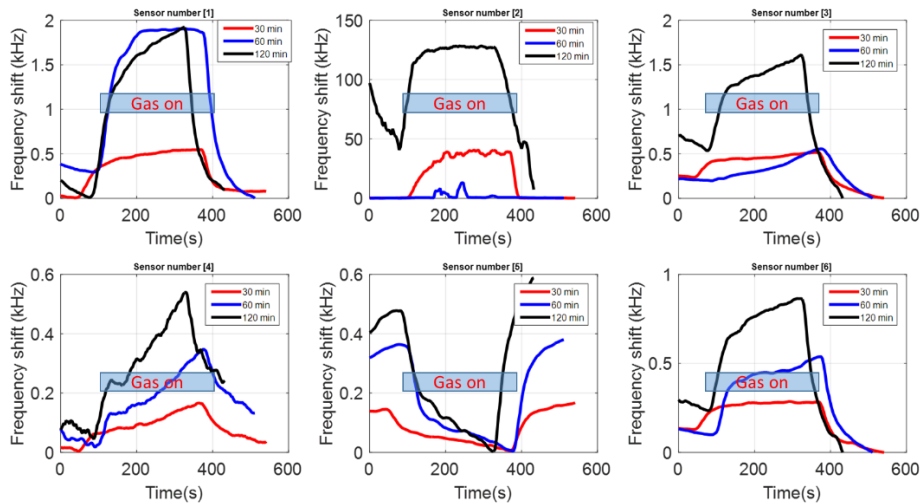


**Figure 9.** Responses of the sensors against hexane with three different concentrations.
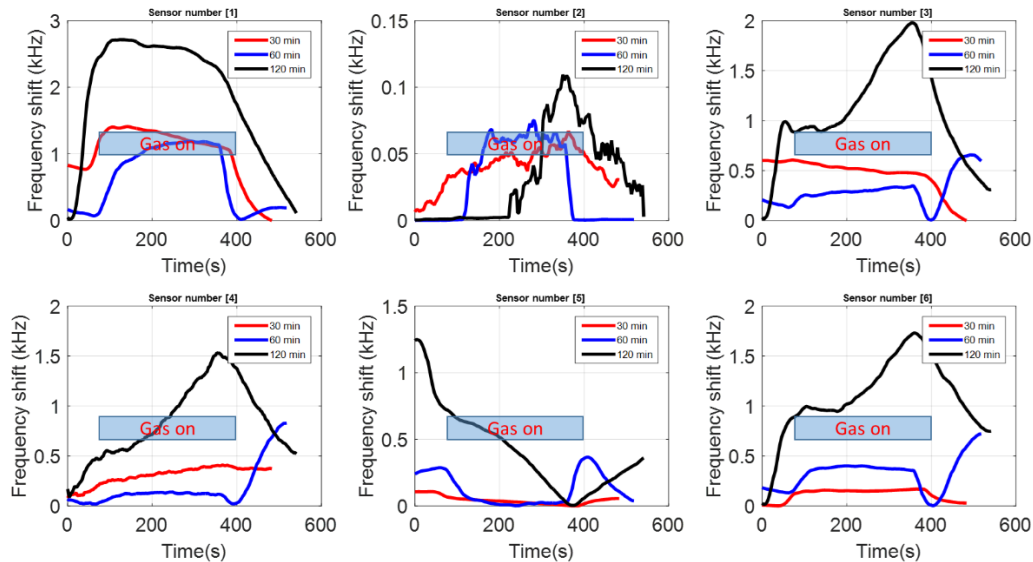
**Figure 10.** Responses of the sensors against toluene with three different concentrations.

Sensor responses increased as parallel as accumulation time of SPE and measurement ambient has not affected the response. $CaCl_2$ was absorbed water vapor in the air and prevented reaching the sensors. This situation has been observed via changing 1-2% on the humidity level on the humidity sensor. The interaction between gas and sensors has specified the selectivity and sensitivity. The sensitivity of the SAW-based sensor depends not only on the interaction relationship between gas and sensors but also on the acoustoelectric effect. According to equation 1, if the $4C_e \frac{f_0}{v_0^2}(\Delta hG')$ term increases by the effect of absorption and/or decreases the conductivity of the sensor film response direction will be changed. This effect can be seen by comparing sensor responses of sensor5 and sensor6 against ethanol and other gases. Consequently, the elasticity part is another important parameter of SAW-based sensors and whether it will be dominant or not depends on the type of interaction between the gas and the sensor.

The difference in sensor behavior in the uncontrolled and controlled atmosphere can be seen in the response pattern on Sensor2. The uncontrolled atmosphere is one of the best examples in the real application. Because of, although it is desired to remove moisture from the uncontrolled gas samples during the application it is not possible to say that this is achieved completely. For this reason, partial changes in the sensor characteristics will be expected in this situation. The sensor2 has a good response in Fig. 4,5 on the contrary in the uncontrolled atmosphere has a lower response except for hexane. Similar situations are partially present on other sensors.

**3.3. Principal Component Analysis**
Principal Component Analysis (PCA) is a mathematical method for mapping data to how does distributed and dependent on each other. This method decreases the dimensionality of data while keeping the relation of variations. Therefore, the data which has more than two variables can be shown clearly using two-dimension. The largest eigenvalue of the normalized data set and its

corresponding eigenvector are defined as the first PCA, and then the second and third PCA vectors are defined by relative numbers. The relative numbers can be plotted to understate the relation between the data sets of similarity or dissimilarity and whether samples can be grouped[22, 23]. The main purpose of PCA applications on sensor data is to reveal the possible variations in the sensor characteristics caused by the detected gases and varying humidity. To obtain the best PCA classification each sensor must have a different sensing profile compared to others. PCA was performed after normalization of the sensor response and centering thanks to GNU Octave which is free license mathematical software[24]. PCA analysis in a mapping of loadings and scores is shown in Fig. 11.
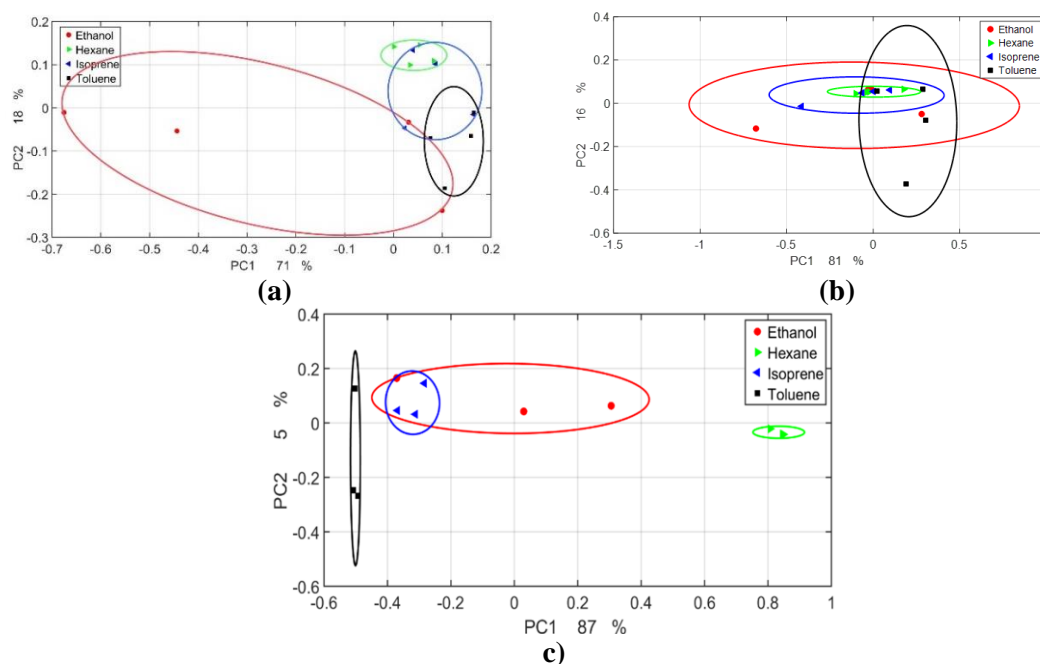


**Figure 11.** PCA mapping of recorded sensor data at a) 0 % Rh, b) 80 %Rh, and c) laboratory atmosphere with added $CaCl_2$ tube in front of E-Nose system.

The first two principal components contain about 100 % of the total variance. The analyte locations were found to be separated on the PCA map for the controlled atmosphere that can be shown in Fig. 11a. The varying humidity was caused by the change of PCA pattern and also the location of analytes in the PCA map was intertwined (Fig. 11b). Using $CaCl_2$ was being positive effect removing the intertwine problem and the distance of the analyte location was being increased as can be seen in Fig. 11c. In fact, that, this positive distribution in the PCA map shows us the advanced data processing methods such as Artificial Neural Network or Deep Learning can identify the gas components easily.

## 4. CONCLUSION

Many studies in the literature were conducted in dry air and special condition. Therefore, the high sensitivity and selectivity of the sensors or high-rate discrimination performance of the data analysis

methods can be seen. On the contrary, in the real case, these methods or performance cannot obtain the case of the complex atmosphere as well as the varying humidity level. E-nose systems can be used in different applications which are varying from explosive and chemical hazardous detection to health applications using breath analysis such as lung cancer, and Covid-19 diagnosis. The most critical important problem encountered in practice is the negative effects of the uncontrollable changing of ambient humidity.

In this study, it was proposed to equipped the $CaCl_2$ tube to prevent the humidity effect on the sensor. However, it should not be overlooked that $CaCl_2$ may also have partial absorption properties for some gases. $CaCl_2$ may be preferred in applications depending on where the E-nose will be used. It is predicted that there will be significant improvement especially in studies on breath analysis such as diagnosis of lung cancer or COVID 19. Up to now, various methods have been used to prevent the effect of the humidity on the sensor signals [25, 26]. These methods are based on mathematical models and specific algorithms. It is impossible to claim that these methods have high performance at high humidity and low analyte concentrations. In this study, it has been shown that the success of the proposed method was obtained at very low concentrations regardless of humidity level.

Another important obtained result is that the SAW sensor responses against VOC's are more pronounced with this method and they are dissociated from the effect of the humidity. This effect can be more easily seen by comparing the PCA results.

## ACKNOWLEDGEMENT

## REFERENCES

[1]  Tisch U. and Haick H.,(2013), *Chemical sensors for breath gas analysis: the latest developments at the Breath Analysis Summit 2013.* Journal of Breath Research 2014; 8(2): 027103.

[2]  Kus F., Altinkok C., Zayim E., Erdemir S., Tasaltin C., and Gurol I.,(2020), *Surface Acoustic Wave (SAW) Sensor for Volatile Organic Compounds (VOCs) Detection with Calix [4] arene Functionalized Gold Nanorods (AuNRs) and Silver Nanocubes (AgNCs).* Sensors and Actuators B: Chemical 2020: 129402.

[3]  Phillips M.,(1997), *Method for the collection and assay of volatile organic compounds in breath.* Analytical biochemistry 1997; 247(2): 272-278.

[4]  Pauling L., Robinson A.B., Teranishi R., and Cary P.,(1971), *Quantitative analysis of urine vapor and breath by gas-liquid partition chromatography.* Proceedings of the National Academy of Sciences; 68(10): 2374-2376.

[5]  Jansson B. and Larsson B.,(1969), *Analysis of organic compounds in human breath by gas chromatography-mass spectrometry.* The Journal of laboratory and clinical medicine; 74(6): 961-966.

[6] Dubowski K.M.,(1974), *Biological Aspects of Breath-Alcohol Analysis.* Clinical Chemistry; 20(2): 294-299.

[7] Das S., Pal S., and Mitra M.,(2016), *Significance of exhaled breath test in clinical diagnosis: a special focus on the detection of diabetes mellitus.* Journal of medical and biological engineering ; 36(5): 605-624.

[8] Lärstad M., Torén K., Bake B., and Olin A.C.,(2007), *Determination of ethane, pentane and isoprene in exhaled air–effects of breath- holding, flow rate and purified air.* Acta Physiologica ; 189(1): 87-98.

[9] Scholpp J., Schubert J.K., Miekisch W., and Geiger K.,(2002), *Breath markers and soluble lipid peroxidation markers in critically ill patients.* Clinical Chemistry and Laboratory Medicine (CCLM) ; 40(6): 587-594.

[10] McGrath L., Patrick R., Mallon P., Dowey L., Silke B., Norwood W., and Elborn S.,(2000), *Breath isoprene during acute respiratory exacerbation in cystic fibrosis.* European Respiratory Journal ; 16(6): 1065-1069.

[11] Miekisch W., Schubert J.K., and Noeldge-Schomburg G.F.,(2004), *Diagnostic potential of breath analysis—focus on volatile organic compounds.* Clinica chimica acta ;347(1-2): 25-39.

[12] Davies S., Spanel P., and Smith D.,(1997), *Quantitative analysis of ammonia on the breath of patients in end-stage renal failure.* Kidney international ;52(1): 223-228.

[13] Turner C., Španěl P., and Smith D.,(2006), *A longitudinal study of ammonia, acetone and propanol in the exhaled breath of 30 subjects using selected ion flow tube mass spectrometry, SIFT-MS.* Physiological Measurement ; 27(4): 321.

[14] Gulbag A., Temurtas F., Tasaltin C., and Ozturk Z.Z.(2007),, *A study on radial basis function neural network size reduction for quantitative identification of individual gas concentrations in their gas mixtures.* Sensors and Actuators B-Chemical; 124(2): 383-392.

[15] Mumyakmaz B., Ozmen A., Ebeoglu M.A., and Tasaltin C.,(2008), *Predicting gas concentrations of ternary gas mixtures for a predefined 3D sample space.* Sensors and Actuators B-Chemical; 128(2): 594-602.

[16] Röck F., Barsan N., and Weimar U.,(2008), *Electronic nose: current status and future trends.* Chemical reviews ; 108(2): 705-725.

[17] Tasaltin C., Ebeoglu M.A., and Ozturk Z.Z.,(2012), *Acoustoelectric effect on the responses of saw sensors coated with electrospun ZnO nanostructured thin film.* Sensors ;12(9): 12006-12015.

[18] Penza M., Aversa P., Cassano G., Wlodarski W., and Kalantar-Zadeh K.,(2007), *Layered SAW gas sensor with single-walled carbon nanotube-based nanocomposite coating.* Sensors and actuators B: Chemical ; 127(1): 168-178.

[19] Tasaltin C.,(2019), *Sensor properties of Pd doped SnO2 nanofiber enshrouded with functionalized MWCNT.* arXiv preprint arXiv:1906.03031.

[20] Kus F., Tasaltin C., Albakour M., Gurek A.G., and Gurol I.,(2019), *Macromolecular hexa-asymmetric zinc(II) phthalocyanines bearing triazole-modified triphenylene core: Synthesis, spectroscopy and analysis towards volatile organic compounds on Surface Acoustic Wave devices.* Journal of Porphyrins and Phthalocyanines ; 23(4-5): 477-488.

[21] Płotka-Wasylka J., Szczepańska N., de La Guardia M., and Namieśnik J.,(2016), *Modern trends in solid phase extraction: new sorbent media.* TrAC Trends in Analytical Chemistry ; 77: 23-43.

[22] Singh T.S., Verma P., and Yadava R.(2019), *Fuzzy subtractive clustering for polymer data mining for SAW sensor array based electronic nose.* in *Proceedings of Sixth International Conference on Soft Computing for Problem Solving.* Springer.

[23] Lelono D., Abdillah M.Z., Widodo T.W., and Apandi M.(2019), *Clusterization of pure and formalin fresh noodles with electronic nose based on kernel principal component analysis.* in *2019 5th International Conference on Science and Technology (ICST).* IEEE.

[24]  https://www.gnu.org/software/octave/index.

[25] Mumyakmaz B., Ozmen A., Ebeoglu M.A., Tasaltin C., and Gurol I., (2010),  *A study on the development of a compensation method for humidity effect in QCM sensor responses.* Sensors and Actuators B-Chemical; 147(1): 277-282.

[26] Nenova Z. and Dimchev G.(2011), *Compensation of the impact of temperature and humidity on gas sensors.* in *XLVI International Scientific Conference on Information, Communication and Energy Systems and Technologies–ICEST.*

RESEARCH ARTICLE

# DETERMINATION of the NATURAL RADIOACTIVITY DISTRIBUTION and CONSUMPTION EFFECTIVE DOSE RATE of CEREAL CROPS in ARDAHAN PROVINCE, TURKEY

Gülçin BİLGİCİ CENGİZ[1,*], İlyas ÇAĞLAR[2]

[1] Kafkas University, Faculty of Science and Letters, Department of Physics, Kars, gulcincengiz@kafkas.edu.tr, ORCID:0000-0002-6164-3232
[2] Kafkas University, Kazım Karabekir Vocational School of Technical Sciences, Department of Electricity and Energy, Kars, ilyas.caglar@kafkas.edu.tr, ORCID:0000-0002-6958-8469

## ABSTRACT

A total of 141 samples; wheat flour samples (66 samples) and cereal product samples (75 samples) such as barley, wheat, vetch, rye and oat collected from local residences, small markets and regional farmers in different districts of Ardahan City were analyzed using a gamma spectrometer with NaI (Tl) scintillation detector. It was observed that the activity concentrations of $^{226}$Ra, $^{232}$Th and $^{40}$K in wheat flour samples used in the nourishment of living creatures varied between $9.22 \pm 1.71$ - $38.32 \pm 5.74$ Bq kg$^{-1}$, $10.53 \pm 2.82$ - $32.70 \pm 2.85$ Bq kg$^{-1}$ and $204.31 \pm 32.14$ - $429.54 \pm 45.8$ Bq kg$^{-1}$, respectively. Activity concentration values of $^{226}$Ra, $^{232}$Th and $^{40}$K for cereal crops detected are compatible with similar studies conducted in the world. The estimated total annual effective dose, based on intake of $^{226}$Ra, $^{232}$Th and $^{40}$K in cereal crops, ranged from $27.56 \pm 5.43$ (barley) $\mu$Svy$^{-1}$ and $207.32 \pm 44.8$ (wheat flour) $\mu$Svy$^{-1}$. These values show that the consumption dose rate resulting from the ingestion of cereal crops by the people of the study region is low and no harmful health effects are expected for living things.

**Keywords:** *Natural radioactivity, NaI(Tl) detector, Cereal crops, Wheat flour, Consumption dose.*

## 1. INTRODUCTION

People are constantly and inevitably exposed to naturally sourced ionizing radiation throughout their lives. Cosmo genic nuclides were formed by high-energy cosmic rays coming into the atmosphere and radioactive nuclides found in the various degrees in the earth's crust are the two main sources of ionizing radiation. Therefore; determining the levels of radioactivity created by natural and artificial radionuclides in the environment is of great importance in determining the effects of both terrestrial and artificial ionizing radiation that people are exposed to [1, 2]. Natural radiation sources constitute approximately 80% of the total radiation dose exposed to the world population. The annual average effective dose that the world population is exposed to it from natural radiation sources has been reported by UNSCEAR (United Nations Scientific Committee on the Effect of Atomic Radiation) is 2.4 mSvy$^{-1}$ per person [3].

Many investigations have been performed entire of the globe to work out the activity concentrations of natural radionuclides in environmental specimens and to calculate the radiation dose exposed from them. Gamma spectrometric analysis of Pakistan's soil samples and food products (such as wheat, potatoes) used by local people in their daily diets was performed using a high-pure germanium (HPGe) detector. Average activity concentrations in soil samples were measured as 56.2 Bqkg$^{-1}$, 58.5 Bq kg$^{-1}$, 851.9 Bqkg$^{-1}$ and 13.39 Bqkg$^{-1}$ for $^{226}$Ra, $^{232}$Th, $^{40}$K and $^{137}$Cs, respectively. In addition, the transfer factors of these radioactive nuclides from soil to food products were also studied in this study. Transfer factors of $^{40}$K, $^{226}$Ra, $^{232}$Th and $^{137}$Cs radioactive nuclides to food products were found as 0.17, 0.07, 0.16 and 0.23, respectively [4]. Activity concentrations of natural radionuclides in wheat samples collected from agricultural lands in India were determined using gamma spectrometer with HPGe detector. Mean activity concentration values of $^{226}$Ra, $^{232}$Th and $^{40}$K were calculated as 0.7, 1.1 and 102.9 Bqkg$^{-1}$, respectively [5]. Ballesteros et al. in 2015 carried out evaluations on typical foods from all over Spain in Environmental Radioactivity Laboratory (LRA), within the trackt of various monitoring programmes supported by the Generalitat Valenciana, in Spain. They analysed a total of 2200 samples of fruits, grains, vegetables, fish, milk, eggs and meat from markets and small producers. They analysed all samples with gamma ray spectrometry and detected $^{40}$K in all samples [6].

The $^{226}$Ra, $^{232}$Th and $^{40}$K activity concentrations and distributions of barley, wheat, vetch, rye and oat cereal crops obtained from local farmers in Ardahan province and its surrounding districts were determined. As a result of the recently changing nutrition habits in our country, as in the world, cereal crops are used as an ingredient in various healthy foods in human nutrition. Therefore, determining the natural radioactivity levels of cereal crops consumed by human beings is great importance for human health. In addition, cereal crops grown in the region are widely used in sheep growing, cattle breeding and poultry farming. It will be beneficial to examine the foods such as meat, milk, cheese and eggs obtained from these animals in the terms of environmental health as they are consumed by local people and people living in different regions of our country for nutritional purposes.

## 2. MATERIALS AND METHODS

### 2.1. Sample collection
In this work, a total of 75 barleys, wheat, vetch, rye and oat samples grown in different districts of Ardahan province and widely used in animal husbandry were taken from local farmers in the study area, each at least 3 kg.

**Figure 1.** Stations where wheat flour and feed crops are obtained.

The wheat grown in the study area is transformed into flour and is mostly used by the local people for making bread, pasta and bakery products. Total of 66 wheat flour samples were obtained from 15 different stations in the study area, each at least 2 kg. The stations where wheat flour samples and cereal crops were collected are shown in Figure 1.

### 2.2. Gamma-ray spectrometry analysis

All collected samples were brought to the laboratory in labeled plastic bags. Samples were thoroughly purified from impurities in them. The samples pulverized with the mixer were sieved and oven dried at 105 °C for 24 hours [7]. Subsequently, the samples were placed in a 100 ml volume, 65x55 mm in size, transparent pathological sample containers with tared screw caps and weighed with precision scales and recorded in kilograms [8]. Samples were stored in sample containers for forty days to ensure stabilize between $^{226}$Ra, $^{232}$Th and their short-lived degradation [7, 8]. Gamma spectrometric analyzes of $^{226}$Ra, $^{232}$Th and $^{40}$K radionuclides were performed using 3"x3" NaI (Tl) scintillation detector with 20% relative efficiency and ScintivisionTM-32 (A35-B32) computer program. Energy and relative efficiency calibration of the gamma spectrometer were defined using IAEA-375 (standard calibration material) [9]. The minimum detectable activity (MDA) was approximately 5.50, 2.88 and 60.1 Bq kg$^{-1}$ for $^{226}$Ra, $^{232}$Th and $^{40}$K, respectively.

For the calculation of the activity concentrations, the areas under each photo peak were chosen, taking into account the corresponding photo peaks at various energies. While calculating the net peak area, in order to calculate the external contributions, the natural background was 86400 seconds to determine the activity of the background and samples. The gamma peak of 1460 keV was analyzed to calculate the $^{40}$K activity concentration. $^{226}$Ra concentration was determined by measuring 609, 1120 and 1764 keV gamma rays from $^{214}$Bi, while gamma rays at 583 and 2614 keV from $^{208}$Tl were used to determine the activity concentration of $^{232}$Th [10].

## 3. RESULTS AND DISCUSSION

### 3.1. Radioactivity in wheat flour and cereal crops

When the flour samples in the study area were examined, the mean activity concentrations of $^{226}$Ra, $^{232}$Th and $^{40}$K were found to be $12.00 \pm 2.40$ Bq kg$^{-1}$, $12.41 \pm 2.50$ Bqkg$^{-1}$ and $314.62 \pm 21.6$ Bqkg$^{-1}$, respectively. The minimum value of $^{226}$Ra activity concentration was found to be $9.22 \pm 1.71$ Bqkg$^{-1}$ and the maximum value of $16.12 \pm 2.61$ Bqkg$^{-1}$ in the examined wheat flour samples, while the lowest value of $^{232}$Th activity concentration was found to be $7.23 \pm 1.91$ Bqkg$^{-1}$ and the highest value was found to be $19.50 \pm 2.50$ Bqkg$^{-1}$. In wheat flour samples consumed daily by humans, $^{40}$K activity concentration was measured as the lowest $185.72 \pm 26.20$ Bqkg$^{-1}$ and the highest $446.11 \pm 25.20$ Bqkg$^{-1}$.

The average activity concentrations of $^{226}$Ra, $^{232}$Th and $^{40}$K in studied cereal crops were obtained as $16.97 \pm 3.90$ Bqkg$^{-1}$, $20.66 \pm 2.55$ Bqkg$^{-1}$, $245.42 \pm 46.81$ Bqkg$^{-1}$ for barley samples; $18.05 \pm 4.93$ Bqkg$^{-1}$, $30.97 \pm 1.88$ Bqkg$^{-1}$, $303.64 \pm 42.73$ Bqkg$^{-1}$ in wheat samples; $18.95 \pm 2.47$ Bqkg$^{-1}$, $18.14 \pm 2.05$ Bqkg$^{-1}$, $360.52 \pm 36.42$ Bqkg$^{-1}$ in vetch samples; $16.85 \pm 2.97$ Bqkg$^{-1}$, $14.64 \pm 2.61$ Bqkg$^{-1}$, $411.91 \pm 45.63$ Bqkg$^{-1}$ in rye samples and finally $24.37 \pm 5.04$ Bqkg$^{-1}$, $21.48 \pm 2.34$ Bqkg$^{-1}$, $212.21 \pm 57.64$ Bqkg$^{-1}$ in oat samples, respectively.
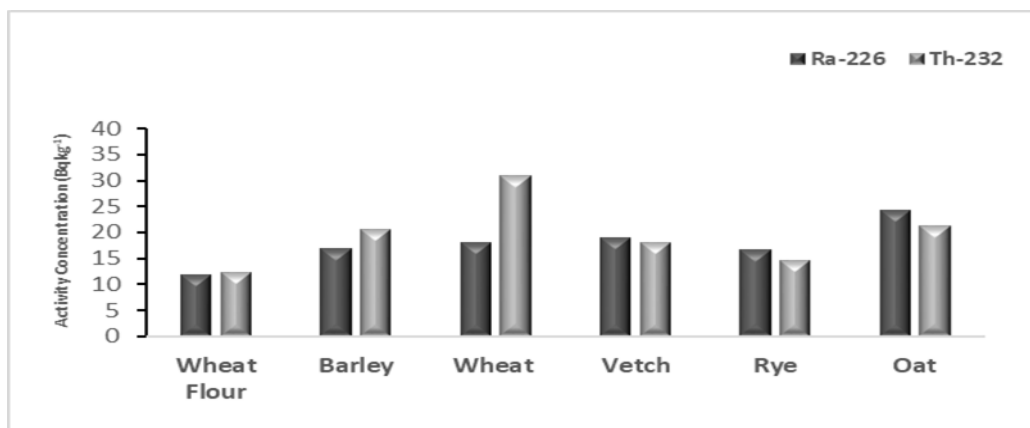


**Figure 2.** The average activity concentrations of $^{226}$Ra and $^{232}$Th in wheat flour and cereal crops.
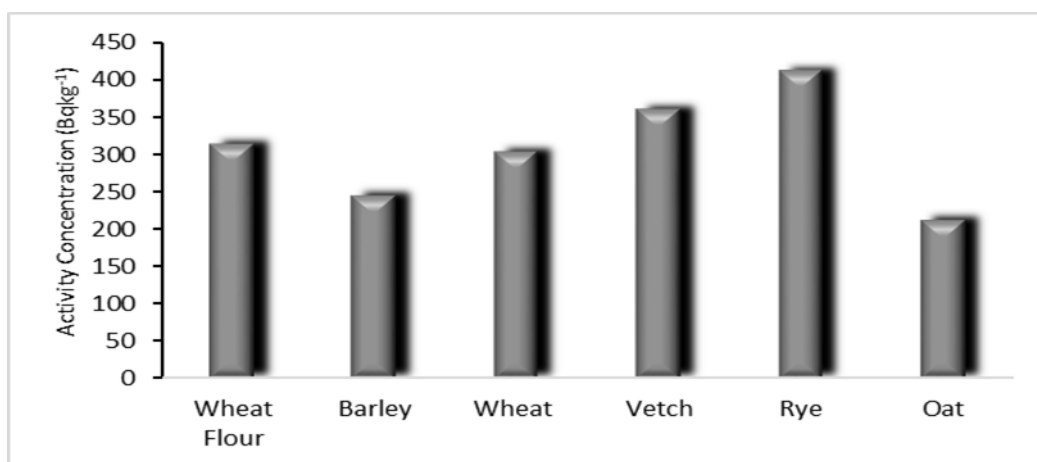
**Figure 3.** Distribution of $^{40}$K in wheat flour and cereal crops taken from the study area.

As can be seen in Figures 2 and 3, the lowest $^{226}$Ra and $^{232}$Th activity concentrations were evaluated in the wheat flour specimens and the lowest $^{40}$K activity concentrations were measured in the oat samples. The highest $^{226}$Ra, $^{232}$Th and $^{40}$K activity concentrations were measured in oat, wheat and rye samples, respectively.

In Table 1, the comparison of the average values of natural radioactivity levels of wheat flour and cereal crops collected from the study area with the values reported in some studies in the literature were given. In this study, the average activity concentrations of $^{232}$Th and $^{40}$K for wheat flour, barley, wheat, vetch, rye and oats were lower than the average activity concentrations reported for pasture crops in Digor district of Kars province, but average activity concentrations of $^{226}$Ra for wheat vetch and oat were higher than reported values [11].

In the study that carried out in the Gediz Basin, the $^{226}$Ra and $^{40}$K activity concentrations for corn samples were presented 25.82 ± 2.3 Bqkg$^{-1}$ and 491.62 ± 52.61 Bqkg$^{-1}$, respectively [12]. For the cabbage samples examined in the Western Anatolia region, the activity concentrations of $^{232}$Th and $^{40}$K were reported as 45.5 ± 5.2 Bqkg$^{-1}$ and 766.0 ± 40 Bqkg$^{-1}$, respectively [13]. It is seen that our obtained mean activity concentrations values for all examined cereal samples were below their reported activity concentrations values.

In this work the average activity concentrations of $^{232}$Th for wheat flour and cereal crops were found to be higher than the activity concentration of $^{232}$Th in market tea in Turkey [14]. The $^{40}$K activity concentrations in the examined wheat flour were found to be higher than the $^{40}$K average activity concentrations in wheat flour in West Anatolia and Iraq [13, 15].

When compared the results of this study with the studies conducted in different regions of the world, it was observed that the $^{226}$Ra, $^{232}$Th and $^{40}$K obtained activity concentrations for wheat samples were higher than the activity concentrations in the wheat samples reported for Pakistan, India, Spain, Iraq and Egypt [4-6, 16,17]. The $^{40}$K activity concentration was measured for the barley samples was found to be consistent with the $^{40}$K activity concentration of the barley samples reported for Iraq [16].

**Table 1.** Comparison of the average valuations of natural radioactivity levels of plant samples with the with the valuations informed in the published works.

| | | | Activity concentrations (Bqkg$^{-1}$) | | |
|---|---|---|---|---|---|
| **References** | **Region Worked** | **Name of Samples** | **$^{226}$Ra** | **$^{232}$Th** | **$^{40}$K** |
| This work | Ardahan | Wheat flour | 12.0 0 ± 2.40 | 12.41 ± 2.50 | 314.62 ± 21.60 |
| This work | Ardahan | Barley | 16.97 ± 3.90 | 20.66 ± 2.55 | 245.42 ± 46.81 |
| This work | Ardahan | Wheat | 18.05 ± 4.93 | 30.97 ± 1.88 | 303.64 ± 42.73 |
| This work | Ardahan | Vetch | 18.95 ± 2.47 | 18.14 ± 2.05 | 360.52 ± 36.42 |
| This work | Ardahan | Rye | 16.85 ± 2.97 | 14.64 ± 2.61 | 411.91 ± 45.63 |
| This work | Ardahan | Oat | 24.37 ± 5.04 | 21.48 ± 2.34 | 212.21 ± 57.64 |
| [11] | Digor | Pasture plant | 17.9 ± 10.4 | 75.9 ± 19.5 | 630.6 ± 12.3 |
| [12] | Gediz | Corn | 25.82 ± 2.34 | | 491.62 ± 52.61 |
| [13] | West Anatolia | Cabbage | | 45.5±5.2 | 766.0 ± 40 |
| | | Wheat flour | 6.1 ± 5.8 | | 128 ± 45 |
| [15] | Iraq | Wheat flour | | 1.94 ± 1.33 | 133.09 ± 67.04 |
| [14] | Turkey | Market Tea | | 5.9 ± 1.7 | 766.0 ± 40 |
| [5] | India | Wheat | 0.7 ± 0.1 | 1.1 ± 0.02 | 102.9 ± 9.8 |
| [6] | Spain | Barley | | | 78.0–222.4 |
| | | Wheat | | | 67.0–122.6 |
| [4] | Pakistan | Wheat | 3.7 | 8.4 | 130.7 |
| [16] | Iraq | Barley | 1.92 ± 0.36 | 1.94 ± 0.34 | 242.22 ± 10.76 |
| | | Wheat | 1.46 | 1.38 | 180.54 ± 8.52 |
| [17] | Egypt | Wheat | 1.00- 1.55 | 1.05- 1.20 | 103.0- 120.3 |

### 3.2. Consumption dose to human being

The annual effective dose that indicates the importance of the stochastic health impacts for the whole body. The annual effective dose due to radionuclide intake through food ingestion can be calculated if the amount of activity concentration of certain radionuclides deposited depending on the food stuff and the annual average consumption rate are known.

The annual committed effective dose ACD$_{eff}$ (μSv y$^{-1}$) of radionuclides to human beings owing to the consumption of cereal crops are reckoned with the equation 1 [18];

$$ACD_{eff} = A_C \times I_C \times F_{DC} \tag{1}$$

where A$_C$ is the activity concentration of $^{226}$Ra, $^{232}$Th, and $^{40}$K in cereal crops (Bq kg$^{-1}$); F$_{DC}$ is the dose conversion factor for $^{226}$Ra, $^{232}$Th and $^{40}$K radionuclides (Sv Bq$^{-1}$) and I$_C$ is the annual consumption rate of the cereal crops (kg y$^{-1}$). The amount of cereal crops consumption rates was obtained from published report of Turkish Statistical Institute (TUİK) in 2020 [19]. The values dose

conversion factors due to the ingestion of [226]Ra, [232]Th, and [40]K from cereal products for adults are $2.8 \times 10^{-7}$ Sv Bq$^{-1}$, $2.3 \times 10^{-7}$ Sv Bq$^{-1}$ and $6.210^{-9}$ Sv Bq$^{-1}$, respectively [20]. Annual consumption rates of wheat flour and cereal products per person (kg y$^{-1}$) in Ardahan region of Turkey and the effective dose values calculated owing to ingestion of these foodstuffs are shown in Table 2.

The annual effective dose in µSv y$^{-1}$ due to the consumption of cereal crops by adults were calculated using equation 1. The mean values and ranges of annual effective doses owing to intake of [226]Ra, [232]Th, and [40]K from consuming cereal crops were determined as $31.95 \pm 8.88$ (10.05–102.45) µSv y$^{-1}$, $29.91 \pm 3.45$ (8.23–89.93) µSv y$^{-1}$ and $15.02 \pm 6.66$ (2.50–55.61) µSv y$^{-1}$, respectively. According to the existence of natural radionuclides in the collected wheat flour samples, the average of ingestion effective dose was calculated as 207.32 µSv y$^{-1}$. These calculated values are less than 321.3 µSvy$^{-1}$, which is the average annual effective dose value found as a result of studies carried out with wheat flour in Iraq and is also very compatible with the average annual effective dose value (213.1 µSv y$^{-1}$) in Pakistan [15, 21].

Cereal products are mostly used in the feed industry. However, as a result of changing dietary habits, cereal plants are used as an ingredient in various healthy foods. The annual effective dose, has a minimum value in barley grain due to least consuming by adults in Turkey. Depending on the consumption of wheat and barley, the annual effective consumption dose rate calculated as 20.60 µSv y$^{-1}$ in this study, lower than the average annual effective consumption dose rate (67.73 µSv y$^{-1}$) for the same cereal products in Iraq [22]. From those results, it can be concluded that the annual consumed effective dose for [40]K, [232]Th and [226]Ra in examined cereal crop samples is lower than the allowable limits of 1 mSv y$^{-1}$ by the International Radiological Protection Commission [23].

**Table 2.** Annual per capita consumption rate of some cereal products in Ardahan and its surroundings and annual effective doses depending on the consumption of these products.

| Cereal Crops Name | Annual Consumption (kg y$^{-1}$) | Annual Effective Dose (µSv y$^{-1}$) | | | |
|---|---|---|---|---|---|
| | | [226]Ra | [232]Th | [40]K | Total |
| Wheat Flour | 25.4 | 85.34 | 72.44 | 49.54 | 207.32 |
| Barley | 2.5 | 11.88 | 11.87 | 3.80 | 27.56 |
| Wheat | 5.8 | 29.31 | 41.31 | 10.92 | 81.54 |
| Rye | 2,7 | 12.74 | 9.09 | 6.90 | 28.73 |
| Oat | 3.0 | 20.47 | 14.82 | 3.95 | 39.24 |

## 4. CONCLUSION

In this study, the natural radioactivity levels of a number of 141 wheat flour and cereal crops samples which are collected from Ardahan province and its surrounding districts were determined using NaI (Tl) scintillation detector. The lowest [226]Ra and [232]Th activity concentrations were measured in the rye samples and the lowest [40]K activity concentrations in oat samples in crops. The highest [226]Ra, [232]Th and [40]K activity concentrations were measured in oat, wheat and rye samples, respectively. These different natural radioactive activity values obtained in the samples which examined can be explained by the physicochemical properties of the soil in whic cereal crops are grown, the transfer factors of radioactive nuclides from the soil to cereal crops and the metabolic features of these plants. In addition, the amount of organic fertilizers and chemical fertilizers used to increase soil fertility and plant production by affecting the stable element content of the soil are among the reasons for the

differences in the natural radioactive activity values in the samples examined. The radiation dose from the consumption of wheat flour and some cereal products has been found, to be lower than the annual world average of 290 $\mu$Sv y$^{-1}$ therefore, consumption of these crops has not been found, not to pose a threat to public health. The findings obtained from this study can be utilized as reference data to help identify likely changes in environmental radioactivity from nuclear, industrial and other people activities .

**REFERENCES**

[1] Agbalagba E.O., Avwiri G.O., Chad-Umoreh Y.E., (2012), γ-Spectroscopy measurement of natural radioactivity and assessment of radiation hazard indices in soil samples from oil fields environment of Delta State, Nigeria, J. Environ. Radioact, 109, 64-70.

[2] Sroor A., El-Bahi S.M, Ahmed F., Abdel-Haleem A.S., (2001), Natural radioactivity and radon exhalation rate of soil in southern Egypt, Appl. Radiat. Isot., 55, 873–879.

[3] United Nations Scientific Committee on the Effects of Atomic Radiation. 2000. Sources and Effects of Ionizing Radiation, UNSCEAR, 2000 Report Vol.1 to the General Assembly with scientific annexes, New York: United Nations Sales Publication, United Nations.

[4] Khan H.M, Chaudhry Z.S., Ismail M., Khan K., (2010), Assessment of radionuclides, trace metals and radionuclide transfer from soil to food of Jhangar Valley (Pakistan) using Gamma-ray spectrometry, Water Air Soil Pollut., 213, 353–362.

[5] Pulhani V.A., Dafauti S., Hegde A.G., Sharma R.M., Mishra, U.C., (2005),  Uptake and distribution of natural radioactivity in wheat plants from soil, J. Environ. Radioact., 79, 331-346.

[6] Ballesteros L., Ortiz J., Gallardo S., Martorell S., (2015), An overview of measurements of radionuclides in foods of the Comunidad Valenciana (Spain), Radiat. Phys. Chem., 116, 111–115.

[7] Gezer F., Turhan Ş., Kurnaz A., Ufuktepe Y., (2019), Radiometric characterization of zeolite minerals used in many industries and assessment of radiological risk, Appl. Radiat. Isot., 152: 57-63.

[8] Cengiz G.B., Çağlar İ,. (2016), Determination of the health hazards and life time cancer risk due to natural radioactivity in soil of Akyaka, Arpaçay and Susuz Areas of Kars, Turkey, International Journal of Scientific &Engineering Research, 7(3), 619-626.

[9] Altzitzoglou T., Bohnstedt A., (2016), Characterization of the IAEA-375 soil reference material for radioactivity, Appl. Radiat. Isot., 109, 118-121.

[10] Akçay N., (2021), On the 30th anniversary of the Chernobyl nuclear power plant accident, assessment of the activity concentrations and the radiological hazard parameters of soil samples collected from Rize province and districts, Appl. Radiat. Isot., 168, 109435.

[11] Bilgici Cengiz, G., (2019), Transfer factors of $^{226}$Ra, $^{232}$Th and $^{40}$K from soil to pasture-grass in the northeastern of Turkey, J. Radioanal. Nucl. Chem., 319**,** 83–89.

[12] Bolca M., Saç M.M., Çokuysal B., Karalı T., Ekdal E., (2007), Radioactivity in soils and various foodstuffs from the Gediz River Basin of Turkey, Radiation Measurements, 42, 263–70.

[13] Topcuoğlu S., Karahan G., Güngör N., Kırbaşoğlu Ç., (2003), Natural and artificial in Emendere thermal spring area in Western Anatolia, J. Radioanal. Nucl. Chem., 256(3), 395-398.

[14] Kiliç Ö, Belivermiş M, Topcuoğlu S, Çotuk Y. $^{232}$Th, $^{238}$U, $^{40}$K, $^{137}$Cs radioactivity concentrations and $^{137}$Cs dose rate in Turkish market tea. Radiat. Eff. Defects Solids, 2009;164(2):138-143.

[15] Abojassim A.A., Al-Gazaly H.H, Kadhim S.H., (2014), Estimated the radiation hazard indices and ingestion effective dose in wheat four samples of Iraq markets, Int. J. Food Contam., 1, 6.

[16] Pourimani, R. and Shahroudi, S.M.M., (2018), Radiological assessment of the artificial and natural radionuclide concentrations of wheat and barley samples in Karbala, Iraq, Iran J. Med. Phys., 15,126-131.

[17] Alharbi, A. and El-Taher A., (2013), Life Sci. J., 10, 532-539

[18] Biira, S., Ochom, P., Oryema, B., (2021), Evaluation of radionuclide concentrations and average annual committed effective dose due to medicinal plants and soils commonly consumed by pregnant women in Osukuru, Tororo (Uganda), J. Environ. Radioact., 227, 106460.

[19] TUİK, 2020, Çok Alanlı İstatistikler Resmi İstatistik Programı, 2019 Yılı İzleme Raporu, ANKARA, TÜRKİYE

[20] Alomari, A.H., Saleh, M.A., Hashim, S., Naif Al-Hada, Abukashabeh A., Alsayaheen A. and Hamad M., (2020), Radiological dose and health impact to Jordanian populace due to radioactivity in staple food crops from four representative soils in Jordan, J. Radioanal. Nucl. Chem., 326, 1679–1689.

[21] Khan, I. U., Sun, W., Lewis, E., (2020), Radiological impact on public health from radioactive content in wheat flour available in Pakistani Markets, J. Food Prot., 83 (2), 377–382.

[22] Kheder, M.H., Najam, L.A., Mahmood, R.H. and Majeed, F.A., (2020), Radioactivity concentrations in barley and wheat crops in Nineveh plain region in Iraq, Int. J. Nucl. Sci. Tech., 14(1), 50–60.

[23] ICRP (1996) International Commission on Radiological Protection, Age Dependent Doses to Members of the Public from Intake of Radionuclides: Part 5 Compilations of Ingestion and Inhalation Dose Coefficients (ICRP Publication 72). Pergamon Press, Oxford.

RESEARCH ARTICLE

# HYDROGEN PRODUCTION from HYDRAZINE on SOME TRANSITION METAL (Sc, Ti and V) -EMBEDDED GRAPHENE

Hilal Küçük[1]

Gazi University, Department of Physics, Ankara, hilakucuk@gazi.edu.tr, ORCID: 0000-0002-0777-1102

## ABSTRACT

The investigation of N2H4 decomposition catalysts is a highly popular subject because of the demand for clean and renewable energy sources. Herein, $N_2H_4$ adsorption energy and decomposition kinetics are analyzed to find a better 2D single-atom catalyst (SAC) using modified graphene by embedding light 3d-transition metals. Hydrogen selection of hydrazine decomposition over Sc,Ti and V atoms catalysts are studied on two pathways: the N-N bond scission ( $N_2H_4 \rightarrow NH_2 + NH_2$ ) and N-H bond split ($N_2H_4 \rightarrow N_2H_3 + H$). On graphene embedded by Sc and Ti metal produces easily $2NH_2$ because their activation energy is almost close to 0 eV. The activation of energy of N-H cleavage on graphene embedded by vanadium atom is lower (0.99 eV) than that of N-N cleavage (1.36 eV). Therefore, H production from hydrazine on V metal surface is more favorable than $2NH_2$ production.

**Keywords:** *TM embedded graphene with single vacancy; hydrazine decomposition; hydrogen generation; single-atom catalysis.*

## 1. INTRODUCTION

After industrial growth, enormous energy in the order of exajoules is needed because of the increment of the human population, and this demand is increasing more and more each day[1]. Conventional energy is produced by natural coal, gas, oil and nuclear energy, coal, oil, wood, and coal. However, they cause serious global warming and traditional fuels are not renewable. Nowadays, industrial countries endeavor to investigate completely carbon-free and sustainable economies within the next decades[1-3]. For reaching carbon-free energy sources, hydrazine $(N_2H_4)$ can be exploited through the high hydrogen continent of hydrazine (12.5 wt %) as a mobile hydrogen source[4-6]. $N_2$, $H_2$, and $NH_3$ with hydrogen $(H)$ can be generated through its decomposition without harmful carbon productions[7]. The application areas of hydrazine are fuel cells as a portable battery in space ships, automobiles, and laptops, agriculture for the preparation of pesticides, and the missile system for the military [8, 9]. Hydrazine can appear as gauche, cis and anti due to the internal rotation of $NH_2$ group around N-N bond [10-13]. The large dipole moment

of gauche conformation and the coplanar repulsions in the cis and anti-conformation cause that hydrazine tends to appear as gauge form in the gas phase [14, 15].

There are many researches to understand catalysts effects on hydrazine such as, bare surface; Ni (111), Ir(111) [16], Pt(111) [11], Ni (111)[17], Fe(211) [18], Cu(111)[19], monometallic nanoparticle catalysts[5]. Due to increase catalytic effects, transition metal alloys are used as well. For instance, $Ni_xMg/Ni(111)$ (M is transition metal, x=8,14,15) materials are investigated for adsorption of hydrazine. The finding is that these surfaces are much more effective candidates than Ni(1 1 1) sheet for hydrazine adsorption [20].

N-N bond can be broken more easily because N-N bond is weaker than N-H bond in gaseous. Therefore, an effective catalyst for dehydrogenation from hydrazine has not yet been found until now[21]. However, research on hydrogen production from hydrazine is crucial and still needed because of clean energy using hydrogen. The investigations on graphene embedded by transition metal are necessary for many reactions because they can be one of the effective, durable, and affordable catalysts[22, 23]. Transition-metal-carbon materials can be inexpensive compared to metal-based catalysts. In this study, graphene is modified by embedding with some light 3d transition metal to change its magnetic properties and bandgap. Our goal is to achieve a better catalytic effect on hydrazine decomposition. For hydrogen generation, N-H bond cleavage will be worked compared with N-N bond cleavage on graphene embedded surfaces.

## 2. COMPUTATIONAL DETAIL

Using density functional theory (DFT), all analyses were calculated with Quantum Espresso software package[24, 25]. (PAW) potential (pbe-n-kjpaw) were chosen[26, 27]. The kinetic energy parameter for wavefunctions was 50 Ry for Sc and V metal, and 55 Ry for Ti metal. This energy parameter for potential and charge density was 500 Ry for Ti metal and V metal, and 402 Ry for Sc. Three surfaces were modeled with 4x4x1 cells and 32 atoms. To contain van der Waals interactions corrections the term Grimme-D2 was implemented[28]. The lattice parameters are a=9.8 Å and c=20 Å and also Monkhorst-Pack k-point grid is 4x4x1.

The central M transition metals (Sc, Ti, V) are embedded in the graphene sheet. The surface models with different perspectives are seen in Figure 1.
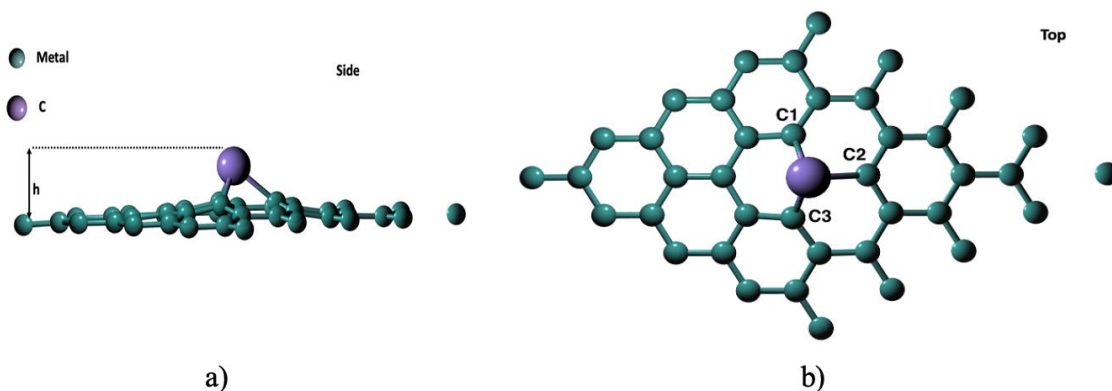
**Figure 1.** M (Sc, Ti and V) embedded into graphene surface a) Graphene sheet from side view b) Graphene sheet from the top view. The colors of C and transition metal are green and violet respectively.

Table 1 represents the distance between the transition metal and C atom on the lowest level, bond distances, magnetic moments after optimization for the different surfaces. In all sections, the result will be given in order such as Sc, Ti, and V metal, unless stated otherwise. According to the previous research by G. Santos's group[29], the heights are ~1.7 Å, ~1.5 Å, ~1.4 Å and the bond distances between metal and C atoms ($d_{M-C}$) are ~2.1 Å, ~1.95 Å, ~1.85 Å. Additionally, the magnetics are $0.0\ \mu_B$, $0.0\ \mu_B$, $1.0\ \mu_B$. The finding between mentioned study and our findings in Table 1 are quite close to each other.

**Table 1.** The bond distances, magnetic moments after optimization for the different surfaces.

| M | Distance-h (Å) | $d_{M-C_1}$, $d_{M-C_2}$, $d_{M-C_3}$ (Å) | Magnetic Mom. ($\mu_B$) |
|---|---|---|---|
| Sc | 1.7 | 2.06 | 0.0 |
| Ti | 1.5 | 1.92 | 0.0 |
| V | 1.4 | 1.88 | 1.0 |

The adsorption energies ($E_{ads}$);

$$E_{ads} = E_{\text{M− graphene+molecule}} - E_{\text{M− graphene}} - E_{\text{molecule}} \tag{1}$$

While the total energy of the adsorption system and the total energy of the surface are respectively $E_{\text{M−graphene+molecule}}$ and $E_{\text{M−N4 in graphene}}$ and, also $E_{\text{molecule}}$ is the energy of molecule in the gas phase. A negative $E_{ads}$ value shows a release of energy during adsorption.

NEB method (the nudged elastic band) determines the transition state (TS) for reactions [30, 31]. The activation ($E_{act}$) is

$$E_{act} = E_{TS} - E_{IS} \tag{2}$$

The reaction energy ($E_r$) is,

$$E_R = E_{FS} - E_{IS} \tag{3}$$

The process is exothermic if $E_R$ is negative. Its positive sign is endothermic. $E_{TS}$ is the energy of Transition State, and $E_{IS/FS}$ is the energy of the initial state (IS) or the final state (FS).

## 3. RESULT AND DISCUSSION

### 3.1 Adsorption of $N_2H_4$ and $NH_2$ in graphene-embedded by M = Sc, Ti and V surface

Gauche conformer of hydrazine was observed on the lowest energy structure on graphene embedded surfaces although it has three different formations known as gauche, trans, and eclipsed in nature. Figure 2 illustrates the molecule on graphene embedded surfaces after optimization. After optimization, while almost all bond lengths of N-H increase, the bond lengths of $N_2 - H_3$ remain the same on Ti and V metal surfaces as seen in Table 2. There are increments on N-N bonds of adsorbed hydrazine, 1.455 Å for Sc, 1.457 Å for Ti, 1.456 Å for V metal from 1.44 Å on gas phase. The bonds M-N are 2.47 Å for Sc metal, 2.33 Å and 2.23 Å for Ti and V metal.

The highest adsorption energy belongs to V embedded surface, -1.49 eV, others are -1.31 eV for Ti metal and -1.22 eV for Sc metal. If the distance between the molecule and the surface is smaller, the adsorption energy is much higher because high interaction occurs between hydrazine and the surfaces. According to the bond lengths and the adsorption energies, the interaction on all surfaces is chemical. These adsorption energy values are higher than that of Li-decorated graphene sheets worked by H. Zeng and colleagues (-1.004 eV) [32].
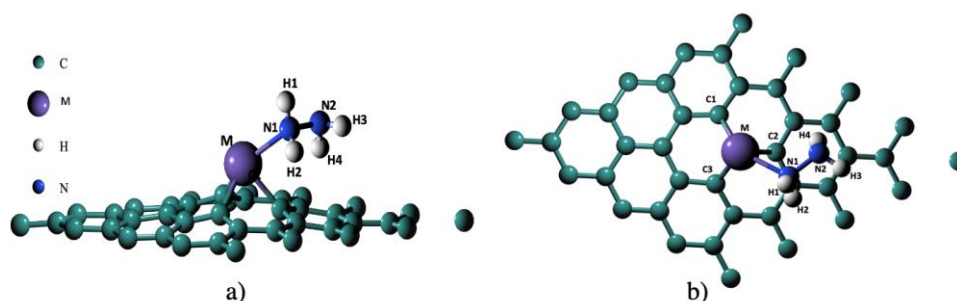


**Figure 2.** Hydrazine molecule on graphene surface embedded M (M=Sc, Ti, V) a) Side view b) Top view. C atom, M metal, N atom and H atom are illustrated by green, violet, blue and white colors respectively.

Δq is known as the electron transfer found by subtracting the charge in adsorbed hydrazine on the graphene embedded sheet from the charge in the gas phase using Bader charge analysis[33]. The meaning of the negative sign of Δq is donating electron while the positive sign is gaining electron from the molecule. Hydrazine molecule gains the most electrons ($0.038\ e^-$) on V metal surface which has the highest adsorption energy. If Table 2 is considered, the adsorption energy has a relationship with the charge transfer. Higher adsorption energy is higher than the charge transfer.

**Table 2.** Related parameters for $N_2H_4$ on M embedded graphene.

| | $E_{ads}$ (eV) | $d_{M-N_1}$ ($\dot{A}$) | $d_{N_1-N_2}$ ($\dot{A}$) | $d_{N_1-H_1}$ ($\dot{A}$) | $d_{N_1-H_2}$ ($\dot{A}$) | $d_{N_2-H_3}$ ($\dot{A}$) | $d_{N_2-H_4}$ ($\dot{A}$) | $\Delta q(N_2H_4)$ ($e^-$) |
|---|---|---|---|---|---|---|---|---|
| $N_2H_4$ in gas phase | | | 1.44 | 1.021 | 1.025 | 1.025 | 1.021 | |
| Sc | -1.22 | 2.44 | 1.455 | 1.023 | 1.032 | 1.026 | 1.028 | 0.015 |
| Ti | -1.31 | 2.33 | 1.457 | 1.023 | 1.031 | 1.025 | 1.027 | 0.032 |
| V | -1.49 | 2.23 | 1.456 | 1.024 | 1.031 | 1.25 | 1.028 | 0.038 |



a)      b)
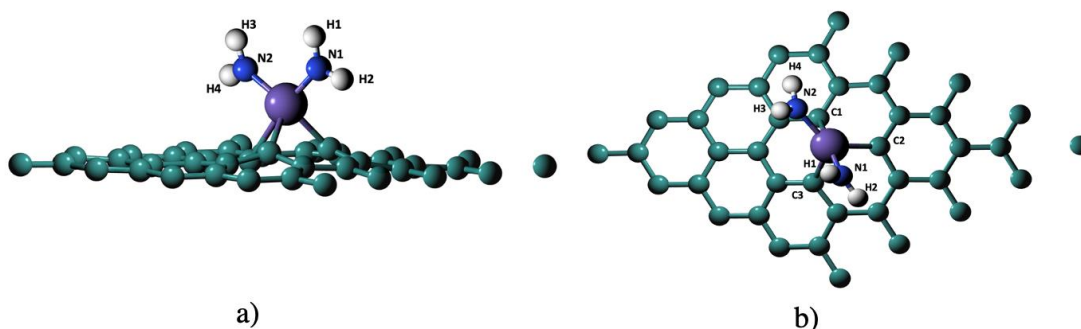
**Figure 3.** The adsorption of $NH_2$ on graphene embedded by M (M=Sc, Ti, V) a) Side view b) Top view. C atom, M metal, N atom, and H atom are illustrated by green, violet, blue and white colors respectively.

N-N bond cleavage ($N_2H_4 \rightarrow NH_2 + NH_2$ ) is the second reaction path on hydrazine as seen in Figure 3. The bond length of $N_1 - H_1$ and $N_1 - H_3$ squeeze on all surfaces except the $N_1 - H_3$ bond which does not change on the V metal surface as shown in Table 3 . The big differences in the bond lengths of $N_1 - H_2$ and $N_1 - H_4$ after adsorption do not occur on the surfaces but ones of $N_1 - H_2$ on V metal embedded surface shrinks from $1.021\dot{A}$ to $1.017\dot{A}$. The adsorption energy of $NH_2$ on Sc, Ti, V embedded surface are

-3.47 eV, -3.94 eV, and -4.49 eV. These adsorptions are quite stronger than that of analysis of $NH_2$ on pure graphene sheet (-0.778 eV) worked by Junkermeier, C.E. et al. [34]. Two $NH_2$ lose electrons as 1.22 $e^-$ for Sc metal, -1.01 $e^-$ for Ti metal and 0.87 $e^-$ for V metal. The chemical interactions between $NH_2$ and graphene embedded surfaces with higher value exist compared to the adsorption on $N_2H_4$.

**Table 3.** Related parameters for $NH_2$ on M embedded in graphene.

| | $E_{ads}$ (eV) | $d_{M-N_1}$ ($\dot{A}$) | $d_{M-N_2}$ ($\dot{A}$) | $d_{N_1-H_1}$ ($\dot{A}$) | $d_{N_1-H_2}$ ($\dot{A}$) | $d_{N_2-H_3}$ ($\dot{A}$) | $d_{N_2-H_4}$ ($\dot{A}$) | $\Delta q(NH_2)$ ($e^-$) |
|---|---|---|---|---|---|---|---|---|
| $NH_2$ in the gas phase | | | | 1.025 | 1.021 | 1.025 | 1.021 | |
| $Sc$ | -3.47 | 2.002 | 2.002 | 1.022 | 1.022 | 1.022 | 1.022 | -1.22 |
| $Ti$ | -3.94 | 1.918 | 1.926 | 1.021 | 1.022 | 1.023 | 1.02 | -1.01 |
| $V$ | -4.49 | 1.89 | 1.90 | 1.023 | 1.017 | 1.025 | 1.022 | -0.87 |

### 3.2 Hydrazine decomposition steps on graphene embedded surface

According to our knowledge, a weaker N-N bond in gaseous causes more possible the N-N bond split [21]. The below hydrazine decomposition reaction paths are used to find more proper catalysis for hydrogen production.

$$N_2H_4 \rightarrow N_2H_3 + H \tag{6}$$
$$N_2H_4 \rightarrow NH_2 + NH_2 \tag{7}$$

The configurations of the first pathway on all surfaces are viewed in Figure 4 and the configurations of the second way for all surfaces are Figure 5. The first reaction and second reaction of hydrazine decomposition are seen in Figure 6. The activation barriers ($E_a$) of N-H bond breakup are 1.97 eV, 1.59 eV and 0.99 respectively on Sc, Ti and V metal embedded graphene surface, while N-N bond scissions are 0.12 eV for Sc, 0.19 eV for Ti and 1.36 eV for V. The reaction energies of the N-H bond split are 1.73 eV for Sc, 0.55 eV for Ti and 0.63 eV for V, and also the reaction energy on the N-N bond scissions -1.02 eV, -1.04 eV and -1.5 for Sc, Ti and V embedded surface respectively.

The exothermic reaction gives the negative result of reaction energy while its positive result shows an endothermic reaction. An exothermic reaction occurs on the N-N bond split on all surfaces and the reactions on the N-H bond split are endothermic. Our previous finding on graphene embedded by Ni metal is that the activation barriers and the reaction energies on the N-H bond scission are respectively 0.85 eV and +0.71 eV as they are also 0.51 eV and -0.61 eV on the N-N bond scission[10].
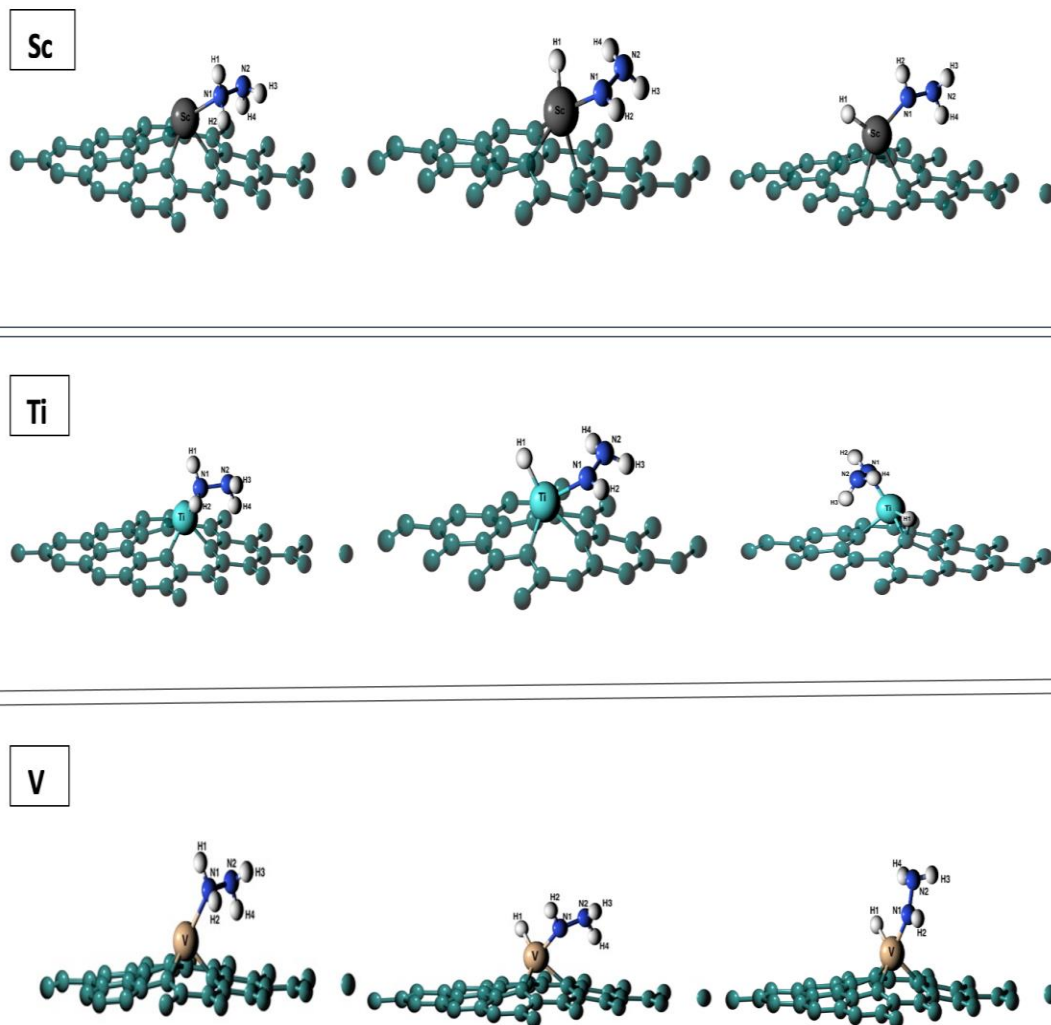
**Figure 4:** $N_2H_4 \rightarrow N_2H_3 + H$ pathway. The configurations of N-H bond cleavage are shown for graphene sheet various transition metal embedded surfaces. The left figure on the surface is the initial state (IS), the middle one is the conformation of the transition state (TS) and, the right figure is the final state (FS).
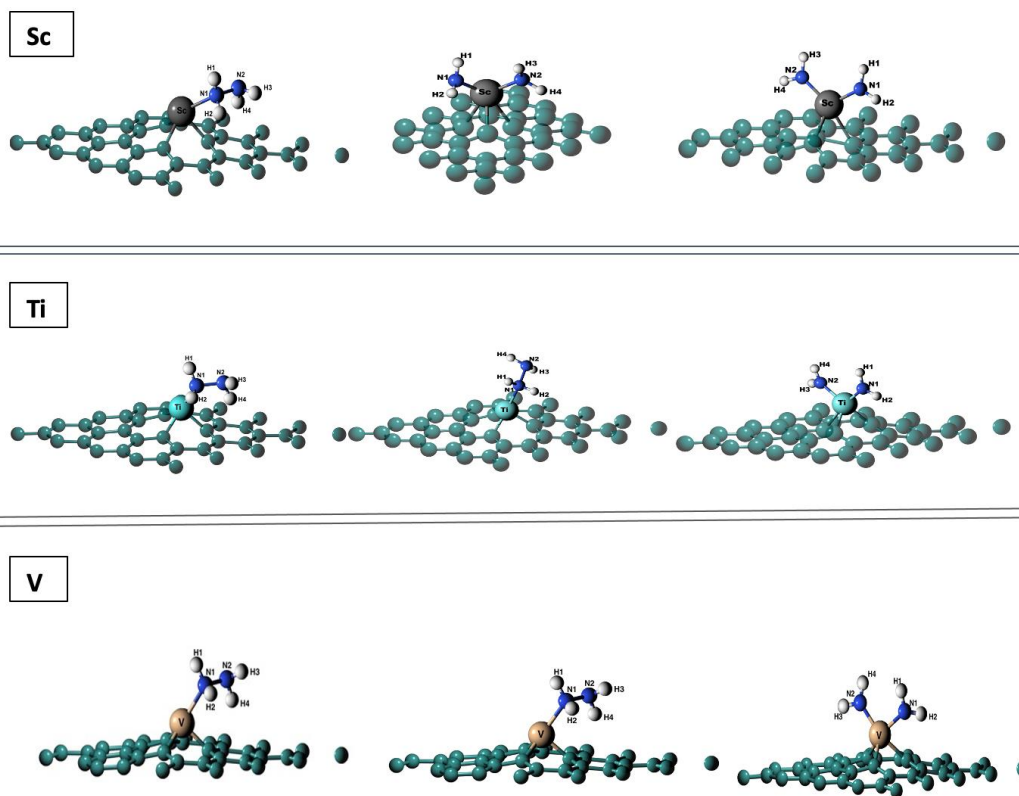
**Figure 5:** $N_2H_4 \rightarrow NH_2 + NH_2$ decomposition. The configurations of N-N bond cleavage are shown for graphene sheet various transition metal embedded surfaces. The left figure on the surface is the initial state (IS), the middle one is the transition state (TS) and, the right figure is the final state (FS).
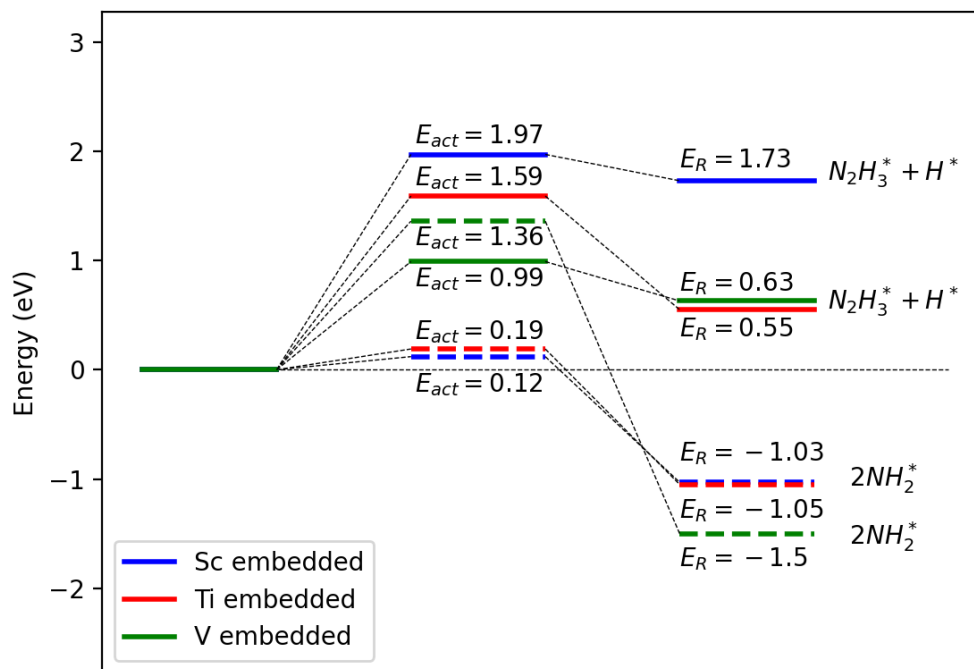
**Figure 6:** Hydrazine decomposition reaction energy diagram. Blue, red and green straight lines are for the N-H bond cleavages for Sc, Ti, and V respectively as their dashed lines are for the N-N bond separation.

## 4. CONCLUSION

In this analysis, the hydrazine decomposition reaction on Sc, Ti and V embedded graphene sheets have been investigated using hydrogen production and two $NH_2$ splits. The chemical interactions are observed on $N_2H_4$ on the surfaces so the surfaces are quite sensitive for hydrazine sensor. $NH_2$ splits on the Sc and Ti embedded surface can exist almost spontaneously and the main production is $2NH_2$ on these two surfaces instead of H production because they have very low activation energies. According to our result, hydrazine molecule on these two surfaces loses highly charge more than 1 $e^-$ when it becomes $2NH_2$ compared to V metal surface, this case may cause a much weaker the N-N bond and the N-N bond splits easily. The activation energy of N-H cleavage on graphene embedded by V metal is 0.99 eV while that of N-N split is 1.36 eV. On V metal surface, H production and $2NH_2$ can be produced. $NH_2$ production on V metal surface does not occur immediately, first of all, the reaction must overcome an energy barrier of 0.37 eV. Therefore, this makes it more advantageous to produce H over V metal graphene. In another word, H production is more favorite than $NH_2$. Although previous theoretical studies found that the N-N

bond scission arises more likely than that of the N-H bond, the dehydrogenation on graphene surface embedded by V is quite promising and graphene embedded by V sheet can be efficient catalysts for hydrazine dehydrogenation.

## ACKNOWLEDGEMENT

## REFERENCES

[1] Staffell, I., et al. (2019). The role of hydrogen and fuel cells in the global energy system [10.1039/C8EE01157E]. Energy & Environmental Science, 12(2), 463-491. https://doi.org/10.1039/C8EE01157E

[2] Council, W.E. (2017). World Energy Issues Monitor.

[3] Pudukudy, M., et al. (2014). Renewable hydrogen economy in Asia – Opportunities and challenges: An overview. Renewable and Sustainable Energy Reviews, 30, 743-757. https://doi.org/https://doi.org/10.1016/j.rser.2013.11.015

[4] Peng, L. and Z. Wei. (2020). Catalyst Engineering for Electrochemical Energy Conversion from Water to Water: Water Electrolysis and the Hydrogen Fuel Cell. Engineering, 6(6), 653-679. https://doi.org/https://doi.org/10.1016/j.eng.2019.07.028

[5] Cheng, Y., X. Wu, and H. Xu. (2019). Catalytic decomposition of hydrous hydrazine for hydrogen production. Sustainable Energy & Fuels, 3(2), 343-365.

[6] Singh, S.K. and Q. Xu. (2013). Nanocatalysts for hydrogen generation from hydrazine. Catalysis Science & Technology, 3(8), 1889-1900.

[7] (2010). National Research Council (US) Committee on Acute Exposure Guideline Levels. Acute Exposure Guideline Levels for Selected Airborne Chemicals. National Academies Press (US), 8.

[8] Zheng, F., et al. (2019). Adsorption of hydrazine on XC3 (X= B, Al, N, Si, and Ge) nanosheets: A computational study. International Journal of Hydrogen Energy, 44(12), 6055-6064.

[9] Zeng, H., X. Cheng, and W. Wang. (2018). A first-principles study on adsorption behaviors of pristine and Li-decorated graphene sheets toward hydrazine molecules. Applied Surface Science, 435, 848-854.

[10] Agusta, M.K., et al. (2011). Theoretical study of hydrazine adsorption on Pt (111): Anti or cis? Surface science, 605(15-16), 1347-1353.

[11] Alberas, D.J., et al. (1992). Surface chemistry of hydrazine on Pt(111). Surface Science, 278(1), 51-61. https://doi.org/https://doi.org/10.1016/0039-6028(92)90583-R

[12] Daff, T.D., et al. (2009). Density Functional Theory Calculations of the Interaction of Hydrazine with Low-Index Copper Surfaces. The Journal of Physical Chemistry C, 113(35), 15714-15722. https://doi.org/10.1021/jp904054n

[13] Agusta, M.K. and H. Kasai. (2012). First principles investigations of hydrazine adsorption conformations on Ni(111) surface. Surface Science, 606(7), 766-771. https://doi.org/https://doi.org/10.1016/j.susc.2012.01.009

[14] Williams, J.O., et al. (1981). Ab initio studies of structural features not easily amenable to experiment: Part III. The influence of lone pair orbital interactions on molecular structure. Journal of Molecular Structure: THEOCHEM, 76(1), 11-28. https://doi.org/https://doi.org/10.1016/0166-1280(81)85109-3

[15] He, Y.B., J.F. Jia, and H.S. Wu. (2015). The interaction of hydrazine with an Rh (1 1 1) surface as a model for adsorption to rhodium nanoparticles: a dispersion-corrected DFT study. Applied Surface Science, 327, 462-469.

[16] Lu, X., et al. (2020). Mechanistic study of hydrazine decomposition on Ir (111). Physical Chemistry Chemical Physics, 22(7), 3883-3896.

[17] Yin, H., et al. (2018). Understanding of selective H2 generation from hydrazine decomposition on Ni (111) surface. The Journal of Physical Chemistry C, 122(10), 5443-5451.

[18] McKay, H.L., S.J. Jenkins, and D.J. Wales. (2011). Dissociative chemisorption of hydrazine on an Fe {211} surface. The Journal of Physical Chemistry C, 115(36), 17812-17828.

[19] Tafreshi, S.S., et al. (2014). Adsorption of hydrazine on the perfect and defective copper (111) surface: a dispersion-corrected DFT study. Surface science, 622, 1-8.

[20] He, Y.-B., J.-F. Jia, and H.-S. Wu. (2015). Selectivity of Ni-based surface alloys toward hydrazine adsorption: A DFT study with van der Waals interactions. Applied Surface Science, 339, 36-45. https://doi.org/https://doi.org/10.1016/j.apsusc.2015.02.136

[21] He, L., et al. (2017). Design strategies of highly selective nickel catalysts for H2 production via hydrous hydrazine decomposition: a review. National Science Review, 5(3), 356-364. https://doi.org/10.1093/nsr/nwx123

[22] Karaman, C., et al. (2020). Preparation of high surface area nitrogen doped graphene for the assessment of morphologic properties and nitrogen content impacts on supercapacitors. Journal of Electroanalytical Chemistry, 868, 114197. https://doi.org/https://doi.org/10.1016/j.jelechem.2020.114197

[23] Akça, A., et al. (2021). Theoretical Insights into the NH3 Decomposition Mechanism on the Cu-and Pt-Embedded Graphene Surfaces: A DFT Approach. ECS Journal of Solid State Science and Technology, 10(10), 101008.

[24] Giannozzi, P., et al. (2009). QUANTUM ESPRESSO: a modular and open-source software project for quantum simulations of materials. Journal of Physics: Condensed Matter, 21(39), 395502. https://doi.org/10.1088/0953-8984/21/39/395502

[25] Giannozzi, P., et al. (2017). Advanced capabilities for materials modelling with Quantum ESPRESSO. Journal of Physics: Condensed Matter, 29(46), 465901. https://doi.org/10.1088/1361-648x/aa8f79

[26] Kohn, W. and L.J. Sham. (1965). Self-Consistent Equations Including Exchange and Correlation Effects. Physical Review, 140(4A), A1133-A1138. https://doi.org/10.1103/PhysRev.140.A1133

[27] Blöchl, P.E. (1994). Projector augmented-wave method. Physical Review B, 50(24), 17953-17979. https://doi.org/10.1103/PhysRevB.50.17953

[28] Stefan Grimmea), J.A., Stephan Ehrlich, and Helge Krieg. (2010). A consistent and accurate ab initio parametrization of density functional dispersion correction (DFT-D) for the 94 elements H-Pu. J. Chem. Phys., 132(154104). https://doi.org/https://doi.org/10.1063/1.3382344

[29] Santos, E.J., A. Ayuela, and D. Sánchez-Portal. (2010). First-principles study of substitutional metal impurities in graphene: structural, electronic and magnetic properties. New Journal of Physics, 12(5), 053012.

[30] Mills, G. and H. Jónsson. (1994). Quantum and thermal effects in H 2 dissociative adsorption: Evaluation of free energy barriers in multidimensional quantum systems. Physical review letters, 72(7), 1124.

[31] Mills, G., H. Jónsson, and G.K. Schenter. (1995). Reversible work transition state theory: application to dissociative adsorption of hydrogen. Surface Science, 324(2-3), 305-337.

[32] Genç, A.E., et al. (2020). Hydrazine decomposition on nickel-embedded graphene. International Journal of Hydrogen Energy, 45(58), 33407-33418. https://doi.org/https://doi.org/10.1016/j.ijhydene.2020.09.035

[33] Henkelman, G., A. Arnaldsson, and H. Jónsson. (2006). A fast and robust algorithm for Bader decomposition of charge density. Computational Materials Science, 36(3), 354-360. https://doi.org/https://doi.org/10.1016/j.commatsci.2005.04.010

[34] Junkermeier, C.E., D. Solenov, and T.L. Reinecke. (2013). Adsorption of NH2 on Graphene in the Presence of Defects and Adsorbates. The Journal of Physical Chemistry C, 117(6), 2793-2798. https://doi.org/10.1021/jp309419x

*RESEARCH ARTICLE*

# THE EFFECTS of DIFFERENT RATIO for GADOLINIUM (GD) and TUNGSTEN (W) on NEUTRON CONTAMINATION CAUSED by MEDICAL LINAC COLLIMATOR

Yiğit Ali ÜNCÜ[1,*], Onur KARAMAN[2], Aycan ŞENGÜL[2], Gizem ŞİŞMAN[3], Kadir AKGÜNGÖR[4]

[1] Akdeniz University, Vocational School of Technical Sciences, Department of Biomedical Equipment Technology, Antalya, yuncu@akdeniz.edu.tr, ORCID: 0000-0001-7398-9540
[2] Akdeniz University, Vocational School of Health Services, Department of Medical Imaging Techniques, Antalya, onurkaraman@akdeniz.edu.tr, ORCID: 0000-0003-3672-1865
[2] Akdeniz University, Vocational School of Health Services, Department of Medical Imaging Techniques, Antalya, aycansahin@akdeniz.edu.tr, ORCID: 0000-0003-4548-5403
[3] Dokuz Eylül University, Research and Application Hospital, Institute of Health Science, Department of Medical Physics, İzmir, gizem.sisman@ogr.deu.edu.tr, ORCID: 0000-0002-6134-9623
[4] Dokuz Eylül University, Science Faculty, Department of Physics, İzmir, kadir.akgungor@deu.edu.tr, ORCID: 0000-0003 1071-4405

## ABSTRACT

The linear accelerators (LINACs) produce high-energy X-rays and electron beams. The interaction between material and radiation is the basis of radiotherapy for the treatment of cancer patients. Neutron contamination is produced in electron beams of medical LINAC by the contribution of the primary and secondary collimators in LINAC as external beam radiotherapy. The photoneutrons produced are easily distributed and spread into the clinical region. As a result, it is recommended that treatment planning be carried out in the patient's tumor volume as well as places outside of this volume. The primary and secondary collimators were found to contribute roughly 52 and 30 percent of the neutron contamination, respectively. The aim of paper is to determine the neutron dose contamination in a LINAC from various materials. Using the Geant4-based Architecture for Medicine-Oriented Simulations (GAMOS) and TALYS 1.95 algorithms, the effects of different material ratios in secondary collimators, such as Gadolinium (Gd) and Tungsten (W), on neutron contamination have been investigated.

## 1. INTRODUCTION

Immunotherapy, surgery, chemotherapy, radiotherapy, and/or a combination of these treatments may be used to treat cancer. One of the cancer therapies that employs high doses of radiation to destroy cancer cells and shrink tumors is radiotherapy. One of the most essential procedures utilized in the treatment of many types of cancer is radiotherapy. It is based on the interaction of ionizing radiation with tumor cells and the biological consequences that result in malignant tissue management and treatment [1].

The linear accelerators (LINACs) are machines that produce high-energy X-rays and electron beams For the treatment of cancer patients, Radiotherapy works by interacting with matter, namely the electrons that surround the nucleus in cells. Ionizing radiation is used to break the DNA of the cells during treatment. As a result, the interaction between radiation and matter translates radiation physics into cancer treatment in the clinic [1].

The treatment method used in cancer treatment is the treatment with X-rays obtained by striking the electrons accelerated in the LINAC to the tungsten (W) target. Linear accelerators are used in the treatment of many types of tumors with the photons and electrons they produce at different energies [2,3]. The collimator designs of LINACs are directly related to the semi-shadow formed at the radiation field edge. Collimation system, dose reduction between 20% and 80% at the radiated edge determines the amount of their penumbra. While it is the same for the x and y collimators that form the field edges for some LINAC heads [4]. X-rays travel through the medium, they interact with the electrons in the medium and cause ionization.

The photoneutrons formed can be scattered and spread out from the LINAC head and into the treatment room. As a consequence, an additional neutron-induced dose occurs in the tumor volume of the patient [5]. In addition to the dose that will occur in the patient, it will cause a significant amount of biological side effects in the patient due to the high linear energy transfer of the neutron [6]. This undesirable dose will increase the risk of secondary cancer in the patient [7]. The creation of a radiation protection protocol suitable for the device used can be created by calculating the neutron dose that patients and employees will receive. In the literature, using the Monte Carlo (MC) based code, the effect of using different composite materials and field sizes with high neutron absorption cross-sections in secondary collimators on neutron dose equivalent (NDE) is also investigated [8,9].

GEometry ANd Tracking 4 (GEANT4) has recently been applied in a variety of disciplines, including high-energy physics, medical physics, and space sciences. GEANT4's modularity allows users to load, utilize, and modify only the components they require. The physics models utilized may be easily understood because to the GEANT4 design and accessibility [10]. Thanks to its sophisticated scripting language, the Geant4-based Architecture for Medicine-Oriented Simulations (GAMOS) is a GEANT4-based MC code meant to be the most widely operable in medical physics applications without the requirement for C++ coding [11].

Our previous study was evaluated the contribution of photoneutron contamination in LINAC by the different composite materials. We compared the condition experimental results to MC Fluka code simulations, and the effect of field size and distance from the isocenter on NDE was İnvestigated [12-14].

The present study aims to calculate the neutron contamination of LINAC via 18 MeV in the case of various materials by using GAMOS and TALYS 1.95. Using the GAMOS and TALYS 1.95 programs, the effect of using different composite materials with high neutron absorption cross-section in secondary collimators on NDE was demonstrated.

## 2. MATERIAL AND METHOD

We used to determine the new material used on the secondary collimator via TALYS 1.95 code. TALYS is commonly used by researchers in nuclear reaction calculations. Radioisotope production

cross-section calculations [15-17], astrophysical[18], level density model calculations [17, 19], photoneutron reactions [16] are some of TALYS's capabilities. $natGd(\gamma,n)$ and $natW(\gamma,n)$ reactions cross sections have been calculated to compared neutron production of two materials. In addition to photoneutron reactions, neutron capture reaction cross-sections of both elements have been computed to investigate the absorption of neutrons caused by the primary collimator. Reaction cross-section calculations have been performed by using the Two-Component Exciton Model [20]. Constant Temperature Fermi Gas Model [21] has been selected as level density model whereas Kopecky-Uhl Lorentzian Model [22] has opted for gamma-ray strength function model.The Medical LINAC head geometry has been shown, and 18 MeV spectrum data was used in the simulations in Fig. 1. The detector, which measures 50x50x0.5 cm$^3$, is placed at a distance of 100 cm from the source skin.
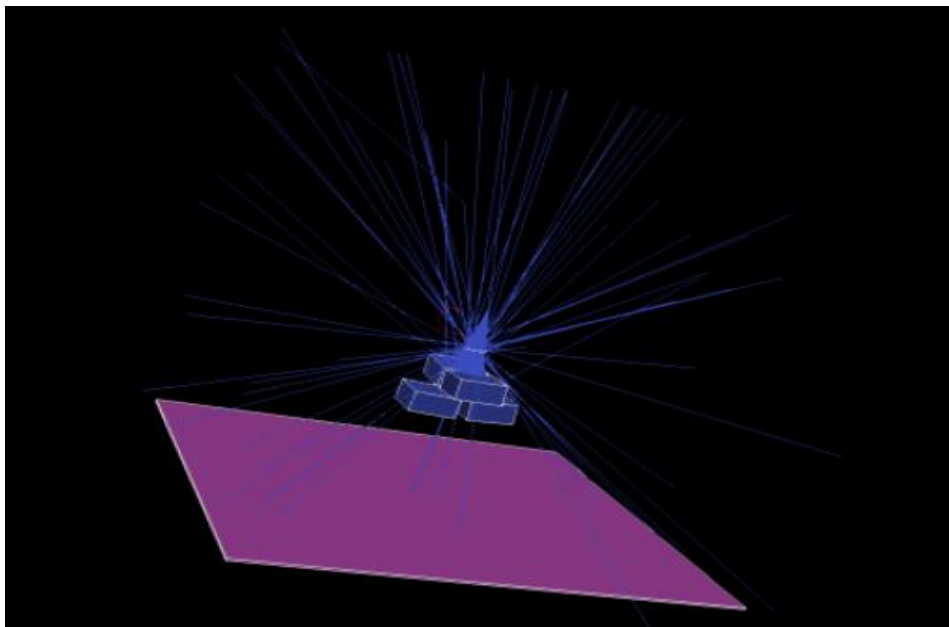


**Figure 1.** The geometry of the Medical LINAC.

GAMOS 5.1.0 version installed on Linux Mint operating system was used. The geometry used in simulation consists of the point source, tungsten flattening filter, x and y jaws. After passing the 18 MeV cone photon, flattening filter, and jaws, it reaches the detector placed away from the source distance of 100 cm to read the surface flux. The physics package used in the simulation was the G4QGSP_BIC_HP package. While scoring, all neutrons reaching the surface were counted using surface flux and neutron filter. While all physical processes were included in the scoring, variance reduction techniques were not used. The number of $10^7$ photons, which gave sufficient results, was used to increase the accuracy of MC calculations and to generate a low statistical error. The calculation time for each simulation took approximately 20 hours, and parallel calculation was not used. W materials doped with Gd in different proportions were created in Table 1.

**Table 1**. The different ratio for $W(\gamma,n)$ and $Gd(\gamma,n)$ density and density values.

| Material | W% | Gd% | Density (gr/cm$^3$) |
|---|---|---|---|
| 100%W0%Gd | 100 | 00 | 19.30 |
| 90%W10%Gd | 90 | 10 | 18.16 |
| 80%W20%Gd | 80 | 20 | 17.02 |
| 70%W30%Gd | 70 | 30 | 15.88 |

## 3. RESULTS AND DISCUSSION

The effect of different materials in secondary collimators on neutron contaminations were investigated in this paper. First, the photon spectrum at 18 MV, which is given in Fig. 2., has been used in GAMOS simulations. Photon per MeV per incident electron is a maximum of approximately 1 MeV.
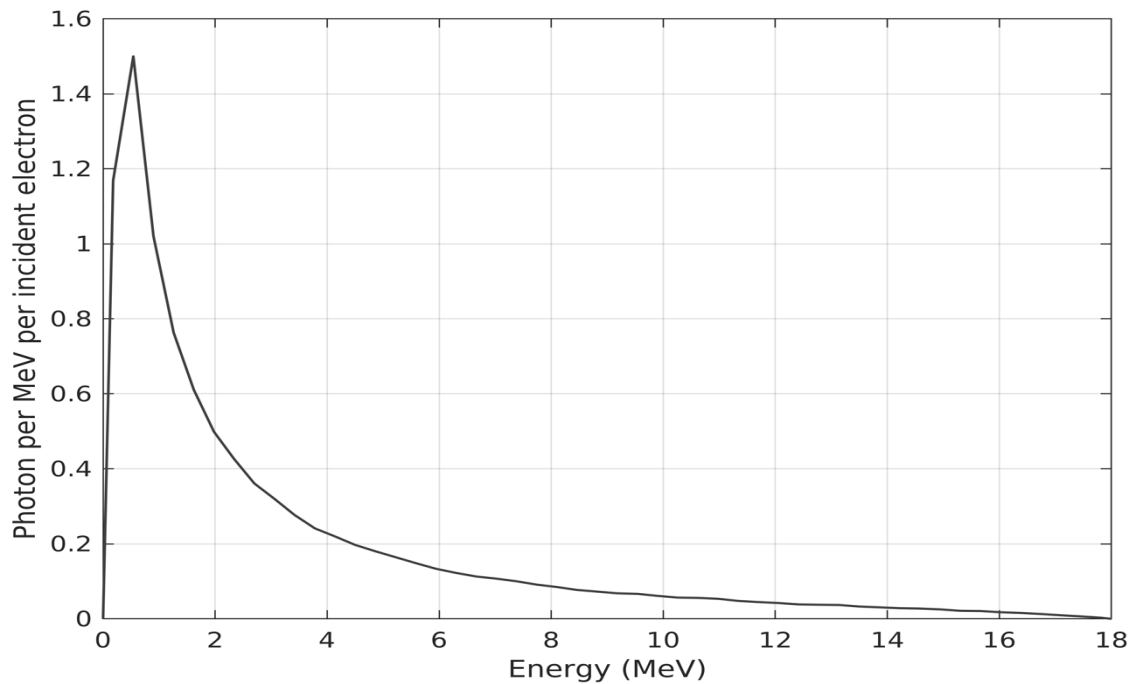


**Figure 2**. Photon Spectrum at 18 MV.
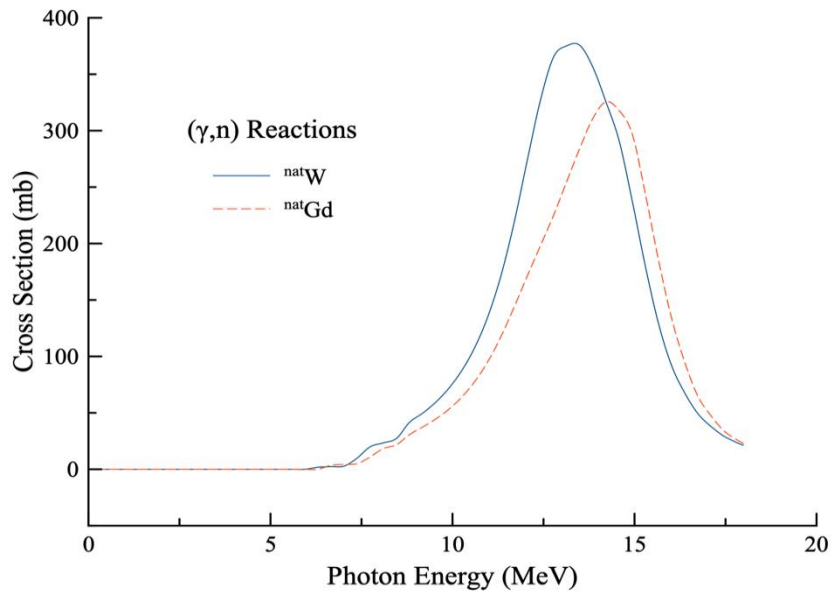
**Figure 3.** Comparison of $W(\gamma, n)$ and $Gd(\gamma, n)$ reaction cross-section calculations.

After the photon spectrum at 18 MV, TALYS 1.95 code has been used for selecting candidate materials. Photon energies, calculated via GAMOS, have been used as energy inputs on TALYS 1.95. TALYS 1.95 calculations have been divided into three steps. Then, photoneutron reaction cross-sections of $natGd(\gamma, n)$ and $natW(\gamma, n)$ have been calculated to compare the probabilities of two reactions in Fig. 3. The maximum cross-section of $natW(\gamma, n)$ is 375.72 mb whereas it is 325.621 mb. This result supports that the use of Gd can reduce neutron contamination caused by secondary collimators.
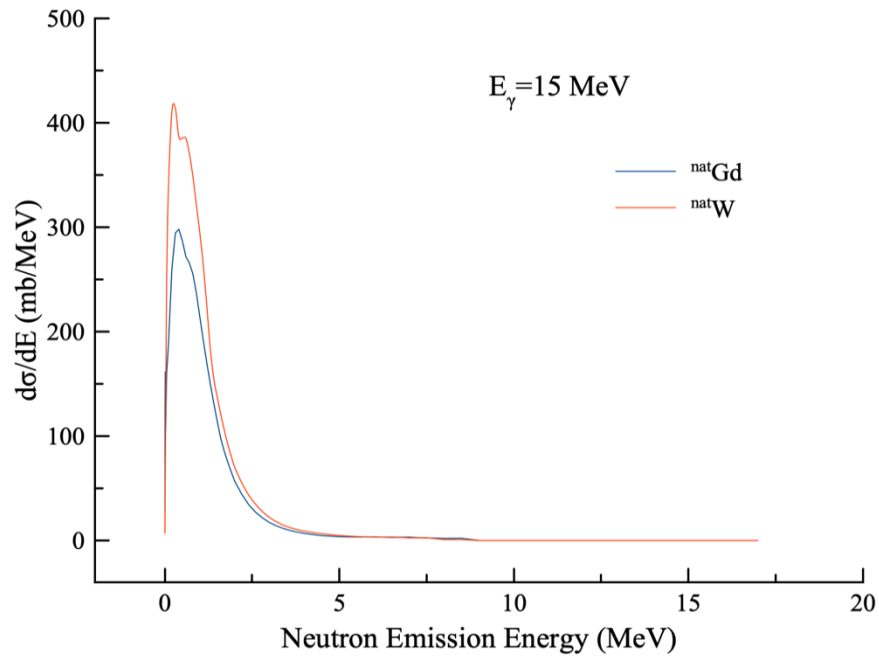
**Figure 4.** $W(\gamma, n)$ and $Gd(\gamma, n)$ calculations at 15 MeV photon energy.

Then neutron energy spectrums of $natW(\gamma, n)$ and $natGd(\gamma, n)$ reactions have been calculated and presented in Fig. 4. Photon energy has been chosen 15 MeV, because approximately at this photon energy $natGd(\gamma, n)$ reaction cross-section is maximum. It can be found that the neutron energy spectrum of both reactions is equal but have different possibilities. Fig. 3 and Fig. 4 have shown Gd can be reduced neutron contamination caused by secondary collimators. However, it is well known that neutron contamination caused by primary collimator has a 52% ratio.
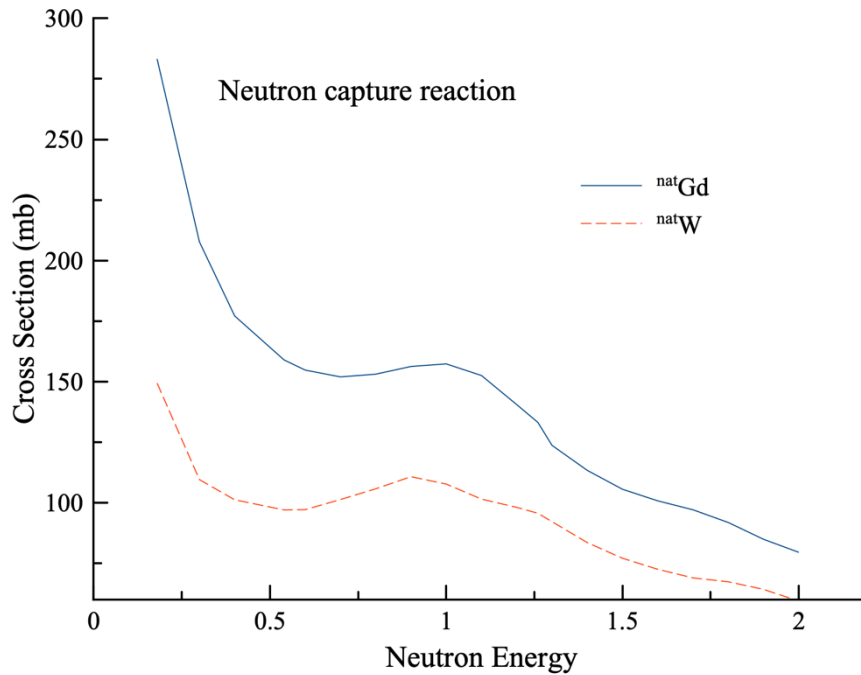
**Figure 5.** Comparison of $W(\gamma, n)$ and $Gd(\gamma, n)$ reaction cross-section calculations for neutron capture reactions.

We have focused on neutron capture cross-sections of both elements. The comparisons of neutron capture reaction cross sections have been shown in Fig. 5. It is determined that neutron capture reaction cross-sections of Gd are higher than W's. Consequently, it can be speculated that Gd can stop neutrons caused by collimators.

After determining the used Gd on the secondary collimators, GAMOS simulations have been performed for different Gd ratios which are given in Table 1. Total neutron flux has been obtained for this size; 0x0 cm$^2$, 10x10 cm$^2$, and 40x40 cm$^2$. Total neutron fluxes through the size of the different fields and Gd ratios have been presented in Table 2.

**Table 2**. The neutron flux (particle per cm$^2$) for different material compositions of secondary collimators.

| Field size (cm$^2$) | Ratio of W/Gd | | | |
|---|---|---|---|---|
| | 100/0 | 90/10 | 80/20 | 70/30 |
| 40x40 | 6.4 E-08 | 5.9 E-08 | 4.8 E-08 | 3.7 E-08 |
| 10x10 | 4.9 E-08 | 4.7 E-08 | 4 E-08 | 3.6 E-08 |
| 0x0 | 4.6 E-08 | 4.5 E-08 | 4 E-08 | 3.7 E-08 |

In 0x0 cm$^2$ field size total neutron flux of original LINAC whose secondary collimators consist only W, is 4.6 ×10$^{-8}$ particle/cm$^2$, whereas 4.5 ×10$^{-8}$, 4 ×10$^{-8}$ and 3.7 ×10$^{-8}$ particle/cm$^2$ for %10, %20 and %30 Gd, respectively. As can easily be seen in Table 2, Gd doped has been reduced neutron contamination at 0x0 cm$^2$ field size. For 10x10 cm$^2$ field size, neutron flux has been found 4.9 ×10$^{-8}$, 4.7 ×10$^{-8}$, 4 ×10$^{-8}$ and 3.6 ×10$^{-8}$ particle/cm$^2$ for 100%, 90%, 80% and 70% W, respectively. As 0x0 cm$^2$ field size, neutron contaminations have reduced on 10x10 cm$^2$ field size in Table 2. The last field size investigated in this paper is 40x40 cm$^2$. Neutron flux of secondary collimators which consist of W has been computed 6.4 ×10$^{-8}$ particle/cm$^2$. However, neutron fluxes of Gd doped secondary collimators have been found 5.9×10$^{-8}$, 4.8 ×10$^{-8}$ and 3.7×10$^{-8}$ particle/cm$^2$ for 10%, 20% and 30% Gd respectively in Table 2.

There are several similar studies evaluating neutron contamination dose in the case of different materials in collimators in LINACs [7, 12, 13]. LINACs are the most widely used medical device for external beam radiation treatments for cancer [1]. The calculation of photoneutrons in LINACs has become important nowadays. The use of Monte Carlo methods in computations, on the other hand, provides more precise data concerning photoneutron properties in radiotherapy [8,10,11]. The goal of this research was to reduce neutron contamination caused by a secondary collimator. As a result, collimators and flatting filters were simulated to examine neutron contamination generated by the secondary collimator using the GAMOS 5.1.0 and TALYS 1.95 codes for Medical LINAC.

Gd and W materials used in different proportions in the secondary collimator changed the neutron flux. Consequently, the contribution of the neutron dose is reduced in the total dose due to the Gd neutron capture is more than W. As a new material, Gd, the simulation was carried out in high dose using GAMOS. The results of these measurements provided important feedback on material development and the dose contribution of Gd and W in irradiation was determined comparatively at different rates

## 4. CONCLUSION

The generation of neutrons in high-energy photon beams used in radiotherapy is examined in this paper. Our results use W / Gd (70/30) composite material to be an effective method to reduce neutron contamination in secondary collimators. These results have been provided crucial information about unwanted NDE and radiation protection policy for clinic staff and also patients.

## ACKNOWLEDGEMENT

## REFERENCES

[1] World Health Organization (WHO) (2020). report on cancer: setting priorities, investing wisely and providing care for all. Geneva: World Health Organization;. Licence: CC BY-NC-SA 3.0 IGO.

[2]   Darestani, H., et al. (2011). Measurement of neutron dose component in central axis absorbed dose of 18 MV photon beam by TLD600 and TLD700 dosimeters. Basic & Clinical Cancer Research, 3(3&4): 22-29.

[3]   ICRP. (2019). Proceedings of the Fifth International Symposium on the System of Radiological Protection. Ann. ICRP49(S1): 32-34.

[4]   Khan, F.M., Gibbons, J.P. (2014). Khan's the physics of radiation therapy: Lippincott Williams & Wilkins.

[5]   Vylet, V., Liu, J. C. (2001). Radiation protection at high energy electron accelerators. Radiation protection dosimetry, 2001. 96(4): p. 333-343.

[6]   ICRP. (1991). Recommendations of the International Commission on Radiological Protection. ICRP Publication 60. Ann. ICRP21: 1-3.

[7]   Howell, R.M., et al. (2005). Investigation of secondary neutron dose for dynamic MLC IMRT delivery. Medical physics, 32(3): 786-793.

[8]   Ma, A., et al. (2008). Monte Carlo study of photoneutron production in the Varian Clinac 2100C linac. Journal of Radioanalytical and Nuclear Chemistry, 276(1): 119-123.

[9]   Jahangiri, M., et al. (2015). The effect of field size and distance from the field center on neutron contamination in medical linear accelerator. International Journal of Advanced Biological and Biomedical Research (IJABBR), 3(1): 97-104.

[10]  Carrier, J.F., et al. (2004). Validation of GEANT4, an object- oriented Monte Carlo toolkit, for simulations in medical physics. Medical physics, 31(3): 484-492.

[11]  Arce, P., et al. (2008). GAMOS: A Geant4-based easy and flexible framework for nuclear medicine applications. in 2008 IEEE Nuclear Science Symposium Conference Record, IEEE.

[12]  Karaman, O., Tanir A.G., Karaman C., (2019). Investigation of photoneutron contamination from the 18-MV photon beam in a medical linear accelerator, Materiali In Tehnologije, 55(3): 699-704.

[13]  Karaman, O., et al. (2020). Investigation of the effects of different composite materials on neutron contamination caused by medical LINAC/Untersuchung der Auswirkungen verschiedener Verbundmaterialien auf die Neutronenkontamination durch medizinische LINAC. Kerntechnik, 85(5): 401-407.

[14]  Karaman, O., Tanir, A.G. (2020). Radyoterapi Odasının Farklı Noktalarında Nötron Kirliliğinin Ölçülmesi. Süleyman Demirel Üniversitesi Fen Edebiyat Fakültesi Fen Dergisi, 15(1): 36-44.

[15]  Özdoğan, H., Şekerci, M., Kaplan, A. Photo-neutron cross-section calculations of 54, 56Fe, 90, 91, 92, 94Zr, 93Nb and 107Ag Isotopes with newly obtained Giant Dipole Resonance parameters. Applied Radiation and Isotopes, 165: 109356-0.

[16] Özdoğan, H., Şekerci, M., Kaplan, A. (2021). Production cross–section and reaction yield calculations for 123-126I isotopes on 123Sb (α, xn) reactions. Kuwait Journal of Science, 48(2): 1-11.

[17] Şekerci, M., Özdoğan, H., Kaplan, A. (2020). Level density model effects on the production cross-section calculations of some medical isotopes via (α, xn) reactions where x= 1–3. Modern Physics Letters A, 35(24): 2050202-0.

[18] Şekerci, M., Özdoğan, H., Kaplan, A. (2020). Astrophysical S-Factor Calculations under the Effects of Gamma-Ray Strength Functions for Some Alpha Capture Reactions. Moscow University Physics Bulletin, 75(6): 585-589.

[19] Özdoğan, H., Çapalı, V., Kaplan, A. (2015). Reaction Cross-Section, Stopping Power and Penetrating Distance Calculations for the Structural Fusion Material 54 Fe in Different Reactions. Journal of Fusion Energy, 34(2): 379-385.

[20] Kalbach, C. (1986). Two-component exciton model: basic formalism away from shell closures. Physical Review C, 33(3): 818-833.

[21] Ignatyuk, A.V., Istekov, K.K., Smirenkin, G.N., (1979). The role of collective effects in the systematics of nuclear level densities. Yad. Fiz. 29, 875–883.

[22] TALYS–1.8 (2019). A Nuclear Reaction Program, User Manual, NRG, The Netherlands., A. 1st ed.Koning, Hilaire, S., Goriely, S.

RESEARCH ARTICLE

# A SURVEY OF GENE EXPRESSION DURING UREDOSPORE GERMINATION IN *PUCCINIA SORGHI*

Mehmet Ali SÜDÜPAK[1]

[1]Yozgat Bozok University, Faculty of Arts and Sciences, Department of Biology, Yozgat, mali.sudupak@yobu.edu.tr,
ORCID:0000-0001-9439-0916

## ABSTRACT

Transcript profiling is commonly used to identify genes that are expressed under various conditions, in different tissues and developmental stages of organisms. Transcripts tags detected from germinating uredospores of *Puccinia sorghi* T09 isolate using a modified cDNA-AFLP approach were characterized in the current study. GenBank similarity searches and sequence mapping of 56 sequence tags to available genome sequence of Argentinian strain RO10H11247 revealed 38 *P. sorghi* similar sequences, corresponding to 31 individual Genbank records. With the obtained similarities and protein domain searches, presumed functions associated with the 27 *Ps* TDFs were inferred, the majority of which appear to encode products that appear to be important in host invasion, pathogen growth and proliferation. Among them, chitinase, oligopeptide transporter protein, peptidyl-tRNA hydrolase, signal peptide, small secreted proteins, velvet and cutinase domain containing proteins are the prominent ones. Expressions of four selected genes, three of which are newly identified, were verified in germinating spores and infected plant leaf material cDNA preparations with RT-sqPCR. Together with the newly identified and annotated *P. sorghi* genes, obtained profile, in general, represent a gene set whose products are conceivably involved in host invasion and pathogenesis along with the basic housekeeping functions.

**Keywords**: *P. sorghi, germinating uredospore, cDNA-AFLP, Expressed Sequence Tag.*

## 1. INTRODUCTION

The common maize rust is one of the important diseases of corn caused by the *Puccinia sorghi* Shew., which appears to inflict significant yield loses up to 40% depending on the severity of infection [1]. As an obligate biotrophic basidiomycete, *P. sorghi* (*Ps*) manifests its main pathogenicity during the uredospore cycle propagation on corn. Genes conditioning race-specific resistance to the *Ps* races have been identified from various sources of corn germplasms and employed to same extent in rust control [2,3]. However, the protection provided by these vertical resistance factors depends on the presence of their corresponding avirulance/effector gene products in the invading pathogen, and this race specific resistance often breaks down by the appearance of the new virulent races.

Various techniques, such as gel-based DDRT-PCR, cDNA-AFLP, hybridization based macroarray, microarray and sequence based SAGE, transcriptome sequencing have been used to detect expressed

sequences and study gene expression changes in cells/organisms during development and under different environmental conditions. Expressed Sequence Tag (EST) analysis is one of these techniques that has been used to generate EST databases, which are valuable source in gene characterizations, expression analysis and microarray designs. A number of EST studies have been conducted in fungi to examine gene expression at various developmental stages and structures. Hahn et al. [4] studied expressed genes during the *Uromyces faba* infection of broad bean at uredospore germination stage and haustorium. They detected dramatic expressional changes between these transcript profiles. EST analysis covering resting uredospore, germinating uredospore, appressorium, haustorium formation stages of *Puccinia triticina* infections of susceptible and resistant wheat genotypes with 13 different cDNA libraries generated 25.558 sequence tags [4]. Zhang et al. [6] obtained a set of 4798 EST sequences from germinating uredospores of *Puccinia striiformis*, and found that 23.9% and 13.3% of the identified 1118 unisequences are homologous to functionally characterized proteins and hypothetical proteins, respectively while 62.8% unisequences had no significant homologs. A number of other EST studies were conducted in fungi to obtain gene expression profiles under various conditions [7,8].

Elucidation of mechanisms and underlying genetic factors in the pathogen, such as virulence factors, effectors and other infection facilitating activities participating in host invasion and pathogenesis are essential to both understanding and manipulation of the pathosystems. Factors functioning in host resistance and pathogen avirulance/virulence are elucidated to some extent in a number of obligate host-parasite systems [9-11]. The maize-*Ps* pathosystem, however, has not been characterized sufficiently in this regard. Recent *Ps* genome sequencing and annotation [12] provide a valuable genomic tool to functional genomic studies and addressing to the specific aspects of the *Ps* growth and infections. Current study uses this genomic information [13] and other sequence databases and describes a survey of the messages expressed in germinating *Ps*. uredospores and infected plant material.

## 2. MATERIALS AND METHODS

### 2.1. Biological material preparation and total RNA isolation

*Puccinia sorghi* race T09 uredospores grown on A188 seedlings and infected A188 leaf material were used in the study. Total rust RNA isolations were carried out from freshly collected ~1 mg spores, which were germinated overnight on a 15 ml sterile $dH_2O$ in (6x1) petri dishes in a dark cabin at room temperature (18-24 $^o$C). Similarly, leaf materials were prepared as two parallel sets, one for control and one for inoculation sample as described in Südüpak [14] (2014). Control and inoculation seedlings were kept at 24-27 $^o$C under natural daylight with a light/dark photoperiod of 16/8 h, and leaf materials were sampled at 24, 48, 72 and 96 post inoculation hour (pih) intervals as ~100 mg 2nd leaf segments. Both fungal mat formed by the germinated uredospores and leaf samples were individually collected and quickly placed into 1.5 ml. tubes individually and frozen in liquid nitrogen. Without thawing, the sampled materials were grounded individually into fine powders in their tubes, and RNAzol (Molecular Research Center, MRC) extraction buffer was added to powder at the scale of 100 μl per mg rust material and 1 ml per 100 mg plant material and mixed to obtain a homogenates. RNA extractions were carried out according to the manufacturer's instructions. At the final step, RNA pellets were washed with 400 μL of 75% ethanol (prepared with DEPC-treated water) twice and briefly dried to evaporate ethanol. Pellets were dissolved in 50 μL. DEPC-treated water and stored at -20. Nucleic acid concentrations were measured spectrophotometrically at 260 nm with $A_{260}/A_{280}$ ratio of 1.8-1.9 and $A_{260}/A_{230}$ ratio around 2.3.

## 2.2. cDNA synthesis, TDF generation and sequencing

cDNA synthesis, other nucleic acid manipulations and cDNA-AFLP detection of mRNA tags were carried out as described in Südüpak [14]. Elution of TDF (Transcript Derived Fragment) bands, cloning and preparation to sequencing reactions are also given in Südüpak [14]. Only 9 TDFs were directly sequenced using either one of the cDNA-AFLP primers while colony PCR amplified products were sequencing template in others. TDF sequencing was conducted by the commercial service providers, and results were provided as sequencing files. 3'-RACE experiments for the isolation of AC/CC R2-4 transcript end were carried out using a forward gene specific primer and an oligo designed to bind to mRNA 3' ends.

## 2.3. Bioinformatics

Sequence data were first manually examined in SnapGene Viewer for the presence of adapter and primer tags. TDF sequences with trimmed adapter segments were compiled into a text file in FASTA format to be used in similarity searches and mapping to *Ps* scaffolds. Sequence data were first *Ps* genome blasted in NCBI (ncbi.nlm.nih.gov/BLAST) and TDF sequences displaying significant (<1e-4) similarities to *Ps* genome sequence (GCA_001263375) scaffolds were determined. These sequences were then submitted to blast/blat routine of the Ensembl Genomes [13] (fungi.ensembl.org/Puccinia_sorghi_gca_001263375/Tools/Blast) to confirm and visualize the TDF similarity regions on scaffolds with the annotated genes, if there is any. TDFs mapping (with very high similarity) very closely to (e.g. to presumed 5'-UTR or 3'-UTR) or as part of an annotated genes were considered as the annotated gene derivatives and designated accordingly. TDF mapping to regions with no annotated genes were studied in gene prediction programs in that the genomic sequences surrounding the TDF similarity region with the size of an average *Ps* gene were copied and submitted to FGENESH routine of Softberry (softberry.com) website with the organism=Puccinia (rusts) selection, probable genes, if there is any, were predicted. Search reveals structure of the predicted gene with its ORF and encoded polypeptide sequence. Predicted gene and its ORF sequence were then examined to position TDF sequence. Majority of the TDFs mapped to 3' ends of the annotated and predicted genes, which is consistent with the strategy used in their isolation. Protein products of previously annotated and newly predicted genes were examined to make inferences about their structures and functions using protein databases and tools such as UniProt (uniprot.org) InterProScan, iPSORT, SignaIP [15].

## 2.4. RT-sqPCR validations of selected TDF expressions

Three newly identified (MN199982, MT677935, MT677936) and two previously predicted, *PsOPT* (KNZ51092) and *PsChi* (KNZ44027) genes were selected for validation studies (Table 1). A pair of RT-PCR primers were designed for each gene using the web-based program, Primer3Plus (sourceforge.net/projects/primer3), with its modified parameters for amplifying products between 90 and 250 bp size range covering the TDF BLAST homology segments. Primers and other oligos used in the study were synthesized by Oligomer Biotechnology (Ankara) while enzymes and other reagents were purchased from Fermentas-Thermo, Sigma and Merck.

In expressional verification studies, material preparation, RNA isolation and cDNA synthesis for two-step RT-sqPCR experiments were carried out essentially as given in Südüpak [14]. RT-sqPCRs were prepared as individual 25 μl mixtures containing 2.5 μl 10x reaction buffer (Fermentas-Thermo), 2.5 mM MgCl$_2$, 0.2 mM dNTP mix, 10 pmoles of each Forward and Reverse gene specific primers, 0.5 U *Taq* DNA polymerase (Fermentas-Thermo) and 2 μl of 10x diluted first strand cDNA template. Temperature and time profiles of the PCRs were setup as follows; an initial denaturation period of 3

min at 95 °C, followed by 35 cycle-PCR, each cycle consisting of a denaturation step at 94 °C for 20 sec., an annealing at 59 °C for 30 sec. and extension at 72 °C for 50 sec, amplifications were finalized with a 5 min. extension period at 72 °C. Reaction mixtures were individually mixed with 5 μl of 6X loading dye and electrophoresed for 2 hours in 2% 0.5XTBE agarose gels containing 0.4 μg ml$^{-1}$ ethidium bromide, and products were visualized and documented on a 312 nm UV transilluminator.

**Table 1.** List of genes with their RT-PCR primers used in expression verification studies.

| Genes (GI, accession #) | Primer sequences, 5'→3' F/R | Product (bp) | PCR annealing temperature (°C) |
|---|---|---|---|
| *HKG-U* (GRMZM2G047204) | GCGTGCTCTTTCGTCAGATGTG<br>CCTACTGTTGGCTGGAGACTGG | 156 | 59 |
| *Ps1-2* (MN199982) | TGTAAGCAAGTTGGCGTTAG<br>CTCCTGTTGAGGTCAATGTC | 131 | 59 |
| *Ps2-4* (MT6777935) | CCGGTGTGATTGCTTCTCCT<br>GTATGTTCCGCCGTATGGGT | 161 | 59 |
| *PsChi* (KNZ44027.1) | CACCTGAACATCTGGTCCCA<br>TGGTTCTCAGTGTACGACCG | 105 | 59 |
| *PsOPT* (KNZ51092.1) | GATGGTGGCACCCAGATCAT<br>GGGACAGACCTAGGAGGGTT | 116 | 59 |

### 3. RESULTS

Rust TDFs generated in a previous cDNA-AFLP study were utilized to examine the expressed messages in the germinated *Ps* T09 uredospores and infected plant material. Sequence characterized 56 TDFs with a size range between 24 bp to 354 bp were divided into two groups as *Ps* similar and non-Ps similar according to the obtained blast similarity results. Among 49 *Ps* similar TDFs, 38 displayed significant similarities (<1e-6) to 31 *Ps* GenBank entries, the majority of which have annotated functions. Nine contigs (TDFs derived from the segments of same gene) were identified in the data set while many of the TDFs represented as singletons (Table 2). Obtained similarities for 11 TDFs were not significant (1e-4<), thus, they are not listed in the table. Five of the non *Ps* similar TDFs displayed similarities to sequences from other fungi, one of which displaying a significant similarity to the rust infecting RNA virus is listed in table. Remaining two TDFs found to be similar to organelle and bacterial DNA sequences are not listed in the Table 2 as well.

**Table 2.** Expressed Sequence Tags (EST) identified in the study.

| TDF # | Size* | Accession # | GenBank record showing the closest similarity | +E-val. |
|---|---|---|---|---|
| *Newly identified and annotated gene TDFs* | | | | |
| [1]AC/GG R1-2 | 354 | MN199982 | *Ps* **uncharacterized (secreted) protein** | 0.0 |
| AC/CC R5-2 | 117 | MN199982 | Maps to 3' end of MN199982, revealing its 3'-UTR sequence. | 0.0 |
| [1]AC/CC R2-4 | 281 | MT677935<br>MT677936 | *Ps* **uncharacterized (secreted) protein** similar to MN199982 (identical two copies reside on a ~4 kb tandemly duplicated gDNA) | 0.0 |
| AC/CG R3 | 198 | MT677935 | Aligns to 5' end of the *Ps*. AC/CC R2-4 | 6e-57 |

| | | MT677936 | duplicated genes, revealing their 5'-UTR sequences. | |
|---|---|---|---|---|
| AC/GG R2-3 | 306 | MN190718 | *Ps* **cytochrome C oxidase subunit 1** (tag covers ORF 3'end and 3' UTR segments) | 0.0 |
| AC/CG R1 | 300 | NC_044103.1 | *P.tiriticina* mt **NADH-ubiquinone oxidoreductase subunit 1**, aligns to the *Ps* **mt scaffold_46**, annotated in this study. | 5e-137 |
| GG/TG R5-5 | 120 | LAVV01008557.1 | Maps to the scaffold_354, positioning ~1500 bp to 3' end of KNZ52507. A new ORF close to the tag position, whose aa sequence is similar (3e-62) to KNZ64419.1 was identified | 7e-54 |

*TDFs from genes with unknown and known functions or bearing a domain*

| | | | | |
|---|---|---|---|---|
| GG/CA R9 | 95 | KNZ54019.1 | *Ps.* **uncharacterized protein containing cutinase domain** | 3e-41 |
| AC/GG R3-4 | 198 | KNZ56820.1 | *Ps* **uncharacterized protein containing velvet domain** | 1e-97 |
| [1]TG/GA R3 | 144 | KNZ51092.1 | *Ps.* **putative oligopeptide transporter** (OPT) | 8e-39 |
| GA R5 | 48 | KNZ45441.1 | *Ps.* **uncharacterized conserved protein**, putative **monocarboxylate transporter 2** | 1.7e-7 |
| GA R4 | 80 | KNZ54866.1 | *Ps.* **putative signal peptide** | 9e-23 |
| AC/CC R6-5 | 173 | KNZ63665.1 | *Ps* **protein (serine/threonine) kinase** | 0.0 |
| GG/TG R3, R4 | 170 | KNZ54998.1 | *Ps.* **Rab family protein GTPase, Rab4** | 7e-80 |
| AC/CC R8-3 | 115 | KNZ50565.1 | *Ps.* **nucleotide, nucleic acid binding hypothetical protein,** | 0.0 |
| [2]AC/GG A2, R2-1 | 228 | KNZ64435.1 | *Ps* **peptidyl tRNA hydrolase** mRNA | 2e-124 |
| [1]AC/CC-A11, R11, R4, R12-5 | 94 | KNZ45394.1 | *Ps,* putative **phosphatidylethanolamine binding protein** | 8e-42 |
| AC/CG R4 | 190 | KNZ60925.1 | *Ps.* **uncharacterized Zn binding protein** (may be a Zinc finger protein) | 3e-34 |
| AC/CC R16-5 | 57 | KNZ50028.1 | *Ps.* **hypothetic protein containing wax synthase domain** | 0.0 |
| [1]AC/GG R7-2 | 87 | KNZ44027.1 | *Ps* **chitinase** | 4e-30 |
| AC/GG R5-2 | 96 | KNZ51711.1 | *Ps* **hypothetical (secreted) protein** | 3e-143 |
| AC/CG R6 | 119 | KNZ54287.1 | *Ps* **hypothetical protein** similar to **syntaxin binding** protein | 1e-36 |
| GT R6 | 95 | KNZ44173.1 | *Ps.* **uncharacterized protein containing DUF3759 domain** | 1e-4 |
| AC/CC R13, R14 | 76 | KNZ59498.1 | *Ps.* **hypothetic protein similar to steroid reductase** | 1e-33 |
| AC/CC R9-3, R10 | 108 | KNZ62659.1 | *Ps.* predicted **exodeoxyribonuclease V** | 4e-51 |
| AC/GG R6-1 | 73 | KNZ54883.1 | *Ps* **hypothetical protein, dihydrolipoamide dehydrogenase** | 2e-26 |
| AC/GG R8-2 | 56 | KNZ52430.1 | *Ps* **histon 3.1** (similar to 3' UTR) | 2e-34 |
| AC/CC R3-4 | 240 | LAVV01006726.1 | *Ps* **28S rRNA 3'-end fragment** | 8e-121 |

| AC/CC R5-5 | 98 | | *Ps* 2**8S rRNA sequence, derived from 5' end.** | 8e-48 |
|---|---|---|---|---|
| AC/CC R7-3 | 126 | KNZ46759.1 | *Ps* **hypothetical protein** | 0.0 |
| GG/CA R14 | 71 | KNZ49933.1 | *Ps.* **uncharacterized protein** | 2e-15 |

*TDFs displaying significant similarities to sequences from other fungi*

| GG/TG R2 | 200 | GW673618.1 | *Melampsora larici-populina* mRNA sequence, derived from narnavirus RNA dependent RNA polymerase seq. | 8e-30 |
|---|---|---|---|---|

[1]Expressed in both germinating *Ps* spores and infected plant.
[2]Expressed in infected plant.
[+]Nucleotide sequence similarity E-value.
[*]Fragment sizes are in bp. In cases where more than one TDF displayed closer similarity to the same GenBank record, only the largest product size is listed in the column.

ESTs, AC/CC R1-2, AC/CC R2-4, AC/CC R5-2 and AC/CG R3 were derived from transcripts of the genes that were not previously identified. GenBank similarity and coding sequence searches revealed that fragments correspond to ORF containing genomic segments. Gene prediction and sequence mapping of the AC/CC R1-2 TDF to the available Argentinian *P. sorghi* race RO10H11247 genome sequence, scaffold (LAVV01007405.1) has shown that fragment was derived from a transcript with a 327 bp ORF which resides on a minimum of 498 bp genomic segment containing three-exons intervened by two short introns (80 and 71 bp respectively), which encodes 108 aa polypeptide with an unknown function. This TDF contained all three exons along with 21 bp 5' UTR sequence. TDF AC/CC R5-2 corresponded to the 3' UTR of this gene. Sequence was GenBank accessioned as MN199982 (Table 2). Similarly, *Ps* genome blast searches revealed that TDFs, AC/CC R2-4 and AC/CG R3 were derived from the Scaffold_1712 (Sequence ID: LAVV01006518.1, Length: 7291 bp), which contained two tandemly duplicated genomic segments, each copy bearing a previously unknown gene whose first two exons and 3rd exon 5' end sequences are represented on AC/CC R2-4 while AC/CG R3 tag derived from the 5'-UTR sequence. RACE experiments were conducted to recover the transcript 3' end. A sequence data covering the partial 5'-UTR, coding sequence (CDS) and the (presumably) complete 3'-UTR were obtained. Aligning this sequence to the same scaffold indicated the presence of an extra intron residing in the 3' UTRs of the both copies. Sequences and duplicated gene annotations were GB accessioned as MT677935 and MT677936. All three genes (MN199982 MT677935 and MT677936) encode polypeptides that are similar in length and sequence containing a number of nearly perfect PYGGY repeats at their C-terminal ends and have typical signal peptides at the N-terminals (details are given in GenBank records)

Functional assessment of the identified ETSs provide information about the expression profile displayed during uredospore germination and host infection. The most abundantly expressed contig represented by four TDFs was phosphatidylethanolamine binding protein, which was detected in both germinating spores and infected leaf samples. Peptidyl tRNA hydrolase similar TDFs (contig) found in majority of the studies are similarly expressed in both germinating spores and infected plant tissues. Also, newly identified gene (MN199982, MT6777935 and MT6777936) contigs each represented by two TDFs are expressed in germinating spores and infected plant tissue (Figure 1). Similarly, three other gene contigs (Rab family protein GTPase, exodeoxyribonuclease V and hypothetic protein similar to steroid reductase) each represented by two TDFs expressed in germinating spores without information about their in planta expression. Genes identified with singleton similarities also bear functions that are known to be important in fungal growth and the process of host colonization:

Chitinase, 28S rRNA encoding sequence, oligopeptide transporter, putative monocarboxylate transporter 2, hypothetic protein containing wax synthase domain, hypothetic protein similar to steroid reductase, cytochrome C oxidase subunit 1 appear to be examples of fungal growth promoting ones while cutinase domain containing protein, several small secreted protein encoding ones including three newly identified genes, signal peptide and velvet domain containing uncharacterized protein encoding messages presumably function in host invasion and pathogenesis. Protein (serine/threonine) kinase, zinc finger similar protein, nucleotide, nucleic acid binding hypothetical protein and syntaxin binding protein similar ones could have function in either or both of these processes.
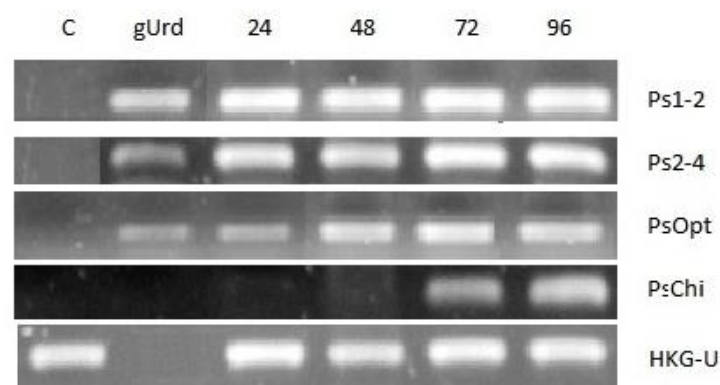


**Figure 1.** RT-sqPCR expression profiles obtained from the selected genes (*Ps1-2*, *Ps2-4*, *PsOPT*, *PsChi*) along with the maize housekeeping gene (*HKG-U*). Abbreviations and numbers indicate; C, uninfected plant control, gUrd, germinating uredospore, 24, 48, 72 and 96 hrs of post-inoculation plant material cDNA samples.

Expressions of four rust genes along with a maize housekeeping gene [16] were studied in germinating spore and infected plant material time course samples (Table 1). RT-sqPCR results revealed that *Ps1-2* (MN199982) *Ps2-4* (MT6777935 and MT6777936) and *PsOPT* are expressed relatively weakly in germinating spores whereas a marked expression increase was apparent in the infected plant material parallel to the post-infection hour increase as seen in Figure 1. Chitinase expression in germinating spores were found to be barely detectable and this was also the case at the initial infection hours while an apparent induction occurred at 72 and 96 post-infection hour infected plant materials.

## 4. DISCUSSION

Functional assessment of identified genes in transcriptome studies provides information about the functional spectrum and expressional modulations involved in the studied processes. Studies with the rust fungi have revealed that host penetration and colonization require functions involved in host defense suppression and acquiring nutrients from the host metabolism. Transcriptome analyses of spores and germinated urediniospores revealed that genes involved in cell proliferation, releasing energy from stored lipid reserves and processing them via glyoxylate/gluconeogenesis pathways are upregulated [17]. Haustoria, specialized infection structures formed inside the host cells, are the sites where energy production and biosynthetic process related functions are predominantly expressed

along with the haustorially expressed secreted proteins (HSPs) [11,17]. Many of these secreted proteins are also expressed in germinated spores [18].

Present survey reveals a function profile that appear to be important in fungal growth, host invasion and colonization. Four small-secreted proteins along with the oligopeptide and monocarboxylate transporters and several hydrolytic enzymes detected in the study (Table 2) corroborate the reported aspects of this type of studies. Up-regulation of transcripts coding for small secreted proteins, secreted hydrolytic enzymes, and transporters in germinating spores and in planta have been reported in a number of studies [11,18]. These functions, some of which are represented as the expanded gene families and up regulated during infection in rust fungi, presumably play important roles in host infection, nutrient acquisition and regarded as specific adaptations to the extreme parasitic lifestyle [19]. Small-secreted protein genes, many of which are known to be species-specific indication of rapid evolution, constitute an important component of the rust and mildew genomes and are presumed to be involved subverting host immune responses [11]. Chitinase expression during spore germination and host infection is also commonly detected message, which apparently functions in fungal morphogenesis and proliferation. A cutinase domain containing protein encoding message expression in germinating spores suggest that it participate in host invasion as well. Velvet domain containing proteins found in fungi are known to participate in fungal development, pathogenicity and virulence [20,21]. Detected message tag indicates that velvet proteins are also expressed during rust infections and may function in host invasion. ESTs individually displaying significant similarities to a serine/threonine kinase, a Rab family protein GTPase, a signal protein and a zinc finger protein presumably are utilized in signal transduction and transcriptional regulation during the early stages of the infection [22,23]. Lineage-specific family expansions in genes encoding zinc-finger proteins were observed in rusts. Nucleotide, nucleic acid binding proteins detected in the expression profile are also frequently reported and up-regulated messages in rust infections [18,19]. Phosphatidylethanolamine binding protein encoding transcript derived tags, detected as the most abundant EST in the expression profile, suggest that it may function in the processes of host penetration and colonization. Peptidyl-tRNA hydrolases, cleaving amino acid ester bond of the peptidyl-tRNAs, function as one of the rescue factors of the stalled ribosomes [24]. Accumulation of peptidyl-tRNAs is detrimental to cell, which could hinder fungal proliferation. These enzymes are regarded as target for antimicrobials. Two tags detected in the expression profile indicate that they are expressed and presumably function during *P. sorghi* infections.

In conclusion, as obligat biothrophic fungal pathogens, rusts are known to use intricate mechanisms in penetration and establishing intimate contacts to host cells and in manipulating host physiology and defense [25]. A number of genes that appear to be important in these mechanisms have been identified as ESTs in the present study. Several of them are presumably involved in signal transduction, such as, serine/threonine kinase, Rab4. Similar functions are being reported to be upregulated during urediniospore germination and plant infection [23]. Several other identified genes encode products, such as cutinase, secreted proteins, that are possibly involved in breaching host defenses and suppressing host immunity. A number other genes encodes functions that are involved in metabolite transfer, modification and fungal proliferation. The transcript levels of four selected genes in germinated urediniospores and infected maize leaves were studied by sqRT-PCR assays. All of them are expressed in germinated uredospores except for chitinase and induced in the infected material samples, which suggests that their products conceivably play some roles during spore germination and *P. sorghi* growth in plant tissues.

**ACKNOWLEDGEMENTS**

**REFERENCES**

[1] Sahah, D. A., Dillard, H. (2006), Yield loss in sweet corn caused by *Puccinia sorghi*: A meta-analysis. Plant Disease, 90, 1413-1418.

[2] Hooker, A. L. (1969), Widely based resistance to rust in corn. In: Browning J. A., editor. Disease Consequences of Intensive and Extensive Culture of Field Crops. Special Report 64, Agricultural and Home Economics Experiment Station. Ames, IA, USA: Iowa State University of Science and Technology, pp. 28–34.

[3] Hulbert, S. H. (1997), Structure and evolution of the *rp1* complex conferring rust resistance in maize. Annual Review of Phytopathology, 35, 293–310.

[4] Hahn, M., Mendgen, K. (1997), Characterization of in planta-induced rust genes isolated from a haustorium-specific cDNA library. Molecular Plant Microbe Interactions, 10, 427-437.

[5] Hu, G. G., Linning, R., Mccallum, B., Banks, T., Cloutier, S., and Bakkeren, G. (2007), Generation of a wheat leaf rust, *Puccinia triticina*, EST database from stage-specific cDNA libraries. Molecular Plant Pathology, 8, 451-467.

[6] Zhang, Y., Qu, Z., Zheng, W., Liu, B., Wang, X., and Kang, Z. (2008), Stage-specific gene expression during urediniospore germination in *Puccinia striiformis* f. sp tritici. BMC Genomics, 9, 203- doi:10.1186/1471-2164-9-203.

[7] Soanes, D. M., Talbot, N. J. (2006), Comparative genomic analysis of phytopathogenic fungi using expressed sequence tag (EST) collections. Molecular Plant Pathology, 7(1), 61-70.

[8] Lakshman, D. K., Alkharouf, N., Roberts, D. P., Natarajan, S. S., Mitra, A. (2012), Gene expression profiling of the plant pathogenic basidiomycetous fungus *Rhizoctonia solani* AG 4 reveals putative virulence factors. Mycologia, 104 (5), 1020-1035.

[9] Stergiopoulos, I., de Wit, P. J. G. M. (2009), Fungal Effector Proteins. Annual Review of Phytopathology, 47, 233–63.

[10] Rouxel, T., Baledent, M. H. (2010), Avirulance genes. In *Encyclopedia of Life Sciences* (eLS), John Wiley & Sons Ltd, Chichester. http://www.els.net [doi: 10.1002/9780470015902.a0021267].

[11] Tang, C., Xu, Q., Zhao, M., Wang, X., Kang, Z. (2018), Understanding the lifestyles and pathogenicity mechanisms of obligate biotrophic fungi in wheat: The emerging genomics era. The Crop Journal, 6, 60-67.

[12] Rochi, L., Diéguez, M. J., Burguener, G., Darino, M. A., Pergolesi, M. F., and Sacco, F. (2018), Characterization and comparative analysis of the genome of *Puccinia sorghi* Schwein, the causal agent of maize common rust. Fungal Genetics and Biology, 112, 31–39.

[13] Howe, K. L., Contreras-Moreira, B., De Silva, N., Maslen, G., Akanni, W., and Cambell, L. (2019), Ensembl Genomes 2020-enabling non-vertebrate genomic research. Nucleic Acids Research 48, database issue, D689–D695, doi: 10.1093/nar/gkz890.

[14] Südüpak, M. A. (2014), A cDNA-AFLP protocol with reciprocally arranged 2-enzyme sequential digestion and silver staining detection. Turkish Journal of Biology, 38, 260-270.

[15] Petersen, T. N., Brunak, S., von Heijne, G., Nielsen, H. (2011), SignalP 4.0: discriminating signal peptides from transmembrane regions. Nature Methods, 8, 785–786.

[16] Lin, F., Jiang, L., Liu, Y., Lv, Y., Dai, H., Zhao, H. (2014), Genome‑wide identification of housekeeping genes in maize. Plant Molecular Biology, 68, 543-554.

[17] Upadhyaya, N. M., Garnica, D. P., Karaoglu, H., Sperschneider, J., Nemri, A., Xu, B., and Dodds, P. N. (2014), Comparative genomics of Australian isolates of the wheat stem rust pathogen *Puccinia graminis* f. sp. *tritici* reveals extensive polymorphism in candidate effector genes. Frontiers in Plant Sciences, 5, 759-.

[18] Cuomo, C. A., Bakkeren, G., Khalil, H. B., Panwar, V., Joly, D., and Fellers, J. P. (2017), Comparative analysis highlights variable genome content of wheat rusts and divergence of the mating loci. G3-Genes Genomes Genetics, 7, 361–376.

[19] Duplessis, S., Cuomo, C. A., Lin, Y. C., Aerts, A., Tisserant, E., and Martin, F. (2011), Obligate biotrophy features unraveled by the genomic analysis of rust fungi. Proc. Natl. Acad. Sci. U. S. A. 108, 9166–9171.

[20] López-Berges, M. S., Concepción, H., Michael, S., Katja, S., Javier, C., and Antonio, D. (2012), The velvet complex governs mycotoxin production and virulence of *Fusarium oxysporum* on plant and mammalian hosts. Molecular Microbiology, 87 (1), 49–65.

[21] Wang, R., Leng, Y., Shrestha, S., Zhong, S. (2016), Coordinated and independent functions of velvet-complex genes in fungal development and virulence of the fungal cereal pathogen *Cochliobolus sativus*. Fungal Biology, 120 (8),948–960.

[22] Idnurm, A., Howlett, B. J. (2001), Pathogenicity genes of phytopathogenic fungi. Molecular Plant Pathology, 2, 241-255.

[23] Zhang, Y., Qu, Z., Zheng, W., Liu, B., Wang, X., and Kang, Z. (2008), Stage-specific gene expression during urediniospore germination in *Puccinia striiformis* f. sp tritici. BMC Genomics, 9, 203- doi:10.1186/1471-2164-9-203

[24] Sharma, S., Kaushik, S., Sinha, M., Kushwaha, G. S., Singh, A., and Singh, P. (2014), Structural and functional insights into peptidyl-tRNA hydrolase. Biochimica et Biophysica Acta, 1844, 1279–1288.

[25] Voegele, R. T., Hahn, M., Mendgen, K. (2009), The uredinales: cytology, biochemistry, and molecular biology. The Mycota, 5. Plant relationships/Vol. ed. H. B. Deising. Berlin: Springer, 2. ed., pp. 69-98.

*RESEARCH ARTICLE*

# POTENTIAL of ENZYMATIC METHODS and BIOLOG ECOPLATE ANALYSIS for INVESTIGATION of MICROBIAL FUNCTIONALITY in AGRICULTURAL SOILS

Nilgun POYRAZ,[1*], Suat SEZEN[2], Mehmet Burcin MUTLU[3]

[1] Kutahya Dumlupinar University, Faculty of Science and Humanities, Department of Biology, Kutahya,
nilgun.kavak@dpu.edu.tr, ORCID: 0000-0002-5861-7922
[2] Eskisehir Technical University, Faculty of Science, Department of Biology, Eskisehir, suatsezen93@gmail.com,
ORCID: 0000-0002-5901-5747
[3] Eskisehir Technical University, Faculty of Science, Department of Biology, Eskisehir,
mbmutlu@eskisehir.edu.tr, ORCID: 0000-0002-9404-6389

## ABSTRACT

Agricultural systems and applications affects the soil ecological conditions and microbial structure. However, it is important that the interventions do not disturb the balance and quality of the microbial content of the soil. For this reason, enzymatic methods and Biolog Ecoplate method were applied to research and evaluate the status of functional microbial diversity in four different agricultural soil samples (A, B, C, D).

The results indicated that the pH, electrical conductivity, amounts of total nitrogen (N) and humidity were generally similar but calcium carbonate rates were higher in A and B agricultural soils. Soil enzymatic activity results showed some differences among the four different agricultural soils. The activity measurements of urease, phosphatase and dehydrogenase were high and results showed the differanties. Enzymatic activities and microbial populations correlated with each others and content of organic carbon.

Evaluation of substrate utilization profiles and the diversity indices concluded that microbial community structure and composition were different related to various conditions. The average well color development (AWCD) which was calculated in the Biolog EcoPlate analysis showed some variations in the catabolic ability of four different agricultural soil samples' microbial communities. Compared to other samples, C and D agricultural soil samples had a higher overall AWCD value. AWCD of C soil was significantly higher than in the others. Lowest used substrates were α-Cyclodextrin, α-Ketobutyric acid, β-Methyl-D-glucoside, α-D-Lactose and 2- hydroxybutyric acid. The most extensively used substrates were aminoacids and carbohydrate groups. These results indicates the degradation potential. With the Biolog EcoPlate and enzymatic measurements, changes in the microbial community in agricultural soils can be detected, and also agricultural management and application methods for tillage can be evaluated.

**Keywords:** *Dehydrogenase, urease, phosphatase, AWCD, Biolog EcoPlate, microbial activity*

## 1. INTRODUCTION

Soil microorganisms have important roles in most of soil reactions such as organic matter formation, decomposition, respiration and nutrient cycle [1, 2]. The physical and chemical properties of the soil changes quite slowly, but the biodiversity and biochemical reactions in the soil microflora are affected very quickly by changes and give a rapid reaction so they are sensitive reactions and signatures for evaluating soil quality [3, 4]. Soil microbial communities differ metabolically and genetically in response to different applications in the organic farming practices. The microbial structure of the soil is very critical for the ecosystem to create sustainable plant communities based on quality soil structure and biological interactions [5]. Also protection of the microbial activity and diversity in the soil is very important for sustainable agriculture management [6]. Many agricultural applications such as different soil managements and tillage techniques cause to modifications in size structure and biological reactions of soil microbiota [7, 8]. Organic modification of agricultural systems is thought to increase soil quality, biologically and chemically [9]. Organic and inorganic substances are applied for supporting nutrient intake to plants [10]. Organic substances in the soil stimulate plant growth and affect the physical properties of the soil [11]. However organic and inorganic substances can cause to changes in the population structure, composition, physiology and ecology of soil microorganisms [10]. For example, balanced use of key elements (N, P, K) in fertilization can be beneficial for efficient plant growth, but farmers follow an economic strategy rather than an agricultural strategy. This creates negative consequences. Unbalanced fertilization is common, but data on the effect of this process on soil microbial community is limited [12]. Changes in factors such as the type, quality, seasonal distribution, nutrient inputs of plant residues, rotation in the soil during agricultural production affect microbial structure, density, diversity and processes [13]. The response and change of microorganisms to different applications such as pedoclimate and crop rotation are still not fully understood. The density of different microorganism groups is also an indicator of the changes that occur in the soil ecosystem when different plants are cultivated. Nutrient cycle is very important for plant production efficiency in crop rotation applications. Soil microorganisms and soil enzymes take part in the nutrient cycle [14]. In addition, studies on chemical and biological properties of different agricultural soils are unkonown [15].

Microbial community analysis in soils can be detected with many different methods. Their effected rate can be detected with the determination of changes in different reactions, such as soil respiration, metabolic activity, microbial biomass, cultural and direct microscopic countings, chloroform fumigation incubation, ATP measurements, total amount of phospholipid fatty acids, Biolog and molecular analysis [6, 16].

However, most of the methods are not completely accurate and determination of microbial diversity also does not reflect functionality, as most of the microorganisms in the soil are in rest and inactive phases. The Community Level Physiological Profile (CLPP) of soil bacteria is effective and pioneering method which analysis soil quality [17]. Analysis based on the use of carbon resources is essential in this method and detect functional diversity changes of soil microorganisms [16]. Using the CLPP method, the effects of soil additives can be evaluated by examining the changes in the activity and diversity of microorganisms in the soil [18, 19]. CLPP generates vast amounts of data that are extremely difficult and complex to interpret. Biolog-generated data include the AverageWell Colour Development (AWCD), the Shannon diversity index (H), substrate richness (SR)  and Shannon

evenness (E) for analysis. AWCD values indicates the microbial community's potential metabolic activity. The Shannon diversity index (H) is used for the calculation of the physiological diversity of bacterial communities. The Biolog EcoPlate can be used in effects of heavy metals, hydrocarbons, estimating the impact of stress factors (salinity, pH) [19].

Using of soil enzymes to search and examine soil biological activity is another method [20]. Usually for this purpose in studies monitoring of β-glucosidase, dehydrogenase and urease activities is used. β-Glucosidase is a hydrolytic enzyme and urease is responsible for providing the nitrogen to plants. These enzymes indicate the soil quality. Dehydrogenase is an oxidoreductase and can be used in determination of soil microbial activity [21-23].

Therefore, in this study, it was aimed to evaluate different agricultural soils and reveal how catabolic diversity, microbial structure, composition and function were changed at the community level. For these purposes, enzymatic methods and Biolog EcoPlate were used for microbiota activity and functionality.

## 2. MATERIALS and METHODS

### 2.1. Field Sampling

Four agricultural soil samples (A, B, C, D) from lands which coordinates were near the 39°59'43.14" N, 32°20'39.09" S in Ayaş, Ankara (Figure 1) were collected on April 2019 from 20 cm depth using a soil auger. Collected soil samples were brought to the laboratory for physicochemical, microbiological, and biochemical analysis. The soils were then stored at 4 °C. For analysis, agricultural soil samples were used by sieving and air drying. For microbiological and biochemical analysis of soils, moist soils were used.



**Figure 1.** The study area on the map and sampling point.

## 2.2. Physico-Chemical Soil Properties

The pH value of the agricultural soil samples were determined with the HACH HQ40D multi-parameter pH meter and their electrical conductivity were detected with the HACH HQ40D multi-parameter EC meter. A total of 10 g of soil and 10 ml of distilled water was stirred with a vortex mixer in a centrifuge tube and then a pH was measured [24]. Then, electrical conductivity (EC) was measured with 1:2.5 of soil:water slurry.

## 2.3. Calcium Carbonate Analysis

Scheibler calcimeter was used for carbonate determination by volumetric method. For this, 1 g dried agricultural soil samples were weighed and put into 25 ml conical flasks. 1/3 of HCl was filled into an acid tube and carefully put into the erlenmeyer with the help of pliers without pouring. The pure water level of the calcimeter was set to zero and the mouth of the flask was closed with the rubber stopper on the calcimeter, and the acid in the erlenmeyer was contacted with the soil and $CO_2$ output was provided. The volume of $CO_2$ emitted was recorded in the calcimeter. The amount of lime in % was found by calculating the obtained values [25].

## 2.4. Soil Humidity Analysis

10 g of agricultural soil samples taken for moisture analysis were weighed and left to dry at 105 °C. The dried soil samples were weighed again, the weight was noted and the % moisture content was calculated and determined.

## 2.5. Soil Nitrogen Analysis

Nitrogen amount in agricultural soil samples was determined by Semi-Micro Kjeldahl method [26]. For the method; Soil samples were weighed in a precision balance of 1 g. The weighed soil samples were placed in nitrogen combustion tubes and 2 pieces of $Cu_2SO_4$ + $K_2SO_4$ tablets were placed on them as catalysts. Afterwards, 12 ml of concentrated $H_2SO_4$ was placed in each tube and placed in the burning apparatus. Four of the tubes were prepared for blanking without a sample. Burning process was carried out for 1 hour at 420 °C. After waiting 10-15 minutes for the tubes to cool, blanking was performed with the samples in the Kjeldahl device and this value was entered into the Kjeldahl device by taking the average of the values. After entering each weighing value for the samples, the readings were made and the results were recorded and the calculation process was carried out.

## 2.6. Soil Enzyme Activities

For measurement of the dehydrogenase enzyme activity of the agricultural soil samples, analysis was applied according to the modified protocol of Tabatabai, 1994. Agricultural soil samples were weighed as 5 g according to the protocol and were treated with 5 ml 0.5% triphenyl tetrazolium chloride (TTC) and incubated at 37 °C for 24 hours. When the incubation period was completed, the samples were extracted with methanol, the resulting intensity of red color measurements were made at 480 nm wavelength in UV spectrophotometer and enzyme activity was calculated. The analysis was done in triplicate and the results were averaged.

In order to determine the phosphatase enzyme activities of the agricultural soil samples, 1 g of each sample was weighed and 0.25 ml of toluene, 4 ml of acetate buffer (pH 5.8) and 250µl of p-nitrophenol phosphate were added and left for 1 hour incubation at 37 °C. When the incubation period was completed, 1 ml 0,5 M $CaCl_2$ and 4 ml sodium hydroxide (0.5 M) was added and the measurement was made at 410

nm wavelength in UV spectrophotometer. The enzyme activity was calculated and expressed as μg p-nitrophenol [27]. The results were averaged by performing three repetitions from each sample.

For determination of urease enzyme activity method of Tabatabai, 1994 [27] was used. 5 g of soil sample was weighed and it was treated with 0.2 ml of toluene, 9 ml of THAM (6.1 g Tris 0,2 M $H_2SO_4$) buffer solution and 1 ml of 0.2 mol /L urea solution. and left to incubation at 37 °C for 2 hours. When the incubation period was completed, enzyme activity was stopped by adding 35 ml KCl-$Ag_2SO_4$ solution. For the determination of NH4 + -N concentration, samples were extracted with 2 mol/L KCl and the ammonium concentrations in the extracts were measured using the indophenol blue method [28].

### 2.7. Mesophilic Bacterial Density
For calculating the number of total mesophilic bacteria, agricultural soil samples were prepared in various dilutions and inoculated on PCA (plate count agar) medium with the spread plate method. It was incubated for 96 hours at 37 °C. The total mesophilic bacteria number was calculated by counting the colonies formed as a result of incubation.

### 2.8. Biolog EcoPlate Test
Biolog EcoPlate (Biolog Inc., Hayward, California) was applied to determine the metabolic fingerprint of the microbial community in the agricultural soil samples. 10 g of soil samples were weighed and suspended in 90 ml of physiological saline water. It was shaked at 150 rpm and 37 °C for 1 hour. Then, the soil particles were left to settle and serial dilution was made with physiological saline water without touching the collapsed part. 150 μl of the $10^{-1}$ and $10^{-3}$ dilutions was added to the ecoplate wells. 150 μl of physiological saline water was added to the control wells. At the end of this process, the Biolog EcoPlates were left to incubate at 37 °C. Absorbances at 590 nm for up to five days at 24 hour intervals were measured at Biolog Microstation [29].

### 2.9. Statistics
In Biolog EcoPlate normalization process was applied to the each of the carbon source OD (Optical Density) values by using the readings in control wells OD values [30]. After normalization step, other analysis values were calculated from to data. One of the common analysis is kinetic analysis, which is time-dependent and a kind of color change analysis. At the end of the analysis as a result, a sigmoidal curve is often obtained. The AWCD values for all samples in each reading interval were calculated [31]. For analysis and calculations, the following formula (Eq.1) was used [32]:

$$AWCD = \sum_{n=1}^{31}\left(\frac{ODi}{31}\right) \tag{1}$$

In the formula ODi means the normalized optical density of each well.
For calculation of AUC (Area Under the Curve) value, following formula (Eq. 2) was used [33]:

$$AUC = \sum_{n=1}^{31}\frac{A_n+A_{n+1}}{2x(t_{n+1}-t)} \tag{2}$$

$A_n$ and $A_{n+1}$ is the absorbance value of each well in two consecutive time intervals. The $t_n$ and $t_{n+1}$ refers to two consecutive times.

Incubation time effects and different parameters on the functional diversity were evaluated with calculations such as AUC and AWCD.

Data was obtained for 96 hours and then was used for calculations and analyses of diversity indices. Shannon-Wiener functional diversity index (H) was calculated by the following formula (Eq.3), [34]:

$$H = - \sum_{n=1}^{31}(pi(Inpi) \qquad (3)$$

pi in the formula is the ratio of the absorbance of each substrate (ODi) to sum of the absorbance for the all substrates ($\sum$ODi).

Substrate/catabolic richness (S) value was calculated for every 24 hours as the total number of oxidized substrate (C). The total number of the oxidized substrates were determined which were wells in the absorbance value over 0.25.

In addition to other calculations, Shannon Evenness (E) index was determined by the following formula using these values (Eq.4):

$$E = \frac{H}{InS} \qquad (4)$$

## 3. RESULTS AND DISCUSSION

In this study four different agricultural soils were evaluated. For a sustainable production system, soil must have high and stable biological diversity and nutrient cycling [35]. Living and non-living factors in the ecosystem cause changes in the microbial community structure. Some of these factors are humidity, type of plant, nutrient concentrations and temperature [36]. The microbial cells have some adaptations to survive in different environmental conditions [37]. In the light of these explanations, both the physicochemical properties of the soil were determined and the enzymatic and metabolic potentials were measured within the scope of microbial fertility.

The pH measurement and electrical conductivity results of the agricultural soil samples were shown in Table 1. Average pH measurements of samples were recorded around 8.2. Their electrical conductivity varied between 406-524.5 $\mu$S cm$^{-1}$.

**Table 1.** pH and EC values of agricultural soil samples

| Soil Samples | pH (-log[H+]) | | Electrical conductivity (EC) ($\mu$S cm-1) |
|---|---|---|---|
| A | 8.22 | Medium alkaline | 447.5 |
| B | 8.27 | Medium alkaline | 429 |
| C | 8.23 | Medium alkaline | 524.5 |
| D | 8.21 | Medium alkaline | 406 |

Information on calcium carbonate values, humidity rates anad nitrogen amounts determined in agricultural soil samples were given in Table 2. When the data was examined, soil samples were

defined as calcareous and very calcareous. The % moisture content of soil samples were calculated average nearly 30%. The amount of nitrogen determined by the Semi-Micro Kieldahl method in soil samples were varied between 0.1 and 0.3.

**Table 2.** % lime values of agricultural soil samples.

| Soil Samples | Lime (%) | | Humidity rate (%) | Nitrogen Content (%) |
|---|---|---|---|---|
| A | 17.576 | Very calcareous | 30.718 | 0.3304 |
| B | 17.210 | Very calcareous | 38.312 | 0.1876 |
| C | 13.365 | Calcerous | 41.043 | 0.1484 |
| D | 11.534 | Calcerous | 37.551 | 0.3723 |

For the bacteria count, the number of aerobic mesophilic bacteria was calculated by counting the colonies formed after 96 hours of incubation at 37 °C. The calculation results were given in Table 3. Although there was a significant difference between the calcium carbonate content of soil samples, there was no significant difference of soils' pH and EC. These differences may be due to rotation, tillage, residue type and fertilization time on different agricultural soil samples. Measurements and controlling pH, EC and moisture values were crucial for agricultural soils biological balance and and associated with plant productivity [38, 39].

**Table 3.** Total mesophilic bacteria count of agricultural soil samples.

| Soil Samples | Number of mesophilic bacteria (cfu/ml) |
|---|---|
| A | $2.66 \times 10^6$ |
| B | $1.2 \times 10^6$ |
| C | $2.02 \times 10^6$ |
| D | $4.365 \times 10^6$ |

Dehydrogenase enzyme activity, phosphotase enzyme activity and urease enzyme activity of soil samples were given in Table 4. Soil microbial communities change when exposed to different agricultural practices. Soil enzyme activity is correlated with indirectly soil microbial activity [40]. One of these enzymes is urease. This enzyme hydrolyzes the urea fertilizers used in agricultural applications. However urease can cause to increasing in pH [41]. Urease activity values were nearly same, but in A sample was in low level than the others. The activity of dehydrogenases and phosphatase enzymes is directly related to the presence of carbon, nitrogen and phosphorus for plants [42]. If the organic carbon level in the soil is high, microbial activity and enzyme activity are also high. Dehydrogenase enzyme is an indicator of viable microbial cells, microbial respiration and microbial activity in samples [43]. Alkaline phosphatase is another enzyme that is responsible for hydrolization of phosphours [44]. Enzyme activity results show correlation with organic carbon. Soil enzymes are found to be significantly compiled into soil health. In our study dehydrogenease activity and cell count results were in positive correlation.

**Table 4.** Enzyme activity results of agricultural samples.

| Soil Samples | Dehydrogenase enzyme activity (μg TPF g$^{-1}$ soil/ h$^{-1}$) | SD(±) | Phosphotase enzyme activity (μg p-nitrophenol) | SD(±) | Urease enzyme activity (μg NH$_4$-N g$^{-1}$ soil h$^{-1}$) | SD(±) |
|---|---|---|---|---|---|---|
| A | 39.219 | 7.929 | 8.876 | 0.472 | 94.479 | 1.183 |
| B | 30.592 | 2.020 | 11.422 | 3.592 | 118.500 | 1.621 |
| C | 38.110 | 4.517 | 9.950 | 0.807 | 110.708 | 1.270 |
| D | 33.628 | 1.92 | 11.617 | 3.583 | 132.437 | 1.738 |

Similar to other results, positive correlation was obtained between soil biodiversity indicators and the main groups of compounds in the Biolog EcoPlate analysis. Also, the soils collected from different agricultural region revealed the highest biological activity and diversity. AWCD, Shannon-Wiener functional diversity index (H), catabolic richness (S), Shannon Evenness (E) index and AUC (Area Under the Curve) values of agricultural soil samples were shown in Table 5.

**Table 5.** AWCD, (H), (S), (E) and AUC values of agricultural soil samples.

| Samples (24 hour) | | Indices | | | | |
|---|---|---|---|---|---|---|
| | | AWCD | H | E | S | AUC |
| | A | 0.703±0.053 | 3.424 ± 0.005 | 0.997 ± 0.001 | 31 | |
| | B | 0.749± 0.010 | 3.425 ± 0.008 | 0.997 ± 0.002 | 30.667 ± 0.577 | |
| | C | 0.756 ± 0.014 | 3.429 ± 0.003 | 0.999 ± 0.001 | 31 | |
| | D | 0.796± 0.023 | 3.426 ± 0.005 | 0.998 ± 0.001 | 31 | |
| Samples (48 hour) | | Indices | | | | |
| | | AWCD | H | E | S | AUC |
| | A | 0.727± 0.057 | 3.424± 0.003 | 0.997 ± 0.001 | 31 | |
| | B | 0.802± 0.048 | 3.424± 0.010 | 0.997 ± 0.003 | 30.667 ± 0.577 | |
| | C | 0.978 ± 0.069 | 3.401± 0.012 | 0.990 ± 0.004 | 31 | |
| | D | 0.900± 0.061 | 3.420± 0.010 | 0.996± 0.003 | 31 | |
| Samples (72 hour) | | Indices | | | | |
| | | AWCD | H | E | S | AUC |
| | A | 0.869± 0.148 | 3.407± 0.011 | 0.992 ± 0.003 | 31 | |
| | B | 0.926± 0.115 | 3.405± 0.025 | 0.991 ± 0.007 | 30.667 ± 0.577 | |
| | C | 1.189 ± 0.123 | 3.388± 0.005 | 0.987 ± 0.001 | 31 | |
| | D | 1.029± 0.149 | 3.408± 0.021 | 0.992± 0.006 | 31 | |
| Samples (96 hour) | | Indices | | | | |
| | | AWCD | H | E | S | AUC |
| | A | 1.062± 0.243 | 3.374± 0.007 | 0.983 ± 0.002 | 31 | 59.484 |
| | B | 1.028± 0.115 | 3.389± 0.026 | 0.987 ± 0.007 | 30.667 ± 0.577 | 62.789 |
| | C | 1.320 ± 0.093 | 3.366± 0.004 | 0.980 ± 0.001 | 31 | 76.938 |
| | D | 1.040± 0.167 | 3.400± 0.031 | 0.990± 0.009 | 31 | 68.321 |

Substrates were grouped as carbohydrates, carboxylic acids, amino acids, polymers, and amines/amides for comparision. In most of the soils, all of the carbon sources were used. This was resulted by the high diversity index values. Figure 2 and 3 shows carbon utilization heat map after 24 and 96 hours.
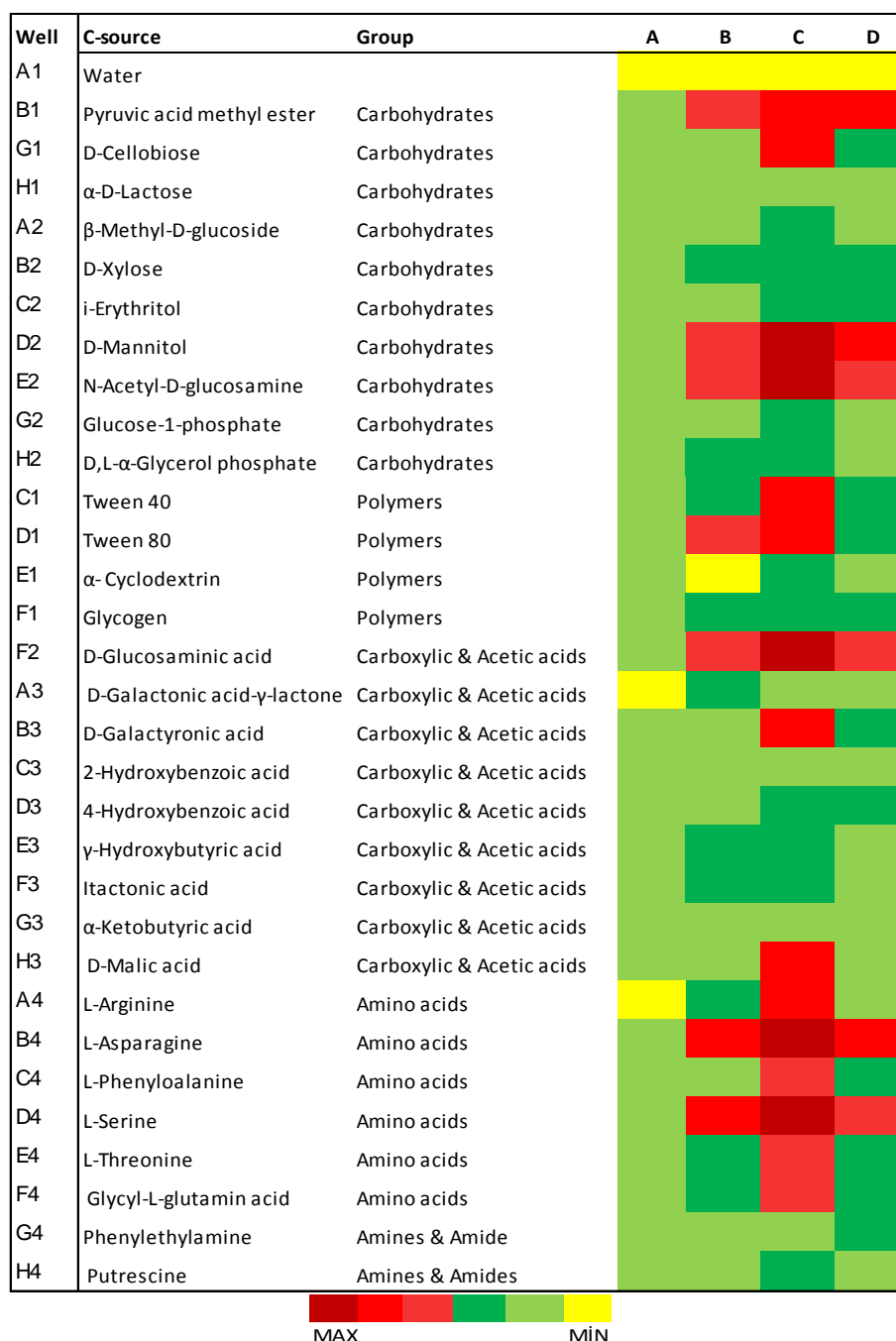
| Well | C-source | Group | A | B | C | D |
|------|----------|-------|---|---|---|---|
| A1 | Water | | | | | |
| B1 | Pyruvic acid methyl ester | Carbohydrates | | | | |
| G1 | D-Cellobiose | Carbohydrates | | | | |
| H1 | α-D-Lactose | Carbohydrates | | | | |
| A2 | β-Methyl-D-glucoside | Carbohydrates | | | | |
| B2 | D-Xylose | Carbohydrates | | | | |
| C2 | i-Erythritol | Carbohydrates | | | | |
| D2 | D-Mannitol | Carbohydrates | | | | |
| E2 | N-Acetyl-D-glucosamine | Carbohydrates | | | | |
| G2 | Glucose-1-phosphate | Carbohydrates | | | | |
| H2 | D,L-α-Glycerol phosphate | Carbohydrates | | | | |
| C1 | Tween 40 | Polymers | | | | |
| D1 | Tween 80 | Polymers | | | | |
| E1 | α-Cyclodextrin | Polymers | | | | |
| F1 | Glycogen | Polymers | | | | |
| F2 | D-Glucosaminic acid | Carboxylic & Acetic acids | | | | |
| A3 | D-Galactonic acid-γ-lactone | Carboxylic & Acetic acids | | | | |
| B3 | D-Galactyronic acid | Carboxylic & Acetic acids | | | | |
| C3 | 2-Hydroxybenzoic acid | Carboxylic & Acetic acids | | | | |
| D3 | 4-Hydroxybenzoic acid | Carboxylic & Acetic acids | | | | |
| E3 | γ-Hydroxybutyric acid | Carboxylic & Acetic acids | | | | |
| F3 | Itactonic acid | Carboxylic & Acetic acids | | | | |
| G3 | α-Ketobutyric acid | Carboxylic & Acetic acids | | | | |
| H3 | D-Malic acid | Carboxylic & Acetic acids | | | | |
| A4 | L-Arginine | Amino acids | | | | |
| B4 | L-Asparagine | Amino acids | | | | |
| C4 | L-Phenyloalanine | Amino acids | | | | |
| D4 | L-Serine | Amino acids | | | | |
| E4 | L-Threonine | Amino acids | | | | |
| F4 | Glycyl-L-glutamin acid | Amino acids | | | | |
| G4 | Phenylethylamine | Amines & Amide | | | | |
| H4 | Putrescine | Amines & Amides | | | | |

MAX      MİN

**Figure 2.** Carbon utilization heat map after 24 hours.

| Well | C-source | Group | A | B | C | D |
|------|----------|-------|---|---|---|---|
| A1 | Water | | | | | |
| B1 | Pyruvic acid methyl ester | Carbohydrates | | | | |
| G1 | D-Cellobiose | Carbohydrates | | | | |
| H1 | α-D-Lactose | Carbohydrates | | | | |
| A2 | β-Methyl-D-glucoside | Carbohydrates | | | | |
| B2 | D-Xylose | Carbohydrates | | | | |
| C2 | i-Erythritol | Carbohydrates | | | | |
| D2 | D-Mannitol | Carbohydrates | | | | |
| E2 | N-Acetyl-D-glucosamine | Carbohydrates | | | | |
| G2 | Glucose-1-phosphate | Carbohydrates | | | | |
| H2 | D,L-α-Glycerol phosphate | Carbohydrates | | | | |
| C1 | Tween 40 | Polymers | | | | |
| D1 | Tween 80 | Polymers | | | | |
| E1 | α- Cyclodextrin | Polymers | | | | |
| F1 | Glycogen | Polymers | | | | |
| F2 | D-Glucosaminic acid | Carboxylic & Acetic acids | | | | |
| A3 | D-Galactonic acid-γ-lactone | Carboxylic & Acetic acids | | | | |
| B3 | D-Galactyronic acid | Carboxylic & Acetic acids | | | | |
| C3 | 2-Hydroxybenzoic acid | Carboxylic & Acetic acids | | | | |
| D3 | 4-Hydroxybenzoic acid | Carboxylic & Acetic acids | | | | |
| E3 | γ-Hydroxybutyric acid | Carboxylic & Acetic acids | | | | |
| F3 | Itactonic acid | Carboxylic & Acetic acids | | | | |
| G3 | α-Ketobutyric acid | Carboxylic & Acetic acids | | | | |
| H3 | D-Malic acid | Carboxylic & Acetic acids | | | | |
| A4 | L-Arginine | Amino acids | | | | |
| B4 | L-Asparagine | Amino acids | | | | |
| C4 | L-Phenyloalanine | Amino acids | | | | |
| D4 | L-Serine | Amino acids | | | | |
| E4 | L-Threonine | Amino acids | | | | |
| F4 | Glycyl-L-glutamin acid | Amino acids | | | | |
| G4 | Phenylethylamine | Amines & Amide | | | | |
| H4 | Putrescine | Amines & Amides | | | | |

MAX        MIN

**Figure 3.** Carbon utilization heat map after 96 hours.

Compared to other samples, C and D agricultural soil samples had a higher overall AWCD value. The microbial communities in the C and D soil samples utilized more amino acids than the others. The differences in the use of substrate as a result of the analysis of different soils indicate the various metabolic capabilities of soil microbial communities. There can be many reasons for these results, for example, nitrogenous fertilizer application changes and affects the catabolization ability of soil microorganisms. AWCD values are related with the oxidative ability of microorganisms. The same results were obtained for AUC values. The metabolically richest samples were C and D soil samples. High AWCD, H, R, S, E and AUC results show microbial activity and high number of oxidized C substrates [45, 46]. In Biolog EcoPlate results after 96 hours incubation, it was detected that 31 carbon sources used. However, the presence of carbon sources with a lower utilization rate was detected within 24, 48 and 72 hours. Carbon utilization profiles were different of the soil samples as shown in Figure 2 and 3. Evaluation of samples carbon source utilization potentials, some sources were utilized slowly within the first 24 hours. In B soil sample α- Cyclodextrin, α-Ketobutyric acid, β-Methyl-D-glucoside, α-D-Lactose were used slowly. In C soil sample, all sources were consumed efficiently within the first 24 hours especially amino acid and carbohydrate groups. These results showed in C soil sample have to the high degradation and catabolic capacity also may have high number of heterotrophic bacteria. AWCD calculation results indicated that C and D soil samples had highest values. AWCD values can be showed the lag and exponential phases of microorganisms. Lag phase can be show that the microorganism number is low. In this phase microbial community adapt to substrate degradation and synthesize new enzymes. A and B soil samples reached exponential phase too late than C and D as shown in Figure 4.
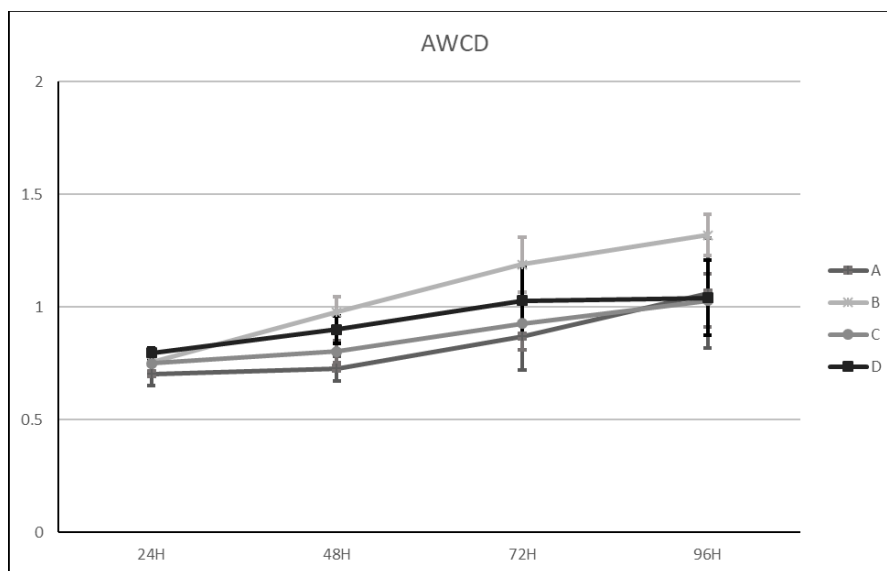


**Figure 4.** AWCD values for agricultural soil samples.

Biolog EcoPlates is a common method to characterize changes in microbial community of soils [17, 47]. This technique supplies a quick results about community structure. In this study experimental

findings revealed that substrates utilization profiles and the high diversity indices values indicated highly active and diverse microbial communities.

## 4. CONCLUSIONS

Our results showed that enzymatic values and Biolog EcoPlate are potential alternative tools to detect soil microbial communities' structure and changes, physiological properties and utilized carbon sources. These methods are practice and economical. In our preliminary study we used enzymatic methods for bacteria monitoring. These preliminary results can be used for efficient agriculture treatments. If necessary alternative methods and detailed analysis may be apply for detailed community structure analysis.

## ACKNOWLEDGMENT

## REFERENCES

[1] Schimel, J. , & Schaeffer, S. M. (2012). Microbial control over carbon cycling in soil. Frontiers in microbiology, 3, 348.

[2] Delgado- Baquerizo, M. , Grinyer, J., Reich, P. B., & Singh, B. K. (2016). Relative importance of soil properties and microbial community for soil functionality: insights from a microbial swap experiment. Functional Ecology, 30(11), 1862-1873.

[3] Anderson, S. A. , Sissons, C. H., Coleman, M. J., & Wong, L. (2002). Application of carbon source utilization patterns to measure the metabolic similarity of complex dental plaque biofilm microcosms. Applied and environmental microbiology, 68(11), 5779-5783.

[4] Giacometti C., Demyan M.S., Cavani L., Marzadori C., Ciavatta C., Kandeler E. (2013). Chemical and microbiological soil quality indicators and their potential to differentiate fertilization regimes in temperate agroecosystems. Applied Soil Ecology, 64, 32–48.

[5] Lopez-Lozano, N. E., Carcaño-Montiel, M. G., & Bashan, Y. (2016). Using native trees and cacti to improve soil potential nitrogen fixation during long-term restoration of arid lands. Plant and Soil, 403(1-2), 317-329.

[6] Insam, H. (2001). Developments in soil microbiology since the mid 1960s. Geoderma, 100(3-4), 389-402.

[7] Wakelin, S. A., Barratt, B. I., Gerard, E., Gregg, A. L., Brodie, E. L., Andersen, G. L., ... & O'Callaghan, M. (2013). Shifts in the phylogenetic structure and functional capacity of soil microbial communities follow alteration of native tussock grassland ecosystems. Soil Biology and Biochemistry, 57, 675-682.

[8] Järvan M., Edesi L., Adamson A., Võsa T. (2014): Soil microbial communities and dehydrogenase activity depending on farming systems. Plant, Soil and Environment, 60, 459–463.

[9] Fließbach, A., Oberholzer, H. R., Gunst, L., & Mäder, P. (2007). Soil organic matter and biological soil quality indicators after 21 years of organic and conventional farming. Agriculture, Ecosystems & Environment, 118(1-4), 273-284.

[10] Marschner, P., Kandeler, E., & Marschner, B. (2003). Structure and function of the soil microbial community in a long-term fertilizer experiment. Soil Biology and Biochemistry, 35(3), 453-461.

[11] Chang, E. H., Chung, R. S., & Tsai, Y. H. (2007). Effect of different application rates of organic fertilizer on soil enzyme activity and microbial population. Soil Science and Plant Nutrition, 53(2), 132-140.

[12] Chu, H., Lin, X., Fujii, T., Morimoto, S., Yagi, K., Hu, J., & Zhang, J. (2007). Soil microbial biomass, dehydrogenase activity, bacterial community structure in response to long-term fertilizer management. Soil Biology and Biochemistry, 39(11), 2971-2976.

[13] Govaerts, B., Mezzalama, M., Unno, Y., Sayre, K. D., Luna-Guido, M., Vanherck, K., ... & Deckers, J. (2007). Influence of tillage, residue management, and crop rotation on soil microbial biomass and catabolic diversity. Applied soil ecology, 37(1-2), 18-30.

[14] Ngosong, C., Jarosch, M., Raupp, J., Neumann, E., & Ruess, L. (2010). The impact of farming practice on soil microorganisms and arbuscular mycorrhizal fungi: Crop type versus long-term mineral and organic fertilization. Applied Soil Ecology, 46(1), 134-142.

[15] Acosta-Martinez, V., Mikha, M. M., Sistani, K. R., Stahlman, P. W., Benjamin, J. G., Vigil, M. F., & Erickson, R. (2011). Multi-location study of soil enzyme activities as affected by types and rates of manure application and tillage practices. Agriculture, 1(1), 4-21.

[16] Dumontet, S., Cavoski, I., Ricciuti, P., Mondelli, D., Jarrar, M., Pasquale, V., & Crecchio, C. (2017). Metabolic and genetic patterns of soil microbial communities in response to different amendments under organic farming system. Geoderma, 296, 79-85.

[17] Garland, J. L., & Mills, A. L. (1991). Classification and characterization of heterotrophic microbial communities on the basis of patterns of community-level sole-carbon-source utilization. Applied and environmental microbiology, 57(8), 2351-2359.

[18] Huang, N., Wang, W., Yao, Y., Zhu, F., Wang, W., & Chang, X. (2017). The influence of different concentrations of bio-organic fertilizer on cucumber Fusarium wilt and soil microflora alterations. PLoS One, 12(2), e0171490.

[19] Feigl, V., Ujaczki, É., Vaszita, E., & Molnár, M. (2017). Influence of red mud on soil microbial communities: Application and comprehensive evaluation of the Biolog EcoPlate approach as a tool in soil microbiological studies. Science of the Total Environment, 595, 903-911.

[20] Zhang, C., Zhou, T., Zhu, L., Du, Z., Li, B., Wang, J., ... & Sun, Y. (2019). Using enzyme activities and soil microbial diversity to understand the effects of fluoxastrobin on microorganisms in fluvo-aquic soil. Science of The Total Environment, 666, 89-93.

[21] Guo, P., Zhu, L., Wang, J., Wang, J., Xie, H., & Lv, D. (2015). Enzymatic activities and microbial biomass in black soil as affected by azoxystrobin. Environmental Earth Sciences, 74(2), 1353-1361.

[22] Sun, X., Zhu, L., Wang, J., Wang, J., Su, B., Liu, T., ... & Shao, Y. (2017). Toxic effects of ionic liquid 1-octyl-3-methylimidazolium tetrafluoroborate on soil enzyme activity and soil microbial community diversity. Ecotoxicology and Environmental Safety, 135, 201-208.

[23] Zhang, Q., Zhu, L., Wang, J., Xie, H., Wang, J., Wang, F., & Sun, F. (2014). Effects of fomesafen on soil enzyme activity, microbial population, and bacterial community composition. Environmental monitoring and assessment, 186(5), 2801-2812.

[24] Kalra YP (1995) Determination of pH of soils by different methods: collaborative study. Journal of AOAC International 78, 310–324.

[25] Loeppert, R. H., & Suarez, D. L. (1996). Carbonate and gypsum. Methods of Soil Analysis: Part 3 Chemical Methods, 5, 437-474.

[26] Nielsen, J.P. (2003). Evaluation of malting barley quality using exploratory data analysis. II. The use of kernel hardness and image analysis as screening methods. Journal of Cereal Science, 38, 247-255.

[27] Tabatabaı, M.A.(1994). Soil enzymes. In: Weaver, R.W., Angel, S., Bottomley, P., Bezdicek,D.,Smith,S.,Tabatabai, A. and Wollum, A. (Eds.), Methods of Soil Analysis, Part 2 – Microbiological and Biochemical Properties. SSSA Book Series No. 5. Soil Science Society of America, Madison, WI, pp. 775–833,

[28] Keeney, D. R., & Nelson, D. W. (1982). Nitrogen-Inorganic Forms. In A. L. Page (Ed.), Methods of Soil Analysis, Agronomy Monograph 9, Part 2 (2nd ed., pp. 643-698). Madison, WI: ASA, SSSA.

[29] Xu, W., Ge, Z., & Poudel, D. R. (2015). Application and optimization of biolog ecoplates in functional diversity studies of soil microbial communities. In MATEC Web of Conferences (Vol. 22, p. 04015). EDP Sciences.

[30] Classen, A. T., Boyle, S. I., Haskins, K. E., Overby, S. T., & Hart, S. C. (2003). Community-level physiological profiles of bacteria and fungi: plate type and incubation temperature influences on contrasting soils. FEMS Microbiology Ecology, 44(3), 319-328.

[31] Garland, J. L., Mills, A. L., & Young, J. S. (2001). Relative effectiveness of kinetic analysis vs single point readings for classifying environmental samples based on community-level physiological profiles (CLPP). Soil Biology and Biochemistry, 33(7-8), 1059-1066.

[32] Gomez, E., Garland, J., & Conti, M. (2004). Reproducibility in the response of soil bacterial

community-level physiological profiles from a land use intensification gradient. Applied Soil Ecology, 26(1), 21-30.

[33] Jałowiecki, Ł., Chojniak, J. M., Dorgeloh, E., Hegedusova, B., Ejhed, H., Magnér, J., & Płaza, G. A. (2016). Microbial community profiles in wastewaters from onsite wastewater treatment systems technology. PloS one, 11(1), e0147725.

[34] Zak, J. C., Willig, M. R., Moorhead, D. L., & Wildman, H. G. (1994). Functional diversity of microbial communities: a quantitative approach. Soil Biology and Biochemistry, 26(9), 1101-1108.

[35] Rapport, D. J. (1995). Ecosystem health: More than a metaphor?.Environmental values, 4(4), 287-309.

[36] Bowles, T. M., Acosta-Martínez, V., Calderón, F., & Jackson, L. E. (2014). Soil enzyme activities, microbial communities, and carbon and nitrogen availability in organic agroecosystems across an intensively-managed agricultural landscape. Soil Biology and Biochemistry, 68, 252-262.

[37] Spedding, T. A., Hamel, C., Mehuys, G. R., & Madramootoo, C. A. (2004). Soil microbial dynamics in maize-growing soil under different tillage and residue management systems. Soil Biology and Biochemistry, 36(3), 499-512.

[38] Yegül, U., Eminoğlu, M. B., & Türker, U. (2019). Buğdayın Verim ve Kalite Parametrelerinin Toprağın Elektriksel İletkenliği ile İlişkisinin Belirlenmesi. Tekirdağ Ziraat Fakültesi Dergisi, 16(3), 270-283.

[39] Deveci, H., Konukcu, F., & Altürk, B. (2019). Effect of climate change on wheat grown soil moisture profile in Thrace district. Journal of Tekirdag Agricultural Faculty, 16(2), 202-218.

[40] Burns, R. G., DeForest, J. L., Marxsen, J., Sinsabaugh, R. L., Stromberger, M. E., Wallenstein, M. D., ... & Zoppini, A. (2013). Soil enzymes in a changing environment: current knowledge and future directions. Soil Biology and Biochemistry, 58, 216-234.

[41] Byrnes, B. H., & Amberger, A. (1988). Fate of broadcast urea in a flooded soil when treated with N-(n-butyl) thiophosphoric triamide, a urease inhibitor. Fertilizer research, 18(3), 221-231.

[42] Anna, G., Karolina, G., Jarosław, G., Magdalena, F., & Jerzy, K. (2017). Microbial community diversity and the interaction of soil under maize growth in different cultivation techniques. Plant, Soil and Environment, 63(6), 264-270.

[43] Tejada, M., Benítez, C., Gómez, I., & Parrado, J. (2011). Use of biostimulants on soil restoration: Effects on soil biochemical properties and microbial community. Applied Soil Ecology, 49, 11-17.

[44] Maestre, F. T., Puche, M. D., Guerrero, C., & Escudero, A. (2011). Shrub encroachment does not reduce the activity of some soil enzymes in Mediterranean semiarid grasslands. Soil Biology and Biochemistry, 43(8), 1746-1749.

[45] Kapanen, A., Vikman, M., Rajasärkkä, J., Virta, M., & Itävaara, M. (2013). Biotests for environmental quality assessment of composted sewage sludge. Waste Management, 33(6), 1451-1460.

[46] Gryta, A., Frąc, M., & Oszust, K. (2014). The application of the Biolog EcoPlate approach in ecotoxicological evaluation of dairy sewage sludge. Applied biochemistry and biotechnology, 174(4), 1434-1443.

[47] Ghimire, R., Norton, J. B., Stahl, P. D., & Norton, U. (2014). Soil microbial substrate properties and microbial community responses under irrigated organic and reduced-tillage crop and forage production systems. PloS one, 9(8), e103901.

**RESEARCH ARTICLE**

# REMOVAL of METHYLENE BLUE FROM AQUEOUS SOLUTIONS USING PINE CONE and STATISTICAL COMPARISON of ADSORBED MATERIAL

Tuğba GÜR[1], Canan DEMİR[1], Ali Rıza KUL[1]

[1]Yüzüncü Yıl University, Vocational School of Health Services ,Department of Health Care Services, Van, tugbagur@yyu.edu.tr, ORCID: 0000-0001-7220-0210
[1]Yüzüncü Yıl University, Vocational School of Health Services, Department of Medical Documentation and Secretarial, Van, canandemir@yyy.edu.tr, ORCID: 0000-0002-4204-9756
[1]Yüzüncü Yıl University, Vocational School of Health Services ,Department of Health Care Services, Van, alirızakul@yyu.edu.tr, ORCID: 0000-0001-9331-775X

## ABSTRACT

In this study, pine cone, a previously unused biosorbent substance, was used to remove methylene blue from the aqueous solution. For this purpose, pine cones were first cut into pieces, then dried at room temperature, passed through a grinder, sieved in a 230 mesh sieve and brought to the appropriate dimensions and used in experimental processes. On pine cone and methylene blue biosorption; effects such as initial dye concentration, temperature, amount of biosorbent and equilibrium contact time were investigated. In the adsorption of methylene blue with pine cone, descriptive statistical analyzes and comparisons of time-dependent concentrations were made and the results were significant. Descriptive statistical analyzes and comparisons of the concentration were also made and it was seen that the adsorption did not varied depending on the temperature at different methylene blue concentrations.

**Keywords:** *Methylene Blue, Pine cone, Biosorbent*

## 1 .INTRODUCTION

Environmental pollution is one of the most important problems affecting human health in recent times. As a result of industrial processes, waste water is produced and most of them are produced as a result of the processes carried out in plants that do not have a treatment system such as paint and textile factory and are delivered directly to the receiving environment. This type of wastewater is continuously supplied to the environment such as rivers and lakes and prevents the transmission of these colored waters to sunlight, thus decreasing the dissolved oxygen concentration and photosynthetic activity. As a result, anaerobic conditions occur and aerobic organisms die [1,2].

Scientists are constantly working on the development of the most suitable methods for the removal of color and other impurities from dyes in waste water. Physical and chemical methods are generally used for this purpose, but these techniques have disadvantages such as being inexpensive in terms of facilities, equipment and materials and not completely eliminating the problem of environmental pollution. Methods used to remove harmful substances from water include ozonation, adsorption,

chemical coagulation-flocculation, bio-absorption, chemical and photo-oxidation, nanotechnology and ion exchange. Color removal obtained by these methods varies according to the type of paint in the waste water, makes it difficult to choose the most appropriate method to be used for color removal from waste water [3].

Adsorption is one of the methods with high purification potential used to remove dyestuff organic substances from waste water [5, 6]. As an alternative to the expensive and complex activated carbon used in adsorption applications, which is one of the methods used in purification processes, many low cost and easily available materials are being searched. Among these biological adsorbents with high adsorption power, many microorganisms such as corn cob, peanut shell, sawdust, agricultural waste, rice waste, orange peel and fungus are used for color removal in dyestuff [7]. Numerous studies have been conducted among researchers on the removal of unwanted substances from wastewater. One of them is Özer et al. this is a study of dried peanut shells and the adsorption of methylene blue from aqueous solution. In this study, the effect of initial dye skin, temperature, particle size was investigated and optimum experimental conditions were determined. As a result of the study, it was concluded that dried peanut shells are a good adsorbent in removing methylene blue [8]. In addition, Faraco et al. in their study, they studied the color removal capacities of Pluerotus ostreatus and Phanerochaete chrysosporium fungi on 11 different dyes. As a result, they observed that pluerotus ostreatus on direct blue 1, and Phanerochaete chrysosporium on Reactive red 4, direct black 38 and disperse yellow 3 dyes provided 100% color removal [9]. In another study, Giahi et al. used waste tea as a biosorbent in the biosorption of methylene blue, a cationic dye from wastewater. In thermodynamic studies, it was observed that the adsorption equilibrium constant (KL) and maximum adsorption capacity (qmax) increased as the temperature increased. As a result of thermodynamic studies, the DH and DS values were calculated as 11,356 kJ/mol and 20.563 J/(mol K), respectively[10]. In this study, we investigated the statistical evaluation of some parameters such as initial dye concentration and temperature on the removal of methylene blue from wastewater by using natural pine cones as a biosorbent material.

In this study, we used natural pine cones as biosorbent material.Among the dyestuffs, methylene blue is a dark blue dye that is easily soluble in water (4g / L), ethanol and chloroform and has strong water retention[11,12]. This dye is of a cationic molecular structure with a molecular weight of 373.9 g mol-1. The molecular formula is (C16H18ClN3S.3H2O) (3,7-bis (dimethylamino) -phenazothium chloride). Methylene blue was chosen for this study because its adsorption ability was very strong. Although methylene blue is a weak antiseptic, it has a very effective use in combination with other antiseptic mixtures. One of the most common uses is its use as a redox indicator. As redox indicator in milk analysis and Au, B, Bi, Ce, Cu, Ga, Ge, Hg, In, Sb, Se, Sn, Tl, U, Zn, Pb, Fe, Cr, Ti, V, Mo, Sn and It is reported that it is used as a titrant or indicator in the determination of dissolved O2 [11, 13]. Methylene blue can be used to stain diphtheria bacterial cells and nerve tissue [12,14] or can be used to stain cotton in pure blue tones. In addition, the adsorption power of charcoal is measured using methylene blue [15]. Methylene blue is encountered in wastewater due to its use especially in textile sector and mentioned areas. Numerous studies are available in the literature on the determination and removal of toxic organic substances in waste water.

In this study, it is aimed to remove methylene blue dye from aqueous solutions by using pine cones obtained from natural environment. We also made descriptive statistics and comparisons of the adsorption of dye ions on the pine cone and the descriptive statistics and comparisons between the concentration amount and temperature.

## 2.MATERIAL and METHOD

In the experimental stage, pine cone was used as adsorbent material (biosorbent) in adsorption studies.

### 2.1. Preparation of Pine cone:

The pine cone used in the study was collected from the campus area of Yüzüncü Yıl University in Van region. The pine cones (biosorbent) obtained therefrom were first cut into pieces by hand and kept at room temperature and removed from moisture. It was grinded into a powder, then it was brought to the appropriate dimensions using a 230 mesh sieve and used as such in the study.

### 2.2. Properties of Methylene Blue Dye:

Methylene blue; C16H18N3SCl.3H2O and a cationic dye with a molecular weight of 373.9 gmol-1. It has strong adsorption ability. In this study, it has been deemed appropriate to use this dyestuff. The following figure shows the chemical structure of Methylene Blue dye.
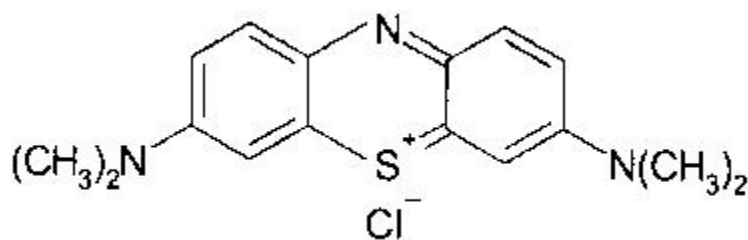


**Figure 1.** Chemical structure of methylene blue dye.

### 2.3. Statistical Analysis

Descriptive statistics for the feature emphasized;

Average; $\bar{x} = \frac{1}{n}\sum_{i=1}^{n} x_i$, Standard deviation; $s = \sqrt{\frac{\sum_{i=1}^{n}(x_i - \bar{x})^2}{n-1}}$ calculated worths ve minimum $(x_{min})$ ve maksimum $(x_{max})$ values were determined. For the eight concentrations, one-way analysis of variance (ANOVA) was used to define whether there was a distinction between both time and temperature levels. Tukey multiple comparison test was used to define which group (s) the differentiation was caused by variance analysis. Statistical meaning level was taken as 5% in the calculations and SPSS statistical package program was used for the analyzes.

## 3. RESULTS

Descriptive statistics and comparison results of adsorption of methylene blue ions on pine cone; The concentration (100 ppm, 150 ppm, 200 ppm, 250 ppm and 300 ppm) and times were given in Table 1. According to Table 1; The variation between the timesand at the different concentrations were meaning (p <0.001). According to a concentration of 100 ppm, methylene blue ions were adsorbed for an average of 57.99 units at 5 minutes, while 84.04 units were adsorbed at 300 minutes.Likewise, at a

concentration of 150 ppm; 66.84 units were adsorbed on average at 5 minutes and 115.65 units were adsorbed on average at 300 minutes. In the 200 ppm concentration, 105.42 units of sample at 5 minutes and 139.28 units of sample were adsorbed at 300 minutes. For the other 250 ppm concentration studied, the adsorption amount of 125.61 units and 171.68 units, respectively, was found as a result of 5 minutes and 300 minutes of treatments. In the same way, in the 300 ppm concentration the adsorption amount of 134.46 units and 196.38 units , respectively, was found as a result of 5 minutes and 300 minutes of procedures.

**Table 1.** Descriptive statististics and comparison results of absorbance values for various time intervals

| | Time | n | Mean | Std. D. | Min | Max | p | | Time | n | Mean | Std. D. | Min | Max | p |
|---|---|---|---|---|---|---|---|---|---|---|---|---|---|---|---|
| 100 ppm | 5 | 3 | 57,99 | 6,02 | 51,276 | 62,884 | 0,001 | 250 ppm | 5 | 3 | 125,61 | 3,47 | 121,96 | 128,876 | 0,001 |
| | 10 | 3 | 63,73 | 3,28 | 60,327 | 66,873 | | | 10 | 3 | 132,97 | 5,31 | 128,324 | 138,754 | |
| | 15 | 3 | 66,51 | 3,05 | 63,817 | 69,814 | | | 15 | 3 | 136,14 | 4,93 | 131,903 | 141,554 | |
| | 20 | 3 | 69,44 | 1,43 | 67,97 | 70,823 | | | 20 | 3 | 142,5 | 6,79 | 138,334 | 150,33 | |
| | 30 | 3 | 72,02 | 1,28 | 70,554 | 72,886 | | | 30 | 3 | 153,24 | 13,79 | 141,626 | 168,476 | |
| | 40 | 3 | 74,5 | 0,6 | 73,816 | 74,891 | | | 40 | 3 | 160,65 | 8,57 | 152,814 | 169,807 | |
| | 50 | 3 | 76 | 1,24 | 74,864 | 77,326 | | | 50 | 3 | 160,87 | 7 | 153,816 | 167,816 | |
| | 60 | 3 | 77,5 | 0,98 | 76,91 | 78,634 | | | 60 | 3 | 162,96 | 6,55 | 156,993 | 169,96 | |
| | 70 | 3 | 79,36 | 1,31 | 77,873 | 80,329 | | | 70 | 3 | 163,99 | 5,65 | 159 | 170,124 | |
| | 80 | 3 | 80,33 | 1,85 | 78,336 | 81,986 | | | 80 | 3 | 164,85 | 4,94 | 161,999 | 170,554 | |
| | 90 | 3 | 81,48 | 2,73 | 78,903 | 84,34 | | | 90 | 3 | 166,1 | 4,14 | 163,606 | 170,88 | |
| | 100 | 3 | 82,68 | 2,93 | 79,814 | 85,667 | | | 100 | 3 | 166,54 | 3,9 | 163,804 | 170,999 | |
| | 110 | 3 | 83,04 | 2,83 | 80,329 | 85,984 | | | 110 | 3 | 168,7 | 4,18 | 163,876 | 171,31 | |
| | 120 | 3 | 83,88 | 2,66 | 81,563 | 86,787 | | | 120 | 3 | 169,46 | 5,07 | 163,634 | 172,886 | |
| | 140 | 3 | 84,01 | 2,57 | 81,959 | 86,886 | | | 140 | 3 | 169,56 | 5,02 | 163,792 | 172,997 | |
| | 160 | 3 | 84,01 | 2,7 | 81,733 | 86,999 | | | 160 | 3 | 169,91 | 4,41 | 164,856 | 172,986 | |
| | 180 | 3 | 84,24 | 2,67 | 81,681 | 87,016 | | | 180 | 3 | 170,06 | 4,14 | 165,323 | 172,99 | |
| | 200 | 3 | 84,43 | 2,26 | 82,814 | 87,017 | | | 200 | 3 | 169,85 | 5,27 | 163,863 | 173,806 | |
| | 240 | 3 | 83,4 | 3,38 | 80,329 | 87,014 | | | 240 | 3 | 170,5 | 5,87 | 163,812 | 174,815 | |
| | 300 | 3 | 84,04 | 2,64 | 81,987 | 87,015 | | | 300 | 3 | 171,68 | 4,39 | 166,803 | 175,33 | |
| 150 ppm | 5 | 3 | 66,84 | 2,67 | 63,814 | 68,864 | 0,001 | 300 ppm | 5 | 3 | 134,46 | 3,77 | 130,816 | 138,336 | 0,001 |
| | 10 | 3 | 74,45 | 4,82 | 70,629 | 79,863 | | | 10 | 3 | 145,12 | 3,56 | 142,334 | 149,136 | |
| | 15 | 3 | 85,5 | 17,64 | 72,884 | 105,664 | | | 15 | 3 | 156,86 | 1,66 | 155,82 | 158,777 | |
| | 20 | 3 | 89,34 | 16,02 | 79,34 | 107,814 | | | 20 | 3 | 163,91 | 4,89 | 160,4 | 169,5 | |
| | 30 | 3 | 93,77 | 13,73 | 85,814 | 109,626 | | | 30 | 3 | 170,66 | 2,07 | 168,82 | 172,896 | |
| | 40 | 3 | 97,11 | 11,26 | 88,626 | 109,889 | | | 40 | 3 | 175,7 | 4,68 | 170,33 | 178,886 | |
| | 50 | 3 | 101,67 | 8,75 | 92,83 | 110,324 | | | 50 | 3 | 177,95 | 4,94 | 172,29 | 181,36 | |
| | 60 | 3 | 102,92 | 8,04 | 94,895 | 110,981 | | | 60 | 3 | 180,75 | 5,63 | 174,36 | 185 | |
| | 70 | 3 | 106,46 | 5,02 | 101,874 | 111,816 | | | 70 | 3 | 184,53 | 2,72 | 181,91 | 187,337 | |
| | 80 | 3 | 108,99 | 3,07 | 105,856 | 111,984 | | | 80 | 3 | 186,11 | 1,93 | 184,864 | 188,328 | |

| | | | | | | | | | | | | |
|---|---|---|---|---|---|---|---|---|---|---|---|---|
| | 90 | 3 | 109,98 | 1,23 | 108,61 | 110,999 | | 90 | 3 | 188,27 | 2,9 | 186,336 | 191,6 |
| | 100 | 3 | 112,56 | 0,51 | 111,976 | 112,856 | | 100 | 3 | 191,02 | 1,63 | 189,85 | 192,88 |
| | 110 | 3 | 113,87 | 2,33 | 111,326 | 115,906 | | 110 | 3 | 193,09 | 1,26 | 191,886 | 194,403 |
| | 120 | 3 | 114,9 | 1,84 | 112,814 | 116,286 | | 120 | 3 | 195,5 | 3,57 | 191,782 | 198,903 |
| | 140 | 3 | 115,35 | 2,16 | 112,876 | 116,804 | | 140 | 3 | 195,56 | 3,56 | 191,885 | 198,986 |
| | 160 | 3 | 115,03 | 1,82 | 112,984 | 116,482 | | 160 | 3 | 195,78 | 3,87 | 191,887 | 199,633 |
| | 180 | 3 | 115,38 | 2,07 | 112,982 | 116,589 | | 180 | 3 | 195,5 | 4,47 | 190,874 | 199,786 |
| | 200 | 3 | 115,12 | 2,72 | 111,999 | 116,981 | | 200 | 3 | 195,76 | 4 | 191,724 | 199,716 |
| | 240 | 3 | 115,6 | 3,16 | 111,974 | 117,814 | | 240 | 3 | 195,58 | 4,89 | 190,56 | 200,333 |
| | 300 | 3 | 115,65 | 3,31 | 111,843 | 117,897 | | 300 | 3 | 196,38 | 6,18 | 190,479 | 202,803 |
| 200 ppm | 5 | 3 | 105,42 | 4,5 | 100,814 | 109,814 | | | | | | | |
| | 10 | 3 | 111,2 | 2,31 | 109,863 | 113,866 | | | | | | | |
| | 15 | 3 | 116,77 | 3,46 | 112,889 | 119,527 | | | | | | | |
| | 20 | 3 | 120,03 | 5,04 | 114,334 | 123,874 | | | | | | | |
| | 30 | 3 | 123,93 | 6,98 | 115,864 | 127,981 | | | | | | | |
| | 40 | 3 | 127,16 | 8,29 | 117,864 | 133,806 | | | | | | | |
| | 50 | 3 | 129,01 | 7,13 | 120,894 | 134,28 | | | | | | | |
| | 60 | 3 | 130,62 | 6,75 | 123 | 135,866 | | | | | | | |
| | 70 | 3 | 132,21 | 7,63 | 123,893 | 138,876 | | | | | | | |
| | 80 | 3 | 133,71 | 6,53 | 126,884 | 139,9 | | | | | | | |
| | 90 | 3 | 136,21 | 4,42 | 132 | 140,816 | | | | | | | |
| | 100 | 3 | 136,92 | 3,52 | 134,889 | 140,987 | | | | | | | |
| | 110 | 3 | 137,81 | 2,75 | 135,894 | 140,96 | | | | | | | |
| | 120 | 3 | 139,37 | 3,2 | 135,976 | 142,324 | | | | | | | |
| | 140 | 3 | 139,53 | 3,3 | 135,977 | 142,488 | | | | | | | |
| | 160 | 3 | 139,52 | 3,33 | 135,979 | 142,582 | | | | | | | |
| | 180 | 3 | 139,59 | 3,38 | 135,976 | 142,662 | | | | | | | |
| | 200 | 3 | 139,25 | 4,06 | 134,818 | 142,786 | | | | | | | |
| | 240 | 3 | 139,29 | 4,07 | 134,864 | 142,86 | | | | | | | |
| | 300 | 3 | 139,28 | 4,12 | 134,803 | 142,91 | | | | | | | |

The statistical results of the adsorption of methylene blue ions on pine cones at concentration (100 ppm, 150 ppm, 200 ppm, 250 ppm and 300 ppm) and temperature (25°C, 35°C and 45°C) values are shown in Table 2. According to Table 2, it was observed that the adsorption values of dye ions at different concentrations did not change depending on the temperature.

**Table 2.** Comparison of adsorption results at different temperatures and concentrations and descriptive statistics.

| | °C | n | Mean | Std. Deviation | Min | Max | p |
|---|---|---|---|---|---|---|---|
| 100 ppm | 25 | 20 | 75,527 | 8,412 | 51,276 | 82,814 | |
| | 35 | 20 | 77,466 | 7,604 | 59,816 | 84,033 | 0,231 |
| | 45 | 20 | 79,897 | 7,904 | 62,884 | 87,017 | |

| 150 ppm | 25 | 20 | 107,177 | 12,494 | 63,814 | 112,984 | |
| | 35 | 20 | 101,029 | 16,866 | 68,864 | 117,208 | 0,436 |
| | 45 | 20 | 102,365 | 17,439 | 67,833 | 117,897 | |
| 200 ppm | 25 | 20 | 129,895 | 9,701 | 100,814 | 135,979 | |
| | 35 | 20 | 127,753 | 12,016 | 105,634 | 140,142 | 0,110 |
| | 45 | 20 | 134,877 | 10,524 | 109,814 | 142,910 | |
| 250 ppm | 25 | 20 | 156,030 | 13,986 | 121,960 | 166,803 | |
| | 35 | 20 | 158,272 | 15,239 | 128,876 | 172,910 | 0,126 |
| | 45 | 20 | 165,118 | 14,039 | 125,989 | 175,330 | |
| 300 ppm | 25 | 20 | 180,082 | 17,092 | 130,816 | 191,887 | |
| | 35 | 20 | 181,672 | 18,575 | 134,235 | 195,853 | 0,963 |
| | 45 | 20 | 181,018 | 19,798 | 138,336 | 202,803 | |

Figures 2-5, Adsorption of methylene blue dye on Pine Cone ; concentration (100 ppm, 150 ppm, 200 ppm, 250 ppm, 300ppm)
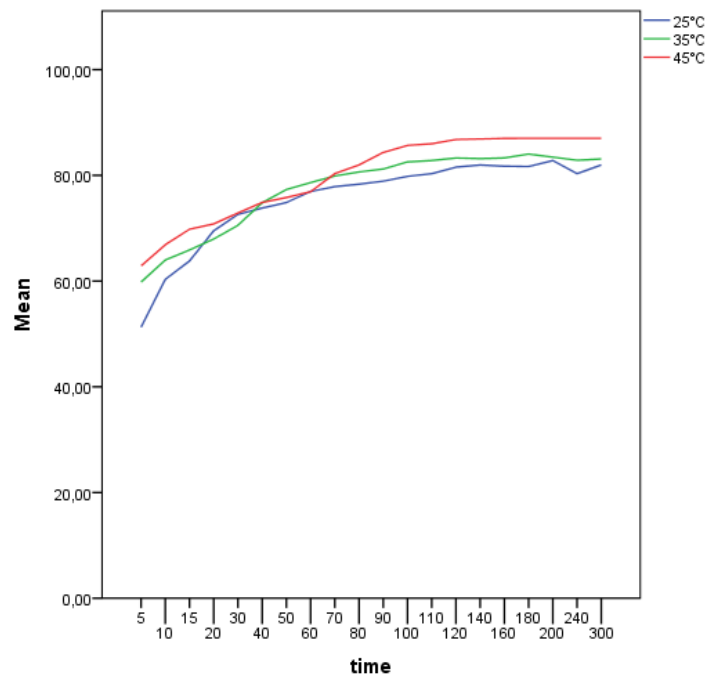


**Figure 2.** 100 ppm
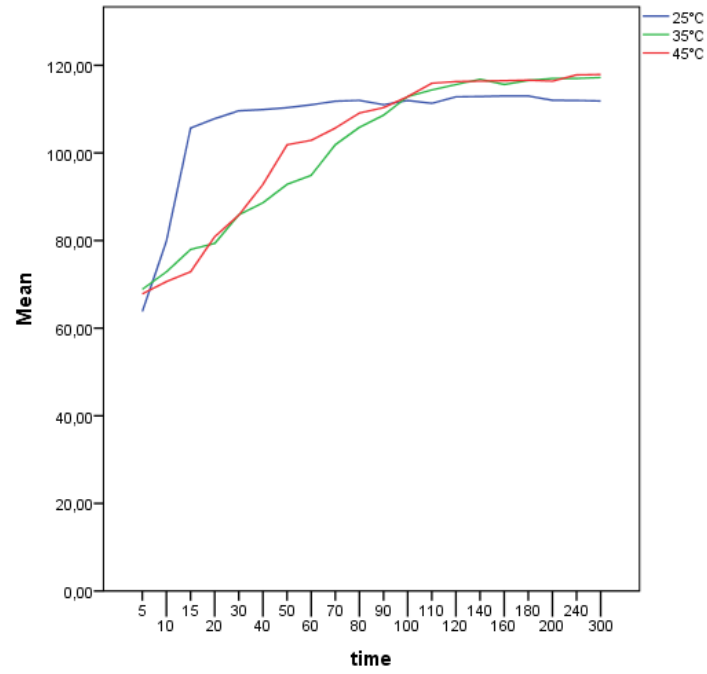
**Figure 3.** 150 ppm.



**Figure 4.** 200 ppm.

241
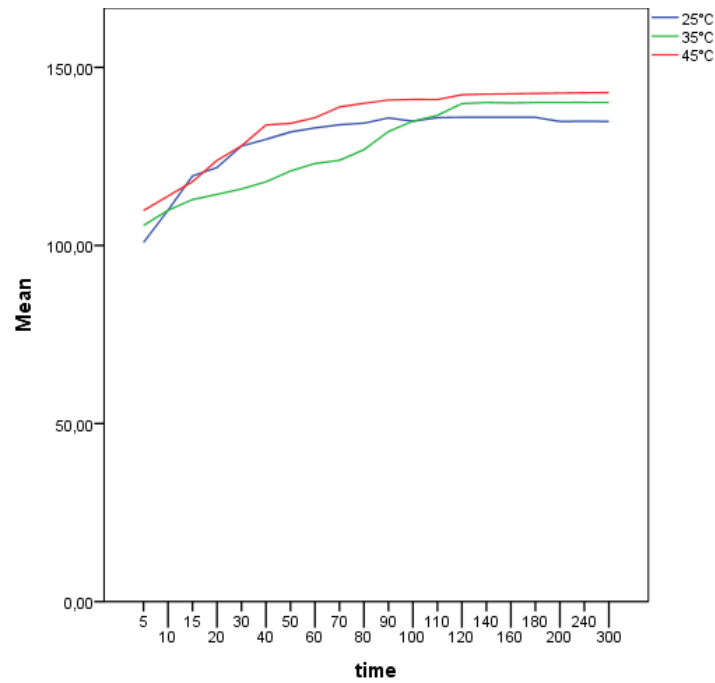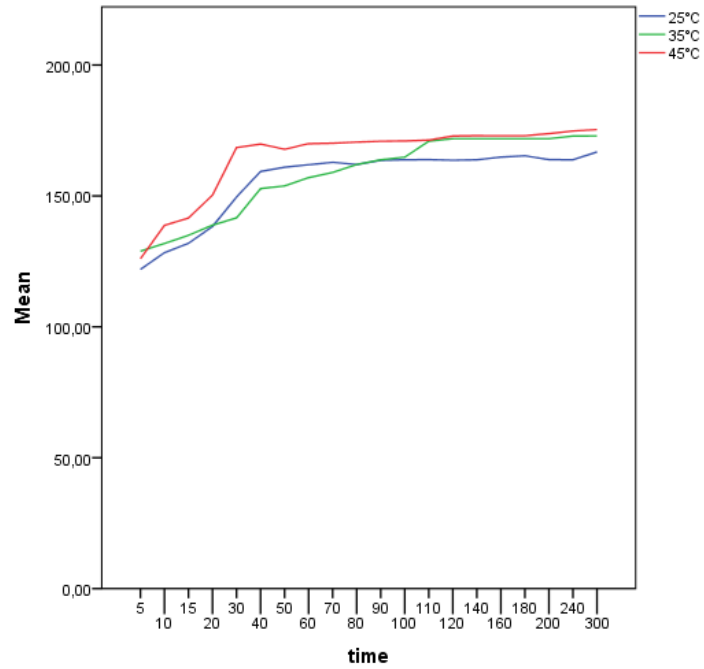
**Figure 5.** 250 ppm.



**Figure 6.** 300 ppm.

242
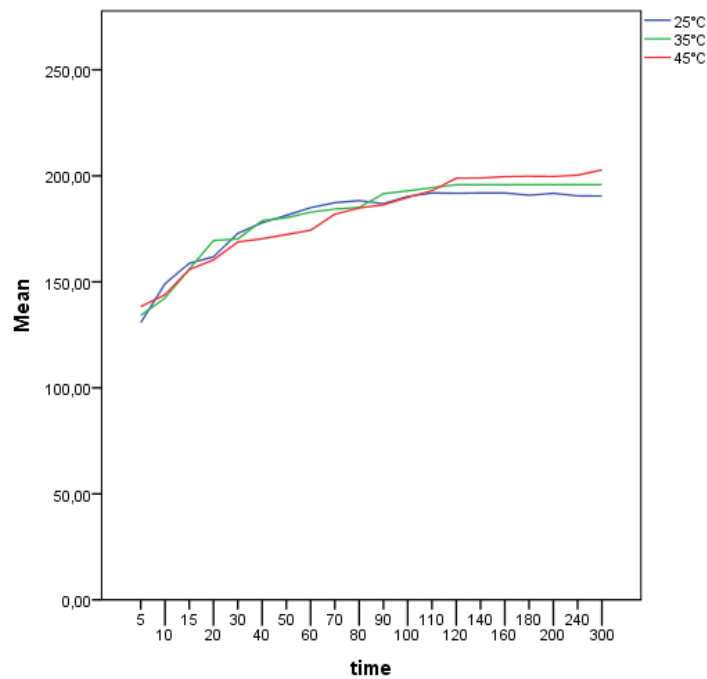
## 4. DISCUSSION AND CONCLUSION

In this study; natural pine cones obtained from the campus of Yüzüncü Yıl University in Van region were used as biosorbents and methylene blue, a dyed organic substance, was removed from the aqueous medium. In this study, the methylene blue solution prepared at various concentrations such as 100 ppm, 150 ppm, 200 ppm, 250 ppm and 300 ppm, at different temperatures ($25^0$C, $35^0$C and $45^0$C) and at various times (5,10,15,20,30,40, 50,60,70,80,90,100,120,140,160,180,200,240,300 min.), The change of adsorption of pine cone was examined. In the adsorption of methylene blue from the aqueous medium with pine cone, descriptive statistics and comparisons were made between concentration amounts and time. By increasing the concentration of methylene blue ions in the solution, the amount of adsorbed material was also increased. By increasing the contact time between the pine cone and the concentrations of methylene blue ions, it was found to increase significantly in adsorption. In this study on the adsorption of methylene blue with pine cone, the relationship between concentration amounts and temperature was also examined statistically. As a result, depending on the temperature, the adsorption of dye ions at various concentrations on the pine cone did not change.

Other studies, similar to this study, in which some parameters related to the initial dye concentration, time and temperature, which we examined on the removal of methylene blue with naturally occurring pine cones, were evaluated statistically, were also carried out by some researchers. In a study, the adsorption process for the removal of methylene blue using Van sour cherry pulp was investigated at pH = 5 according to different concentrations, temperatures and time. In this study, in which the adsorption of dye solution on adsorbent material was compared according to time, the differences between the times and concentrations were seen to be statistically important (p <0.001). Consistent with our study, they observed that the adsorption of dye solution at various concentrations did not change with temperature (25oC, 35oC, 45oC) [16]. In another similar study, models were used to determine the adsorption of Basic Blue 41 (BB 41) dyestuff on activated carbon obtained from apple peel, and it was observed that the adsorption process mostly increased with the increase of BB 41 dye concentration in the solution and the contact time with activated carbon [17].

In recent years, there has been a lot of research on the elimination of waste materials from aqueous solutions by adsorption in order to protect the environment. In one study; color removal of the methylene blue and safranine dyes in the batch and filled column system was investigated by using activated sludge pyrolysis and chemicalactivation with activated carbon and it was found that methylene blue dye was adsorbed faster than safranine dye [18, 19]. In another study; observed that the removal of methylene blue from the aqueous medium using Platanus Orientalis L. Bioma increased the amount of adsorbed substance by increasing the concentration of dyes [20]. Using the data obtained as a result of the study; It is concluded that this material can be used as biosorbent because it is easy and inexpensive to obtain natural pine cone and high dye removal efficiency. We believe that the pine cone that we use in our study is an alternative biosorbent material because it will reduce the pollutant potential of environmental pollutants and it is economical and easily obtainable for the removal of paint pollution caused by industrial wastes. We believe that our study will support the information in the scientific literature and will shed light on other studies to be done from now on.

**REFERENCES**

[1] Kumar, V., Wati, L., Nigam, P., Banat, I.M., Yadav, B.S., Sing, D., Marchant, R. (1998). Decolorization and biodegration of anerobically digested sugarcane molasses spent wash effluent from biomethanation plants by white-rot fungi. Process Biochemistry, 33(1), 83-88.

[2] Seçkin H., Meydan İ., Özdek U., Kömüroğlu A.U., Kul A.R., Çibuk S. (2018). ''Investigation of Coliform And E. Coli Bacteria And Nitrite And Nitrate Levels İn Drinking Waters of Van And Some Provinces'', IOSR Journal of Environmental Science, Toxicology and Food Technology, 12(4); 47-50.

[3] Seçkin, H., Meydan, İ. (2021). "Synthesis and Characterization of Veronica beccabunga Green Synthesized Silver Nanoparticles for The Antioxidant and Antimicrobial Activity". Türkiye Tarımsal Araştırmalar Dergisi, 8: 49-55.

[4] [4] Kannan, N., Sundaram, M. M. (2001).Kinetics and mechanism of removal of methylene blue by adsorption on various carbons a comparative study. Dyes Pigment, 51:25–40.

[5] Aksu, Z. (2005). Application of biosorption for the removal of organic pollutants: a review. Process Biochem, 40:997–1026.

[6] Kahraman, S.S., Yesilada, Ö. (1999). Endüstriyel ve Tarımsal atıkların beyaz çürükçül fungusların lakkaz üretimine etkisi. Kükem Dergisi, 23(2), 139-144.

[7] Özer, D., Dursun, G., Özer, A. 2007. Methylene blue adsorption from aqueous solution by dehydrated peanut hull. Journal of Hazardous Materials, 144 (1-2): 171-179.

[8] Faraco, V., Pezzella, C., Giardina, P., Piscitelli, A., Vanhulle, S., Sannia, G. (2009). Decolourization of textile dyes by the white-rot fungi *Phanerochaete chrysosporium* and *Pleurotus ostreatus*. Journal of Chemical Technology& Biotechnology, 84: 414-419.

[9] Giahi, M., Rakhshaee, R., Bagherinia, M.A. (2011). Removal of methylene blue by tea wastages from the synthesis waste waters. Chinese Chemical Letters, 22: 225–228.

[10] Burns, G.P., Lynn, S., Hanson, D. N.(1979). Energy reduction in phenol recovery system, Report no: LBL 9176, Lawrence Berkeley Laboratory.

[11] Treybal, R.E. (1963).Liquid Extraction, New York, McGraw Hill, p.48.

[12] Kortüm, G., Vogel, W., Andrussow, K. (1961). Pure and Appl.Chem, 1(2-3), 190.

[13] Greminger, D.C., Burns, G.P., Lynn, S., Hanson, D.N., King, C.J.(1982). Solvent Extraction of phenols from water. Ind.Eng.Chem.Process Des.Dev, 2: 51-54.

[14] Joshi, D.K., Senetar, J.J., King, C. J. (1984). Solvent extraction for removal of polar-organic pollutants from water, Ind.Eng.Chem.Process Des.Dev, 23: 748-754.

[15] Yıldız, H., Demir, C and Kul, A.R. (2019). Batch Adsorption of Methylene Blue Dyestuff Using Van Sour Cherry Pulp and Statistical Comparison. J. Int. Environmental Application & Science, 14(4): 177-182.

[16] Demir, C., Yıldız, H., Kul, A.R., Keskin, S. (2020). Basıc Blue 41 Boyar Maddesinin Elma Kabuğundan Elde Edilen Aktif Karbon ile Adsorplanabilirliğinin Matematiksel Olarak Modellenmesi. Journal of Scientific Reports-C, 1: 55-69.

[17] Chu, H. C., Chen, K. M. (2002).Reuse of Activated Sludge Biomass: I. The Rate Processes for the Adsorption of Basic Dye0. Process Biochemistry, 37: 595-600.

[18] Rozada, F., Calvo, L. F., Garcia, A. I., Martin, V. J., Otero, M. (2003). Dye Adsorption by Sewage Sludge-Based Activated Carbons in Batch and Fixed-Bed Systems. Bioresource Technology, 87: 221-30.

[19] İmecik, Z., Dığrak, M., and Halipçi, H. N. (2014). Metilen mavisinin sulu ortamdan Platanus Orientalis L. Biyoması kullanılarak giderimi. Karaelmas fen ve mühendislik dergisi, 4(2),64-69.

*RESEARCH ARTICLE*

# GREEN SYNTHESIS of SILVER, ZINC, and CERIUM NANOPARTICLES USING THERMOPHILIC ANOXYBACILLUS SP. ST7 STRAIN and INVESTIGATION of THEIR VARIOUS BIOLOGICAL ACTIVITIES

Serpil GONCA

[1]Mersin University, Faculty of Pharmacy, Department of Pharmaceutical Microbiology, Mersin, serpilgonca@mersin.edu.tr ,
ORCID: 0000-0002-8544-1184

## ABSTRACT

The antioxidant activities of AgNP, ZnNP and CeNP synthesized extracellular from thermophilic *Anoxybacillus* sp. ST7 were evaluated by DPPH scavenging activity and ferrous chelating activity. The highest DPPH and ferrous chelating activities of AgNP, CeNP, and ZnNP at 200 mg/L concentration were 93.59% and 88.08%, 73.04% and 78.25%, and 77.47% and 82.96%, respectively. Also, the nanoparticles demonstrated significant DNA cleavage activity. The antimicrobial capabilities of NPs were researched in micro-dilution methods and it was observed that Gram +ve bacteria were more susceptible to nanoparticles. The nanoparticles showed more effective microbial cell inhibition viability activity toward *E. coli*. Also, NPs showed important biofilm inhibition activity toward *S. aureus* and *P. aeruginosa*.

## 1. INTRODUCTION

Nanotechnology can be defined a science which investigates at the molecular level (in the range of 1 to 100 nm). Nanotechnology can create materials which have completely new physical, the emergence of structures with chemical and biological properties. Nanomaterials exhibits superior and new features with size-dependent compared to larger particles of the same materials [1], [2]. Nanoparticles can show superior properties by providing certain conditions because they are remarkable very small in size compared to the volumetric structures of materials. For example, the conductivity of the nanostructure that even if a single atom was added to the structure, can be changed completely can change [3]. The properties of nanoparticles are very superior because their shape and morphology can be controlled as well as their size [4].

The NPs are currently utilized in various objects such as from, electronics, cooking vessel to aerospace industry and renewable energy. So far, numerous synthesis techniques that are categorized onto bottom-up or top-down way have been developed for nanoparticles synthesis [5], [6]. Green synthesis is one of the methods that allows nanoparticles to be synthesized using environmentally friendly methods. The term of green nanotechnology can be defined as the production of nanoparticles from living cells which are environmentally friendly with low toxic substance content. This term

within the scope of nanotechnology refers to easy-to-apply, harmless methods that reduce the waste product problem [7]. Green plant extracts and microorganisms are used within the scope of green nanotechnology. Although many living things are used as extracts, *Azadirachta indica*, *Acalypha indica*, *Camellia sinensis*, *Jatropha curcas* and *Aloe vera* can be given as an example for green plant extracts [8]. It was reported by Nematollahi [9] that plants and plant products were cheap and renewable resources for nanomaterial production. In addition, the use of microorganisms' extracts can be considered as an alternative way to physical and chemical methods.

There are various reports on the biological applications of the nanoparticles synthesized in the present study. The antioxidant capabilities of cerium oxide NPs for varies reactive species have been indicated in *in-vitro* and *in-vivo* studies with cerium oxide NPs displaying anti-inflammatory and bio-mimetic antioxidant properties [10]. Moreover, cerium oxide NPs have also been shown to have antimicrobial activity [11]. It has indicated in previous studies that silver nanoparticles exhibit biological activities such as antimicrobial activity, biofilm inhibition activity and anticancer activity [12], [13], [14]. Besides, zinc oxide NPs showed varied biomedical implementations in the areas of drug delivery systems, bio-imaging, tissue engineering, and can also be used as antioxidant, antibacterial, and antidiabetic agents [15].

The aim of this study, synthesized AgNP, ZnNP, and CeNP nanoparticles using thermophilic *Anoxybacillus* sp. ST7 bacterium extracts. The produced NPs were characterized by FTIR, FE-SEM, SEM-EDX, and XRD analyses. The antioxidant capabilities of the produced NPs were evaluated by DPPH scavenging activity and ferrous chelating activity. Moreover, DNA nuclease and biofilm inhibition activity were also tested.

## 2. MATERIALS AND METHODS

### 2.1. Materials
Cerium nitrate (Ce(NO3)3·6 H2O) and zinc sulfate (ZnSO$_4$ ) were obtained from Sigma Aldrich. Silver nitrate (AgNO3) was purchased from Merck. Also, all utilized chemicals were of analytical reagent grade. Distilled water (DW) used in all tests was obtained from purification system.

### 2.2. Nanoparticles Synthesis
10 mM silver nitrate, cerium nitrate, and zinc sulfate solutions were prepared for the synthesis of nanoparticles. 300 mL of each solution were added into the 100 mL bacteria extracts and were left to react for overnight at 70 $^o$C. The prepared nanoparticles were washed with deionize water a few times and dried for 24 h at 80 $^o$C.

### 2.3. Nanoparticles Characterization Methods
The synthesized nanoparticles were characterized by FTIR, XRD, FE-SEM and EDX. Perkin Elmer 400 model FT-IR spectrometer was used to obtain infrared spectrums. X-ray diffraction spectrums were obtained by using X-ray diffractometer (BRUKER AXS D8 ADVANCE). The electron microscopy images and energy dispersive X-ray analysis graphs were obtained using a field-emission scanning electron microscope (ZeissGemini 500).

### 2.4. DPPH Activity
The scavenging capability of AgNP, ZnNP, CeNP upon the DPPH radical was studied with the way expressed by Ağırtaş et al. [16]. A 250 µL of AgNP, CeNP and ZnNP solutions prepared at three various concentrations and were added to the test tubes separately. Then, 1,0 mL of DPPH was joined

to the mixtures and incubated to 30 min at room temperature. Trolox and Ascorbic acid were used as controls and the above-mentioned protocol was performed for them as well. Methanol was used as a blank solution. When the incubation period was over, the reaction mixture was measured at 517 nm in the spectrophotometer. Finally, the scavenging capability was calculated with the equation (1):

$$Capacity \ (\%) = \left( \frac{Abs(control) - Abs(sample)}{Abs(control)} \right) \times 100 \tag{1}$$

$Abs_{control}$ is control absorbance value, $Abs_{sample}$ is the absorbance value of the test compounds and DPPH after 30 min.

## 2.5. Ferrous Chelating Activity

The ferrous chelating ability of AgNP, ZnONPs and CeNP was evaluated by Dinis method [17]. The AgNP, ZnONP and CeNP prepared at different concentrations were treated with $FeCI_2$ for 2 min. Later ferrozine was added to the reaction mixtures. The reaction mixtures were then incubated in the dark for 10 minutes and a spectrophotometer was used to determine the ferrous chelating ability. Subsequently, the absorbance measured at 562 nm. Later the percent of chelating ability was calculated with equation (2):

$$Metal \ Chelating \ Effect \ (\%) = \left( \frac{Abs(control) - Abs(sample)}{Abs(control)} \right) \times 100 \tag{2}$$

$Abs_{control}$ is the absorbance value of the control reaction, $Abs_{sample}$ *is* represents the absorbance value acquired in the existence of compounds or EDTA.

## 2.6. DNA Cleavage Activity

The DNA cleavage activity of the AgNP, ZnONP and CeNP were evaluated using agarose gel electrophoresis method. pBR322 were used as a target DNA. Different concentrations of AgNP, ZnONP and CeNP were mixed with the pBR322 DNA. Subsequently, obtained mixture incubated at 37 °C for 60 min. Subsequently, the reaction mixtures were loaded into gel. Later, electrophoresis process started. Untreated genomic DNA was utilized as a negative control. The gel were imagined via a transilluminator.

## 2.7. Antimicrobial Activity

Microdilution way was studied to appraise the antibacterial activity of the AgNp, CeNp and ZnONP. The tested microbial strains were Gr +ve [Enterococcus faecalis, Enterococcus hirae and Staphylococcus aureus], Gr –ve [Pseudomonas aeruginosa, Escherichia coli, and Legionella pneumophila subsp. pneumophila] and fungal strains [Candida parapisilosis and Candida tropicalis]. The green synthesized nanoparticles solutions were firstly prepared in 96 well plates and a serial two fold dilutions were done from 1024 to 1 mg/mL. Then, the microbial strains which was prepared 0.5 McFarland Scale were added to the microplate-wells and incubated at 37 ℃ for 24 h. When 24 h was over, antimicrobial activity was evaluated with MIC values described as the lowest concentration that inhibits microbial growth.

### 2.8. Biofilm Inhibition activity

The biofilm inhibitory behavior of the green synthesized AgNP, ZnONP and CeNP by using thermophilic *Anoxybacillus* sp. ST7 was examined in 24-well plates based on crystal violet (CV) staining. The bacteria tested in the evaluation of biofilm formation inhibition of nanoparticles were *S. aureus* and *P. aeruginosa*. Bacterium cultures were grown for one night before starting the testing phase. Bacterial strains were inoculated to well plates with $2.9 \times 10^8$ CFU/mL. Bacterial strains incubated at 37 ℃ for 72 h in well plates containing with three concentrations of synthesized nanoparticles at 125, 250 and 500 mg/L. Following, the plate's wells were drained and it cleaned two times with DW. The plates were left to dry for 30 min in the oven set at 80°C to dry. Subsequently, CV dye added into the well to stain biofilm formations for 45 min. CV was then lifted and the plates were washed slowly. The washing of wells was done twice. Ethanol was then added and it was waited for 15 minutes for the absorbed CV to be recovered. Spectrophotometer was used to determine biofilm inhibition and its absorbance was measured at 595 nm. Just *S. aureus* and *P. aeruginosa* containing wells were used as positive controls. Biofilm inhibition activity of NPs was calculated according to the equation (4).

$$Biofilm\ Inhibition\ (\%) = \left( \frac{Abs(control) - Abs(sample)}{Abs(control)} \right) \times 100 \tag{4}$$

### 2.9. Bacterial Viability Test

*E. coli* was utilized to investigated the bacterial cell viability inhibition properties of Ag, ZnO and Ce nanoparticles. Firstly the bacteria was inoculated in Nutrient broth, and then it was incubated to 24 hours at 37°C. When the 24 h was over, *E. coli* was centrifuged for five minutes at 5000 rpm. The microbial residue was then cleaned with 0.9% NaCl to take culture media. The cleaned bacteria was suspended into 10 mL of 0.9% NaCl. This was used for cell viability test. Later bacteria was reacted with Ag, ZnO and Ce nanoparticles at 3 different concentrations (125, 250 and 500 mg/L) to 90 minutes at 37°C. The time was finished, the mixtures were diluted in different proportions and inoculated in NB agar and left to incubate at 37 °C for 24 hours. The same process was performed with control which was not included the NPs. Eventually, the colonies were counted and the bacterial cell viability calculated using with equation (3).

$$Cell\ viability\ (\%) = (A_{control} - A_{sample} / A_{control})\ x\ 100 \tag{3}$$

## 3. RESULTS AND DISCUSSION

### 3.1. Nanoparticles Characterization

Structure, crystalline nature and morphology of the silver, cerium and zinc nanoparticles were carried out by using XRD, FE-SEM, and EDX analysis. The formation of Ag NPs, $Ce_2O(CO_3)_2.2H_2O$ NPs and ZnO NPs biosynthesized were demonstrated via XRD spectrum. (Fig. 1). The XRD peaks for $2\theta$ at 33.4°, 46.3, 55.2°, 64.7°, and 77.9° correspond to 111, 200, 142, 220, and 311 planes for silver (JCPDS card number 04-0783). FE-SEM images of the Ag NPs showed that the particles had an average size of 20 nm with spherical shape (Fig. 2A). Formation of Ag NPs was also proved by SEM-EDX analysis (Fig. 2B). According to X-ray diffraction data for cerium, $2\theta$ at 20.5°, 30.2°, and 38.3° proved the formation of $Ce_2O(CO_3)_2.2H_2O$ NPs (Fig. 3). Formation of the $Ce_2O(CO_3)_2.2H_2O$ NPs was also proved by FE-SEM and SEM-EDX analysis (Fig. 4A and 4B). The results showed that $Ce_2O(CO_3)_2.2H_2O$ NPs had a particle size lower than 100 nm was successfully synthesized (Fig.

4A). Fig. 5. shows the XRD spectrum of the ZnO by two strong amorphous maxima. Formation of the ZnO NPs was studied with FE-SEM and SEM-EDX analysis (Fig. 5A and 5B). The results proved that ZnO NPs had a particle size lower than 100 nm was successfully synthesized (Fig. 5A and 4B).
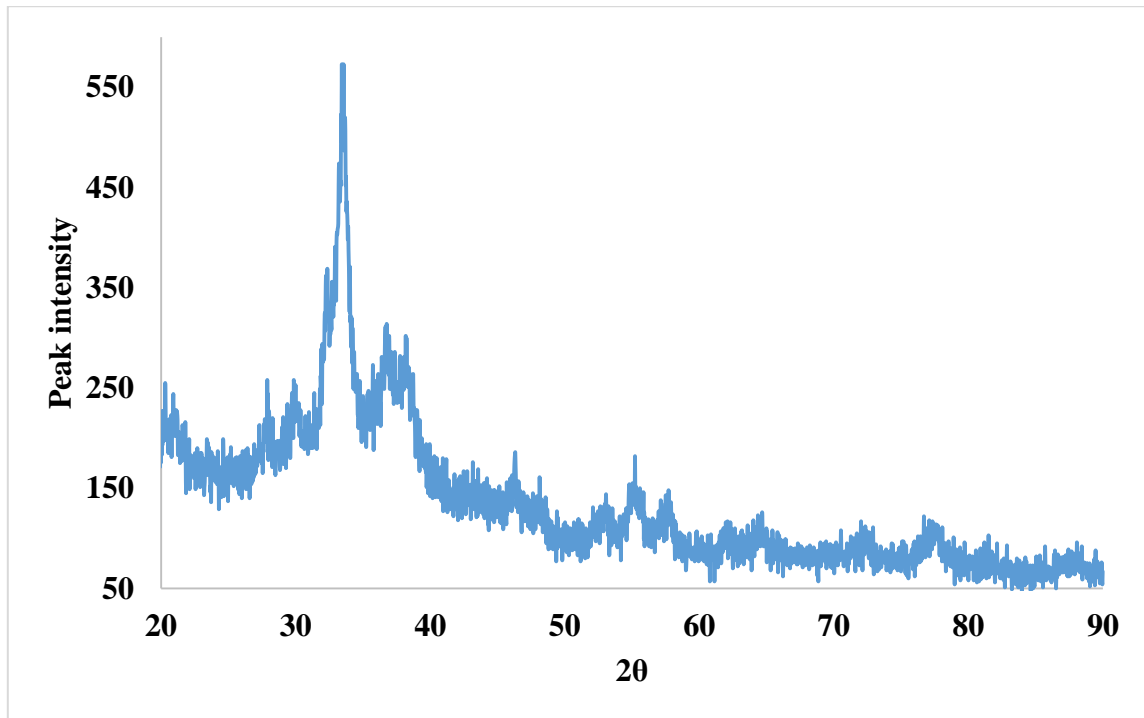


**Fig. 1.** XRD spectrum of Ag NPs.
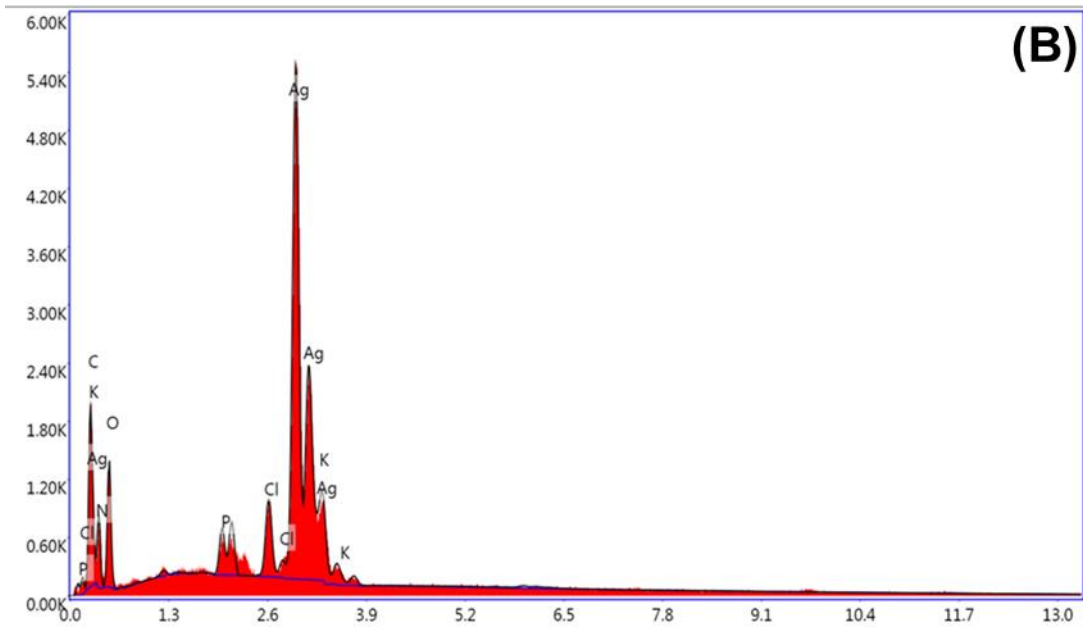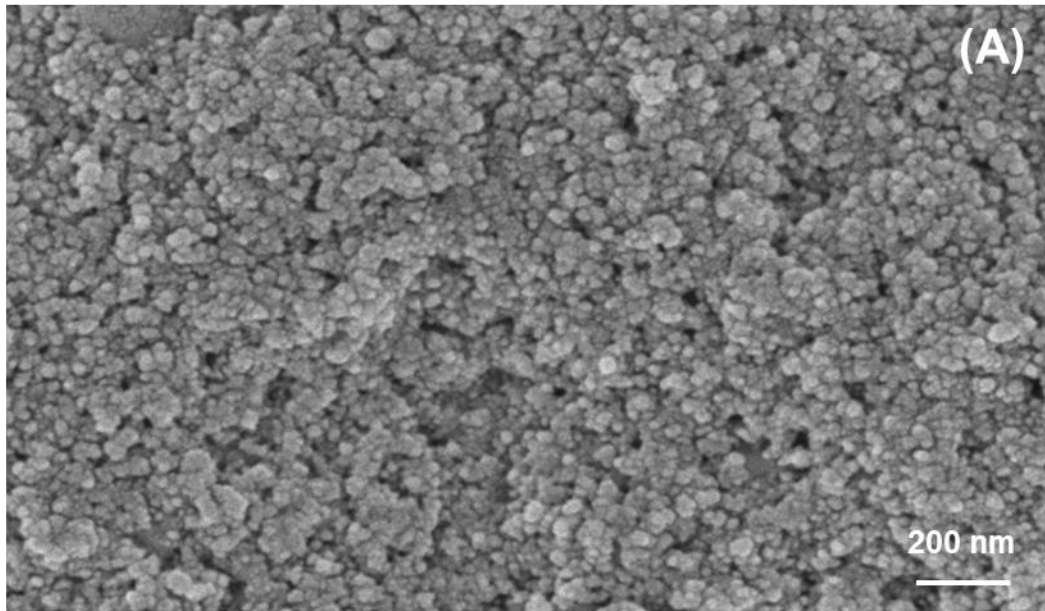
**Fig. 2.** FE-SEM image and SEM-EDX analysis of Ag NPs.
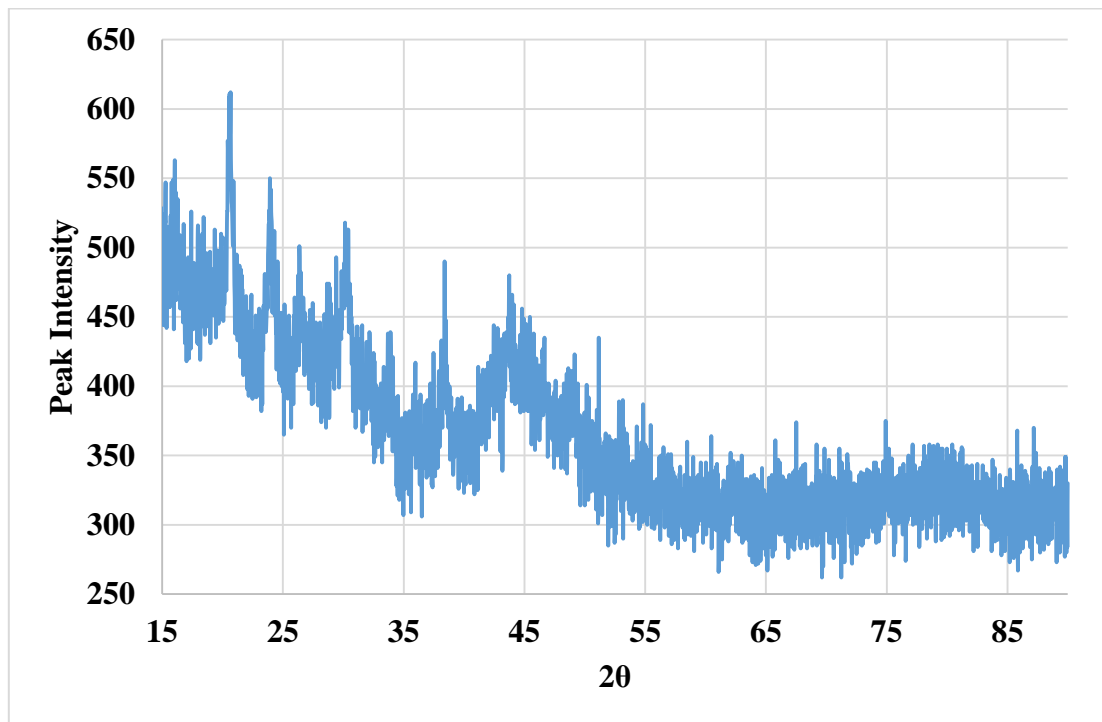
**Fig. 3.** XRD spectrum of $Ce_2O(CO_3)_2.2H_2O$ NPs.
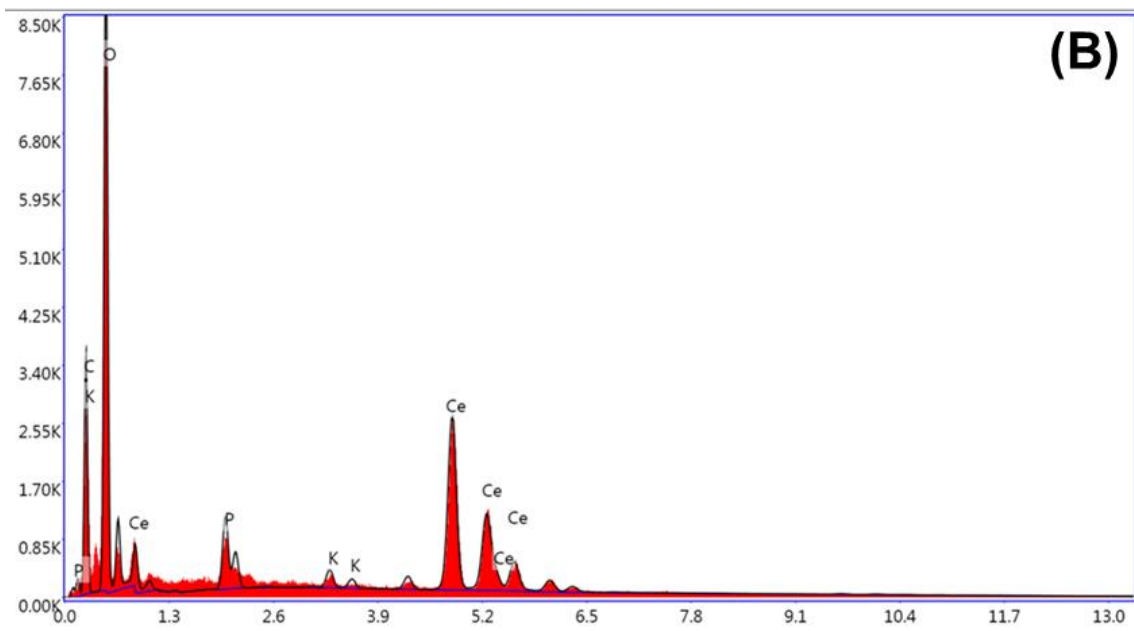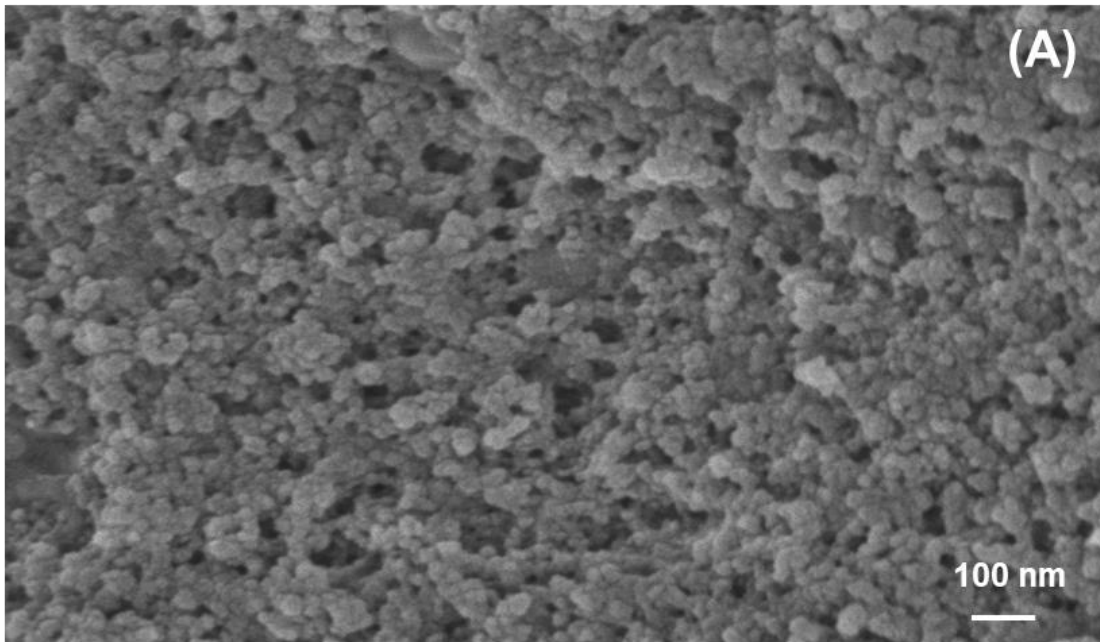
**Fig. 4.** FE-SEM image and SEM-EDX analysis of $Ce_2O(CO_3)_2.2H_2O$ NPs.
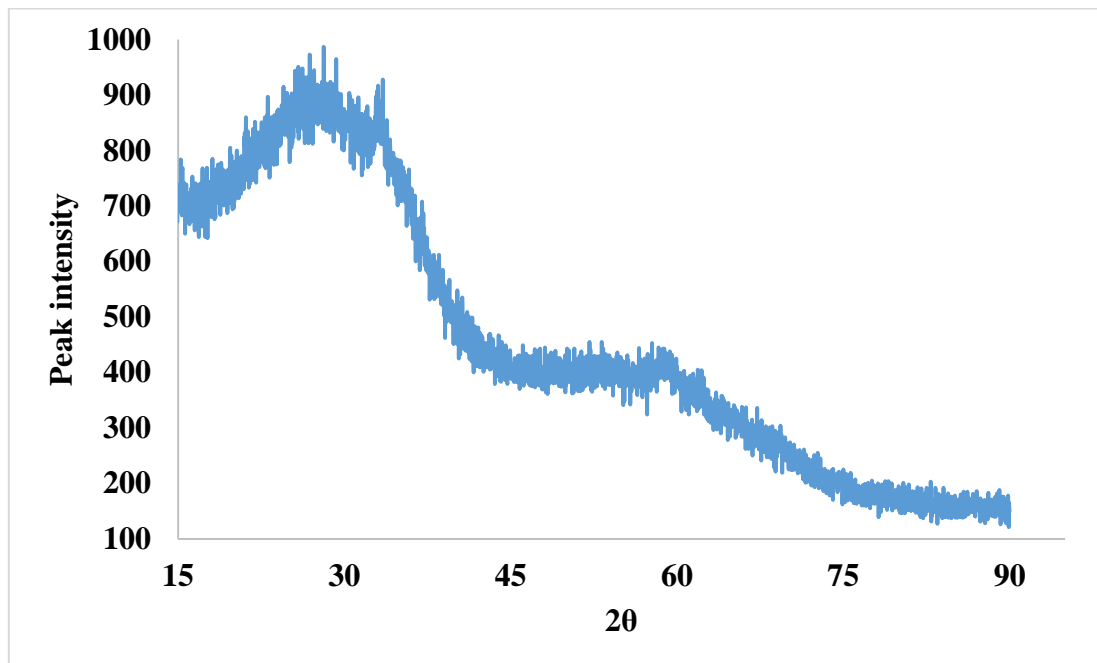
**Fig. 5.** XRD spectrum of ZnO NPs.
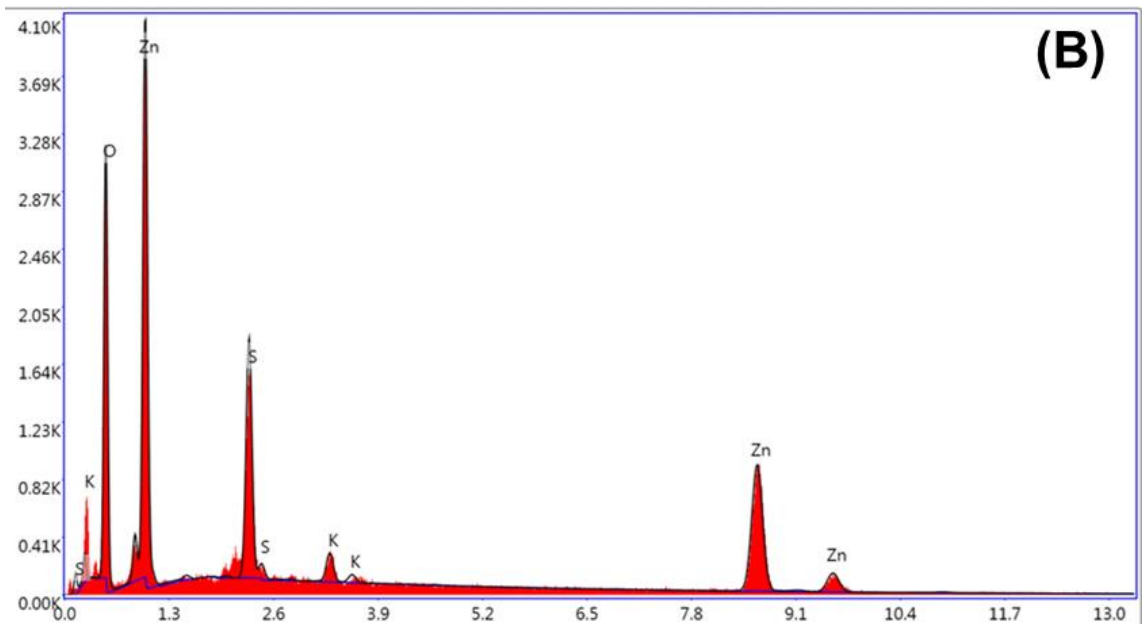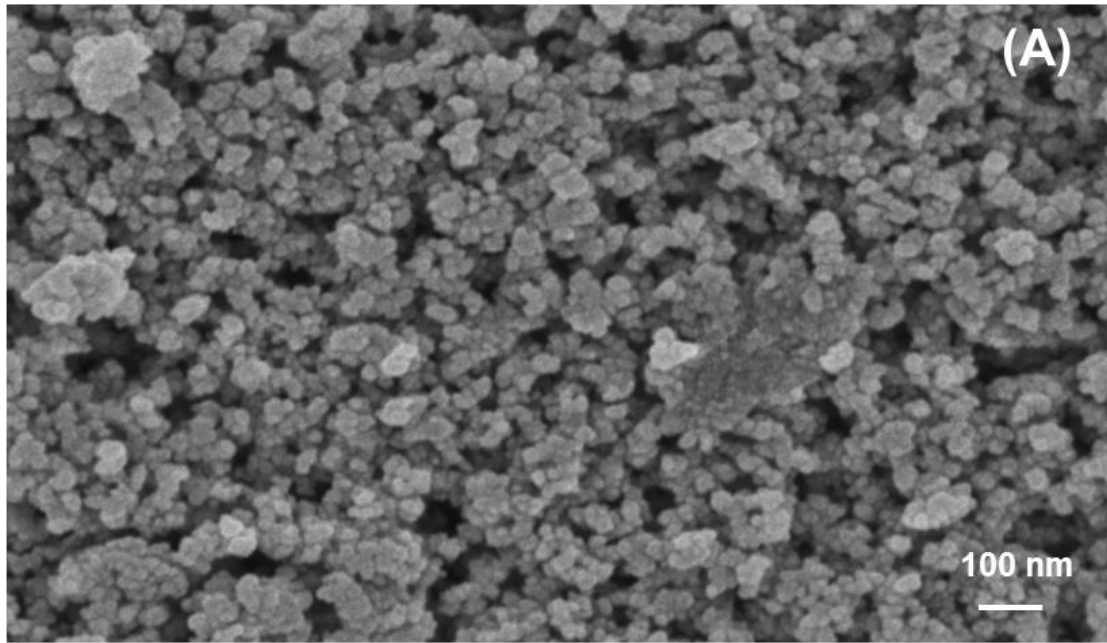
**Fig. 6.** FE-SEM image and SEM-EDX analysis of ZnO NPs.

### 3.2. DPPH Radical Scavenging Activity

The antioxidant activity of synthesized nanoparticles by using thermophilic bacteria was determined by using DPPH assay (Fig. 7). The free radical scavenging activity of nanoparticles tended to increase with increasing its concentration, also new synthesized NPs had a significant inhibitory activity against the DPPH radicals. According to antioxidant activity results new synthesized AgNP, CeNP and ZnONP were showed the efficient free radical scavenging potential (Fig. 7). DPPH activity order at all concentrations was AgNP>ZnONP>CeNP. When the concentration increased from 12.5 mg/L to 50 mg/L, the scavenging activities of AgNP, CeNP and ZnONP were increased from 73,75% to 88,06%, from 57,62% to 67,43% and from 63,63% to 71,38%, respectively. In addition, DPPH activities of AgNP, CeNP, ZnONP, Ascorbic acid and Trolox at a concentration of 200 mg/L were 93,59%, 73,04%, 77,47, 100% and 100%, respectively. In the present study, DPPH activity results show that DPPH activity was dose depended manner and importantly elevated with the concentration of nanoparticles. An increase in the antioxidant activity of nanoparticles with increasing concentration has also been reported in previous studies [18], [19]. The effect of NPs with antioxidant properties on DPPH is thought to be because of their hydrogen donating capabilities [20]. According to our DPPH activity results, it was determined that the synthesized nanoparticles had effective DPPH activity. In particular, AgNP exhibited activity close to the standards with 93% DPPH scavenging activity at 200 mg/L concentration. Farias et al. [21] evaluated antioxidant activity of CeNP, and they noticed that it showed an average antioxidant activity with 15,06%. In our results, 57,62% antioxidant activity was observed even at the lowest concentration (12.5 mg/L). Therefore, our results showed better results than the aforementioned study. Mahabadi et al. [22] biosynthesed of $CeO_2$ NPs and they evaluated its antioxidant activity. As a result of their study the maximum antioxidant activities were seem that at 100 µg/mL concentration with 69,8%. Our antioxidant activity results for the green synthesis CeNP had similar results for the aforementioned study. Ameen et al. [23] synthesized AgNPs using fungal extract and investigated their antioxidant activity. They found that its maximum DPPH activity was 78%. The antioxidant activity results of AgNP in the presented study are quite good compared to the mentioned study. Gur et al., [24] synthesized biogenic ZnO NPs and evaluated its antioxidant activity. They reported that DPPH activity of ZnO NP at 250 µg/mL concentration was 79,67%. In the study, 77,47% DPPH activity was observed at 200 mg/L concentration and it had similar results compared to the mentioned study. The new synthesized nanoparticles can be used as an antioxidant agent with effective DPPH activity, and as a result, it can protect normal cells from the harmful effects of ROS.
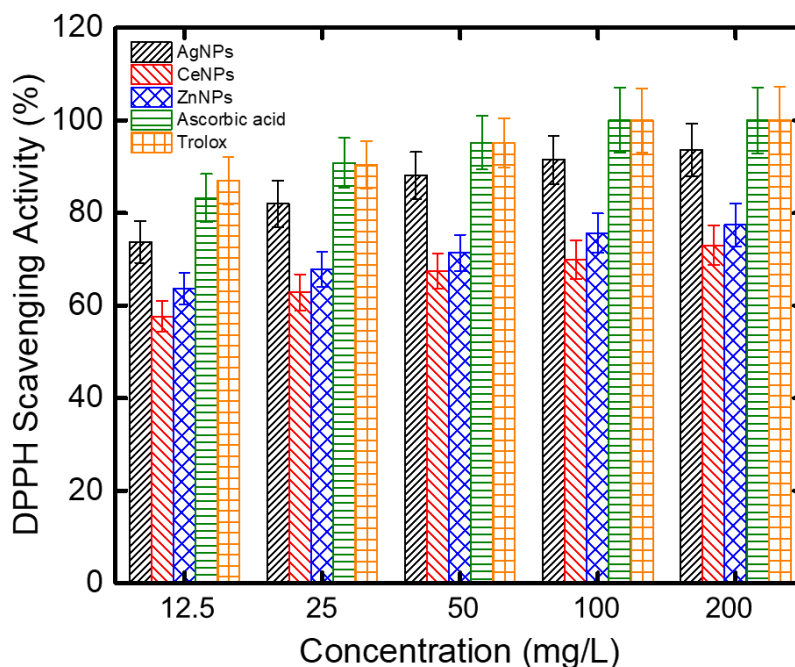
**Fig. 7.** DPPH scavenging activity of AgNP, CeNP and ZnONP.

### 3.3. Ferrous Ion Chelating Activity

Ferrous ion chelating method was also used to investigate the antioxidant activity of the synthesized nanoparticles. The ferrous chelating activity of AgNP, CeNP and ZnONP were demonstrated in Fig. 8. EDTA was used as standard. As can be clearly seen in the figure, the chelating activity of nanoparticles increased in parallel with the concentration. The chelating activity of AgNP, ZnONP and CeNP increased from 67,90% to 81,91%, 36,86% to 75,23%, and 29,94% to 70,40%, respectively, when the concentration increased from 12,5 to 100 mg/L. The chelating activity of AgNP, ZnONP and CeNP at 200 mg/L were 88,08%, 82,96% and 78,25%, respectively. When the metal chelating activities of the green synthesized nanoparticles were compared, the chelating activities were EDTA>AgNP> ZnONP>CeNP at the all tested concentrations. AlSalhi et al. [25] synthesized AgNPs using plant derived and studied in vitro antioxidant activity such as DPPH, ferrous ion chelation activity. They noticed that AgNPs showed ranged from 21,90 to 82,49% chelation activity at 10–100 µg/mL concentration. Our results displayed similar results with the aforementioned investigation. Soren et al. [26] synthesized ZnO NPs by polyol and aqueous method and they reported that they showed ferrous chelating ability. The surplus of free radicals in the body causes oxidative stress, and when the body's antioxidative system is weakened, biomolecules are damaged. Molecules with antioxidant properties extinguish these surplus free radicals in the body [26]. Therefore, the antioxidant behavior of the synthesized nanoparticles is important in order to protect our body from diseases caused by oxidative stress. According to result of metal chelating activity green synthesized and characterized AgNP, ZnONP and CeNP can be used as a metal chelating agent after further studies.
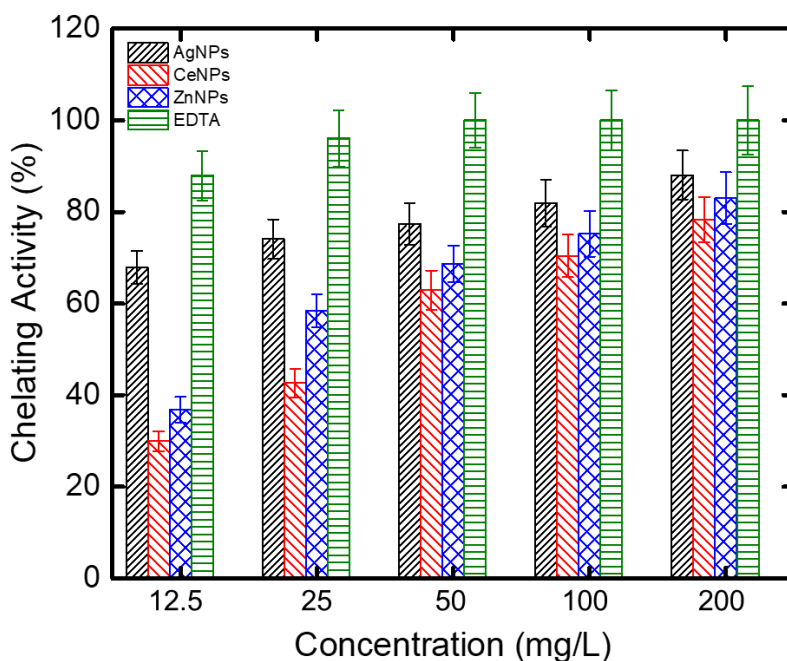
**Fig. 8.** Ferrous chelating activity of AgNP, CeNP and ZnONP.

**3.4. DNA Cleavage Ability**

In order to investigate the DNA nuclease effect of new AgNP, ZnONP and CeNP, pBR322 DNA was used as a goal. The efficiency of nanoparticles was tested by agarose gel electrophoresis. Electrophoresis gel image of the study is given in Fig. 9. As can be seen in the Fig. 9, single strand break occurred in supercoiled DNA for all studied three concentrations with the all synthesized nanoparticles. There was a transition from Form I to Form II (Lane 2-4, Lane 5-7 and Lane 8-10). DNA cleavage study results clearly revealed the effect of synthesized NP's on DNA. When we considered our DNA fragmentation results and other results including antimicrobial, cell viability and biofilm inhibition activity, we can be concluded that nanoparticles may have been exhibited antimicrobial activity by also acting on DNA molecules. DNA cleavage efficacy of nanoparticles has been demonstrated in previous studies. Gonca et al. [27] synthesized AgNPs using *Verbascum thapsus* leaf and the green synthesized AgNP demonstrated DNA cleavage activity. De et al. [28] reported that ZnONPs synthesized by the green synthesis method showed 55% DNA nuclease activity towards *E. coli* DNA. Generally, the results suggest that extracellular green synthesized AgNP, ZnONP and CeNP mediated-thermophilic *Anoxybacillus* sp. ST7 can be used as chemical nuclease for medicine industries after further studies.
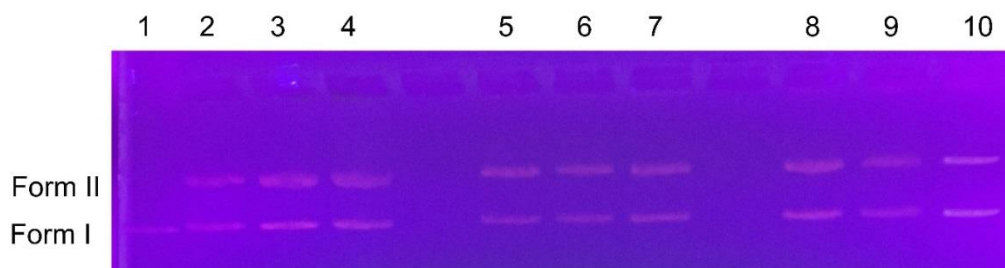
**Fig. 9.** DNA cleavage activity of AgNP, ZnONP and CeNP (Lane 1, pBR 322 DNA + 50 mg/L *Anoxybacillus sp.* ST7 mediated-AgNP; Lane 2, pBR 322 DNA + 100 mg/L of *Anoxybacillus sp.* ST7 mediated-AgNP*;* Lane 3, pBR 322 DNA + 200 mg/L *Anoxybacillus sp.* ST7 mediated-AgNP; Lane 5, pBR 322 DNA + 50 mg/L *Anoxybacillus sp.* ST7 mediated- CeNP; Lane 6, pBR 322 DNA + 100 mg/L of *Anoxybacillus sp.* ST7 mediated- CeNP; Lane 7, pBR 322 DNA + 200 mg/L *Anoxybacillus sp.* ST7 mediated- CeNP; Lane 9, pBR 322 DNA + 50 mg/L *Anoxybacillus sp.* ST7 mediated- ZnONP; Lane 10, pBR 322 DNA + 100 mg/L of *Anoxybacillus sp.* ST7 mediated- ZnONP; Lane 11, pBR 322 DNA + 200 mg/L *Anoxybacillus sp.* ST7 mediated- ZnONP).

## 3.5. Antimicrobial Activity

Diseases caused by microorganisms is a public health problem. Especially, as a result of improper utilise of antibiotics the emergence of drug-resistant microorganisms is the important concern all over the world. NPs have been noticed in the studies as a promising improvement of health produces. In the present study, antibacterial activity of new synthesized nanoparticles was studied against Gram +ve and Gram -ve bacterium and fungal strains by micro dilution method. Antimicrobial activity results are presented in Table 1. The results displayed the MIC value of AgNP, CeNP and ZnONP against selected microorganisms was varied and this variability depends upon the bacterial strains. The AgNP had strong antibacterial activity compared to CeNP and ZnONP. The MIC values of AgNP were 16 mg/L against *E. coli*, *E. hirae* and *E. fecalis*, 32 mg/L against *L. pneumophila* subsp. *pneumophila, S. aureus, C. parapisilosis,* and *C. tropicalis*, and 64 mg/L against *P. aeruginosa*. The MIC values of ZnO were found as 64 mg/L against *E. fecalis,* 128 mg/L against *E. coli*, *E. hirae*, *S. aureus, C. parapisilosis,* and *C. tropicalis*, 256 mg/L against *P. aeruginosa* and 512 mg/L against *L. pneumophila* subsp. *pneumophila*. When the MIC values for CeNP were examined, it was observed that it had a weaker antimicrobial effect compared to the other new synthesized two nanoparticles. According to our results, we can indicate that all three nanoparticles were more effective on Gram +ve bacteria than Gram -ve and fungi. Al-Otibi et al. [29] were synthesized silver nanoparticles using *Malva parviflora* and they reported that the biosynthesized AgNPs effectively reduced the mycelial growth of various fungus. Sharmila et al. [19] synthesized ZnO NPs using *Tecoma castanifolia* and evaluated its antibacterial activity against *E. coli*, *B. subtilis*, *S. aureus*, and *P. aeruginosa*. They reported that ZnO NPs exhibited good antibacterial activity towards all the studied bacterial strains. Similarly, Wang et al. [30] showed that coated $CeO_2$ NPs remarkably inhibited with 55.14% the growth of *P. aeruginosa*. Also, they expressed that PAA (polyacrylic acid)-coated $CeO_2$ NPs could be potential newly materials for various antibacterial implementations. Moreover, ceria NPs have been extensively studied for a diversity of potential implementations in different area, including nanomedicine [31]. Bellio et al. [31] investigated the use of $CeO_2$ NPs as an adjuvant to increase the effect of antibiotics, and as a result, they reported that the antibacterial capability of beta-lactam antibiotics towards *K. pneumoniae* increased when combined with $CeO_2$ NPs. In another study, Kumar et al. [32]

259

synthesized $CeO_2$ NP using secondary plant metabolite Tannic acid. They reported that synthesized $CeO_2$ NPs showed good antimicrobial activity against *B. subtilis* and *E. coli* and indicated that the toxicity of $CeO_2$ NP could be due to the generation of reactive oxygen species (ROS). In the presented study, it can be said that the antimicrobial activities of the synthesized NPs may be due to the generation of ROS. According to the results, also it may use in biomedical and biotechnology areas in the improvemet of a newly nano biomaterial for clinical implementations as a drug candidate in future.

**Table 1.** The MIC of studied microorganisms.
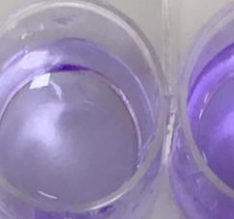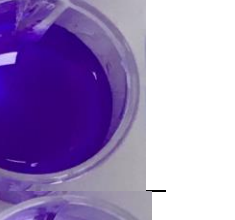
| Microorganisms | Ag | Ce | ZnO |
|---|---|---|---|
| *E. coli* | 16 | 1024 | 128 |
| *P. aeruginosa* | 64 | 512 | 256 |
| *L. pneumophila* **subsp.** *pneumophila* | 32 | 1024 | 512 |
| *E. hirae* | 16 | 512 | 128 |
| *E. fecalis* | 16 | 512 | 64 |
| *S. aureus* | 32 | 512 | 128 |
| *C. parapisilosis* | 32 | 1024 | 128 |
| *C. tropicalis* | 32 | 512 | 128 |

* mg/L

### 3.6. Biofilm Inhibition Capability

Biofilms are described as structured bacterial communities sticked to biological or abiotic surfaces. Biofilms have turn into even more important today because bacteria in biofilms have been shown to be more resistant to antibiotics than individual forms. Biofilm-associated infections affect many people worldwide and causing death. Hence, the need for more efficient compounds such as biogenic effective nanoparticles has received more attention [33]. Regarding the higher ability of *P. aeruginosa* and *S. aureus* to create a biofilm, these strains were selected for present study. The activities of various concentrations of new synthesized AgNP, CeNP and ZnONP nanoparticles on biofilm generation was appraised by monitoring the binding of the CV to attached cells in 24 well plates. As seen in Fig. 10 and 11, this directly reflects the efficacy of biofilm generation. In accordance with the results of biofilm formation inhibition against *S. aureus* (Fig. 10) and *P. aeruginosa* (Fig. 11), the percent inhibition order of nanoparticles at all studied concentrations was AgNP>ZnONP>CeNP. It was also observed that the biofilm inhibition activity was concentration dependent. When the concentrations increased from 100 to 250 mg/L, the percentage inhibitions of biofilm formation by AgNP, CeNP and ZnONP against *S. aureus* increased from 66,7% to 84.2%, from 2,29% to 5,4% and from 69,3% to 81,7% and also the percentage inhibition of biofilm formation by AgNP, CeNP and ZnONP against *P. aeruginosa* increased from 78,5% to 98,63%, from 3,65% to 8,54% and from 35,67% to 48,74%, respectively. The biofilm inhibition activity towards *S. aureus* and *P. aeruginosa* were found as 98,6% and 100% for AgNP, 12,8% and 15,98% for CeNP and 92,6% and 82,63% for ZnONP at 500 mg/L concentration, respectively. Zamanpour et al. [33] were synthesized silver nanoparticles by biosynthesis process. They reported that synthesized NPs indicated good biofilm inhibition activity towards *E. coli* and *P. aeruginosa*. Ishwarya et al. [34] reported that synthesized ZnO NP by green synthesis method inhibited bacterial biofilm formation of different bacteria including *E. coli, P. vulgaris*, *B. pumilis* and *B. licheniformis*. Altaf et al. [35] synthesized $CeO_2$ NPs using *Acorus calamus* aqueous extract and studied its antibiofilm activity towards various microorganisms containing *E. coli*, *S. aureus,* and *P. aeruginosa*. They reported that the biofilm

formation of tested bacterium inhibited by more than 75% by the treatment with CeNPs. Rajivgandhi et al. [36] synthesized AgNPs and studied their antibiofilm inhibition activity against Methicillin-resistant coagulase negative Staphylococci (MR-CoNS). They reported that AgNPs could ensure a safer alternating to traditional antibiofilm agents against studied strain. Khan et al. [37] reported that ZnO, $SnO_2$ and $CeO_2$ NPs can be thinking as probable agents against Gr+ve bacterial infection. Biofilm is one of the new targets in the improving of newly antimicrobial entities, so the results we have obtained especially for Ag and ZnO nanoparticles are very valuable, and they can be utilized as biofilm inhibitory nanodrugs after further investigations.

| Nanoparticles | Concentrations | | | |
| --- | --- | --- | --- | --- |
| | 0 mg/L | 500 mg/L | 250 mg/L | 500 mg/L |
| AgNP | | | | |
| CeNP | | | | |
| ZnONP | | | | |
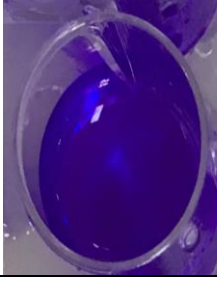
**Fig. 10.** Biofilm Inhibition of *S. aureus*.

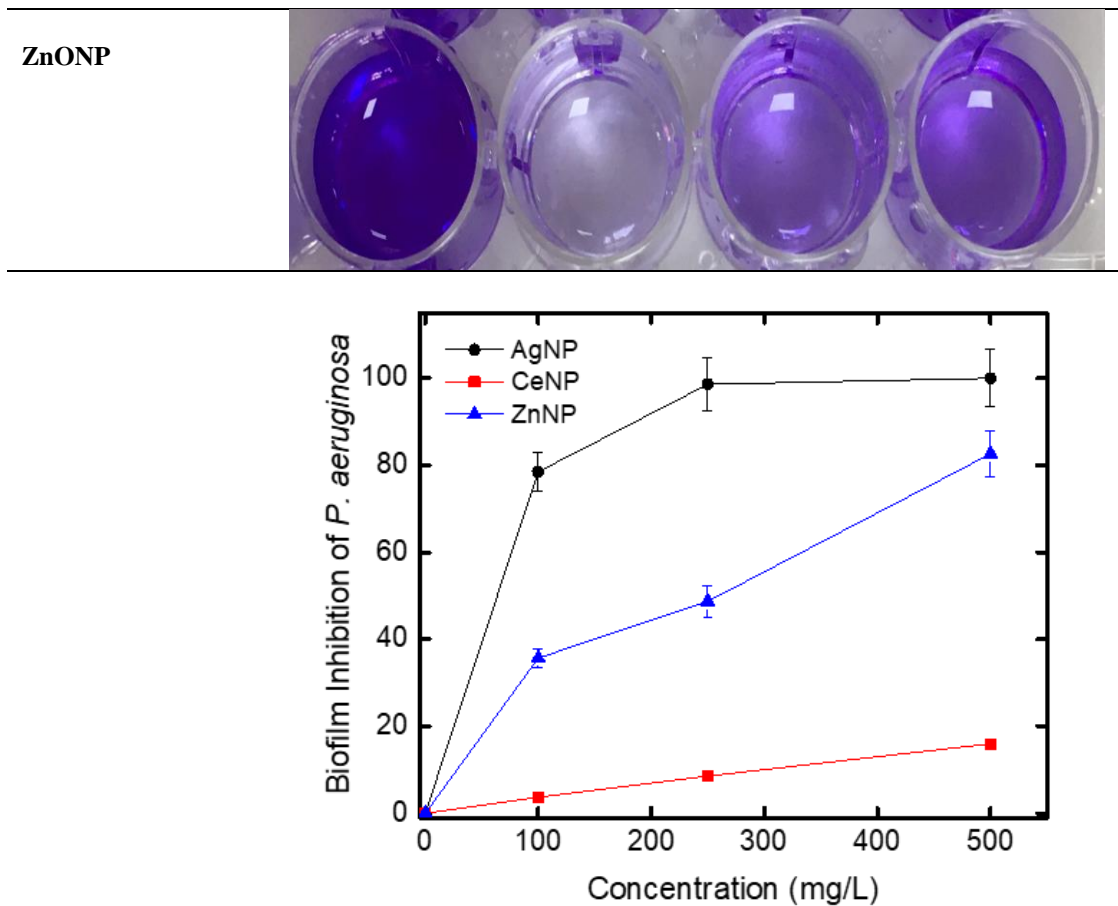| Nanoparticles | Concentrations | | | |
|---|---|---|---|---|
| | **0 mg/L** | **500 mg/L** | **250 mg/L** | **500 mg/L** |
| **AgNP** | | | | |
| **CeNP** | | | | |

| ZnONP |  |



**Fig. 11.** Biofilm Inhibition of *P. aeruginosa*

### 3.7. Microbial Cell Viability

In the present study, we also investigated the *E. coli* cell viability activity. The related results of the cell viability inhibition are showed in Fig. 12. According to our results, all three nanoparticles perfectly inhibited the *E. coli* viability. AgNP, CeNP and ZnONP inhibited the *E. coli* cell viability as 99,99%, 85,12%, and 99,84%, respectively. It was also determined that green synthesized AgNP, CeNP and ZnONP displayed excellent bacterial cell viability inhibition as 100,00 % at the concentration of 500 mg/L. The antibacterial activity mechanism of AgNP, CeNP, and ZnONP in the study can be considered as ZnONP. It's known that antibacterial capability by NPs was mostly because of release of ions, creation of ROS and adhering to bacterial cell membrane. Due to the dissolution and accumulation of NPs, the bacterial membrane permeability changes, causing the proton motive force to disperse [38].
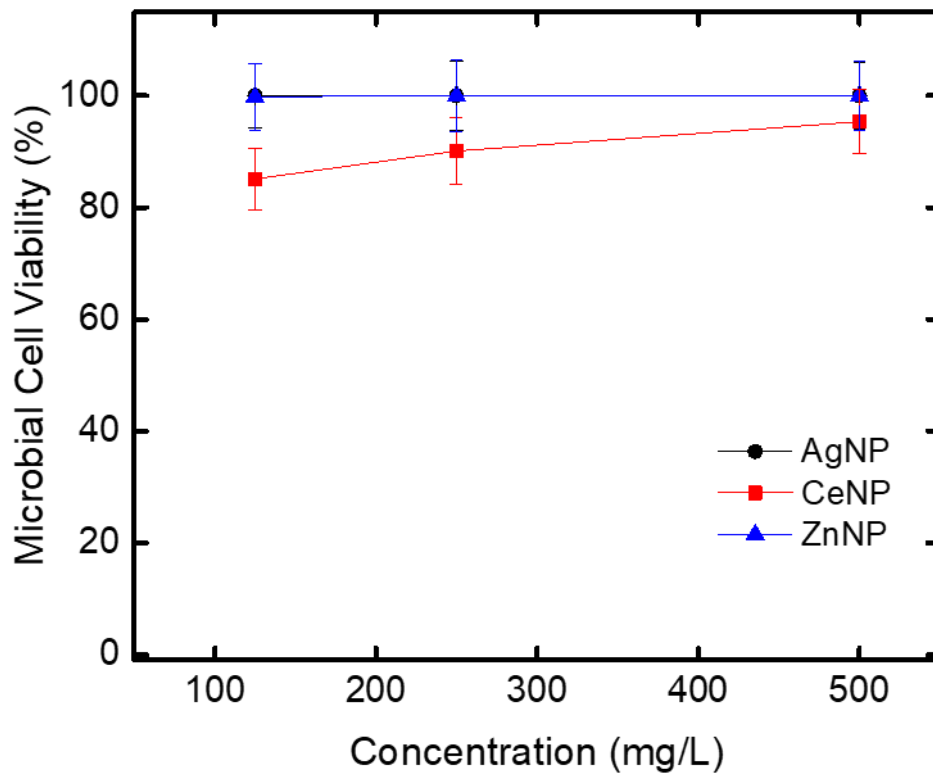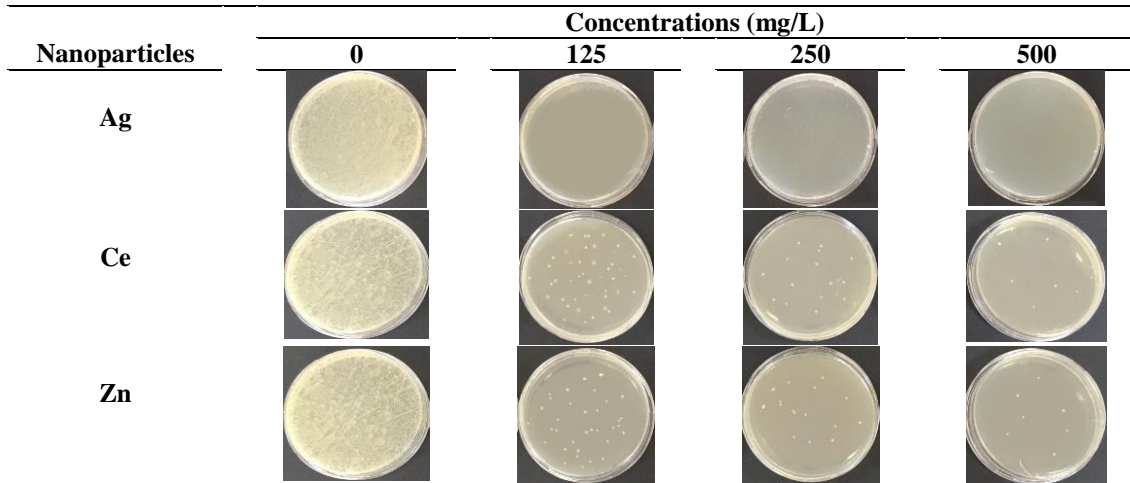
| Nanoparticles | Concentrations (mg/L) | | | |
|---|---|---|---|---|
| | 0 | 125 | 250 | 500 |
| Ag | | | | |
| Ce | | | | |
| Zn | | | | |





**Fig. 12.** Microbial cell viability.

## 4. CONCLUSION

In the presented study, the biological activity results of AgNP, ZnNP and CeNP synthesized extracellular from thermophilic *Anoxybacillus* sp. ST7 were also evaluated. In this context, antioxidant activity including DPPH and ferrous ion chelating activities, antimicrobial activity, DNA cleavage, cell viability and biofilm inhibition activity studies were conducted. When considering the pharmacological properties of nanoparticles, it is crucial to appraise all aspects including their medicinal features. It was determined that the synthesized nanoparticles had very effective DPPH and iron chelating activities. It exhibited effective chemical nuclease activity by creating a single strand break on *E. coli* plasmid DNA. Moreover, the nanoparticles were observed to be more effective on Gr +ve bacteria. It was observed that AgNP at 500mg/L concentration inhibited biofilm formation of *S. aureus* and *P. aeruginosa* close to 100%. In addition, highly effective cell viability results were determined. As a result, this study may supply beneficial details about the biomedical implementations of newly synthesis nanoparticles.

## REFERENCES

[1] Enderby, J. and Dowling, A., Nanoscience and nanotechnologies: Opportunities and Uncertainties, The Royal Society & The Royal Academy of Engineering Report, London, 2004.

[2] Ramsden J., Nanotechnology: An introduction, (ISBN: 978-0-08-096447-8) Elsevier, 2011.

[3] Lines M.G. (2008). Nanomaterials for Practical Functional Uses, Journal of Alloys and Compounds, 449, 242-245, 2008.

[4] Scenihr, The appropriateness of Existing Methodologies to Assess the Potential Risks Associated with Engineered and Adventitious Products of Nanotechnologies, Committee Opinion, 58-59, 2006.

[5] Ealias A.M., Saravanakumar M.P. A review on the classification, characterisation, synthesis of nanoparticles and their application, 14th ICSET-2017, IOP Conf. Series: Materials Science and Engineering 263 (2017) 032019 doi:10.1088/1757-899X/263/3/032019.

[6] Baig, N., Kammakakam, I., Falath W. (2021). Nanomaterials: a review of synthesis methods, properties, recent progress, and challenges, Mater. Adv, 2, 1821–1871.

[7] Duncan, T.V. (2011). Applications Of Nanotechnology In Food Packaging And Food Safety: Barrier Materials, Antimicrobials And Sensors. J Colloid Interface Sci 363(1): 1-24.

[8]   Kumar, A., Chisti, Y., Banerjee, U. (2013). Synthesis of metallic nanoparticles using plant extracts: Biotechnology Advances (31) 346–356.

[9]   Nematollahi, F. (2015). Silver nanoparticles green synthesis using aqueous extract of Salvia limbata C. A. Mey. Research Paper. International Journal of Biosciences ISSN: 2220-6655 (Print), 2222-5234(Online) http://www.innspub.net Vol. 6, No. 2, p. 30-35.

[10]  Stephen Inbaraj B and Chen BH. (2020) An overview on recent in vivo biological application of cerium oxide nanoparticles. Asian J Pharm Sci. 15(5):558–75.

[11]  [11] Eka Putri G, Rilda Y, Syukri S, Labanni A, Arief S.(2021) Highly antimicrobial activity of cerium oxide nanoparticles synthesized using *Moringa oleifera* leaf extract by a rapid green precipitation method. J Mater Res Technol. 15 :2355–64.

[12]  Cheon JY, Kim SJ, Rhee YH, Kwon OH, Park WH. (2019). Shape-dependent antimicrobial activities of silver nanoparticles. Int J Nanomedicine. 14: 2773–80.

[13]  Estevez MB, Raffaelli S, Mitchell SG, Faccio R, Alborés S. (2020). Biofilm eradication using biogenic silver nanoparticles. Molecules. 25(9): 1-14.

[14]  Ruiz AL, Garcia CB, Gallón SN, Webster TJ. (2020). Novel silver-platinum nanoparticles for anticancer and antimicrobial applications. Int J Nanomedicine. 15: 169–79.

[15]  Mishra PK, Mishra H, Ekielski A, Talegaonkar S, Vaidya B. (2017). Zinc oxide nanoparticles: a promising nanomaterial for biomedical applications. Drug Discov Today. 22(12):1825–34.

[16]  Ağırtaş MS, Karatas C, Özdemir S. (2015). Synthesis of some metallophthalocyanines with dimethyl 5- (phenoxy) -isophthalate substituents and evaluation of their antioxidant-antibacterial activities. Spectrochimica Acta Part A : Molecular and Biomolecular Spectroscopy. 135:20–4.

[17]  Dinis T.C.P, Madeira V.M.C, Almeida L.M. (1994). Action of phenolic derivatives (acetaminophen, salicylate, and 5-aminosalicylate) as inhibitors of membrane lipid peroxidation and as peroxyl radical scavengers, Arch. Biochem. Biophys. 315; 161-169.

[18]  Raghava S, Munnene Mbae K, Umesha S. (2021). Green synthesis of silver nanoparticles by Rivina humilis leaf extract to tackle growth of *Brucella* species and other perilous pathogens. Saudi J Biol Sci. 28(1):495–503.

[19]  Sharmilaa G, Thirumarimurugan M, Muthukumarana C. (2019) Green synthesis of ZnO nanoparticles using *Tecoma castanifolia* leaf extract: Characterization and evaluation of its antioxidant, bactericidal and anticancer activities. Microchemical Journal. 45: 578-587.

[20] Shejawal KP, Randive DS, Bhinge SD, Bhutkar MA, Wadkar GH, Jadhav NR. (2020). Green synthesis of silver and iron nanoparticles of isolated proanthocyanidin: its characterization, antioxidant, antimicrobial, and cytotoxic activities against COLO320DM and HT29. J Genet Eng Biotechnol. 18(43), 1-11.

[21] Farias IAP, Santos CCL, Xavier AL, Batista TM, Nascimento YM, Nunes JMFF, Silva PMF, Menezes-Júnior RA, Ferreira JM, Lima EO, Tavares JF, Sobral MV, Keyson D, Sampaio FC. (2021). Synthesis, physicochemical characterization, antifungal activity and toxicological features of cerium oxide nanoparticles. Arab J Chem. 14 (1), 102888.

[22] Mahabadi AG, Mirzakhani A, Azizi A, Chavoshi S, Khaghani S.(2021). Extracts of *Pelargonium hortorum*: A natural and efficient fluid for fast and eco-friendly biosynthesis of CeO$_2$ nanoparticles for antioxidant and photocatalytic applications. Inorg Chem Commun. 127, 108553.

[23] Ameen F, Al-Homaidan AA, Al-Sabri A, Almansob A, AlNAdhari S. (2021). Anti-oxidant, anti-fungal and cytotoxic effects of silver nanoparticles synthesized using marine fungus *Cladosporium halotolerans*. Appl Nanosci. 1-9.

[24] Gur T, Meydan I, Seckin H, Bekmezci M, Sen F. (2022). Green synthesis, characterization and bioactivity of biogenic zinc oxide nanoparticles. Environ Res. 204 (Part A):111897.

[25] AlSalhi MS, Elangovan K, Ranjitsingh AJA, Murali P, Devanesan S. (2019). Synthesis of silver nanoparticles using plant derived 4-N-methyl benzoic acid and evaluation of antimicrobial, antioxidant and antitumor activity. Saudi J Biol Sci. 26 (5):970–8.

[26] Soren S, Kumar S, Mishra S, Jena PK, Verma SK, Parhi P. (2018). Evaluation of antibacterial and antioxidant potential of the zinc oxide nanoparticles synthesized by aqueous and polyol method. Microb Pathog. 119 :145–51.

[27] Gonca S, Arslan H, Isik Z, Özdemir S, Dizge N. (2021). The surface modification of ultrafiltration membrane with silver nanoparticles using *Verbascum thapsus* leaf extract using green synthesis phenomena. Surfaces and Interfaces. 26:101291.

[28] De A, Das R, Kaur H, Jain P. (In Press). Synthesis, physicochemical investigations, DNA cleavage activity of biogenic zinc oxide nanoparticles and their interaction with Calf-Thymus DNA. Mater Today Proc. 1–5.

[29] Al-Otibi F, Perveen K, Al-Saif NA, Alharbi RI, Bokhari NA, Albasher G, Al-Otaibi RM, Al-Mosa MA. (2021). Biosynthesis of silver nanoparticles using *Malva parviflora* and their antifungal activity. Saudi J Biol Sci. 28(4):2229–35.

[30] Wang Q, Perez JM, Webster TJ. (2013). Inhibited growth of *Pseudomonas aeruginosa* by dextran- and polyacrylic acid-coated ceria nanoparticles. Int J Nanomedicine. 8:3395–9.

[31] Bellio P, Luzi C, Mancini A, Cracchiolo S, Passacantando M, Di Pietro L, Perilli M, Amicosante G, Santucci S, Celenza G. (2018). Cerium oxide nanoparticles as potential antibiotic adjuvant. Effects of $CeO_2$ nanoparticles on bacterial outer membrane permeability. Biochim Biophys Acta-Biomembr. 1860(11):2428–35.

[32] Kumar KM, Mahendhiran M, Diaz MC, Hernandez-Como N, Hernandez-Eligio A, Torres-Torres G, Godavarthi S, Gomez LM. (2018). Green synthesis of $Ce^{3+}$ rich $CeO_2$ nanoparticles and its antimicrobial studies. Mater Lett. 214:15–9.

[33] Zamanpour N, Mohammad A, Mashreghi M, Shahnavaz B. (2021). Bioorganic Chemistry Application of a marine luminescent *Vibrio* sp . B4L for biosynthesis of silver nanoparticles with unique characteristics, biochemical properties, antibacterial and antibiofilm activities. Bioorg Chem.; 114:1–12.

[34] Ishwarya R, Vaseeharan B, Kalyani S, Banumathi B, Govindarajan M, Alharbi NS, Kadaikunnan S, Al-anbr MN, Khaled JM, Benelli G. (2018). Facile green synthesis of zinc oxide nanoparticles using *Ulva lactuca* sea weed extract and evaluation of their photocatalytic, antibiofilm and insecticidal activity, J. Photochem. Photobiol. B Biol. 178:249–258.

[35] Altaf M, Manoharadas S, Zeyad MT. (2021) .Green synthesis of cerium oxide nanoparticles using *Acorus calamus* extract and their antibiofilm activity against bacterial pathogens. Microsc Res Tech. 84(8):1638–48.

[36] Rajivgandhi G, Maruthupandy M, Muneeswaran T, Anand M, Quero F, Manoharan N, et al. (2019). Biosynthesized silver nanoparticles for inhibition of antibacterial resistance and biofilm formation of methicillin-resistant coagulase negative Staphylococci. Bioorg Chem. 2019;89 (March):103008.

[37] Khan F, Lee JW, Pham DNT, Khan MM, Park SK, Shin IS, Kim YM. (2020). Antibiofilm Action of ZnO, $SnO_2$ and $CeO_2$ Nanoparticles Towards Grampositive Biofilm Forming Pathogenic Bacteria. Recent Pat Nanotechnol. 14(3):239-24.

[38] Basumatari M, Devi RR, Gupta MK, Gupta SK, Raul PK, Chatterjee S, Dwivedi SK. (2021). Musa balbisiana Colla pseudostem biowaste mediated zinc oxide nanoparticles: Their antibiofilm and antibacterial potentiality. Curr Res Green Sustain Chem. 4 (December 2020):100048.

*RESEARCH ARTICLE*

# THE USE of BLACK COLORANT OBTAINED from DOMESTIC SOURCES in LEADED and BORON GLAZES

Hale YILDIZAY [1], Fikret AYDOĞDU[2]

[1]Kütahaya Dumlupınar University, Kütahya Fine Arts Vocational School, Department of Tile Art and Design, Kütahya,
hale.yildizay@dpu.edu.tr, ORCID: 0000-0002-3896-9912
[1]Kütahaya Dumlupınar University, Kütahya Fine Arts Vocational School, Department of Tile Art and Design, Kütahya,
fikret.aydogdu@dpu.edu.tr, ORCID:0000-0001-8514-0405

## ABSTRACT

In this study, the usability of the black colorant obtained by mixing of MHP composite produced from laterittic nickel, chromite and magnetite ores in certain proportions, in boron and leaded glazes was investigated. Prepared black colorant was added to leaded and boron glaze in varying proportions. The color properties of the colored glazes were measured by spectrophotometer and their values are expressed as "L * a * b *". It has been determined that the color values of this colorant used in leaded and boron glazes are quite similar to commercially used black pigments. As a result, black colorants with high added value were produced with the use of domestic resources and positive results were obtained in their use in leaded and boron glazes.

**Keywords:** *Boron glaze, Leaded glaze, Raw material, Coloring, Characterization*

## 1. INTRODUCTION

The glaze is a glass or glassy structure that melts on the ceramic body surface covering it in a thin form [1]. Specially prepared inorganic synthetic pigments containing natural raw materials, metal oxides or multiple metal oxides are used in the coloring of ceramic glazes. Pigments do not melt in glaze composition and disperse in small grains in the glaze, maintaining their crystal structure [2].

Black color has a 25% share in total pigment consumption in the world [3]. The use of pure oxides in the production of black pigments increases the cost of black colored glazes (4). There are some studies on the production of black pigments with natural raw materials (5) and / or wastes containing precious metals (6) that are cheaper than pure oxides in order to reduce the pigment cost (7). The color performances of black pigments produced in these studies were examined in different glazes.

The production of black pigments used in glazes usually consists of mixtures of iron, cobalt, chromium, nickel, magnesium, and copper oxides in certain proportions (8). Cr-Fe hematite pigments are widely used for black color in some of the glazes (9), while Co-Fe-Cr, Fe-Mn (10) and Ni-Fe-Cr spinel pigments (11) with high thermal and color stability are used in others.

For this purpose, in our study, a new coloring composition was prepared by mixing MHP composite, magnetite and chromite mineral which produced in our country. MHP composite is preferred in the study because it contains high levels of nickel and cobalt oxide. The MHP composite used in the study is produced in our country by acid dissolving (HPAL) method under high pressure, which is the state-of-the-art application of the most efficient hydrometallurgical acquisition method [12].

In this study, the effects of adding the inorganic black colorant obtained by mixing the MHP composite obtained from laterittic nickel ore extracted, chromite, and magnetite mineral in our country to leaded and boron glazes were examined.

## 2. EXPERIMENTAL METHOD

### 2.1. Raw Materials
In the production of colorants; magnetite mineral as iron oxide source was provided from Ferromad mining company in Kutahya, Hisarcik district. Chromite mineral as chromium oxide source was provided from Hayri Ogelman mining company located in Bursa Harmancik district.

In addition, the MHP composite, which guides the study differently; it was used as source of nickel and cobalt oxide and supplied as raw material from Meta Nickel Cobalt company in the Manisa Gördes region. Leaded, boron glazes and their bodies used for colorant trials were obtained from Sedef Handicraft.

The commercial black pigment CK13074 (Ferro Corporation), CP 30 (Itaca S.A.) used in ceramic and tile coloring are taken as reference pigment in this study.

### 2.2 Chemical Analysis Results
Chemical analysis (XRF) before starting to work on the raw materials used, melting of samples was carried out in panalytical Eagon 2 model device, chemical analysis was carried out on Panalytical brand Axios MAX model device (Table 1).

**Table 1.** Chemical analysis of raw materials used in colorant production

| Oxides (%) | Chromite | Magnetite | MHP composite |
|---|---|---|---|
| $SiO_2$ | 10,61 | 2,98 | 0,6 |
| $Al_2O_3$ | 5,22 | 0,95 | 0,34 |
| $Fe_2O_3$ | 20,57 | 89,93 | 0,3 |
| CaO | 0,23 | 1,51 | |
| MgO | 20,64 | 3,91 | 3,91 |
| $Co_3O_4$ | - | - | 3,97 |
| CuO | - | - | 0,34 |
| $Na_2O$ | - | - | 0,07 |
| $TiO_2$ | 0,14 | 0,03 | - |
| $Cr_2O_3$ | 39,56 | - | - |
| $As_2O_3$ | | 0,43 | - |
| $V_2O_5$ | | 0,27 | - |
| $P_2O_5$ | - | 0,09 | - |
| ZnO | 0,12 | - | 0,76 |
| MnO | 0,26 | - | 7,21 |
| NiO | 0,17 | - | 82,5 |
| $SO_3$ | 0,02 | 0,11 | - |
| L.O.I[*] | 0,98 | 0,57 | - |

**L.O.I**[*]: Loss on ignition

### 2.3. Colorant Production

In this study, black colorant synthesis was made using magnetite, chromite and MHP composite raw materials. In the first stage the chromite, magnetite and MHP composite were grinded and then dried. It was determined that 40% chromite, 40% magnetite and 20% MHP composite mixture were the most suitable coloring mixture and studies continued in this direction (Table 2).

**Table 2.** Magnetite, chromite and MHP composite minerals used in colorant production. (%)

| | Magnetite | Chromite | MHP composite |
|---|---|---|---|
| Colorant (%) | 40 | 40 | 20 |

This raw coloring mixture prepared were added to the leaded and boron glazes in proportions of 10%, 15 and 20% and mixed and homogenized for 15 minutes using alumina balls in a jet mill. The coloring effect of leaded glaze and boron glaze is seen in the Figure 1 and Figure2, respectively.
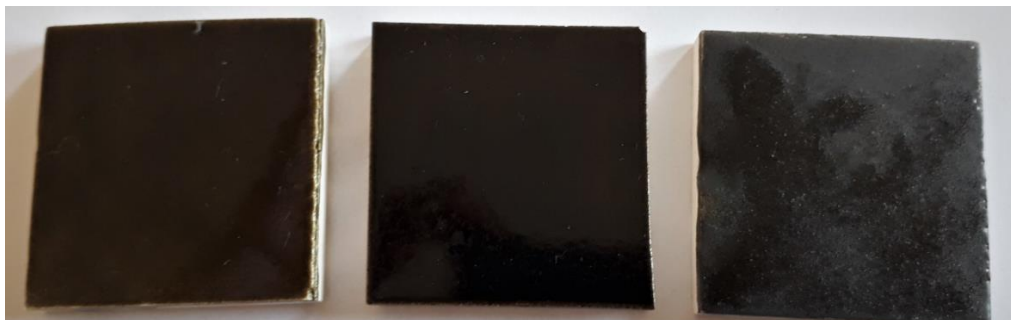
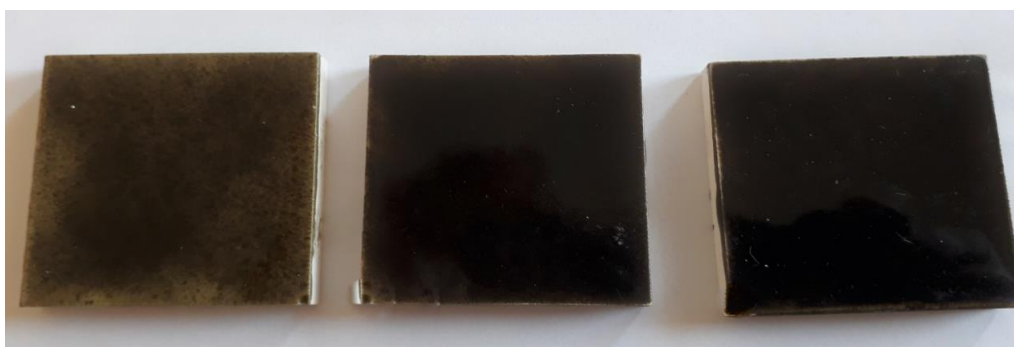**Figure 1.** 10%, 15% and 20% colorants addition into leaded glaze, respectively.



**Figure 2.** 10%, 15% and 20% colorants addition into boron glaze, respectively.

It has been observed that 15% and 20% colorant additions have a good effect on the formation of black color. Therefore, it is thought that 15% mixture is sufficient. Since it is thought that the use of excess colorants will lead to a cost increase, in the study were continued with the addition of 15% colorant.

The colorant obtained by applying heat treatment (calcination) to the colorant, which has a certain chemical composition and crystal structure, was stabilized. When heat is applied, the materials used in the formation of colorants react with each other, forming new chemical compounds and structures. Sometimes the unstable color table that occurs is due to the inability to adequately complete the reactions necessary for color formation. This instability is eliminated by the calcination process.

In the second stage colorant mixture (Table 2) was calcined at 1200ºC in the electric kiln. Porcelain crucibles were used for the calcination process and grinded after calcination. Then, the colorant was dried in the oven and added to the glazes.
The viscosity of the glazes was determined by using the ford cup viscometer. The viscosity of the prepared glazes is set to 15 sec and litre weight to 1450 g/l. The prepared calcined and non-calcined colorants were added to the glaze at a rate of 15%. These glazes were then applied to the body and fired in the laboratory in an electric kiln in the appropriate firing regime. The color effect of the non-calcined colorant (NCC) on leaded glaze is shown in Figure 3a and color effect of the calcined colorant (CC) on leaded glaze is shown in Figure 3b.
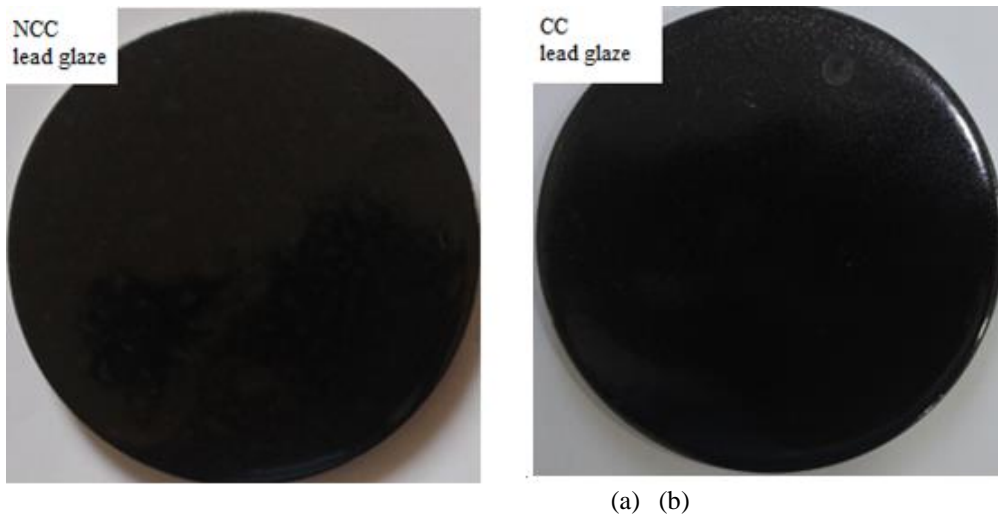
**Figure 3.** a) Color effect of the non-calcined colorant (NCC) on leaded glaze, b) Color effect of the calcined colorant (CC) on leaded glaze.

The color effect of the non-calcined colorant (NCC) on boron glaze is shown in Figure 4a and color effect of the calcined colorant (CC) on boron glaze is shown in Figure 4b.
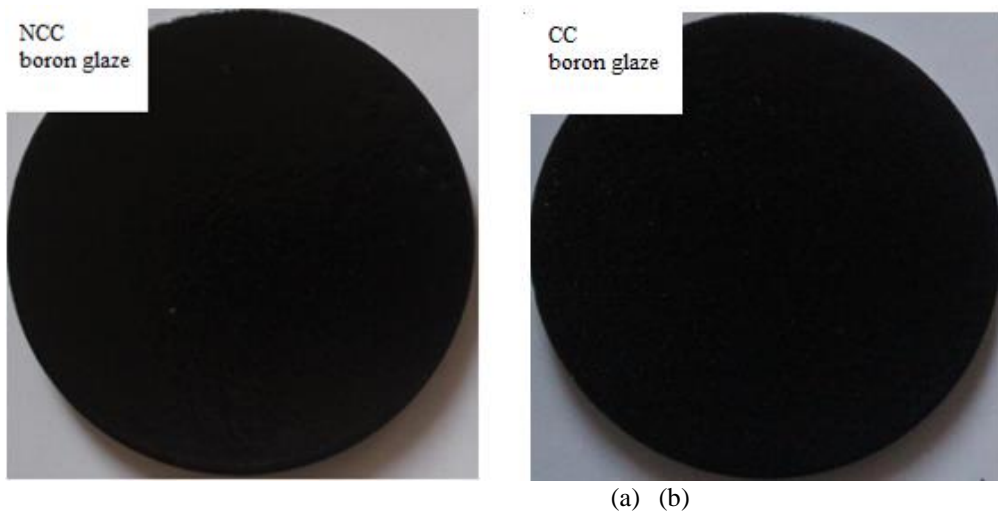


**Figure 4.** a) Color effect of the non-calcined colorant (NCC) on boron glaze, b) Color effect of the calcined colorant (CC) on boron glaze.

### 2.3. Microstructural Analysis

The morphological properties of the leaded and boron glaze samples were examined by the FEI NANO SEM 650. EDS analysis was performed with the EDAX-EDS device connected to a scanning electron microscope (SEM).

## 3. RESULTS

### 3.1. Color Analysis

Black pigment called Ferro CK13074, a supplier of glaze pigment found in our country, was used to compare the leaded and boron glazes used with black color characteristics. The color characteristics of all glazed bodies were measured. Color measurements of colored samples were made by Konica Minolta–Spectrophotometer CM-700d device. The results obtained are expressed in Table 3 as "L* a * b*" parameters. Based on the L*, a*, b* values of commercial black pigments, it is seen in Table 3 that the black pigment to be produced must have L*<31, a* <1, b* <1 values.

**Table 3.** Color values of pigment and colorant samples.

| Colored glazes | L | a | b |
|---|---|---|---|
| Ferro-CK13074 Leaded glaze | 31,06 | 0,13 | -0,58 |
| NCC leaded glaze | 30,52 | -0,09 | -0,45 |
| CC leaded glaze | 27,37 | 0,25 | 0,18 |
| Ferro-CK13074 Boron glaze | 30,47 | -0,05 | -0,4 |
| NCC boron glaze | 28,31 | -0,12 | 0,01 |
| CC boron glaze | 26,26 | 0,4 | 0,07 |

### 3.2. Microstructure Analysis

Microstructural appearance of the distribution of NCC crystals in leaded glaze are given in Figure 5a. In the microstructure images have detected crystals similar to butterfly. Image of butterfly-shaped of crystal in Figure 5b and EDS analysis of crystal is given in Figure 6.
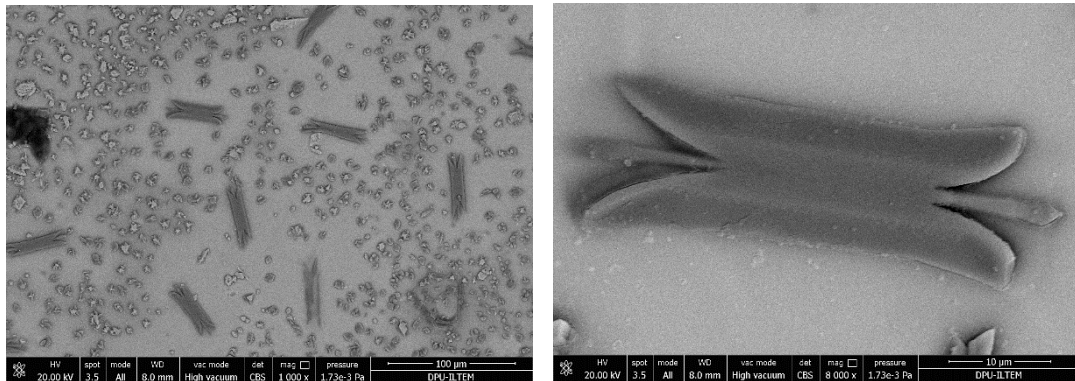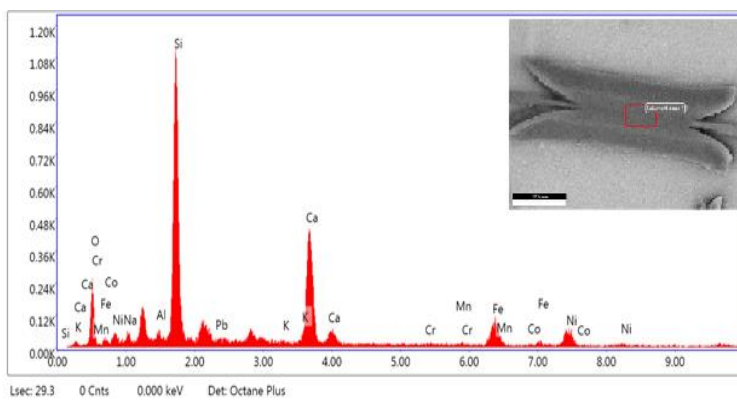
**Figure 5.** SEM microstructure image a) Distribution of NCC crystals in leaded glaze at the 1000X magnification b) NCC crystal in leaded glaze at 8000X magnification.



| Element | Weight (%) |
|---------|------------|
| $Na_2O$ | 0.63 |
| $Al_2O_3$ | 0.67 |
| $SiO_2$ | 42.07 |
| $PbO_2$ | 0.86 |
| $K_2O$ | 0.23 |
| CaO | 27.16 |
| $Cr_2O_3$ | 0.44 |
| MnO | 0.98 |
| $Fe_2O_3$ | 14.94 |
| CoO | 0.72 |
| NiO | 11.31 |

**Figure 6.** EDS analysis of NCC crystals in leaded glaze at 8000X (Fe, Cr, Ni, Pb, Mn and Co quantities on the glaze surface).

Microstructural appearance of the distribution of CC crystals in the leaded glaze are given in Figure 7a. In the microstructure images have detected crystals similar to tetragonal structures. Image of tetragonal-shaped of crystals in Figure 7b and EDS analysis of crystals are given in Figure 8.
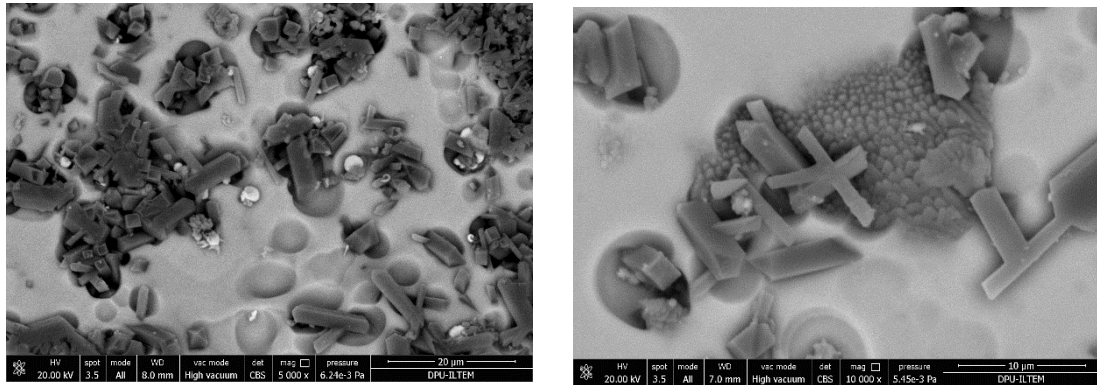
**Figure 7.** SEM microstructure image a) Distribution of CC crystals in leaded glaze at the 5000X magnification b) CC crystals in leaded glaze at 10000X magnification.
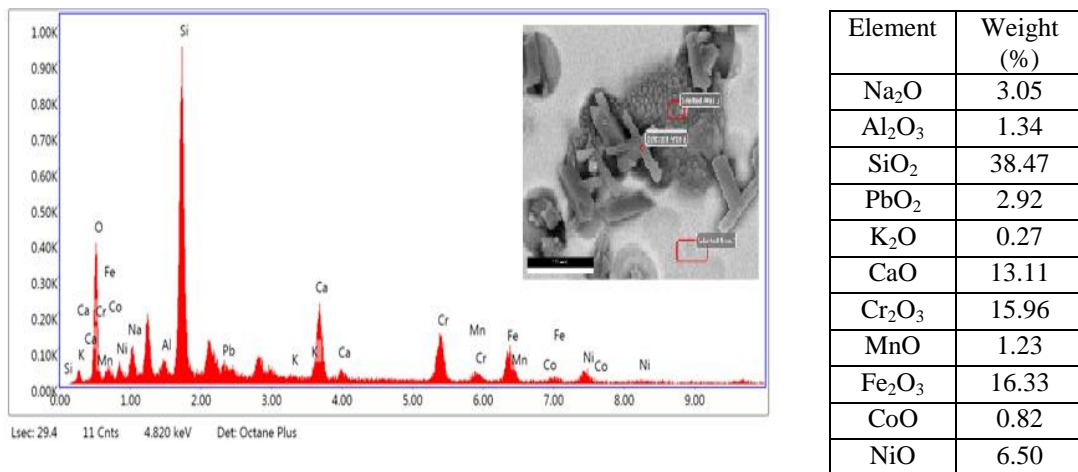


| Element | Weight (%) |
|---------|------------|
| $Na_2O$ | 3.05 |
| $Al_2O_3$ | 1.34 |
| $SiO_2$ | 38.47 |
| $PbO_2$ | 2.92 |
| $K_2O$ | 0.27 |
| $CaO$ | 13.11 |
| $Cr_2O_3$ | 15.96 |
| $MnO$ | 1.23 |
| $Fe_2O_3$ | 16.33 |
| $CoO$ | 0.82 |
| $NiO$ | 6.50 |

**Figure 8.** EDS analysis of CC crystals in leaded glaze at 1000X (Fe, Cr, Ni, Pb, Mn and Co quantities on the glaze surface).

Microstructural appearance of the distribution of NCC crystals in the boron glaze are given in Figure 9a. In the microstructure images have detected in some of the crystals needle-like structures. The needle-like shaped of crystals image are given in Figure 7b and EDS analysis of crystals are given in Figure 8.
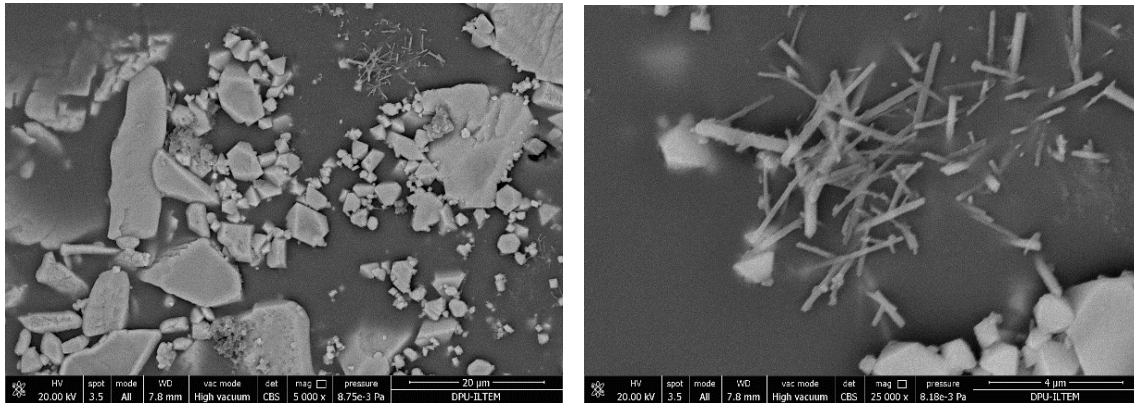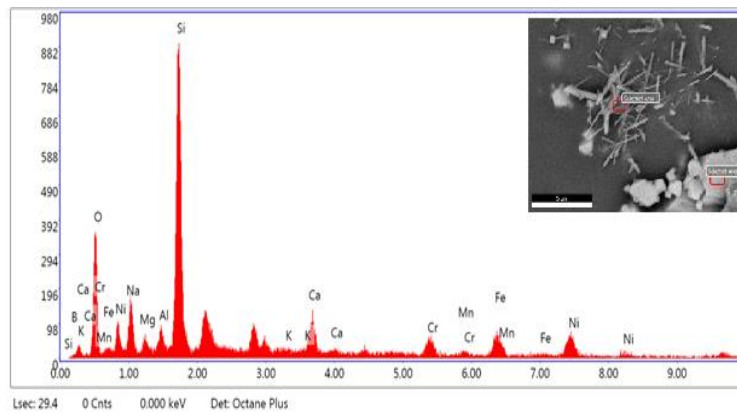
**Figure 9.** SEM microstructure image a) Distribution of NCC crystals in boron glaze at the 5000X magnification b) NCC crystal in leaded glaze at 25000X magnification.



| Element | Weight (%) |
|---------|------------|
| $B_2O_3$ | 17.42 |
| $Na_2O$ | 5.02 |
| $MgO$ | 0.61 |
| $Al_2O_3$ | 1.61 |
| $SiO_2$ | 38.61 |
| $K_2O$ | 0.51 |
| $CaO$ | 6.34 |
| $Cr_2O_3$ | 5.74 |
| $MnO$ | 0.66 |
| $Fe_2O_3$ | 10.56 |
| $NiO$ | 12.91 |

**Figure 10.** EDS analysis of NCC crystals in boron glaze at 25000X (B, Fe, Cr, Ni, Mn quantities on the glaze surface).

Microstructural appearance of the occurring NCC crystals in the boron glaze are given in Figure 11a. The image of the crystals is given in Figure 11b and EDS analysis of crystals are given in Figure 12.
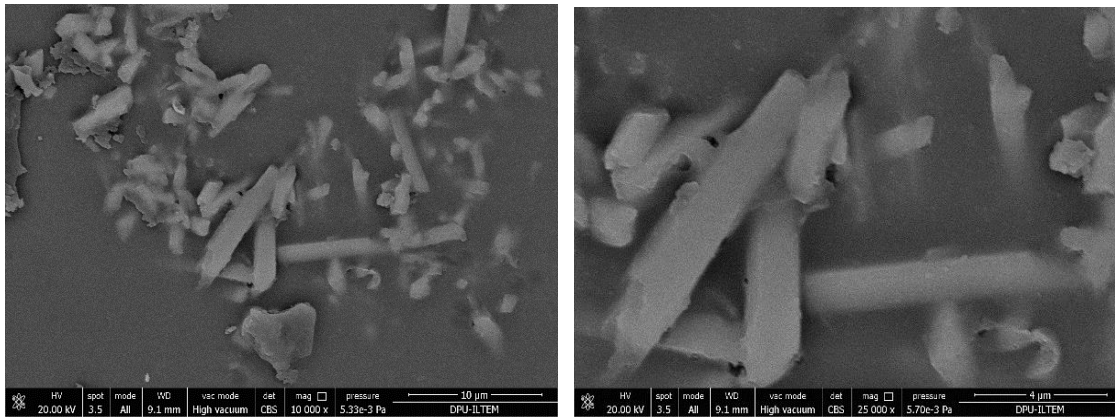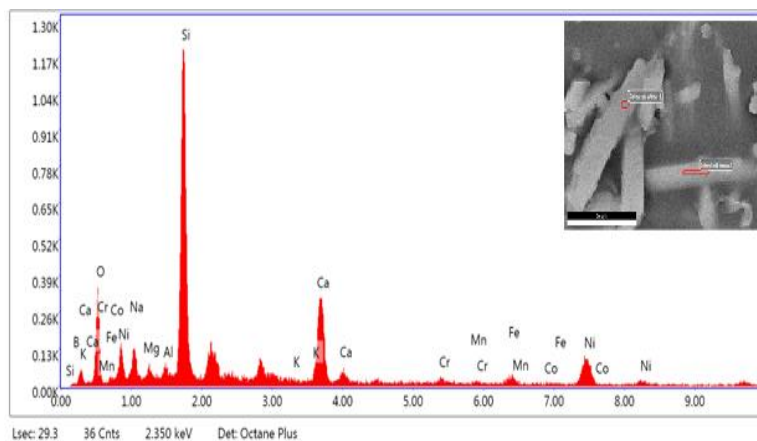
**Figure 11.** SEM microstructure image a) Distribution of CC crystals in boron glaze at the 10000X magnification b) CC crystal in leaded glaze at 25000X magnification.



| Element | Weight % |
|---|---|
| $B_2O_3$ | 15.55 |
| $Na_2O$ | 3.20 |
| $MgO$ | 0.77 |
| $Al_2O_3$ | 1.09 |
| $SiO_2$ | 39.49 |
| $K_2O$ | 0.50 |
| $CaO$ | 16.18 |
| $Cr_2O_3$ | 1.57 |
| $MnO$ | 0.86 |
| $Fe_2O_3$ | 3.86 |
| $CoO$ | 0.93 |
| $NiO$ | 16.00 |

**Figure 12.** EDS analysis of CC crystals in boron glaze at 25000X (B, Fe, Cr, Ni, Co, Mn quantities on the glaze surface).

## 4. DISCUSSION

In this study, the production ability of black colorants for leaded and boron glazes was examined using industrial products such as chromite, magnetite and laterittic nickel ore, the composition of which is stable.

In the prepared colorants, due to $Fe_2O_3$, $CoO$, $NiO$, and $Cr_2O_3$ containing of the raw materials used, a decrease in the L* (whiteness) value of the samples used in the leaded glazes compared to the leaded glazes using commercial pigments was observed. The highest decrease in L* value occurred in leaded

glaze using calcined colorant, with a decrease of 11.88% compared to the leaded glaze using commercial pigment, and the L* value was measured as 27.37.

A decrease was also observed in the L* (whiteness) value of the samples used in boron glazes. The highest decrease in L* value occurred in boron glaze with calcined colorant with a decrease of 13.81% compared to the boron glaze using commercial pigment, and the L* value was measured as 26.26.
It was observed that the b* (yellowness) value and a* (redness) values showed small change, and the obtained a and b values were less than 1.

Microstructure images and EDS analysis, it is seen that the crystals in the glazes have a heterogeneous distribution. In microstructure analysis, these crystals found in insoluble form within the glassy phase played an effective role in color formation. EDS analyzes show that their crystal structures are rich in $Fe_2O_3$, $NiO$, $Cr_2O_3$ and $CoO$. SEM-EDS results; the presence of chromium, iron, nickel and cobalt oxide ensured the acquisition of very good black tones in glazes.

As a result, the obtained colorant and calcination applied to this colorant positively affected the color parameters in the glaze compositions where the colorants were used and the color parameters similar to commercial black colorants were found. The colorants added to the glazes covered the body surface perfectly.

## ACKNOWLEGMENTS

## REFERENCES

[1] Arcasoy, A., (1983)., Seramik Teknolojisi. M.Ü.G.S.F. Seramik, İstanbul., ASD Yay., No:2, 13-14.

[2] Eppler, R.A., (2000)., Glazes and Glass Coatings, Am. Ceram. Soc., Westerville, 130-135.

[3] Costa, G., Della, V.P., Ribeiro, M.J., Oliveria, A.P.N., Monros, G., and Labrincha, J.A. (2008). Synthesis of black ceramic pigments from secondary raw materials. Dyes and Pigments, Vol.77, pp.137–144.

[4] Tanisan, B., and Turan, S. (2011). Black ceramic pigments for porcelain tile bodies produced with chromite ores and iron oxide waste. Journal of Ceramic Processing Research, Vol.12, 462-467.

[5] Ozel, E., Kücük, I., and Turan, S., (2002). Synthesis of an iron-chromium ceramic pigment by using limonite and chromite mixtures. Key Eng. Mater., Vol.206-213, 1227-123.

[6]  Yang, Y.G., Xu, J.H., Cai, B., Wang, Q.C., Xiu, D.P., Zhao, Z.B., Sun, Q. Z., and Cao, S. L. (2013). Synthesis and applications of black ceramic from recycled industrial wastes. Advances in Applied Ceramics, 112, 146-148.

[7]  Tanisan, B., and Turan, S. (2012). Synthesis of Fe-Mn black pigments by using hematite waste and manganese ore mixtures. Trans. Indian Ceram. Soc. Vol.71(1),17-22.

[8]  Calbo, J., Sorli, S.,  Llusar, M., Tena M.A., and Monros, G., (2004). Minimisation of toxicity in nickel ferrite black pigment. British Ceramic Transactions, Vol.103, 3-9.

[9]  Özel E., and Turan S., (2003). Production and characterisation of iron-chromium pigments and their interactions with transparent glazes. Journal of the European Ceramic Society Vol.23, 2097-2104.

[10]  Dondi, M., Zanelli, C., Ardit, M., Cruciani, G., Mantovani, L., Tribaudino, M., and  Andreozzi, G. B. (2013). Ni-free, black ceramic pigments based on Co—Cr—Fe—Mn spinels: a reappraisal of crystal structure, color and technological behaviour, Ceramic Int. 39 (8), 9533–9547.

[11]  Schabbach, L.M., Bondioli, F., Ferrari, A.M., Petter, C.O., and Fredel, M.C. (2009). Colour in ceramic glazes: Efficiency of the Kubelka–Munk model in glazes with a black pigment and opacifier, Journal of the European Ceramic Society, Vol. 29, 2685-2690.

[12]  http://www.metanikel.com.tr